Role of Diabetes Mellitus in Atrial Fibrillation and Potential New Treatments

Thesis submitted for the degree of

Doctor of Philosophy

University of Oxford

Klemen Ziberna

Division of Cardiovascular Medicine

Radcliffe Department of Medicine

&

St John's College

SUPERVISORS

Professor Barbara Casadei

Dr Ricardo Carnicer

January 2020

Abstract

Chapter 1 explains the relative importance of diabetes mellitus (DM) and cardiovascular complications in a global perspective. It then describes the current understanding of how diabetic cardiomyopathy develops and what the underlying mechanisms are. Afterwards, atrial fibrillation (AF), another DM-related complication, is presented followed by the description of the main related pathological mechanisms. Finally, the chapter discusses the therapeutic potential of tetrahydrobiopterin (BH4) as a cofactor of nitric oxide synthase (NOS).

Chapter 2 describes in full detail all methods used in the experimental work of this research thesis.

Chapter 3 shows that the myocardial overexpression of the rate-limiting enzyme for the synthesis of BH4, GTP cyclohydrolase 1 (GCH1), in mice (mGCH1-Tg) prevents the development of left ventricular (LV) diastolic dysfunction in the presence of streptozotocin (STZ)-induced diabetes. Interestingly, the mechanism underpinning this beneficial effect is not suppression of myocardial superoxide production, prevention of BH4 oxidation and restoration of coupled NOS activity, or reduction of interstitial myocardial fibrosis. Instead, the overexpression of GCH1 with an associated increase in the myocardial BH4 level and myocardial NOS activity prevents myocardial energetic impairment in diabetic hearts by increasing glucose uptake *via* the insulin-independent glucose transporter 1 (GLUT-1).

Chapter 4 explores the atrial electrophysiological characteristics of STZ diabetic mice. Diabetic mice have increased risk for *in vivo* pacing-induced AF, enlarged relative atrial size and impaired *in vivo* atrial conduction, as indicated by prolonged ECG PQ interval. Furthermore, experiments in isolated whole atria demonstrate a significant focal increase in fibrosis in the medial part of the right atrium, which results in a significant decrease in the conduction velocity in the same area followed by an increase in the conduction wave-front heterogeneity in the left atrium.

Chapter 5 investigates the electrophysiological phenotype of the mGCH1-Tg mice. The transgenic mice have lower heart rates, they spontaneously develop AV nodal escape rhythm, and have prolonged ECG QT interval. The underlying mechanisms for those changes are a global decrease in the atrial conduction velocity, decrease in the conduction through the AV node, as well an increase in the action potential duration (APD). Furthermore, oral BH4 treatment was also tested in diabetic mice, but it did not decrease the risk of AF or improved LV diastolic dysfunction significantly.

Chapter 6 summarises the key results and presents the relative impact of each finding. It also discusses the main limitations of the study as well as future research directions.

Publications

Simon JN, **Ziberna K**, Casadei B. *Compromised redox homeostasis, altered nitroso-redox balance, and therapeutic possibilities in atrial fibrillation*. Cardiovasc Res. 2016 Apr; 109(4):510-8.

Akbar N, Digby JE, Cahill TJ, Tavare AN, Corbin AL, Saluja S, Dawkins S, Edgar L, Rawlings N, **Ziberna K**, McNeill E, Oxford Acute Myocardial Infarction (OxAMI) Study, Johnson E, Aljabali AA, Dragovic RA, Rohling M, Belgard TG, Udalova IA, Greaves DR, Channon KM, Riley PR, Anthony DC, Choudhury RP. *Endothelium-derived extracellular vesicles promote splenic monocyte mobilization in myocardial infarction*. JCI Insight. 2017 Sep; 2(17).

Oster J, Hopewell JC, **Ziberna K**, Wijesurendra R, Camm CF, Casadei B, Tarassenko L. *Identification of patients with atrial fibrillation, a Big Data exploratory analysis of the UK Biobank*. Physiol. Meas. *In Press*

Carnicer R, Duglan D, **Ziberna K**, Recalde A, Reilly S, Simon JN, Mafrici S, Arya R, Rosello-Lleti E, Chuaiphichai S, Tyler D, Lygate CA, Channon KM, Casadei B. *Tetrahydrobiopterin increases GLUT1-dependent myocardial glucose uptake and preserves left ventricular function and energetics in diabetes*. *Submitted*

Other scientific communication

Ziberna K, Recalde A, Carnicer R, Casadei B. *Myocardial Overexpression of GTP Cyclohydrolase 1 Promotes Atrial Arrhythmias.*

Abstract accepted for oral presentation
Gordon Research Seminar – Cardiac Regulatory Mechanisms
New London, NH (USA), 4.-10.6.2016

Ziberna K, Recalde A, Carnicer R, Casadei B. *Streptozotocin-induced diabetes mellitus increases the risk for atrial fibrillation.*

Abstract accepted for oral presentation
52nd European Association for the Study of Diabetes Annual Meeting
Munich (Germany), 12.-16.9.2016

Ziberna K, Mafrici SF, Duglan D, Simon J, Lygate CA, Channon KM, Casadei B, Carnicer R. *Nitric oxide promotes insulin-independent glucose uptake and preserves cardiac function and energetics in diabetes.*

Abstract accepted for poster presentation
British Cardiovascular Society Annual Conference
Manchester (UK), 5-7.6.2017

Table of contents

Abstract **2**
Table of contents **5**
List of figures **9**
List of tables **13**
List of abbreviations **15**
CHAPTER 1: General introduction **18**
Diabetes mellitus and cardiovascular complications **19**
Diabetes mellitus and diabetic cardiomyopathy **21**
Pathophysiological mechanisms of diabetic cardiomyopathy **24**
OXIDATIVE STRESS *24*
INFLAMMATION *26*
ALTERED METABOLISM *26*
FIBROSIS AND CARDIAC HYPERTROPHY *27*
ALTERED CALCIUM HOMEOSTASIS *28*
AUTONOMIC NEUROPATHY *29*
Diabetes mellitus and atrial fibrillation **29**
Pathophysiological mechanisms of atrial fibrillation in diabetes mellitus **31**
BASIC ELECTROPHYSIOLOGICAL CONCEPTS ASSOCIATED WITH ATRIAL FIBRILLATION *31*
MECHANISMS IMPLICATING DIABETES MELLITUS IN ATRIAL FIBRILLATION *38*
STRUCTURAL REMODELLING *39*
ELECTRICAL REMODELLING *41*
AUTONOMIC REMODELLING *41*
OXIDATIVE STRESS *42*
DERAILED CARDIAC METABOLISM AND MITOCHONDRIAL DYSFUNCTION *44*
Nitric oxide synthase (NOS) and NO signalling **46**
GENERATION OF NO BY NOS *46*
NOS IN THE MYOCARDIUM *46*
The role of BH4 in NOS function **48**
BH4 METABOLISM *48*
NOS UNCOUPLING *50*

The therapeutic potential of tetrahydrobiopterin to prevent diabetic cardiomyopathy and atrial fibrillation **50**

Aims of the thesis **54**

CHAPTER 2: General methods **55**

Introduction **56**

Animal models **56**

C57BL/6JOLAHSD MOUSE STRAIN *56*

MICE WITH MYOCARDIAL-SPECIFIC OVEREXPRESSION OF HUMAN GTP-CYCLOHYDROLASE 1 .... *57*

MOUSE GENOTYPING PROTOCOLS *61*

Animal procedures **66**

STREPTOZOTOCIN INDUCED DIABETES MELLITUS *67*

GENERAL ANAESTHESIA *68*

ECHOCARDIOGRAPHY IN MICE *70*

IN VIVO ATRIAL ELECTROPHYSIOLOGY IN MICE *76*

DIET MODIFICATIONS (TETRAHYDROBIOPTERIN) *84*

Optical mapping of isolated atria **85**

31P magnetic resonance spectroscopy **94**

Cell shortening experiments **96**

Tissue collection **96**

Tissue processing **97**

Tissue extract protein quantification **98**

Western blot **99**

Biopterin measurements **101**

NOS activity measurements **104**

Creatine kinase activity measurements **109**

Total collagen assay **111**

Statistics **114**

CHAPTER 3: The development of diabetic cardiomyopathy is prevented in mGCH1 transgenic mice with high myocardial levels of tetrahydrobiopterin **116**

Introduction **117**

Methods **119**

ANIMAL MODELS *119*

STREPTOZOTOCIN INDUCED DIABETES MELLITUS *119*

ECHOCARDIOGRAPHY IN MICE *120*

CARDIAC 31P MAGNETIC RESONANCE SPECTROSCOPY *120*

CELL SHORTENING EXPERIMENTS *121*

HUMAN SAMPLES *121*

MOLECULAR BIOLOGY MEASUREMENTS *122*
STATISTICS *124*
Results **124**
STREPTOZOTOCIN INJECTED MICE DEVELOPED HYPERGLYCEMIA *124*
MYOCARDIAL GCH1 OVEREXPRESSION PREVENTED THE DEVELOPMENT OF LEFT VENTRICULAR DIASTOLIC DYSFUNCTION *126*
DIABETIC MICE DID NOT HAVE INCREASED MYOCARDIAL OXIDATION OF BH4 OR INCREASED SUPEROXIDE PRODUCTION *131*
MYOCARDIUM OF DIABETIC PATIENTS DID NOT HAVE REDUCED BH4 AVAILABILITY OR INCREASED SUPEROXIDE PRODUCTION *133*
MYOCARDIAL GCH1 OVEREXPRESSION DID NOT PREVENT THE DIABETES-INDUCED MYOCARDIAL FIBROSIS *137*
MYOCARDIAL GCH1 OVERXPRESSION PREVENTED THE DECLINE IN THE CARDIAC ENERGY AVAILABILITY *139*
Discussion **145**
CHAPTER 4: Atrial electrophysiological disturbances in diabetes mellitus **154**
Introduction **155**
Methods **156**
ANIMAL MODELS *156*
STREPTOZOTOCIN INDUCED DIABETES MELLITUS *157*
IN VIVO ATRIAL ELECTROPHYSIOLOGY IN MICE *157*
ECHOCARDIOGRAPHY IN MICE *158*
OPTICAL MAPPING OF ISOLATED ATRIA *158*
MOLECULAR BIOLOGY MEASUREMENTS *159*
Results **159**
MULTIPLE LOW DOSE STREPTOZOTOCIN INJECTIONS RESULT IN STABLE HYPERGLYCAEMIA WITHOUT SEVERE ADVERSE SIDE-EFFECTS *159*
ELECTROPHYSIOLOGY AND PACING INDUCED ARRHYTHMIAS *160*
DIABETIC MICE HAVE MODEST LEFT VENTRICULAR DIASTOLIC DYSFUNCTION, RELATIVE LEFT ATRIAL ENLARGEMENT, BUT NO LEFT VENTRICULAR SYSTOLIC DYSFUNCTION *162*
OPTICAL MAPPING OF ISOLATED PERFUSED ATRIAL PREPARATIONS . *171*
TOTAL COLLAGEN CONTENT OF RIGHT AND LEFT ATRIA *178*
Discussion **179**
CHAPTER 5: The effect of increased levels of tetrahydrobiopterin on atrial electrophysiology and potential role in the treatment of diabetes-induced atrial fibrillation BH4 electrophysiology **188**
Introduction **189**
Methods **190**
ANIMAL MODELS *190*

STREPTOZOTOCIN INDUCED DIABETES MELLITUS *191*
ECHOCARDIOGRAPHY IN MICE.. *192*
IN VIVO ATRIAL ELECTROPHYSIOLOGY IN MICE *192*
MOLECULAR BIOLOGY MEASUREMENTS *193*
OPTICAL MAPPING OF ISOLATED ATRIA.. *193*
STATISTICS.. *194*
Results.. 195
MYOCARDIAL GCH1 OVEREXPRESSION INCREASES THE ATRIAL BH4 CONCENTRATION AND INCREASES THE MYOCARDIAL NOS ACTIVITY... *195*
MICE WITH MYOCARDIAL GCH1 OVEREXPRESSION HAVE SLOWER HEART RATE AND LONGER QT INTERVAL.. *196*
MICE WITH MYOCARDIAL GCH1 OVEREXPRESSION HAVE FREQUENT EPISODES OF AV NODAL ESCAPE RHYTHM *199*
MICE WITH MYOCARDIAL GCH1 OVEREXPRESSION DO NOT HAVE HIGHER PROBABILITY OF PACING INDUCED ATRIAL ARRHYTHMIAS.... *201*
MICE WITH MYOCARDIAL GCH1 OVEREXPRESSION HAVE SLOWER AV NODE CONDUCTION *202*
MICE WITH MYOCARDIAL GCH1 OVEREXPRESSION HAVE LONGER ACTION POTENTIAL DURATION AND SLOWER CONDUCTION VELOCITY *204*
ORAL BH4 SUPPLEMENTATION INCREASES THE ATRIAL BH4 LEVELS AND INCREASES THE NOS ACTIVITY.. *208*
ORAL BH4 SUPPLEMENTATION DOES NOT AFFECT PLASMA GLUCOSE LEVELS OR BODY WEIGHT IN DIABETIC MICE... *211*
BH4 SUPPLEMENTATION DOES NOT REVERSE THE DIABETES INDUCED ELECTROPHYSIOLOGICAL DISTURBANCES.. *212*
BH4 SUPPLEMENTATION DOES NOT REVERSE THE DIABETES INDUCED DIASTOLIC DYSFUNCTION *215*
Discussion 217
CHAPTER 6: Conclusions and general discussion 231
Key findings and implications 232
Future work 239
Main limitations of the study.. 244
Final conclusion 246
REFERENCES 247
APPENDIX 277
Action potential duration calculation 278
Atrial masking for optical mapping.. 291
Analysis of the radioactively labelled products of arginine metabolism 296

List of figures

Figure 1-1 *Schematic illustration of the action patient and main mechanisms involved in the abnormal ectopic firing* 33

Figure 1-2 *Schematic diagram presenting the main factors contributing to the re-entry mechanism of maintenance of arrhythmia* 36

Figure 1-3 *Mechanisms connecting diabetes mellitus and atrial fibrillation* 39

Figure 1-4 *Pathways of BH4 synthesis* 49

Figure 2-1 *Construction of the human GTP-cyclohydrolase 1 (GCH1) transgene* 59

Figure 2-2 *An example of a representative mGCH1-Tg genotyping electrophoresis gel image* 63

Figure 2-3 *An example of a representative Nnt genotyping electrophoresis gel image* 66

Figure 2-4 *An example of plasma glucose (Glc) and body weight (BW) changes over the course of 12 weeks in diabetic and control mice* ... 68

Figure 2-5 *Echocardiography imaging protocol* 71

Figure 2-6 *Examples of echocardiographic recordings demonstrating different views and modalities* 72

Figure 2-7 *Echocardiographic assessment of left atrial size* 73

Figure 2-8 *Bland-Altman plots of the most important echocardiographic parameters measured by two different operators* 75

Figure 2-9 *Schematic representation of the transoesophageal atrial pacing procedure* 77

Figure 2-10 *An example of successful transoesophageal atrial pacing and return to sinus rhythm* 78

Figure 2-11 *Representative traces for measuring SNRT, Wenckebach cycle length, and AV ERP* 80

Figure 2-12 *An example of the heart rate variability (HRV) analysis* 82

Figure 2-13 *Bland-Altman plots of the ECG parameters and the probability of atrial arrhythmias measured by two different observers* 83

Figure 2-14 *Preparation, storage, and dispensing of tetrahydrobiopterin (BH4) supplemented diet.* 85
Figure 2-15 *A picture of pinned down isolated mouse atria prepared for optical mapping recordings* 86
Figure 2-16 *Setup of the optical mapping equipment* 89
Figure 2-17 *A representative signal from the optical mapping recordings and automatic measurements of APD* 91
Figure 2-18 *Main steps in automatic outlining of the atrial region* 93
Figure 2-19 *Ccoffinn analysis of conduction in isolated atria* 94
Figure 2-20 *Representative spectral trace from ^{31}P-MRS in isolated perfused hearts* 95
Figure 2-21 *HPLC setup to sequentially measure the concentrations of tetrahydrobiopterin, dihydrobiopterin, and biopterin* 102
Figure 2-22 *Representative HPLC detector traces for measuring the concentrations of tetrahydrobiopterin, dihydrobiopterin, and biopterin* 104
Figure 2-23 *Metabolic pathways of arginine and significance for NOS activity measurements* 105
Figure 2-24 *HPLC setup to measure the ^{14}C radiolabelled products of arginine metabolism* 108
Figure 2-25 *Representative HPLC detector traces for measuring the ^{14}C radiolabelled products of arginine metabolism* 109
Figure 2-26 *An example of a 96-well plate used for the total collagen assay* 113
Figure 2-27 *An example of the collagen standard curve with superimposed values for the samples* 115
Figure 3-1 *Body weight and plasma glucose in mGCH1-Tg diabetic mice* 125
Figure 3-2 *Plasma insulin concentration at the end of the diabetic protocol* 126
Figure 3-3 *Echocardiographic assessment of LV diastolic and LV systolic function in mGCH1-Tg diabetic mice* 128
Figure 3-4 *Cardiomyocyte shortening in mGCH1-Tg diabetic mice* 130
Figure 3-5 *Myocardial BH4 concentration and NOS activity in mGCH1-Tg diabetic mice* 132
Figure 3-6 *Superoxide production in the LV of mGCH1-Tg diabetic mice* 133

Figure 3-7 *Myocardial BH4 and BH4:BH2+B ratio in patients with DM* 136
Figure 3-8 *Superoxide production in patients with DM* 136
Figure 3-9 *Assessment of cardiac fibrosis in mGCH1-Tg diabetic mice* 138
Figure 3-10 *Measurement of the PCr/ATP ratio in mGCH1-Tg diabetic mice using ^{31}P-MRS in isolated perfused hearts* 140
Figure 3-11 *Enzymatic activity of citric synthase, mitochondrial CK, and cytosolic CK in mGCH1-Tg diabetic hearts* 142
Figure 3-12 *Immunoblots and quantification of VDAC, UCP3, GLUT1, GLUT4 protein levels in mGCH1-Tg hearts* 144
Figure 4-1 *Plasma glucose and body-weight in diabetic mice* 160
Figure 4-2 *Quantification of pacing-induced atrial arrhythmias in diabetic mice* 161
Figure 4-3 *LV diastolic and systolic volumes in diabetic mice* 165
Figure 4-4 *LV mass and indexed LV mass in diabetic mice* 166
Figure 4-5 *LV ejection fraction and cardiac index in diabetic mice* 166
Figure 4-6 *LV diastolic function (E'/A', E/A, E/E') in diabetic mice* 167
Figure 4-7 *LA area and indexed LA area in diabetic mice* 167
Figure 4-8 *Correlation analysis between AF probability, tissue Doppler E'/A', indexed LA area and plasma glucose in diabetic mice* 169
Figure 4-9 *Correlation analysis between AF probability, PQ interval, indexed LA area, tissue Doppler E'/A', PQ interval, and P wave duration in diabetic mice* 170
Figure 4-10 *Action potential duration in RA and LA of diabetic mice* 171
Figure 4-11 *A representative activation map of the isolated perfused atrial preparation of diabetic mice* 172
Figure 4-12 *Conduction time in RA and LA of diabetic mice* 173
Figure 4-13 *Dimensions and total area of isolated diabetic atria* 173
Figure 4-14 *Electrical wave conduction and organizational properties obtained using automated wave tracking analysis of optical mapping recordings in whole perfused isolated atria* 175
Figure 4-15 *Regional variation of electrical wave conduction and organizational properties in diabetic atria* 177
Figure 4-16 *Mass of frozen RA and LA tissue of diabetic mice* 178

Figure 4-17 *Regional variation of total collagen content in diabetic atria* 179
Figure 5-1 *A timeline of the BH4 supplementation study in diabetic mice*.......... 192
Figure 5-2 *mGCH1-Tg atria have increased BH4 concentration in atria and increased NOS activity*.. 196
Figure 5-3 *ECG RR, QT, and QTc interval of mGCH1-Tg mice*......................... 198
Figure 5-4 *Comparison of the uncorrected QT and corrected QT interval of mGCH1-Tg mice* 199
Figure 5-5 *Incidence of AV nodal escape rhythm, PVC, and VT in mGCH1-Tg mice* 200
Figure 5-6 *Quantification of pacing-induced atrial arrhythmias in mGCH1-Tg mice* 202
Figure 5-7 *Heart rate variability (HRV) analysis in mGCH1-Tg mice* 204
Figure 5-8 *APD measurements in isolated atria of mGCH1-Tg mice*................. 205
Figure 5-9 *APD in RA and LA after incubation with AAAN*............................... 206
Figure 5-10 *A representative activation map of the isolated perfused atrial preparation of mGCH1-Tg mice* 207
Figure 5-11 *Conduction time in RA and LA in atria of mGCH1-Tg mice* 208
Figure 5-12 *Concentration of biopterins and NOS activity in atria of diabetic mice treated with BH4* 210
Figure 5-13 *Quantification of pacing-induced atrial arrhythmias in diabetic mice treated with BH4*.. 213
Figure 5-14 *Frequency of different spontaneous arrhythmias observed in the ECG recordings of diabetic mice treated with BH4* 214
Figure 5-15 *Echocardiographic assessment of LV diastolic function of diabetic mice treated with BH4*.. 216
Figure 5-16 *Echocardiographic assessment of LA dimensions and indexed LA area of diabetic mice treated with BH4* 216

List of tables

Table 2-1 *Reagents and primers for genotyping of mGCH1-Tg mice*................62
Table 2-2 *A summary of polymerase chain reaction (PCR) reagent volumes and thermal cycle temperatures*..62
Table 2-3 *Two primer pairs used to test for the deletion of nicotinamide nucleotide transhydrogenase (Nnt) gene* 64
Table 2-4 *Polymerase chain reaction (PCR) for genotyping the presence of Nnt deletion in mice* 65
Table 2-5 *Specifications of the Tyrode solution used in the electrophysiological experiments*..87
Table 2-6 *Specifications of the Krebs solution used in the electrophysiological experiments*..88
Table 2-7 *Specifications of the Krebs-HEPES solution used in the NOS activity measurements*..106
Table 2-8 *Preparation of standard collagen dilutions*......................................112
Table 2-9 *An example of the tissue sample dilution preparation for use with the total collagen assay*..112
Table 3-1 *Echocardiographic measurements evaluating LV size, LV systolic and diastolic function in mGCH1-Tg diabetic mice* 127
Table 3-2 *Patient characteristics of diabetic patients and non-diabetic matched controls where myocardial BH4 concentration and myocardial superoxide production was determined*..........................135
Table 4-1 *ECG properties of diabetic mice compared to their control littermates*..162
Table 4-2 *Echocardiographic measurements evaluating LV size, mass, systolic and diastolic function, cardiac times, and LA dimensions of diabetic mice* 164
Table 5-1 *ECG properties of mGCH1-Tg mice*...197
Table 5-2 *In vivo atrial electrophysiological characteristics of mGCH1-Tg mice* 203

Table 5-3 *Body weight and plasma glucose over the course of the BH4 supplementation study in diabetic mice* 211
Table 5-4 *ECG properties of diabetic mice treated with BH4* 214

List of abbreviations

A	late mitral blood flow velocity
A'	late tissue Doppler mitral annulus velocity
AAAH	aromatic amino acid hydroxylases
AAAN	N-[(4S)-4-Amino-5-[(2-aminoethyl](amino]pentyl]-N'-nitroguanidine (tissue permeable NOS inhibitor)
ACE	angiotensin-converting enzyme
AF	atrial fibrillation
AGE	advanced glycation end-products
ANOVA	one-way analysis of variance
ANP	atrial natriuretic peptide
AP	action potential
APD	action potential duration
AUC	area under the curve
AV ERP	AV node effective refractory period
B	biopterin
BCA	bicinchoninic acid
BH2	dihydrobiopterin
BH4	tetrahydrobiopterin
BMI	body mass index
BNP	brain natriuretic peptide also known as B-type natriuretic peptide
bpm	beats per minute
BSA	bovine serum albumin
BW	body weight
CABG	coronary artery bypass graft surgery
CaMK	Ca/calmodulin kinase
Ccoffinn	Cardiomyocyte Cultures Optically-mapped: Fast Feature extractIoN and tracking toolkit
CK	creatine kinase
CKD	chronic kidney disease
CL	cycle length
CS	citric synthase
CV	conduction velocity
CVD	cardiovascular disease
Cx	connexin – gap junction protein
DAD	delayed afterdepolarization
DAG	diacylglycerol
DHE	dihydroethidium
DM	diabetes mellitus
DNA	deoxyribonucleic acid
DTE	dithioerythritol
E	early mitral blood flow velocity
E'	early tissue Doppler mitral annulus velocity
EAD	early afterdepolarization

ECG	electrocardiogram
EDD	end-diastolic diameter
EDTA	ethylenediaminetetraacetic acid
EF	ejection fraction
EOH	2-hydroxyethidium
ESD	end-systolic diameter
ET	ejection time
FA	fatty acid
FAD	flavin adenine dinucleotide
FMN	riboflavin 5′-monophosphate
FS	fractional shortening
GAPDH	glyceraldehyde 3-phosphate dehydrogenase
GCH1	GTP cyclohydrolase 1
Glc	glucose
GLUT-1	myocardial glucose transporter 1
GLUT-2	myocardial glucose transporter 2
GLUT-4	myocardial glucose transporter 4
GTP	guanosine triphosphate
GTP	guanosine triphosphate
HA	human influenza haemagglutinin
HbA1c	glycated haemoglobin
HF	heart failure
HPLC	high-performance liquid chromatography
HR	heart rate
HRV	heart rate variability
IQR	interquartile range
IVC	inferior vena cava
IVCT	isovolumetric contraction time
IVRT	isovolumetric relaxation time
LA	left atrium
L-NAME	Nω-Nitro-L-arginine methyl ester hydrochloride
LV	left ventricle
MAPK	mitogen-activated protein kinase
mGCH1-Tg	transgenic mouse with myocardial specific overexpression of GCH1
MI	myocardial infarction
Mito CK	mitochondrial isoform of creatine kinase
MPTP	mitochondrial permeability transition pores
MRS	magnetic resonance spectroscopy
MW	molecular weight
NADPH	β-nicotinamide adenine dinucleotide 2'-phosphate
NCX	Na^+-Ca^{2+} exchanger
NF-κB	nuclear factor kappa-light-chain-enhancer of activated B cells
Nnt	nicotinamide nucleotide transhydrogenase gene
nor-NOHA	Nω-hydroxy-nor-Arginine (arginase inhibitor)
NOS	nitric oxide synthase
NRF2	nuclear erythroid 2-related factor 2
OR	odds ratio
OTC	ornithine transcarbamylase
PAD	peripheral arterial disease

PBS	phosphate-buffered saline
PCR	polymerase chain reaction
PCr	phosphocreatine
PKC	protein kinase C
PLB	phospholamban
PVC	premature ventricular contraction
PVDF	polyvinylidene difluoride
qBH2	quinonoid dihydrobiopterin
QTc	ECG QT interval corrected for the RR interval
RA	right atrium
RAGE	receptor for advanced glycation end-products
RIPA	radioimmunoprecipitation assay buffer
ROI	region of interest
ROS	reactive oxygen species
RR	relative risk
RV	right ventricle
RyR	ryanodine receptor
SAN	sinoatrial node
SD	standard deviation
SEM	standard error of the mean
SERCA2a	sarco/endoplasmic reticulum Ca^{2+}-ATPase
SGLT2	sodium-glucose transport protein 2
SNRT	sinus node recovery time
SR	sinus rhythm
STZ	streptozotocin
SVC	superior vena cava
T1DM	type 1 diabetes mellitus
T2DM	type 2 diabetes mellitus
TAC	transverse aortic constriction
TBS-T	Tris-buffered saline containing 10% Tween
TCA	trichloroacetic acid
TDI	tissue Doppler imaging
Tg DM	mGCH1-Tg diabetic mouse
TLR	toll-like receptor
TnI	troponin I
TXNIP	thioredoxin-interacting protein
UCP3	uncoupling protein 3
VDAC	voltage-dependent anion channel
VT	ventricular tachycardia
WT	wild-type
WT DM	wild-type diabetic mouse
α-MHC	alpha myosin heavy chain

CHAPTER 1:

General introduction

Diabetes mellitus and cardiovascular complications

Diabetes mellitus (DM) is a chronic metabolic disease where either the release of the endocrine hormone insulin is insufficient to maintain the normal plasma glucose levels (type 1 DM) or peripheral tissue cannot uptake glucose sufficiently as a result of the insulin resistance (type 2 DM). DM is one of the most important causes of morbidity and early mortality. It is estimated that DM accounts for 14.5% of global all-cause mortality in people aged between 20 and 79 years (1). The worldwide estimated prevalence of DM in 2019 is 9.3% (463 million people) and is estimated to increase to 10.2% (578 million) by 2030 and to 10.9% (700 million) by the year 2045 (2, 3). Prevalence is increasing with age, and was 1.4% among adults aged 20-24 and 19.9% in adults aged 75-79 in 2019. There are only minor gender differences in the estimated prevalence of DM in 2019: 9.0% in women, and 9.6% in men (1, 3). Type 2 DM represents roughly 85% of diabetes cases, type 1 DM 10-15% cases, whereas other types (gestational DM, drug-induced DM, different endocrinopathies, and genetic disorders) account for the remaining 1-5% of cases (4). Furthermore, undiagnosed diabetes is a large global problem since 50.1% of diabetics are unaware of their condition (1). Early diagnosis can lead to appropriate care and thus DM and its complications can be managed to prevent disability and death.

Patients with DM are at higher risk for developing several debilitating chronic complications, such as diabetic retinopathy (35% prevalence with significant vision loss in 12% of patients) (5), chronic kidney disease as a result of the diabetic nephropathy (25-36% prevalence) (6, 7), diabetic peripheral neuropathy (prevalence ranging from 16% to 87%) (8), cardiovascular diseases (32% prevalence) (9), and peripheral artery disease (15% prevalence). In addition, DM is associated with premature death from several cancers, infectious diseases, and neurodegenerative disorders, increased risk for adverse pregnancy outcomes, as well as an increased hazard for death from any cause (10-12).

Cardiovascular complications in patients with DM are the leading cause of early and excess mortality associated with DM (13). A meta-analysis of more than 100 prospective clinical studies showed that patients with DM have around a 2-fold increase in all cardiovascular complications and a similar excess risk for death due to the coronary artery disease and other deaths related to cardiovascular complications (14). Even greater and more detailed insight into excess risk for cardiovascular diseases in patients with type 2 DM came from a recent report from the Swedish National Diabetes Register (15). This study further confirmed the association between the DM and cardiovascular complications. DM was shown to be particularly debilitating in patients who were diagnosed with DM at an early age. Patients with a type 2 DM diagnosis at an age of less than 40 years had a increased relative risk for cardiovascular complications (compared to matched controls without DM): 2.05 for total mortality, 2.72 for cardiovascular-related mortality, 4.33 for coronary artery disease, 3.41 for acute myocardial infarction, 3.58 for stroke, 4.77 for heart failure (HF), and 1.95 for atrial fibrillation (AF) (15).

Increased risk for atherosclerotic cardiovascular disease in patients with DM cannot be fully explained by main risk factors such as age, hypertension, dyslipidaemia, smoking, etc. Hyperglycaemia alone is an important independent risk factor (16, 17). For every 1% increase in HbA1C levels, there is a 14% increase in the risk for myocardial infarction (18). Hyperglycaemia can simultaneously impair multiple components of vascular function. Increased glucose level causes endothelial dysfunction by reducing nitric oxide bioavailability and impairing endothelium-dependent vasodilation, it can increase leukocyte adhesion in endothelial cells and impairs fibrinolytic function (19, 20). Hyperglycaemia also induces proliferation of the vascular smooth muscle cells and activates pro-inflammatory responses in monocytes and macrophages resulting in accelerated atherosclerosis (21, 22).

While there is a strong body of evidence for DM-induced atherosclerotic cardiovascular disease (CVD), there is a less scientific understanding of the involvement of DM in increased risk for other cardiovascular complications, such as diabetic cardiomyopathy and AF. Interestingly, both pathologies can occur in the absence of the underlying atherosclerotic CVD. This suggests that DM is an independent cause of these myocardial changes in atria and ventricles with a complex and multifactorial pathogenesis. Indeed, even patients with DM who are well managed and incorporate all novel pharmacological approaches are still at increased risk for CVD compared to the non-DM patients, therefore there is an urgent need to develop novel targeted therapeutic strategies (23).

Diabetes mellitus and diabetic cardiomyopathy

Diabetic cardiomyopathy is defined as the presence of abnormal cardiac structure and ventricular dysfunction in the absence of other cardiovascular risk factors, such as coronary artery disease, hypertension, and significant valvular disease in patients with DM (24, 25). Several epidemiological studies lead to the finding that DM is a distinct type of myocardial dysfunction. Observations from the Framingham Heart Study showed that female patients with DM have a relative risk (RR) of 2.4 to develop the HF compared to the non-diabetic females, and males with DM have a RR of 5.1 for HF compared to the non-diabetic males (26). The increased risk for HF in DM was independent of concomitant coronary artery disease or hypertension (27). Clinical studies showed that the prevalence of HF in patients with DM is ranging from 4% to 30% (13). Patients with type 2 DM and type 1 DM both had similarly increased risk for developing HF (28).

Diabetic cardiomyopathy, as a specific clinical entity, has been unrecognized for a long time. Therefore, the knowledge of the underlying pathophysiological mechanisms, as well as the details of the natural progression of the disease are not completely understood. Diabetic cardiomyopathy is considered to be asymptomatic at early stages with an early subtle left ventricular (LV) diastolic dysfunction (16, 29). The condition then progresses to the state with a clear LV diastolic dysfunction with or without LV hypertrophy, which is then followed by the symptomatic heart failure with LV systolic dysfunction and LV dilatation. Importantly, LV hypertrophy is a strong predictor of adverse cardiovascular outcomes (30).

This progression of the diabetic cardiomyopathy has been mainly described in animal models of diabetes, whereas the evidence that the diabetic cardiomyopathy in patients with DM progresses in that manner is not entirely clear (13, 31, 32). Particularly patients with type 2 DM often have other comorbidities such as obesity, hypertension, chronic kidney disease, various extent of atherosclerosis with or without peripheral artery disease, and coronary artery disease; all of them can independently cause cardiac dysfunction (13, 16). Thus, it is difficult to differentiate between the consequences of the longstanding DM and effect of other comorbidities on the progressive dysfunction. Furthermore, some authors even argue that the diabetic cardiomyopathy is not a disease that progresses successively from LV diastolic dysfunction to severe LV systolic dysfunction, but rather consider those two as separate entities with different underlying mechanisms (33). On the one hand, the DM can cause a restrictive phenotype with LV diastolic dysfunction and maintained LV ejection fraction (EF), on the other hand, the DM can cause a dilated cardiac phenotype with reduced EF by a different pathological process (33). Patients with a longer duration of the DM have increased risk of being impaired by both forms of cardiac dysfunction (29).

Not only we do not fully understand the clinical progression of the diabetic cardiomyopathy, but we also do not have a clear and unified comprehension of all involved pathophysiological mechanisms. The main disturbances in patients with type 2 DM are hyperglycaemia, insulin resistance, and hyperinsulinemia (16). The main disturbance in patients with type 1 DM is hyperglycaemia without hyperinsulinemia; however, in contrast to patients with type 2 DM, here the native insulin secretion is impaired and the patients are generally treated with exogenous insulin. While exogenous insulin is successful in maintaining normal plasma glucose levels, it cannot perfectly mimic the complex secretion cycles of native insulin. This discrepancy in insulin effects is hypothesized to be one of the causes of cardiac dysfunction in patients with type 1 DM (28). It must be noted that the underlying mechanisms driving the pathogenesis of diabetic cardiomyopathy may be different among both types of DM. Indeed, no studies found myocardial steatosis in type 1 DM in comparison to the hearts of patients with type 2 DM where steatosis often precedes the diastolic dysfunction (34, 35).

Pathophysiological mechanisms of diabetic cardiomyopathy

There are several mechanisms proposed to explain the pathogenesis of the diabetic cardiomyopathy at the cellular and subcellular level. Hyperglycaemia and impaired insulin signalling result in an increase of oxidative stress and inflammation, abnormal extracellular matrix deposition, mitochondrial dysfunction, and metabolic abnormalities in energy production, impaired calcium handling, and cardiac autonomic neuropathy, among others.

OXIDATIVE STRESS

Increased oxidative stress is one of the features of diabetic cardiomyopathy. In the myocardium of diabetic patients, increased oxidative stress was associated with mitochondrial dysfunction caused by an increase in sensitivity to the calcium of mitochondrial permeability transition pore (36, 37). This led to autophagy of cardiomyocytes and cardiac necrosis (37). However, the detailed mechanistic explanation of the effects of oxidative stress within the cardiomyocytes of patients with DM is largely unknown. Nevertheless, studies using cell lines and isolated cardiomyocytes from animal diabetic models suggest several potential mechanisms.

Direct exposure of cardiac myoblasts to high levels of glucose increased intracellular ROS within 3 hours of incubation (38). Increased oxidative stress in diabetic myocardium was detected by several approaches, such as increased lipid peroxidation, hydroxyl radicals, superoxide anions, and nitrotyrosine levels (39-42). The main sources of ROS are mitochondria, xanthine oxidases, lipoxygenases, cyclooxygenases, peroxidases, and NOS (43). Furthermore, hyperglycaemia also decreased the total low-molecular-weight antioxidant capacity in diabetic hearts (44). Hyperglycaemia can also lead to increased non-enzymatic glycation reactions between glucose and amino groups on proteins, which generate ROS. These products then degrade into aldehydes, such as 3-deoxyglucosone, which can crosslink proteins and lead to advanced glycation end products (AGEs) formation (45). Furthermore, AGEs can stimulate ROS and RNS formations in tissues. AGEs bind to RAGE receptors and activate mitogen-activated protein kinase (MAPK) and diacylglycerol (DAG)-protein kinase C (PKC) pathways (46). Activated PKC increases nicotinamide adenine dinucleotide phosphate oxidase system (NADPH oxidase), which generates superoxide anions (47). Some studies suggested that increased superoxide production by NADPH oxidases in cardiomyocytes is considered as one of the key pathways involved in diabetic cardiomyopathy (41, 48). In addition, some authors presented evidence of iNOS uncoupling in diabetic mouse hearts also leading to increased superoxide formation (49).

Oxidants can modulate protein function by reversibly modifying cysteine and methionine amino acids (50). Nitrosylation, sulphenylation, and glutathionylation activate specific redox-activated kinases (e.g. CaMKII, ERK1, ERK2, JNK), or also result in a direct loss of function of the protein, and they can also target gene expression by modifying the transcription factors. Furthermore, mitochondrial ROS can also increase the open probability of the mitochondrial permeability transition pores (MPTP) causing autophagy and necrosis (29). A severe increase in oxidants can also cause the DNA damage, as demonstrated in a study in endothelial cells where hyperglycaemia triggered redox imbalance and DNA strand breaks (51). Increased oxidative stress also activates cardiac fibroblast activity, and thereby cardiac remodelling and increased interstitial fibrosis (52).

The mechanisms involved in cardiac fibrosis are presented in more detail in a later section.

INFLAMMATION

Patients with diabetic cardiomyopathy have chronic low-grade inflammation, which starts early during DM progression as a response to myocardial injury (53). Hearts of patients with DM have increased activation of multiple inflammatory cytokines such as nuclear factor-kappaB (NF-kappaB) and related upregulation of pro-inflammatory cytokines, such as interleukins (IL-6, IL-1β), tumour necrosis factor-α (TNF-α), chemokines (MCP-1 and others), and adhesion molecules (VCAM-1, ICAM-1, and others) (54). Some studies also showed the activation of cardiac toll-like receptors and inflammasome complexes leading to NF-kappaB activation (55). Increased inflammation results in pathological cardiac remodelling, increased interstitial fibrosis, and also in an increase in oxidative stress (29). Myocardial inflammation can also trigger programmed cell death, as seen by an increased number of apoptotic cardiomyocytes in biopsies from patients with diabetic cardiomyopathy in comparison to non-diabetic patients (56).

ALTERED METABOLISM

The healthy adult heart uses free fatty acids (FFAs) as the preferred energy substrate to produce ATP, but can metabolically adapt to use a variety of other substrates, such as glucose, lactate, ketone bodies, and some of the amino acids. However, hyperglycaemia and insulin resistance lead to the loss of metabolic substrate flexibility (57). Thus, the inability to switch to glucose as energy substrate leads to the increase of FFA transporters, higher uptake and internalization of FFAs, as well as an increase of FFA oxidation (34).

Increased FFA utilization leads to impaired oxidative phosphorylation and higher mitochondrial ROS generation, as well as decreased overall cardiac energy efficiency (58). Moreover, an excessive accumulation of FFAs is toxic to the cardiomyocytes and can lead to a decrease in autophagy and an increase in apoptosis (59). Correspondingly, myocardial triglyceride contents assessed by MR spectroscopy are associated with left ventricular diastolic dysfunction in human diabetic hearts (35, 60). However, FFA uptake and beta-oxidation are not always altered in diabetic hearts (61).

Abnormal glucose metabolism also leads to increased polyol pathway of glucose metabolism in diabetic hearts. In this route, aldose reductase reduces glucose to sorbitol in the presence of NADPH, and then sorbitol is oxidized by sorbitol dehydrogenase to fructose, coupled with the reduction of NAD^+ to NADH (62). The increased ratio of NADH/ NAD^+ increases ROS and RNS production by several pathways, such as NADH autoxidation, activation of xanthine oxidase, and inactivation of superoxide dismutase (38, 63).

FIBROSIS AND CARDIAC HYPERTROPHY

Another pathological mechanism involves abnormal extracellular matrix remodelling, which is characterized by an increase in collagen deposition, upregulation of pro-fibrotic factors leading to abnormal protein deposition, and a decrease in the activity of degrading enzyme metalloproteinases (64-66). In addition to the fibrosis in the diabetic heart, there is also AGE formation and deposition with the ability to cross-link collagen molecules, and thus further inhibit their proteolytic degradation (67). Furthermore, AGEs also bind to their cell membrane receptors (RAGE and AGE-R3), thereby increasing expression of oxidative stress mediators and promoting pro-fibrotic and pro-inflammatory signalling

(68, 69). Accumulation of misfolded proteins was also observed inside diabetic cardiomyocytes likely due to the loss of function of the cardiac ubiquitin-proteasome system (UPS), which is responsible for the degradation of misfolded and oxidized proteins (70). UPS dysfunction is an early event in diabetic heart development that is also involved in triggering the pathological heart remodelling (70, 71).

In addition to the fibrosis, LV hypertrophy develops also as a result of cardiomyocyte hypertrophy. Hyperglycaemia can induce cardiac hypertrophy in type 2 DM animal models (31, 72), but also under in vitro conditions where high glucose levels increased cardiomyocyte size. Hyperglycaemia also increases the serum levels of angiotensin II, which stimulates cardiomyocyte hypertrophy and proliferation of cardiac fibroblasts (73). Moreover, a diabetic heart has upregulated hypertrophic genes, such as atrial natriuretic peptide (ANP), B-type natriuretic peptide (BNP), and B-myosin heavy chain (69, 72).

ALTERED CALCIUM HOMEOSTASIS

Another plausible mechanism for the development of the diabetic cardiomyopathy is the impaired calcium homeostasis in cardiomyocytes, which was confirmed in several animal models of both type 1 and type 2 DM. In particular, several studies reported decreased expression an impaired function of ryanodine receptor (RyR), lower activity of sodium-calcium exchanger (NCX), lower activity of sarcoplasmic reticulum calcium pump 2a (SERCA2a), as well as lower activity of plasma membrane calcium ATPase (74-77). Deficient calcium handling leads to defective excitation-contraction coupling, which is one of the characteristic features of the diabetic heart (78).

AUTONOMIC NEUROPATHY

DM is also associated with autonomic neuropathy and can (among others) result in several cardiac complications, such as a reduction in heart rate variability, resting tachycardia, orthostatic hypotension, and sudden death syndrome (79). Progression of autonomic neural dysfunction in DM is compensated by the increase in the cardiac sympathetic tone (80). As a result, this enhances the activation of beta-1 adrenergic receptors, which in the long-term promotes cardiac hypertrophy, interstitial fibrosis, and cardiomyocyte apoptosis (81).

Diabetes mellitus and atrial fibrillation

Atrial fibrillation (AF) is the most common heart rhythm disorder. AF is associated with considerable morbidity, decreased quality of life, and increased mortality as a consequence of abnormal hemodynamics, atrioventricular dyssynchrony, atrial and ventricular mechanical dysfunction, and thromboembolic events (82). AF is related to 25-33% of ischemic strokes (83, 84).

Prevalence of AF in the general population is 1-2% and greatly depends on age, with an estimated 2-fold increase in every decade ranging from 0.1% for adults younger than 55 years, to 9.0% for persons older than 80 years (82, 85, 86). This phenomenon is mainly attributable to an increase in life expectancy and to a lesser extent to a reduction of early deaths from coronary artery disease, decrease in AF-related mortality by use of anticoagulants, and by increase in the prevalence of risk factors for AF (82).

Rather than being a primary electrophysiological condition, AF is usually the final common pathway of several different cardiac and non-cardiac predisposing conditions. Several risk factors for AF are now well established with the most important being: age (2.1-fold risk increase with every decade), male sex (RR 1.5), hypertension (RR 1.7), coronary artery disease (RR 2.2-3.6), valvular heart disease (RR 1.8-3.4), chronic heart failure (RR 4.5-5.9), smoking (RR 1.5), obstructive sleep apnoea (RR 2.2), obesity with BMI $\geq$30 kg/m^2 (RR 1.5-1.7), and type 2 diabetes mellitus (RR 1.4-2.1) (82, 85).

The Framingham Heart Study was the first to demonstrate that DM is an independent risk factor for developing AF (87). Several different prospective observational cohort studies and population-based-case-control studies, as well as meta-analysis, have confirmed this association (88-91). Based on the meta-analysis of 11 studies, the relative risk for developing AF in patients with type 2 DM is 1.39 (95% CI 1.07-1.68) (91). Similarly, a study from the Swedish National Diabetes Register also demonstrated an increased relative risk for AF in patients with T1DM (RR 1.13 for men, RR 1.50 for women) (92).

Poorly controlled DM, as characterised by raised HbA1C levels, increase the risk for AF in patients with T1DM and T2DM (89, 90, 92, 93). However, while tight glucose control targeting normal HbA1c levels (i.e. <7.0%) significantly decrease the incidence of microvascular complications (e.g. retinopathy, neuropathy, and nephropathy), the intensified glucose control did not decrease the risk for AF (compared to the standard treatment regime) (13, 94). Therefore, the optimal glucose-lowering strategy for prevention of diabetes-related AF may not be the same as for the prevention of other complications, specially when considering that hypoglycaemia alone can also induce AF (95, 96). Furthermore, a study in animal diabetic models showed that glucose fluctuations increase the incidence of pacing-induced AF to an even greater degree when compared to a group with constant hyperglycaemia (97).

It must be noted that risk factors other than hyperglycaemia may also mediate the pathogenesis of AF in patients with DM. Obesity is an independent risk factor for AF (RR 1.5-1.7), in particular for permanent AF (RR 2.9), while at the same time being also related to metabolic syndrome and type 2 DM (98, 99). Therefore, it is very difficult to depict to what extent the diabetes-specific mechanisms contribute to the pathology of AF and to what extent the DM is just a coincidental observation in a group of patients with multiple comorbidities. Animal models of DM allow us to study the contribution of one risk factor at the time and can, therefore, provide insights that would otherwise be blurred by the plethora of intertwined abnormalities.

Pathophysiological mechanisms of atrial fibrillation in diabetes mellitus

BASIC ELECTROPHYSIOLOGICAL CONCEPTS ASSOCIATED WITH ATRIAL FIBRILLATION

Normal sinus cardiac rhythm is characterised by a regular initiation of the cardiac impulse from the sinoatrial node, without any irregular ectopic impulses, that then spreads through the atria, followed by electrical activation of ventricles. AF is characterised by an irregular heterogenic atrial electrical activity, which also results in uncoordinated atrial contraction and relaxation as well as in an irregular ventricular activation (100).

Conceptually, there are two main processes that are required for any sustainable arrhythmia: a trigger and a vulnerable substrate. In AF, the electrophysiological trigger is in the form of an abnormal depolarization of the atrial cardiomyocyte. Those atrial cardiomyocytes with abnormal firing are primarily located in the pulmonary veins (101). There are three main mechanisms underlying the abnormal ectopic firing (*Figure 1-1*): enhanced atrial automaticity, delayed afterdepolarizations (DAD), and early afterdepolarizations (EAD).

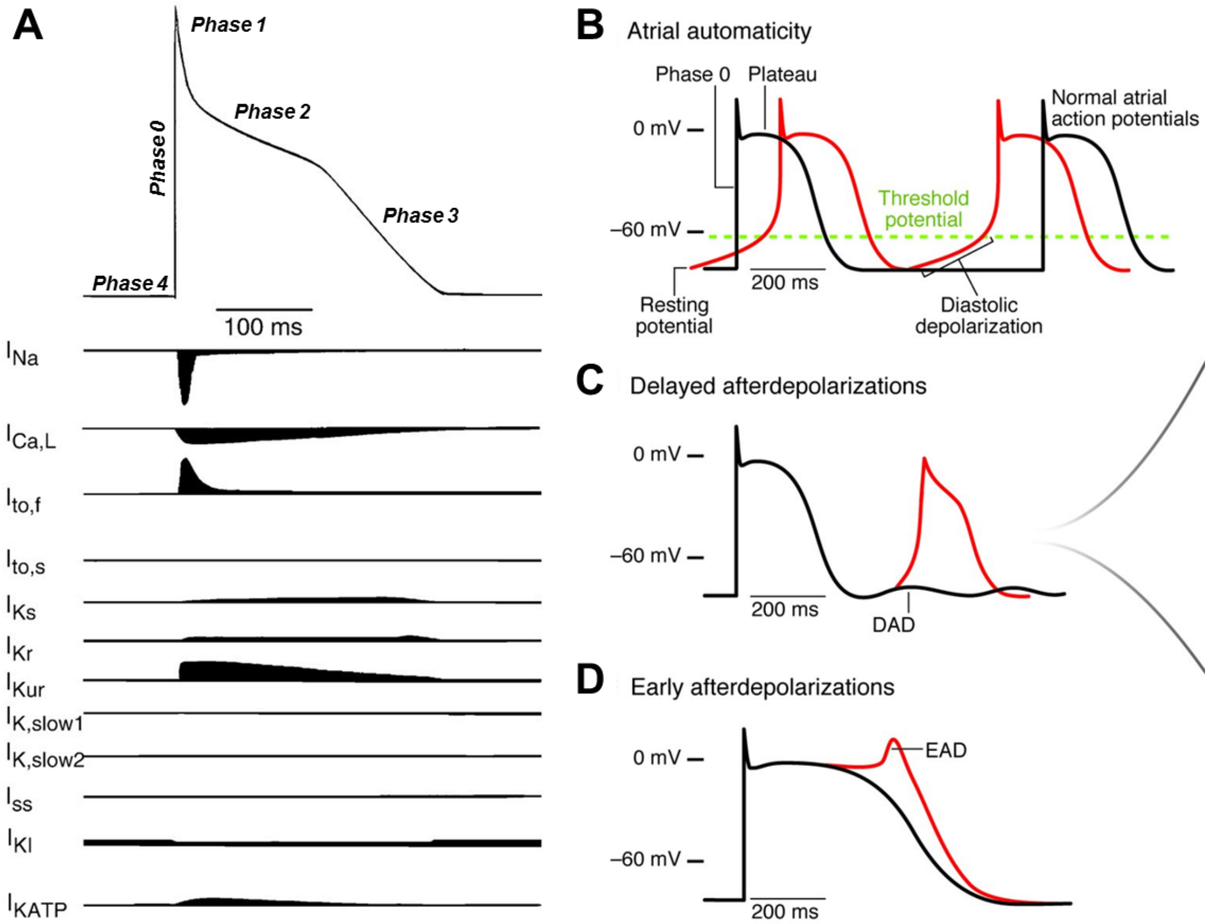

Figure 1-1. Schematic illustration of the human atrial action potential and mechanisms involved in the abnormal ectopic firing. (A) A diagram of the AP and relative contributions of different ion currents over time. Phase 0 represents activation of voltage-dependent Na^+ channels. Phase 1 occurs after inactivation of Na^+ channels and activation of Ca^{2+} and K^+ channels. During phase 2 both Ca^{2+} and K^+ remain open. Phase 3 is characterized by the closure of Ca^{2+} channels resulting in repolarization of the membrane. Phase 4 represents a resting membrane potential. (B) Enhanced atrial automaticity – trace in black represents normal cardiomyocyte action potential sequence, whereas the trace in red illustrates an early abnormal action potential caused by the diastolic depolarization. (C) Delayed afterdepolarizations (DAD) – an increase in the diastolic Ca^{2+} results in activation of the Na^+/Ca^{2+} exchanger resulting in a net-positive inward current causing the membrane depolarization, which can cause an abnormal action potential if the threshold potential is reached. (D) Early afterdepolarizations

(EAD) - during prolonged action potential some membrane L-type Ca^{2+} channels already reactivate and re-open again causing membrane depolarization. Illustration adapted from (102) and (100).

The normal atrial action potential (AP) has several typical phases: rapid membrane depolarization (phase 0) activated by the electrical signal that propagated from the sinoatrial node, followed by a series of repolarization steps (phases 1-3), and in the end a phase of diastolic equilibrium where a cardiomyocyte maintains the resting membrane potential (phase 4). In case the equilibrium of the inward and outward ion currents during phase 4 is changed the membrane potential changes. For example, an increase in the inward Na^{+} or Ca^{2+} currents or a decrease in the outward K^{+} currents during this phase can result in the diastolic depolarization (100, 103). If the diastolic depolarization reached the threshold potential, then a new abnormal AP is started resulting in the ectopic trigger (*Figure 1-1A*).

The DAD occurs when there is an abnormal increase in the cytoplasmic Ca^{2+} concentration during the diastole (104). The diastolic Ca^{2+} increase in the cytoplasm then activates the Na^{+}-Ca^{2+} exchanger (NCX) on the cardiomyocyte membrane, which results in a net positive inward current and in membrane depolarization (103). As above, if the depolarization reaches the threshold potential, then a new abnormal AP is started (*Figure 1-1B*). Multiple events can increase diastolic Ca^{2+} in the cytoplasm, for example, ryanodine receptor (RyR) dysfunction as a result of hyper-phosphorylation, Ca^{2+} overload as a result of the ischemia, β-adrenergic stimulation, and a decrease in the extracellular K^{+} concentration all contribute to the increased probability for DAD (100, 104-106).

EAD is another possible mechanism for triggered activity. The EADs normally occur in the situation where the action potential duration (APD) is prolonged. During prolonged AP some membrane L-type Ca^{2+} channels already reactivate and re-open again causing membrane depolarization (*Figure 1-1C*) (104, 107). As a result, any mechanism causing prolongation of the cardiomyocyte's APD also increases the risk for EAD triggers.

A single abnormal AP in a normal healthy myocardium does not result in the sustained arrhythmia. On the other hand, an abnormal ectopic AP in a vulnerable myocardial "substrate" caused by structural changes in the tissue or electrophysiological changes such as decreased refractoriness or decreased conduction velocity (CV) can result in sustained arrhythmia. A slightly over-simplistic explanation for this observation is the circular re-entry mechanism. A simple explanatory diagram of the re-entry mechanism is depicted in *Figure 1-2 A-C*. Let us imagine a situation where an excitation from an ectopic premature trigger reaches a branch point caused by a non-conductive anatomical obstacle. In normal tissue, the signal will propagate through the branch, but it will not be able to complete the whole circle around the obstacle, as the signal will be stopped because it will reach the area that is refractory for another electrical stimulation (*Figure 1-2A*). However, in a vulnerable substrate that has a decreased refractory period, the same signal from the previous example will not be stopped as the signal will reach the tissue that is already excitable (*Figure 1-2B*). This generates a self-perpetuating "circus movement" re-entry and is one explanation for the maintenance of arrhythmias (104). A similar situation also occurs if the electrical conduction velocity through the tissue is decreased. In this case, the signal will also be able to complete the whole circle, because the time to reach the origin is prolonged making the tissue there excitable again (*Figure 1-1C*). This simple re-entry mechanism can also explain why structural changes such as fibrosis and atrial enlargement contribute to the "vulnerable" substrate (*Figure 1-1D*) as it creates new obstacles for the propagation of the electrical signal and large re-entry circles thus making the tissue more prone for the maintenance of the arrhythmia.

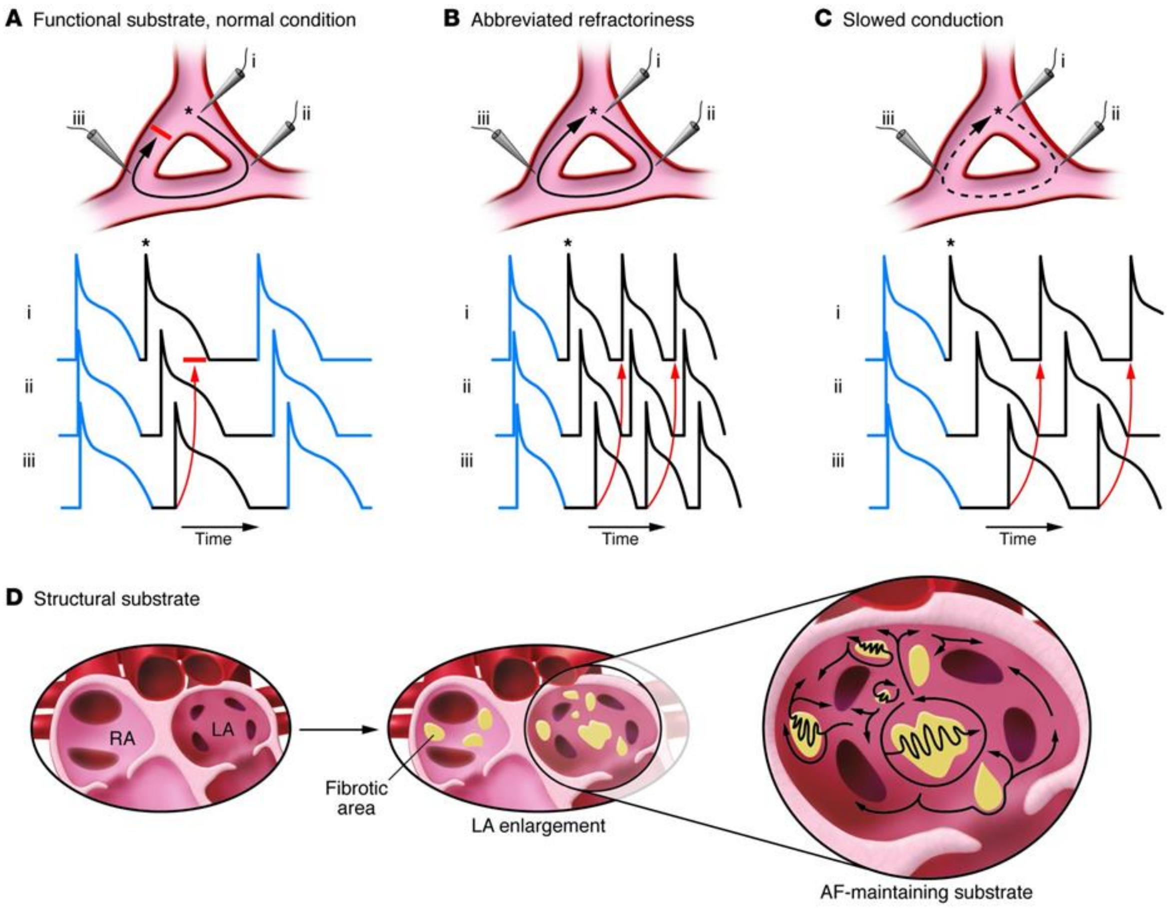

Figure 1-2. Schematic diagram presenting the main factors contributing to the re-entry mechanism of maintenance of arrhythmia. A detailed explanation of the mechanisms is in the main text. AF – atrial fibrillation, LA – left atrium, RA – right atrium. Illustration adapted from (100).

While a simple circular re-entry mechanism is an easy conceptual aid to understand how the arrhythmia can maintain itself, the actual observations of signal propagation during the AF show more complex patterns such as multiple independent wavelets, re-entrant rotors, and even electrical dissociation of epicardial and endocardial layers (108-111). Nonetheless, the factors promoting the stability of the re-entry in all those observed complex patterns are similar to the ones discussed for the simple circular re-entry model: decreased tissue refractoriness, decreased conduction velocity, increased conduction heterogeneity, and increased tissue mass (104, 112).

Decreased tissue refractoriness is a direct consequence of decreased APD in cardiomyocytes. Multiple mechanisms contributing to the shorted APD have been observed in AF, for example, any atrial tachycardia results in shorter APD contributing to the maintenance of arrhythmia (113, 114). Multiple membrane ion channels and their currents, in particular, the ones responsible for repolarization (phase 1-3 of AP) such as L-type Ca^{2+} current (I_{CaL}), background K^+ currents (I_{K1}), and constitutively active acetylcholine-dependent current (I_{KACh}) have been altered in cardiomyocytes prone to AF (100, 104).

Conduction velocity through the myocardial tissue is primarily determined by the sodium current (I_{Na}) and gap junction density. Both systems have been implicated in the pathogenesis of AF. For example, a canine animal model of AF has a decrease in expression of Nav1.5 resulting in a decrease of the I_{Na} current (115). The I_{Na} current is also decreased in atrial cardiomyocytes of patients with AF compared to the patients in sinus rhythm (116). Similarly, the gap junction proteins, namely connexin 40 and connexin 43 can both be altered in the atrial myocardium in the presence of AF (117-119). Furthermore, genetic mutations in the gene GJA5 that is encoding the connexin 40 gap junction protein also predispose individuals to a higher risk of idiopathic AF (120).

Increased atrial myocardial fibrosis and acute ischemia, both common in various chronic conditions associated with AF, result in areas of conduction block. This intensifies the overall conduction heterogeneity and thus increases the risk for AF (100, 112, 121). Finally, atrial enlargement is a common finding in patients with AF and contributes to the vulnerable substrate by enlarging the overall volume through which the arrhythmia can be maintained (104).

MECHANISMS IMPLICATING DIABETES MELLITUS IN ATRIAL FIBRILLATION

Outside of numerous epidemiological and clinical studies associating diabetes mellitus with atrial fibrillation and diabetic cardiomyopathy, there is limited knowledge regarding the links underlying this association. The most commonly suggested, but not thoroughly investigated, mechanistic links between DM and increased risk for AF are structural remodelling, electrical remodelling, autonomic remodelling, oxidative stress, derailed cardiac metabolism, and mitochondrial dysfunction (*Figure 1-3*).

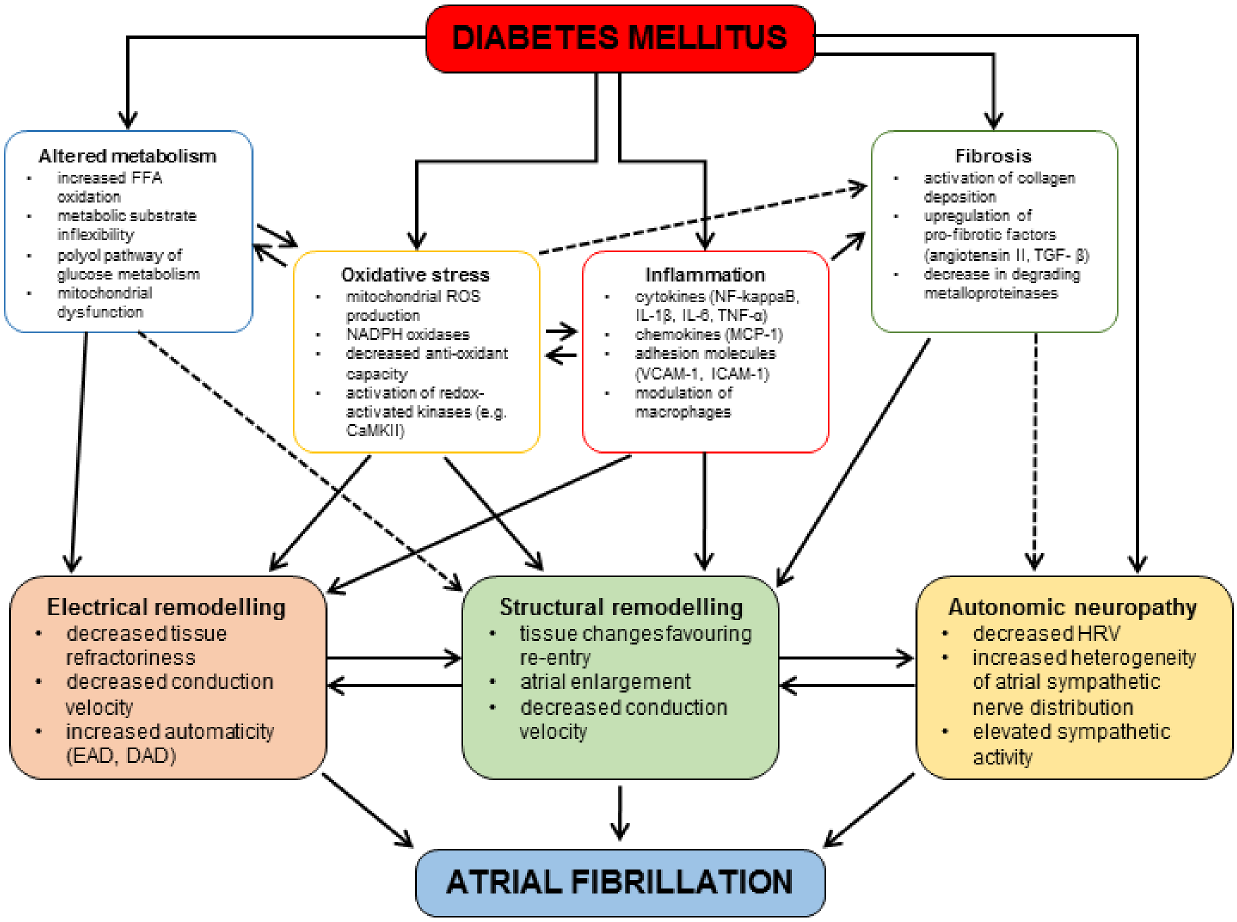

Figure 1-3. Putative mechanisms connecting the diabetes mellitus and atrial fibrillation. FFA – free fatty acids, ROS – reactive oxygen species, EAD – early afterdepolarization, DAD – delayed afterdepolarization, HRV – heart rate variability.

STRUCTURAL REMODELLING

Structural remodelling of atria in DM is characterized by atrial fibrosis, atrial hypertrophy, atrial dilatation and fat deposits. Atrial fibrosis was demonstrated in both type 1 and type 2 DM animal models (122, 123). Fibrosis disrupts the normal architecture of the myocardium resulting in decreased conduction velocity, increased propagation heterogeneity, and even regional conduction block (124). All those components make the substrate more vulnerable to sustained AF. Indeed, isolated atria from type 1 and type 2 DM animal models with increased atrial fibrosis were more prone for pacing-induced atrial arrhythmias (125, 126).

Cardiac fibroblasts are key effectors of remodelling, and once activated under pathological conditions they produce increased levels of type I collagen (127). Fibroblasts exposed to hyperglycaemic environment produce increased levels angiotensin II, TGF-β, and also start secreting collagen (128). Moreover, high glucose levels also lead to advanced glycation end-products (AGEs), which bind to their receptors (RAGEs) on cardiac fibroblasts and lead to increased fibroblast proliferation (129). In addition, AGEs alone enhance interstitial fibrosis due to their capability of forming crosslinks between extracellular matrix proteins (130).

Another important structural change in the hearts of patients with type 2 DM is an increase in the amount of epicardial and pericardial fat (131, 132). Interestingly, the amount of pericardial fat was independently associated with an increased risk for AF (133, 134). Furthermore, patients with type 2 DM and obesity also have patches of fatty infiltration in atrial myocardium (135). These adipocytes in the myocardium eventually undergo lipomatous metaplasia and form fibro-fatty infiltrates that progressively lead to interstitial fibrosis (136). In addition, epicardial and pericardial adipocytes act in paracrine fashion by secreting numerous pro-fibrotic adipokines (e.g. activin A) and pro-inflammatory cytokines (e.g. CRP, IL-6, IL-1β, TNFα) further promoting the vicious cycle of atrial structural remodelling and thus increasing the risk for AF (137, 138).

ELECTRICAL REMODELLING

A common finding in various animal models of DM is the increase in the atrial effective refractory period and the increase in the APD (139, 140). The most commonly described changes in animal models of DM are a decrease in the Na^+ current (I_{Na}), increase in the late Na^+ current ($I_{Na,L}$), reduction in the atrial acetylcholine-activated K+ current (I_{KAch}), decrease in the transient outward K+ current (I_{to}), and reduced expression of small conductance Ca^{2+}-activated K^+ channels (139, 140). The majority of those findings are reported in animal models of DM, but there is very limited knowledge of electrical remodelling of human atria in the presence of DM. Further studies are needed to decrease this gap in knowledge.

AUTONOMIC REMODELLING

Dysfunction of the autonomic nervous system is a common complication of patients with DM and several studies suggest that it might also have a role in the pathogenesis of AF (141, 142). Patients with type 2 DM have decreased heart rate variability (HRV) and a decrease in HRV has been associated with an increased risk for AF (143, 144). Furthermore, impaired heart rate recovery (HRR) – another indicator of cardiac autonomic function – has a positive predictive value for the new-onset AF in patients with T2DM (145). In addition, histological observations of STZ diabetic rat hearts demonstrate increased heterogeneity of sympathetic nerves distribution in atria, with unchanged parasympathetic nerves compared to non-diabetic controls (146). Hearts in an animal model of type 2 DM also show elevated resting cardiac sympathetic nerve activity coupled with reduced beta-adrenergic receptor responsiveness further demonstrating changes in the cardiac autonomic function in the setting of DM (147).

OXIDATIVE STRESS

Oxidative stress is another mechanism commonly implicated in the pathogenesis of DM-induced cardiac dysfunction. While the role of reactive oxygen species (ROS) and altered nitroso-redox balance as a mechanism for causing the arrhythmias has been investigated in detail in relation to AF alone (50, 148), less is known about the potential dysregulation of redox homeostasis in diabetes and its role in increasing the arrhythmogenicity of atria. The main sources of ROS in a metabolic dysfunction seen with DM are presumed to be in mitochondria. Ventricles of the diabetic db/db mice (model of insulin resistance, T2DM, and obesity) have increased mitochondrial oxidative stress as demonstrated by an increase in the production of hydrogen peroxide (H_2O_2) in isolated ventricular mitochondria (149). On the other hand, ventricles of Akita mice (model of T1DM) did not show any signs of mitochondrial oxidative stress (150). Even though the majority of the ROS is generated in mitochondria, there are also other sources generating ROS in other compartments. One of the most studied enzymatic sources of superoxide in the cytosol is the family of NADPH oxidases. Ventricles of Zucker fa/fa rats (model of T2DM) had elevated NOX2 levels with a corresponding increase in the cytosolic superoxide levels (41). Redox changes in atria (not in ventricles) have not been investigated in any of the diabetic animal models so far.

A limited amount of data from human studies do not conclusively determine whether redox dysfunction is an important mechanism in DM related AF. Firstly, a small study (n = 24) on T2DM patients and their matched controls undergoing cardiac surgery demonstrated that T2DM patients' permeabilized muscle fibres from atrial appendages have higher mitochondrial H_2O_2 emissions as well as increased levels of protein nitrosylation and decreased ratio of total to oxidized glutathione (GSH/GSSG) indicating persistent oxidative stress (36). Furthermore, a larger clinical study in 104 consecutive patients undergoing cardiac surgery found out that patients that develop post-operative AF have decreased mitochondrial respiration and higher amount of mitochondrial ROS in atrial appendages and therefore associating the metabolic mitochondrial dysfunction with the arrhythmic outcome (151). On the other hand, the amount of cytosolic ROS and in particular the amount of superoxide production in atria of patients with DM has not been reported yet.

This distinction between mitochondrial ROS and cytosolic ROS is important, as there are several described mechanisms by which an increase in the cytosolic ROS cause arrhythmias. For example, redox-activated kinases such as CaMKII, PKC, and PKA are known to modulate calcium handling proteins and sodium sarcolemmal channels, while in addition multiple potassium and sodium channels are also directly regulated by redox-reactions (50, 152). On the other hand, the mechanisms by which an isolated increase in the mitochondrial ROS production could cause the arrhythmias are largely unknown. Some of the postulated mechanisms involve metabolic adaptions resulting in alterations in ATP dependent sarcolemmal ion transporters as well as activation of redox-sensitive transcription factors such as HIF-1α (152).

DERAILED CARDIAC METABOLISM AND MITOCHONDRIAL DYSFUNCTION

Cardiac metabolism changes considerably during the time course of AF. Hearts from goats that were maintained in AF by atrial burst pacing, had an increase in energy demand for the first 4-8 weeks of AF as characterized by a 60% decrease in phosphocreatine content (153). During this period, atrial myocytes underwent adaptive intracellular structural remodelling: the disappearance of sarcomeres, accumulation of glycogen, and cellular hypertrophy. After 16 weeks phosphocreatine content returned to the initial levels thereby indicating the decrease in energy demand in a structurally altered myocardium. Importantly, similar metabolic shifts were also observed in humans. Atrial samples from patients with chronic AF had decreased myofibrillar creatine kinase (CK) activity compared to patients in sinus rhythm (SR) (154). Furthermore, recent proteomics studies have implicated many more metabolism-related proteins (e.g. NADH dehydrogenase, ATP synthase, pyruvate dehydrogenase enoyl-CoA hydratase, etc.) whose expression levels changed considerably in atrial samples from patients with AF when compared to patients in SR (155, 156).

Little is known about how cellular energy homeostasis influences the susceptibility towards AF. In a canine model of congestive heart failure, decreased atrial CK activity, decreased adenylate kinase activity, and decreased ATP levels were correlated with longer duration of AF induced by in-vivo burst atrial pacing (157). Furthermore, patients undergoing coronary artery bypass graft (CABG) surgery with decreased levels of peroxisome proliferator-activated receptor γ coactivator 1-α (PGC-1α, a regulator of mitochondrial biogenesis) and decreased levels of glucose transporter 3 (GLUT3) were at increased risk for developing postoperative AF (158). All in all, improving the metabolic state of atria is a potential therapeutic approach for AF.

Recently, a prospective study in patients with metabolic syndrome undergoing CABG surgery reported the first evidence of a link between incident AF and atrial mitochondrial dysfunction (151). Atrial tissue of patients who developed postoperative AF had lower maximal mitochondrial respiration of carbohydrates and fatty acids, increased sensitivity for Ca^{2+} opening of the mPTP, increased production of reactive oxygen species (ROS) concentration and higher manganese superoxide dismutase (MnSOD) activity.

Experimental studies have indicated that several different downstream targets may be implicated in arrhythmias associated with mitochondrial dysfunction. Firstly, increased mitochondrial ROS production decreases the current through the cardiac Na^+ channels ($Na_v1.5$) (159). Similarly, an increase in the ratio of NADH/NAD^+ also lowers the $Na_v1.5$ current (160). Both mechanisms of $Na_v1.5$ channel regulation are mediated by activation of protein kinase C and protein kinase A (159, 160). Secondly, sarcolemmal K_{ATP} channels act as sensors of cellular energy levels. Decreased energy levels (decreased ATP/ADP ratio) and activation of the AMP-activated protein kinase can directly regulate the opening of K_{ATP} channels, which in turn can either shorten action potential duration (APD) or make cardiomyocyte non-excitable (if most K_{ATP} channels become open) thus creating a substrate that favours functional re-entry and maintenance of arrhythmia (161, 162). Furthermore, ROS can oxidise Ca/calmodulin kinase (CaMK) II, which, in turn, can lead to an increase in the late Na^+ current, prolongation of APD and increased probability of triggered arrhythmias (163). Lastly, severe mitochondrial dysfunction and a large increase in mitochondrial ROS production can activate intrinsic apoptotic signalling pathway that leads to cardiomyocyte apoptosis again creating the substrate that favours re-entry maintenance of arrhythmias (125, 164, 165).

Nitric oxide synthase (NOS) and NO signalling

GENERATION OF NO BY NOS

Nitric oxide is a highly lipophilic and diffusible gas, thus highly membrane-permeable and able to reach targets distinctively away from the cellular compartment in which it was produced (166). NO is an ideal paracrine molecule with a wide range of biological effects, such as regulation of vascular tone, phagocyte-induced immune responses, a signalling molecule in the nervous system, as well as a regulator of cardiac function. The primary cellular source of NO is a family of enzymes called NO synthases (NOS), consisting of three known isoforms, namely neuronal NOS (nNOS, NOS-1), inducible NOS (iNOS, NOS-2), and endothelial NOS (eNOS, NOS-3) (167). The enzymatic reaction of conversion of L-arginine to L-citrulline and NO is catalysed by NOS isoforms and involves 5 cofactors, namely flavin adenine dinucleotide (FAD), flavin mononucleotide (FMN), heme, calmodulin (CaM), and tetrahydrobiopterin (BH4) (168).

NOS IN THE MYOCARDIUM

In the cardiomyocyte, there are two isoforms of nitric oxide synthase, endothelial (eNOS) and neuronal (nNOS), which are responsible for the constitutive production of NO (169). In the presence of inflammation or acute injury, there is also an expression of inducible NOS isoform (iNOS) (170). Moreover, there is also a typical subcellular spatial localisation of NOS isoforms in the cardiomyocyte. In healthy cardiomyocytes, eNOS associates with caveolin-3 on invaginated regions of cell membranes (caveolae), which have high signalling activities (171). Indeed, there is a co-localisation of eNOS with β-adrenergic receptors, allowing eNOS-generated NO to be within the diffusion distance (172). In addition, eNOS can also be bound to the nuclear membrane (173). On the other hand, nNOS is localized mainly in the sarcoplasmic reticulum (SR), where it associates with ryanodine receptors (RyR), phospholamban (PLB), and xanthine oxidoreductases (172, 174, 175). The nNOS is to a lesser extent also present in the sarcolemmal membrane and can thus modulate the sarcolemmal ion channels (176-178). Importantly, during pathologic states, NOS isoforms can be redistributed inside the cardiomyocytes, such as for example nNOS relocation from the SR to the sarcolemmal membrane during ischemia-reperfusion injury (166, 179).

Under physiological conditions, eNOS-generated NO interacts with β-adrenergic receptors and blunts their inotropic effects (180). Moreover, also nNOS and iNOS can lead to NO-mediated inhibition of beta-adrenergic stimulation in ventricular myocytes (181, 182). Constitutive generation of NO, by eNOS and nNOS activity, regulates intracellular calcium levels by blunting of Ca^{2+} influx through the L-type Ca^{2+} channels (183). The nNOS in the SR can directly modify the RyR by S-nitrosylation (172, 184). Furthermore, nNOS-generated NO enhances phospholamban (PLB) phosphorylation, thus leading to increased SERCA-mediated Ca^{2+} reuptake, and faster relaxation (185). Moreover, NOS activation has a physiological role in reducing myofilament Ca^{2+} sensitivity by PKG-dependent phosphorylation of cardiac troponin (cTnI) and cardiac myosin binding protein-C (cMyBP-C) (186).

Furthermore, nNOS also has an important effect on sarcolemmal ion channels. In particular, nNOS knock-out mice ($nNOS^{-/-}$) have a shorter atrial APD and inhibition of nNOS in human atrial myocytes leads to an increase in I_{to}, I_{Kur} and I_{K1} (187). In addition, activation of nNOS has been reported to induce S-nitrosylation of $Na_v1.5$, which in turn increases late Na current (178, 188). Secondly, NO affects APD by modulating repolarizing potassium currents. For example, NO donors prolong APD by inhibiting $K_v1.5$ and $K_v4.3$ channels via cGMP and cAMP-dependent mechanisms, as well as by S-nitrosylating cysteine residues (189-191).

The role of BH4 in NOS function

BH4 METABOLISM

BH4 is an essential cofactor for several aromatic amino acid hydroxylases (synthesis of tyrosine, L-DOPA, and serotonin), alkylglycerol monooxygenases, and, importantly, nitric oxide synthases (NOS) (192, 193). BH4 is synthesized *de novo* from guanosine triphosphate (GTP) by a series of enzymatic reactions (*Figure 1-4*). The first and also the rate-limiting step of the whole synthetic pathway is the conversion of GTP to dihydroneopterin triphosphate by the GTP cyclohydrolase 1 (GCH1) (194). BH4 is oxidized to dihydrobiopterin (BH2) when participating in the NOS reactions, but it can be converted back to the BH4 by the dihydrofolate reductase (DHFR) via the salvage pathway. BH4 is also a cofactor for the aromatic amino acid hydroxylases (AAAH) where BH4 is converted to tetrahydrobiopterin-4a-carbinolamine, which can be recycled back to BH4 by the enzyme pterin-4a-carbinolamine dehydratase.

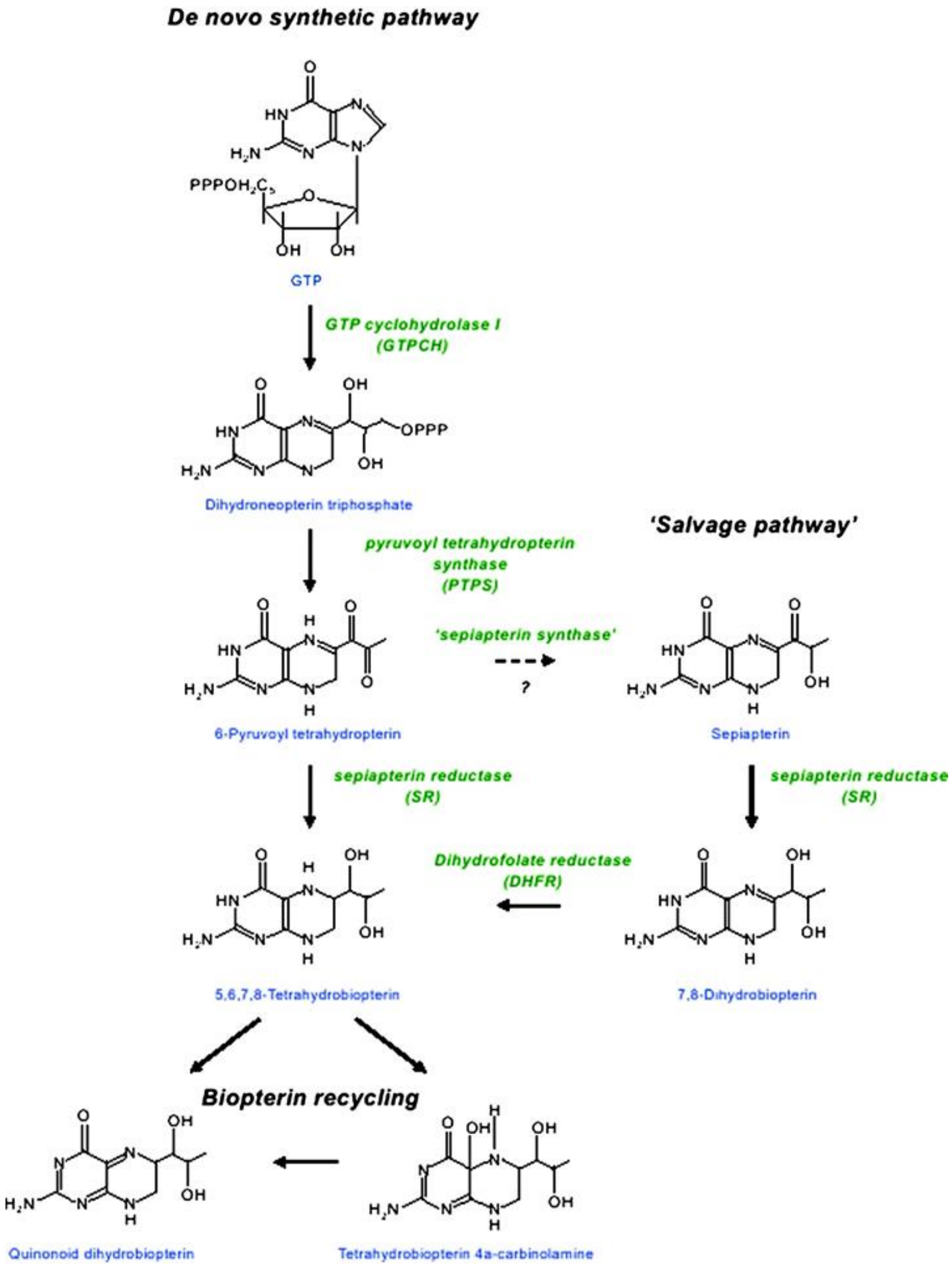

Figure 1-4. Tetrahydrobiopterin (BH4) de novo biosynthesis from guanosine triphosphate (GTP). BH4 is oxidized to dihydrobiopterin (BH2) when used by NOS to create NO. BH2 can be recovered back to BH4 by the dihydrofolate reductase via the salvage pathway. BH4 is converted to tetrahydrobiopterin-4a-carbinolamine when used by the aromatic amino acid hydroxylases (AAAH). Pterin-4a-carbinolamine dehydratase can regenerate BH4 after that reaction. Reaction diagram adapted from (194).

NOS UNCOUPLING

The term NOS uncoupling refers to the process where the NOS enzyme is uncoupled to either a substrate or one of the cofactors (195). In this reaction, the NOS produces the superoxide anion instead of the NO. While the NOS uncoupling was first demonstrated in experiments where L-arginine was depleted, in more physiological conditions this usually occurs due to the BH4 depletion or reduced BH4:BH2 ratio (194, 195). Furthermore, the generated superoxide rapidly reacts with the NO generating the peroxynitrite, which can oxidize BH4 to BH2 (194). As a result, a self-perpetuating vicious circle can occur: a decrease in BH4 results in NOS uncoupling resulting in superoxide production, which further decreases the amount of BH4 and the loop is completed.

The therapeutic potential of tetrahydrobiopterin to prevent diabetic cardiomyopathy and atrial fibrillation

Tetrahydrobiopterin (BH4) is a molecule that has been studied for its potential to protect against vascular disease as well as certain cardiac diseases involving left ventricular (LV) hypertrophy, ischemia, and diabetes-related metabolic dysfunction (194). BH4 is an essential cofactor for several aromatic amino acid hydroxylases, alkylglycerol monooxygenases, and, importantly, nitric oxide synthases (NOS). NO signalling and NOS dysfunction, in particular, the dysfunction of the endothelial NOS (eNOS, NOS3) and its relation the vascular dysfunction has been studied in detail. In animal models of hypertension and atherosclerosis oxidative stress reduces BH4 levels leading to vascular and endothelial dysfunctions (196-198). BH4 depletion causes NOS "uncoupling", a situation where the enzyme rather than generating NO by converting arginine to citrulline, starts producing superoxide. The combined effect of impaired NO production and increased oxidative stress by increased superoxide production results in the endothelial dysfunction and accelerated atherosclerosis (199).

Increasing the intracellular BH4 levels either by overexpressing the GTP cyclohydrolase 1 (GCH – the rate-limiting step in the synthesis of BH4) or by external BH4 supplementation ameliorated effects of vascular dysfunction in animal models of hypertension, atherosclerosis, and diabetes mellitus (198, 200-202). This therapeutic approach has been also investigated in several small clinical trials on patients with essential hypertension, hypercholesterolemia, coronary artery disease, type 2 diabetes mellitus, and chronic smoking with mixed results. Some studies reported improvement of vascular function after acute and chronic addition of BH4 (203-209), while other studies reported no beneficial effects of BH4 on vascular function (210, 211).

The role of BH4 in cardiac function and its role in various pathological states have also been studied. Reduced levels of BH4 in the myocardium have been demonstrated in mouse models of LV pressure overload (in mice with transverse aortic constriction (TAC) or hypertension), severe ischemia, and even in the goat model of atrial fibrillation (AF) (148, 200, 212-215). Furthermore, BH4 is also an essential cofactor for the myocardial constitutive NOS (nNOS, NOS1) and the drop in the BH4 levels also decrease the nNOS activity. The nNOS in the myocardium is involved in the regulation of cardiac contraction and relaxation by affecting the Ca^{2+} currents, ryanodine receptors (RyR), and promoting phospholamban (PLB) phosphorylation (185, 200). The sarcolemmal sodium and potassium channels are also regulated by the nNOS signalling pathways resulting in a prolonged action potential duration (APD) (178, 187-190, 216). Therefore, any disturbance in the BH4 levels or NO signalling caused by any disease may further exacerbate cardiac mechanical and electrophysiological dysfunction. The role of BH4 is not limited to the regulation of calcium and sarcolemmal ion channels but also modulates the intracellular redox state. BH4 itself is an anti-oxidant (by being able to be oxidized to the BH2) and it also has an indirect antioxidant role by reducing the NOS uncoupling and thus decreasing the amount of generated ROS (194). In addition, BH4 might also have immunosuppressive properties. Studies have shown that BH4 through NOS-independent pathways decreases the rejection of the heterotopic heart transplants in mice and rats and thus prolongs survival (217, 218). A potential mechanism for the immunosuppressive function of BH4 is the regulation of the nuclear factor erythroid 2-related factor 2 (NRF2), which is a translational factor that inhibits activation of the inflammatory pathways and initiates transcription of antioxidative genes (219).

BH4 has a diverse function affecting several pathways that are commonly disturbed in various cardiac diseases. Therefore it has been investigated whether BH4 can improve cardiac function in different disease models beyond solely correcting the endothelial function. In the model of hypertension using DOCA-salt mice, BH4 supplementation has prevented diastolic dysfunction by reversing the prolonged relaxation of cardiomyocytes and reducing the glutathionylation of myofilaments (198, 200, 220). Furthermore, the BH4 supplementation in the mouse model of LV pressure overload by transverse aortic constriction (TAC) resulted in improved LV systolic function, less LV hypertrophy and less fibrosis compared to the placebo group (212, 221). Interestingly, the beneficial effect of BH4 in the TAC model was independent of augmenting the NOS function and also independent of improved myocardial redox state (213). In this case, the BH4 rescued the dysfunction by suppressing the expression of inflammatory cytokines resulting in decreased infiltration of macrophages in the early time point after TAC (213).

In summary, treatment with BH4 could potentially prevent the development of diabetic cardiomyopathy and DM-related AF via several potential mechanisms. Firstly, increased BH4 concentration could decrease NOS uncoupling and decrease the ROS generation. Secondly, BH4 treatment increases NOS activity resulting in faster relaxation of cardiomyocytes, which could improve the diastolic dysfunction associated with the diabetic cardiomyopathy. An improved diastolic function could also prevent the atrial enlargement, which could decrease the risk for AF. Furthermore, augmented NOS activity also results in longer APD, which makes the myocardium less vulnerable for arrhythmias. Finally, BH4 is also an immunomodulator and could prevent the formation of fibrosis observed in diabetic myocardium.

Aims of the thesis

I. The aim of the first part of the thesis is to investigate whether impaired BH4 availability and NO signalling contribute to the development of diabetic cardiomyopathy. Furthermore, we will also test whether increasing myocardial BH4 levels and thus augmenting the NOS activity prevents the development of the diabetic cardiomyopathy. We hypothesise that diabetic hearts will have reduced cardiac BH4 levels and decreased NOS activity. The transgenic mouse model with increased myocardial BH4 levels will augment the NOS activity and prevent the development of diabetic cardiomyopathy.

II. The second aim is to determine whether chronic hyperglycaemia alone is sufficient to increase the risk for AF. Also, we will attempt to elucidate the relative importance of different pathological mechanisms that could explain the electrophysiological phenotype in diabetic mouse atria. We hypothesise that diabetic mice will have an increased probability for AF secondary to electrical and structural remodelling caused by oxidative stress and tissue fibrosis.

III. The aim of the last part of the thesis is to examine the electrophysiological changes in mice with high levels of intra-myocardial BH4 and to test whether the BH4 can reduce the probability of pacing-induced AF in diabetic mice. We hypothesise that oral BH4 treatment will decrease the probability for pacing-induced AF in diabetic mice.

CHAPTER 2:

General methods

Introduction

This chapter provides a detailed description of the methods used to perform experiments and collect various data presented in this thesis.

Animal models

Mouse animal models have been used for all the experiments in this thesis. We used two different strains of mice: one was a standard C57BL/6JOlaHsd purchased from Envigo (previously known as Harlan), which is the main United Kingdom distributor of animal models. The second strain of mice was a genetically modified strain with a myocardial specific overexpression of human GTP cyclohydrolase 1 gene (mGCH1-Tg), which was created in our department.

C57BL/6JOLAHSD MOUSE STRAIN

The C57BL/6 mouse strain is the most known and the most commonly used mouse strain in biomedical research (222). The C57BL/6JOlaHsd is a particular substrain that originates from the Jackson Laboratory (Bar Harbor, Maine, USA) and was transported to the Laboratory Animal Centre United Kingdom in 1974 and from there to Harlan Laboratories United Kingdom in 1985.

When C57BL/6J mice are used as a model for any metabolic disorder, it is important to note that the majority of C57BL/6J mice have the Nnt deletion. The deletion of the NNT protein results in impaired glucose regulation and decreased insulin secretion (223). It is estimated that the Nnt deletion occurred spontaneously sometime between 1976 and 1984 in mice bred at the Jackson Laboratory, which is the main source and reference point for the vast majority of mouse models used in research (224). As a result, all C57BL/6J mice that were obtained from Jackson Laboratory after 1984 harbour the Nnt deletion. However, the C57BL6JOlaHsd obtained from Envigo (previously known as Harlan Laboratories) in the United Kingdom do not contain the Nnt deletion and therefore do not have impaired glucose regulation at baseline (222).

All C57BL/6JOlaHsd mice used for experiments in this thesis were continuously purchased from Envigo at the age of 8-10 weeks and then maintained in the Functional Genetics Facility at the University of Oxford. Mice were housed in individually ventilated cages in a temperature-controlled environment (20-22°C) with a 12-hour light-dark cycle. Mice had ad libitum access to food and water. Sentinel animals were kept in the same racks and regularly underwent health monitoring to ensure and confirm specific pathogen-free environment. No breeding of this strain was done internally.

MICE WITH MYOCARDIAL-SPECIFIC OVEREXPRESSION OF HUMAN GTP-CYCLOHYDROLASE 1

Generation of the new transgenic mouse colony

A mouse with the myocardial-specific overexpression of human GTP-cyclohydrolase 1 was created in the Channon's lab at the University of Oxford (185). Firstly, human influenza haemagglutinin (HA) tag was cloned into the human GCH1 gene (*Figure 2-1*). Secondly, this segment was then inserted into the plasmid containing murine alpha myosin heavy chain (α-MHC) promotor. Thirdly, the final transgene construct was excised using NotI endonuclease digestion and purified by sucrose density gradient centrifugation. The gene construct was then dissolved in sterile injection buffer and microinjected into the pronucleus of fertilized eggs from super-ovulated mice of the CBA strain. Putative male founders were genotyped to confirm the presence of human GCH1 transgene using the genotyping protocol described below. A breeding colony was then established by backcrossing the founder to the C57BL/6JOlaHsd background for three generations.

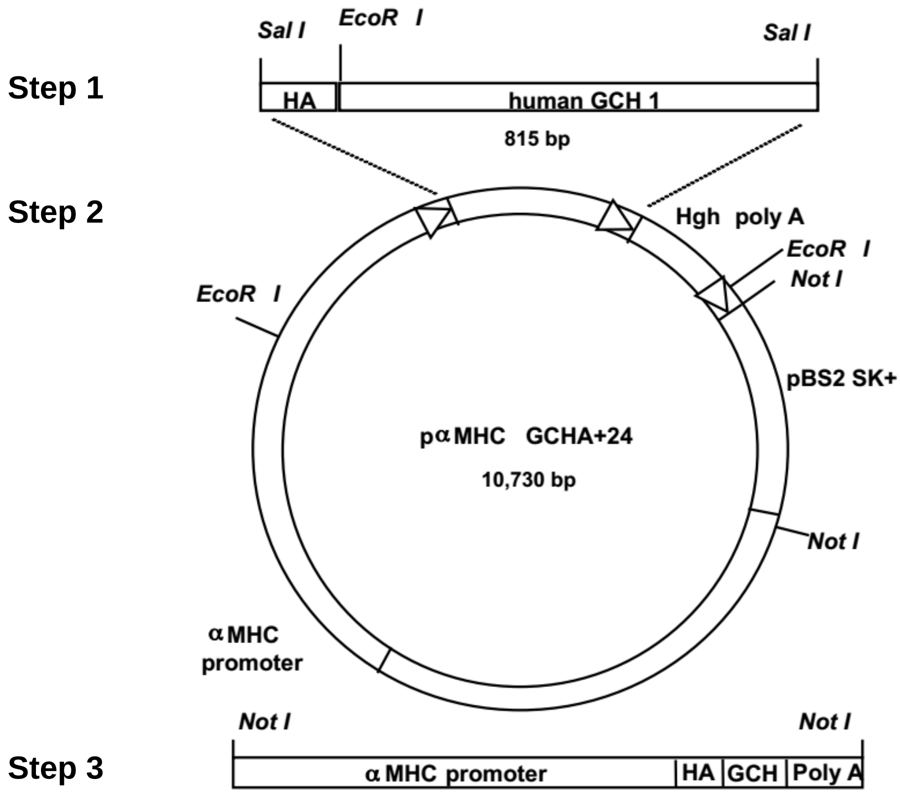

Figure 2-1. Diagram illustrating the steps involved in the construction of the human GTP-cyclohydrolase 1 (GCH1) transgene under control murine alpha myosin heavy chain (α-MHC) promotor. Step 1 – cloning the human GCH1 gene to the human influenza haemagglutinin (HA) tag. Step 2 – cloning the construct containing the human GCH1 gene into the plasmid containing murine α-MHC. Step 3 – excision of the construct containing α-MHC and human GCH1 using NotI restriction endonuclease. Diagram adapted from (185).

Colony breeding and maintenance

Colony breeding was done among heterozygous mGCH1-Tg and wild-type (WT) adult mice (aged 12 – 35 weeks) to ensure that half of the pups would always be transgenic with the other half being WT. This transgenic colony was breeding without any difficulties with the average litter size of 4.7 and no increase in premature deaths or other deleterious phenotypes. Genotyping confirmed that mice were born in an approximately 1:1 Mendelian ratio between WT and mGCH1-Tg.

Four weeks after birth, mice were moved into separate cages. At that point, ears were notched to obtain the tissue for genotyping and to uniquely label mice. Mice were kept in individually ventilated cages in a temperature (20-22°C) and light (12-hour day/night cycle) controlled environment. Mice had ad libitum access to food and water. Sentinel animals were kept in the same racks and regularly underwent health monitoring to ensure and confirm specific pathogen-free environment.

MOUSE GENOTYPING PROTOCOLS

Genotyping protocol of transgenic mice with myocardial-specific overexpression of human GTP-cyclohydrolase 1

The mouse genomic DNA was isolated from an ear notch using a simple "HotSHOT" protocol: lysis in hot alkaline solution (NaOH) followed by neutralization with a strong buffer (Tris-HCl) (225). Firstly, individual ear notches were transferred into clean PCR tubes. Secondly, 75 µl of alkaline lysis buffer was added to the PCR tubes followed by incubation at 95°C for 30 minutes. Afterwards, the solution was neutralized by adding 75 µl of neutralization buffer (*Table 2-1*).

The PCR reaction was prepared using the Taq DNA polymerase (BioMix Red), primer set specifically designed to detect human GCH1 in DNA lysate obtained in the previous step as specified in *Table 2-2*. The final PCR product was then detected using the gel electrophoresis (2% agarose gel, Tris-acetate-TAE buffer, 40 min at 120V) with ethidium bromide as a fluorescent nucleic acid tag. The expected size of the amplified GCH1 product is 480bp. A sample gel electrophoresis is shown in *Figure 2-2*.

Reagents	
Alkaline lysis buffer (buffer A)	NaOH 25mM, EDTA 0.2mM, pH 12
Neutralization buffer (buffer B)	Tris-HCl 40mM, pH 5
Taq DNA polymerase	BioMix Red (Bioline Reagents Ltd.)
Oligonucleotides	
GCH1 forward primer sequence (5'-3')	CCTTCCTCACCCCCTGGCTTGTCC
GCH1 reverse primer sequence (5'-3')	AGTCGGGCACGTCGTAGGGGTAGG

Table 2-1. Reagents and primers for genotyping of mGCH1-Tg mice.

PCR reaction	
final reaction volume: 25 µl	BioMix Red: 12.5 µl forward primer (20 µM): 0.5 µl reverse primer (20 µM): 0.5 µl $MgCl_2$ (50 mM): 0.5 µl ddH_2O: 6 µl genomic DNA lysate: 5 µl
PCR cycles	
Thermal cycler: MJ Research PTC-225	Initialization: 94°C for 5 min 33 cycles: - denaturation: 95° for 60 s - annealing: 64.5°C for 60 s - extension: 72°C for 40 s Final elongation: 72°C for 10 min Final hold: 10°C infinite

Table 2-2. A summary of polymerase chain reaction (PCR) reagent volumes and thermal cycle temperatures.

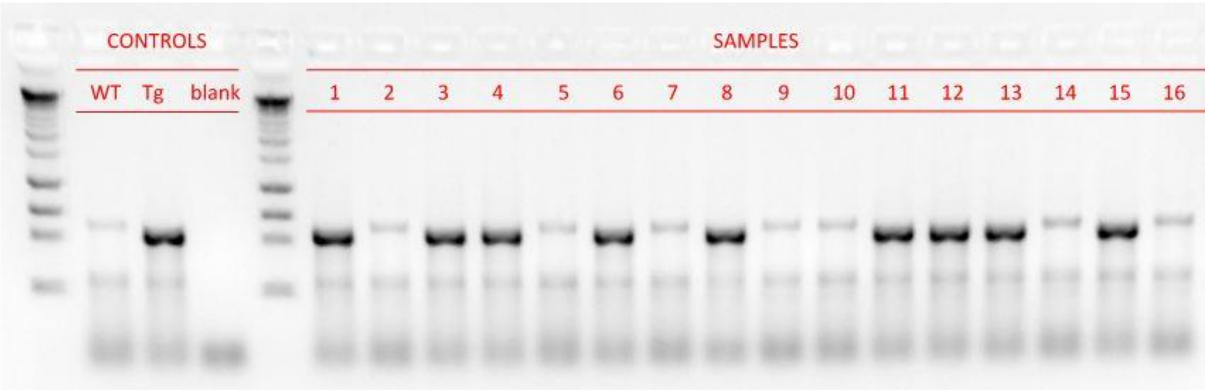

Figure 2-2. An example of a representative mGCH1-Tg genotyping electrophoresis gel image. The expected size of the amplified GCH1 product is 480bp.

Genotyping protocol for testing the Nnt deletion

To test the presence of Nnt deletion, the mouse genomic DNA was isolated from an ear notch using a "HotSHOT" protocol as described above. Similarly, the PCR reaction was prepared using the TaqMan DNA polymerase and primers designed and validated to detect the Nnt deletion present between exons 7 and 11 of the Nnt gene as described before (223, 226). Two primer pairs are used: the first primer pair amplifies the region inside Nnt exons 7-11 (a region with the deletion), which results in a band with a size of 200bp when the common Nnt deletion is absent *(Table 2-3)*. The second primer pair amplifies the region between Nnt exon 6 and 12 (spanning across the deletion), which produces a PCR product with the size of 500bp only when the Nnt deletion is present. The PCR reaction was prepared as specified in *Table 2-4* and products detected using gel electrophoresis as described above. A representative gel image is shown in *Figure 2-3*. None of the mouse colonies used in this thesis contained the Nnt deletion.

Oligonucleotides	
Nnt exon 6-12 forward primer sequence (5'-3')	GTAGGGCCAACTGTTTCTGC
Nnt exon 6-12 reverse primer sequence (5'-3')	TCCCCTCCCTTCCATTTAGT
Nnt inside deletion forward primer sequence (5'-3')	GCAGGTCTCACTGGGA
Nnt inside deletion reverse primer sequence (5'-3')	AACCTGAGATGGCATTGGTC

Table 2-3. Two primer pairs used to test for the deletion of nicotinamide nucleotide transhydrogenase (Nnt) gene. The first primer set (Nnt exon 6-12) spans the regions from exon 6 to exon 12. The second primer set is designed to amplify the region inside the deletion (Nnt exon 7-11).

PCR reaction	
final reaction volume: 25 µl	BioMix Red: 12.5 µl Nnt exon 6-12 forward primer (10 µM): 3 µl Nnt exon 6-12 reverse primer (10 µM): 3 µl Nnt inside deletion forward primer (10 µM): 2 µl Nnt inside deletion reverse primer (10 µM): 2 µl $MgCl_2$ (50 mM): 0.5 µl ddH_2O: 0 µl genomic DNA lysate: 2 µl
PCR cycles	
Thermal cycler: MJ Research PTC-225	Initialization: 95°C for 5 min 35 cycles: - denaturation: 95° for 60 s - annealing: 60°C for 60 s - extension: 72°C for 60 s Final elongation: 72°C for 10 min Final hold: 10°C infinite

Table 2-4. A summary of polymerase chain reaction (PCR) reagent volumes and thermal cycles temperatures for genotyping for the presence of common nicotinamide nucleotide transhydrogenase (Nnt) deletion in mice.

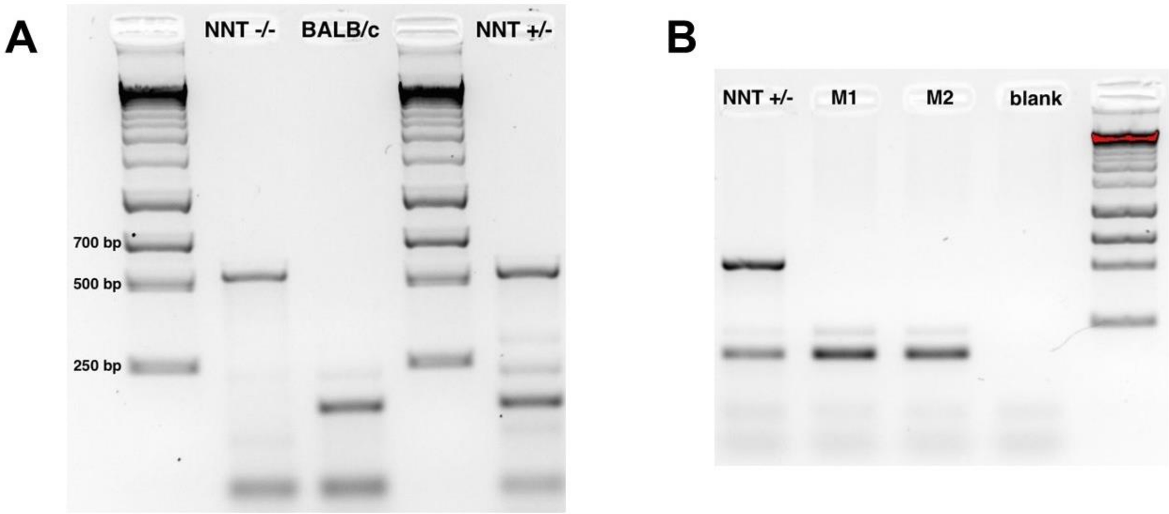

Figure 2-3. An example of a representative Nnt genotyping electrophoresis gel image. A) Gel electrophoresis with all the controls: DNA with the Nnt deletion (NNT -/-), DNA without the Nnt deletion (BALB/c), and heterozygous Nnt (NNT +/-). B) A representative image of the Nnt genotyping of mice used in this thesis (M1, M2).

Animal procedures

All animal procedures were performed in accordance with the United Kingdom Home Office Animals (Scientific Procedures) Act of 1986. Up to 25.1.2016, they were approved by the project licence number PPL 30/2804 (project licence holder: Prof Barbara Casadei). After 25.1.2016 they were approved by the PPL 30/3374 (project licence holder: Dr Ricardo Carnicer Hijazo).

STREPTOZOTOCIN INDUCED DIABETES MELLITUS

Streptozotocin (STZ)-induced diabetic mice were used to study the impact of diabetes mellitus on atrial arrhythmias and left ventricular (LV) diastolic function. STZ is cytotoxic for pancreatic beta-cells: it is structurally similar to glucose and is transported into beta cells by the GLUT2 transporter, where it acts as an alkylating agent causing DNA and protein damage (227, 228). However, GLUT2 is not selectively expressed only in pancreatic beta cells but is widely present in liver, kidney, and in cells of the central nervous system and therefore STZ causes also several off-target effects (229).

Males, aged 12-14 weeks, received intraperitoneal injections of low-dose STZ (50 mg/kg) dissolved in citrate buffer (0.1M, pH 4.5) or intraperitoneal injections of vehicle (citrate buffer) over five consecutive days. During the study, mouse body weight (BW) and plasma glucose levels were regularly monitored. Typical plasma glucose and BW profile over the course of study is presented in *Figure 2-4*. Only males were used in all the diabetes mellitus studies as STZ-injected female mice develop only mild hyperglycaemia (230).

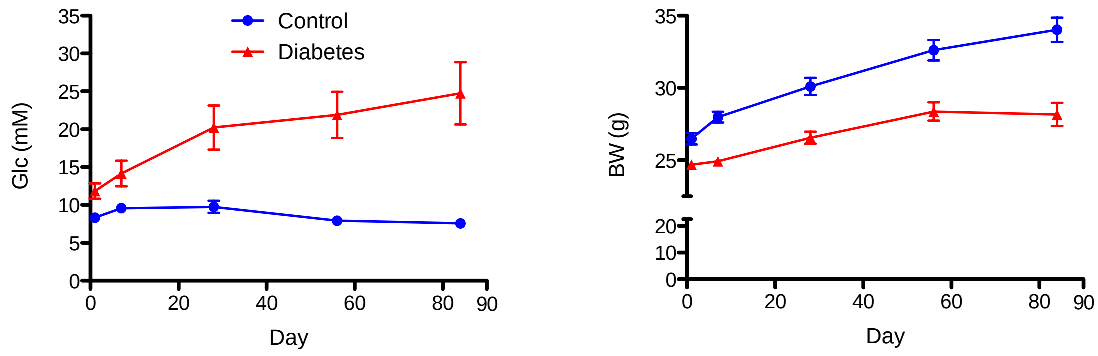

Figure 2-4. An example of plasma glucose (Glc) and body weight (BW) changes over the course of 12 weeks in diabetic and control mice. Day 0 is the day of the last (fifth) injection.

Mice used for the BH4 supplementation study had their diet changed (BH4 supplemented cookies or placebo cookies) after 6 weeks of diabetes. After 12 weeks of the last injection, mice cardiac function was assessed using echocardiography. Two days later all mice underwent transoesophageal atrial pacing study. After the pacing experiments mice were either sacrificed to collect tissue or recovered and used for optical mapping of isolated atria three to five days later.

GENERAL ANAESTHESIA

In order to perform *in vivo* measurements of cardiac function (e.g. echocardiography or atrial pacing experiments) mice need to be anaesthetised. The induction of general anaesthesia was done by putting a mouse in a transparent induction chamber pre-filled with 4% isoflurane. The mouse was then carefully observed as it progressed from light to deeper anaesthesia stages (231). Stage I is characterised as the stage of analgesia, disorientation until loss of consciousness occurs. During Stage II, mouse breathing becomes irregular: interchanging rapid breaths followed by apnea. During the Stage III (stage of surgical anaesthesia) mouse breathing becomes automatic and regular, followed by loss of reflexes. The last stage (Stage IV) is characterised by loss of automatic breathing followed by death.

The mouse was taken out of the induction chamber as soon as the stage of surgical anaesthesia (Stage III) occurred, in particular when respiration became completely regular and the respiratory rate (assessed by counting the number of chest movements in five seconds) dropped below 60/min. After that, the mouse was placed on a heated pad and the mixture of oxygen and isoflurane was delivered through the nose cone. The level of anaesthesia was continuously monitored during the procedure by measuring respiration rate, heart rate and by assessing pedal and corneal reflexes. The level of anaesthesia was adjusted by changing the concentration of inhaled isoflurane (normally between 0.5 and 2.0%). Awareness of stages of anaesthesia is very important to be absolutely sure that the mouse is at the right level for the stage in the procedure. Maintaining the same level of anaesthesia across mice is crucial for consistency in measuring physiological characteristics of interest (e.g. ECG interval, echocardiographic left ventricular parameters, etc.)

After the procedure, the mouse was recovered by stopping the isoflurane delivery and let to breathe 100% oxygen until the consciousness was regained. Afterwards, the mouse was put in a heated recovery box until it fully recovered (assessed by spontaneous walking in the recovery box) at which point the mouse put back to its original cage.

ECHOCARDIOGRAPHY IN MICE

Echocardiography was performed under isoflurane general anaesthesia (1.0-2.0% isoflurane). After induction of the general anaesthesia as described above, the mouse was placed on a heated table with built-in limb ECG electrodes (*Figure 2-5A*). In addition, the whole procedure was performed inside a procedure hood with an increased inside air temperature. The mouse body temperature was monitored throughout the procedure using the rectal temperature probe. To prevent drying of the eyes during the procedure, liquid gel (Viscotears, Novartis) was applied to both eyes. Afterwards, the mouse thorax was shaved with electrical hair clipper to improve image quality.

Echocardiography was performed using a Vevo 2100 (VisualSonics) ultrasound imaging system with an ultra-high frequency MS400 cardiovascular transducer (18-38 MHz). For left ventricular (LV) diastolic function measurements, mouse heart rate needs to drop down to ~350/min in order to see a separation of early and late LV diastolic filling phases (*Figure 5B*). This was achieved by maintaining higher isoflurane concentration (1.5-2.0%) during that phase of the imaging protocol. LV systolic function was assessed at higher, more physiological, heart rates (~500/min). The mouse was recovered from the general anaesthesia after all the echocardiographic recordings were obtained as described above.

Echocardiographic parameters of cardiac function are significantly affected by the heart rate during the measurements (232-234). Therefore a special effort was made that the recordings and measurements were taken at a similar heart rates for all mice (i.e. around 350/min for diastolic function parameters and around 500/min for systolic function parameters). Recordings and measurements significantly outside of this pre-determined range (>30/min) were excluded from further analysis. A potential improvement of the echocardiographic assessment of cardiac function in mice would be to record all images and traces while the heart is being externally paced to ensure a constant heart rate all across the measurements. This approach would be technically feasible in our lab, however the project licence for animal work did not allow us to perform this procedure at the time when the experiments were conducted.

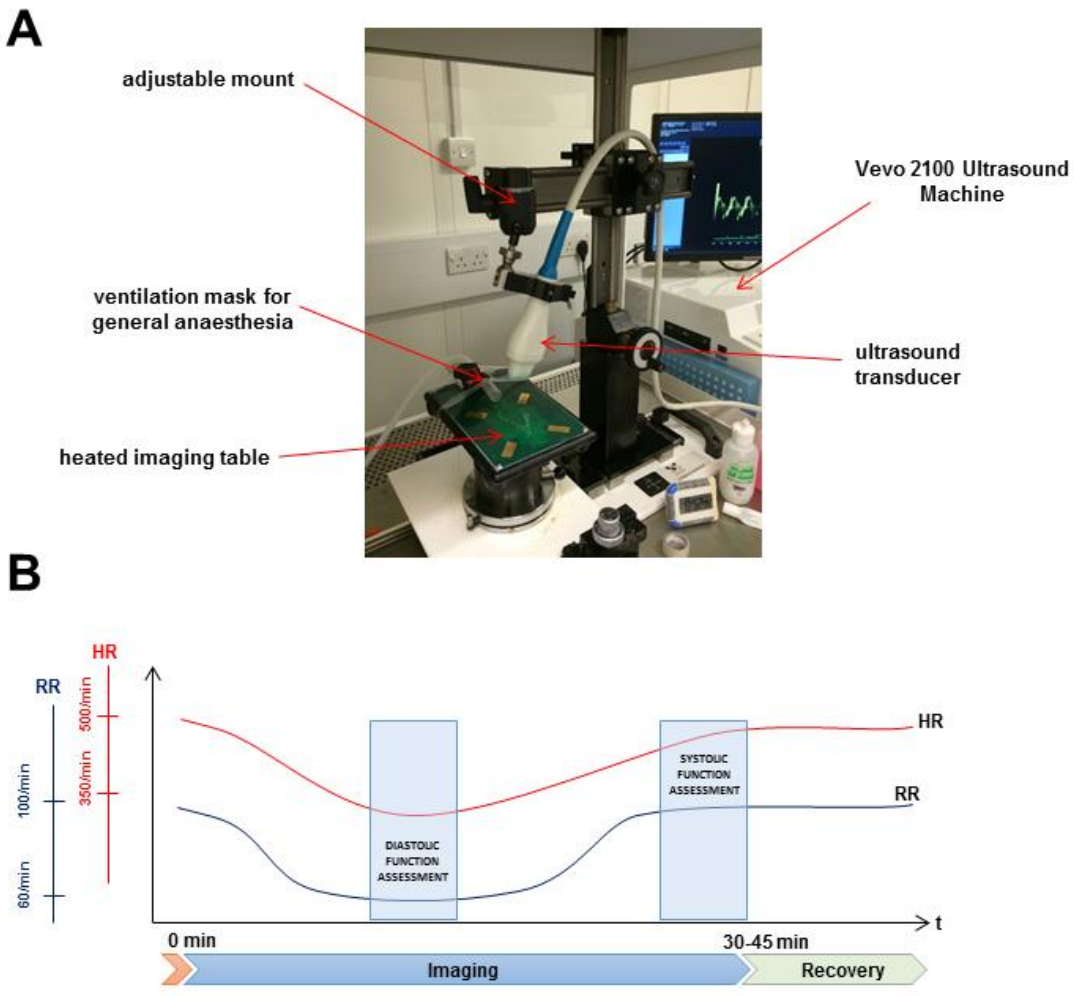

Figure 2-5. A – A photograph demonstrating the Vevo 2100 (VisualSonics) setup for mice echocardiography. B – Echocardiography imaging protocol to obtain diastolic and systolic function measurements. HR – heart rate, RR – respiratory rate.

LV diastolic function was assessed by tissue Doppler imaging (TDI) and mitral valve flow parameters recorded with the pulsed-wave Doppler mode (*Figure 2-6*). LV systolic function was assessed by the ejection fraction (EF) calculated from the motion-mode recordings of the LV short-axis view, at the papillary muscle level (*Figure 2-6*). The same recordings were also used to calculate LV mass was calculated from the diastolic LV internal diameter and LV wall thickness measurements. Left atrial (LA) recordings were obtained from the modified apical-4-chamber view. The precise position was carefully adjusted to capture the LA at their largest size for every single mouse investigation. The LA size was measured at the end of LV systole – the point of the largest LA size (*Figure 2-7*).

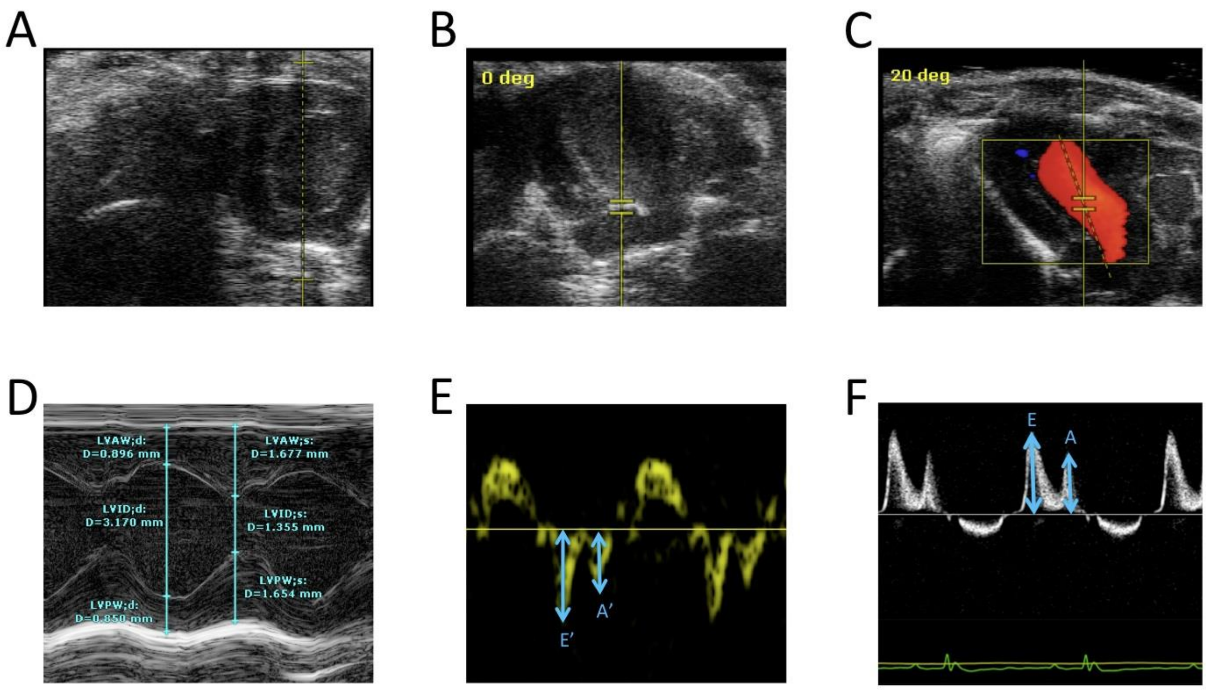

Figure 2-6. Examples of echocardiographic recordings demonstrating different views and modalities: short-axis view (A) and corresponding M-mode trace (D), apical 4-chamber view (B) and corresponding tissue Doppler trace (E), colour Doppler mode (C), and pulsed-wave Doppler trace of mitral valve flow (F).

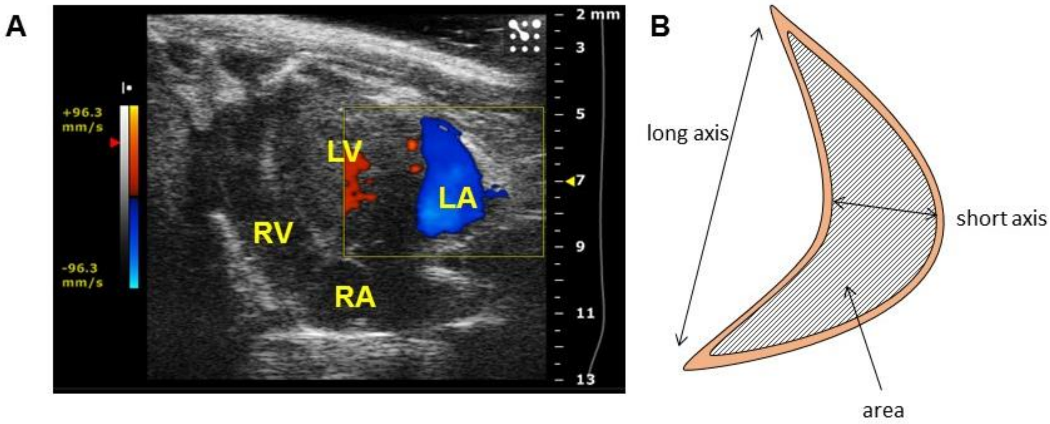

Figure 2-7. (A) Example of apical 4-chamber view at the beginning of diastole demonstrating left ventricular (LV) filling from left atria (LA). (B) LA dimension measurements (area, long axis, short axis) were taken at the point of largest LA size (at the end of systole, just before the start of diastole). RV – right ventricle, RA – right atrium.

As part of my training in mice echocardiography and to assess inter-observer variability, a sub-set of my echocardiographic recordings were also analysed by an experienced echocardiographer. Measurements from two different observers were compared using Bland-Altman plots, which is a method originally designed to compare how well a new measurement technique compares to the gold standard one (235). This method can be generalized to compare the degree of agreement of any pair of techniques or operators evaluating the same characteristic. Bland-Altman plot is constructed by firstly calculating the mean of two observations (obtained by two different methods or operators) for every measurement and then plotting a graph of mean difference from the mean vs. mean value (*Figure 2-7*). Secondly, you can then calculate the mean difference between the two observations and 95% limits of agreement to quantify how similar are the two methods. This type of representation is far superior to the simple correlation plot of observations from two different methods because it allows you to assess any systematic difference between the two methods (i.e. mean difference shifts from zero) as well as evaluate whether the difference between the two methods changes with the size of the measurement (e.g. does one method constantly obtains relatively higher values at smaller size measurements).

Comparison of echocardiographic analysis between two different observers indicates that there is no mean difference in measurements for LV mass, and diastolic function parameters: E'/A' ratio and E/A ratio (*Figure 2-8*). There is a slight systematic bias in EF parameter, where one observer systematically obtains 4% larger values. However, this difference is constant through the range of EF values meaning that this systematic shift does not affect comparisons between two different experimental groups in our studies.

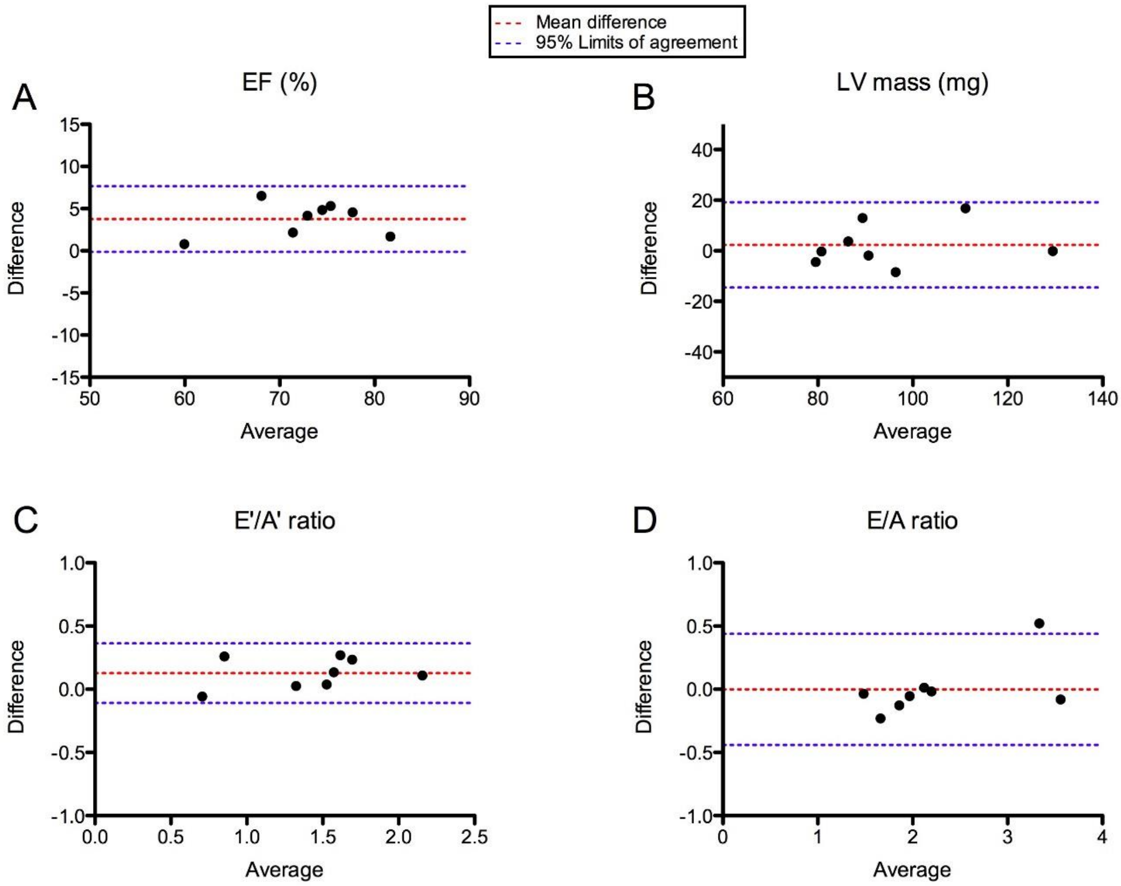

Figure 2-8. Bland-Altman plots of the most important echocardiographic parameters measured by two different operators. EF – ejection fraction, LV – left ventricle, E' – tissue Doppler early diastolic filling phase, A' – tissue Doppler late diastolic filling phase, E – mitral valve flow early diastolic filling phase, A – mitral valve flow late diastolic filling phase, red dotted line – mean difference between the two operators, blue dotted lines – 95% limits of agreement.

IN VIVO ATRIAL ELECTROPHYSIOLOGY IN MICE

Transoesophageal atrial pacing was performed under isoflurane general anaesthesia (1.5-2.0% isoflurane), as previously described (236, 237). Surface electrocardiogram (ECG) was obtained by placing electrodes subcutaneously in all four limbs (*Figure 2-9A*). Next, the distance between the mouse's mouth and the mouse's mid-sternum was measured. This distance was used in the next step to estimate how far the catheter can be advanced in the oesophagus. Afterwards, an octapolar electrophysiological catheter (NuMED CIBER mouse electrophysiology catheter) was advanced into the oesophagus for the length measured in the previous step to approximately reach the level of the left atrium (*Figure 2-9C*). Catheter position was then finely adjusted to obtain the strongest atrial signal in the intraoesophageal electrogram. Afterwards, the pacing was started with cycle length (CL) of 100 ms (shorter than the CL of the mouse’s spontaneous sinus rhythm) followed by a progressive increase in the amplitude of the pacing stimulus (0-3.2 mA) until consistent pacing of the atria was achieved (*Figure 2-10*). The amplitude was then decreased until atrial capture was lost to determine the threshold pacing amplitude. All the subsequent pacing was performed at 2x the threshold amplitude. The pacing protocol for induction of atrial arrhythmias consisted of burst atrial pacing episodes (40x S1 stimuli). The CL of every subsequent pacing episode was decreased (from CL 60ms to CL 10 ms) (*Figure 2-9D*). After every atrial burst pacing episode, the heart rhythm was assessed. The next burst pacing episode was started only after the recovery of sinus rhythm.

Basal ECG interval measurements were obtained from ECG recordings before any pacing was started (*Figure 2-9B*). Atrial arrhythmias were defined as an induced episode of irregular atrial rhythm lasting longer than 2 seconds. The number of arrhythmic episodes and their duration were measured. Data were presented as a probability of inducing atrial arrhythmias and as the longest duration of an arrhythmic episode.

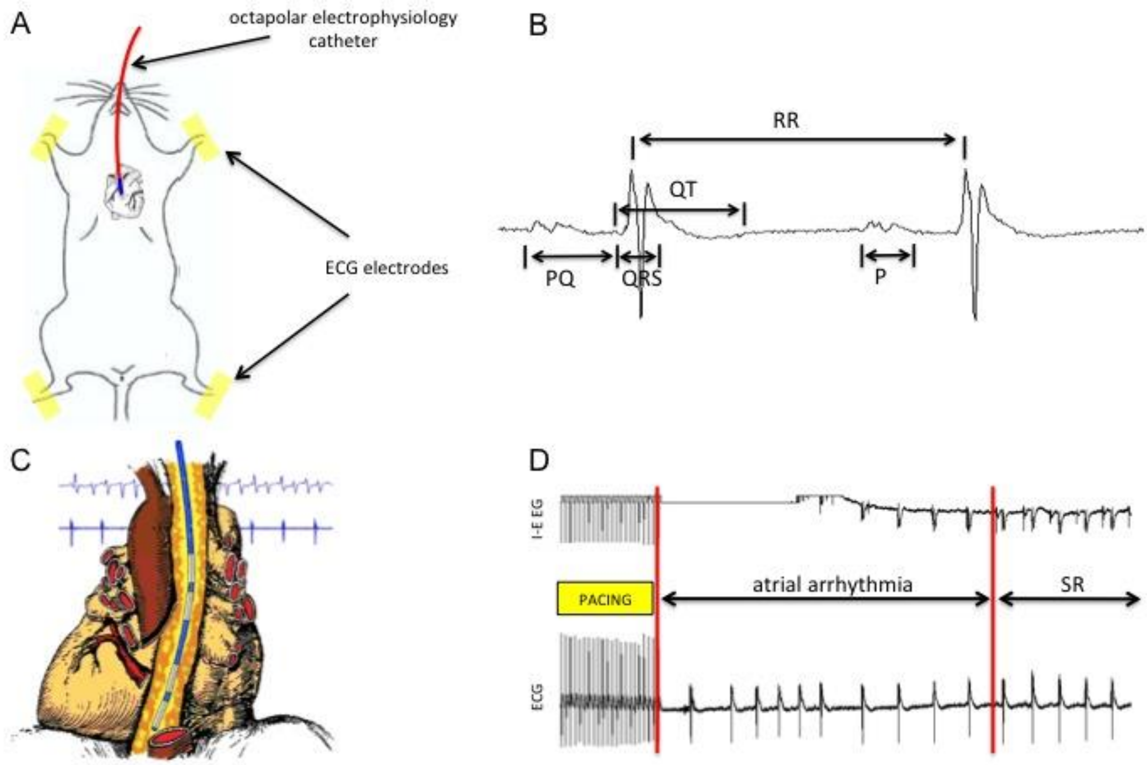

Figure 2-9. A - Schematic representation of the transoesophageal atrial pacing procedure, B - electrocardiogram (ECG) intervals, C - diagram illustrating the anatomical position of the intraoesophageal electrode relative to the heart, modified from (238), D - sample surface ECG and intraoesophageal electrogram (I-E EG) recordings demonstrating the pacing protocol and atrial arrhythmia. SR - sinus rhythm.

Figure 2-10. An example of successful transoesophageal atrial pacing and return to sinus rhythm. ECG – surface electrocardiogram recording, STIM – electrical stimulation recording.

Furthermore, for some mice, we measured additional electrophysiological parameters: sinus-node recovery time (SNRT), Wenckebach cycle length measurements, and AV node effective refractory period (AV ERP). The SNRT assess the time needed for the sinus node to start pacing after being overridden by external pacing. It is measured as the time from the last external pacing stimuli (after continuous pacing at constant CL of 100 ms for 4 seconds) to the R wave of the first spontaneous beat originating from the sinus node (the p wave is clearly visible) averaged over five consecutive pacing runs (*Figure 2-11A*).

The AV node has several physiological functions: it delays the electrical conduction from atria to ventricles to allow the complete filling of ventricles with blood flowing from atria; it also blocks any erroneous rapid electrical firing reaching the ventricles (prevention of ventricular arrhythmias), and, lastly, it can take over as the cardiac pacemaker in case of the sinoatrial node dysfunction. The Wenckebach cycle length measurements characterise the electrical conduction blocking properties of the AV node. Atria are paced at a fixed CL (starting at 40 stimuli at 100 ms) and the ventricular response during pacing is recorded and the 1:1 conduction is verified. The pacing CL is then decreased by 2 ms decrements (e.g. 40 stimuli at 98 ms, followed by 40 stimuli at 96 ms etc.) in the subsequent pacing trains down to pacing CL of 40 ms. Several pacing CL are measured: i) the shortest CL with the last full 1:1 conduction, ii) the CL with the first loss of 1:1 conduction (Wenckebach block), iii) the longest CL with the full 2:1 conduction, and iv) the shortest CL with the full 2:1 conduction (*Figure 2-11B*).

Additionally, the AV node effective refractory period (AV ERP) can be measured by series of pacing trains constituting from pacing at a constant CL followed by a second pacing stimulus (S2 stimulus) with a variable interval (e.g. 40 stimuli at 100 ms followed by S2 stimulus after 20 ms). The S2 interval of pacing trains is incrementally increased, starting from 20 ms and ending at 100 ms. The AV ERP is defined as the longest S2 interval that did not result in a ventricular response (*Figure 2-11C*).

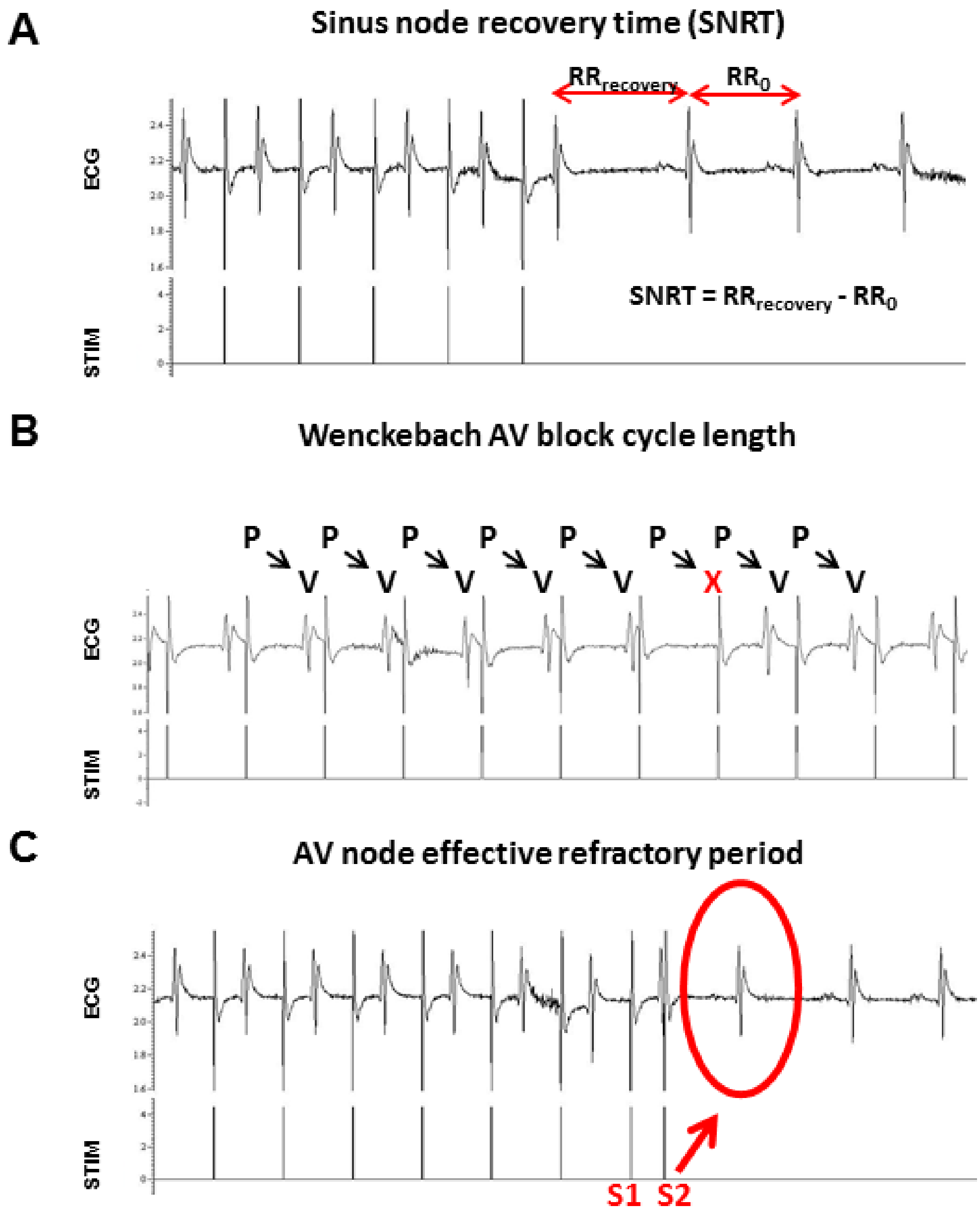

Figure 2-11. Representative traces for measuring additional electrophysiological parameters: (A) sinus-node recovery time (SNRT), (B) Wenckebach cycle length measurements, and (C) AV node effective refractory period (AV ERP). ECG – surface electrocardiogram recording, STIM – electrical stimulation recording.

Heart rate variability (HRV) is a measure of the change in the RR interval between consecutive heartbeats. The main factor that influences the HRV at the sinus-node (the main cardiac pacemaker) is the autonomic nervous system balance (239). An increased parasympathetic tone increases the HRV, whereas an increase in the sympathetic tone decreases the HRV. To measure the HRV parameters we analysed the long (5 minutes) uninterrupted baseline ECG recording of the anaesthetised mice. The ECG signal was then de-trended using a custom-built Matlab script to create a flat baseline ECG signal. The ECG signal was then analysed using the HRV add-on in LabChart 7 (ADInstruments), where the Poincare plot, period histogram, and beat-to-beat delta histogram were created (*Figure 2-12A*). The HRV analysis was only performed on ECG recordings with a regular sinus rhythm. Traces with an irregular cardiac rhythm (*Figure 2-12B*) were excluded from HRV analysis. We compared the standard deviation (SD) of the RR intervals and the SD of ΔRR intervals between investigated groups.

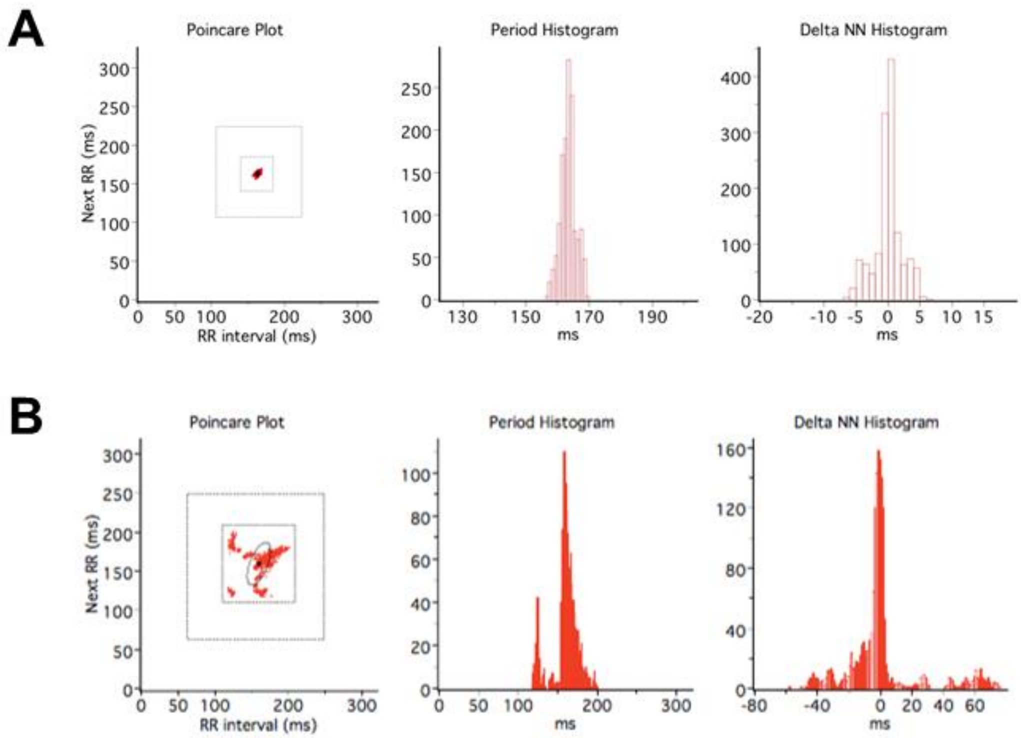

Figure 2-12. An example of the heart rate variability (HRV) analysis graphs created with the HRV add-on in LabChart 7 (ADInstruments). (A) An example of regular sinus rhythm analysis of HRV. Poincare plot shows the RR relationship between two consecutive heartbeats plotted as the RR interval vs. the next RR interval. The period histogram shows the distribution of all RR intervals in the analysed ECG recording. The delta NN histogram shows the distribution of the beat-to-beat variability (delta RR intervals) in the analysed ECG recording. (B) An example of irregular rhythm when analysed using the same HRV protocol – those traces were excluded from HRV measurements.

As a part of my training in transoesophageal atrial pacing and to assess inter-operators variability, a sub-set of electrophysiological recordings were analysed by an experienced electrophysiologist. Measurements from two different operators were compared using Bland-Altman plots (*Figure 2-13*). There is no mean difference in measurements of RR, P wave, and PQ intervals, as well as no mean difference in the measured probability of atrial arrhythmias. There is a slight systematic bias in measurements of QRS and QT intervals. Those two intervals are also the most variable between the two observers underlying the fact that the end of the QRS and QT intervals in mouse ECG is not as clearly demarcated as it is in human ECG and thus increases the potential subjective bias.

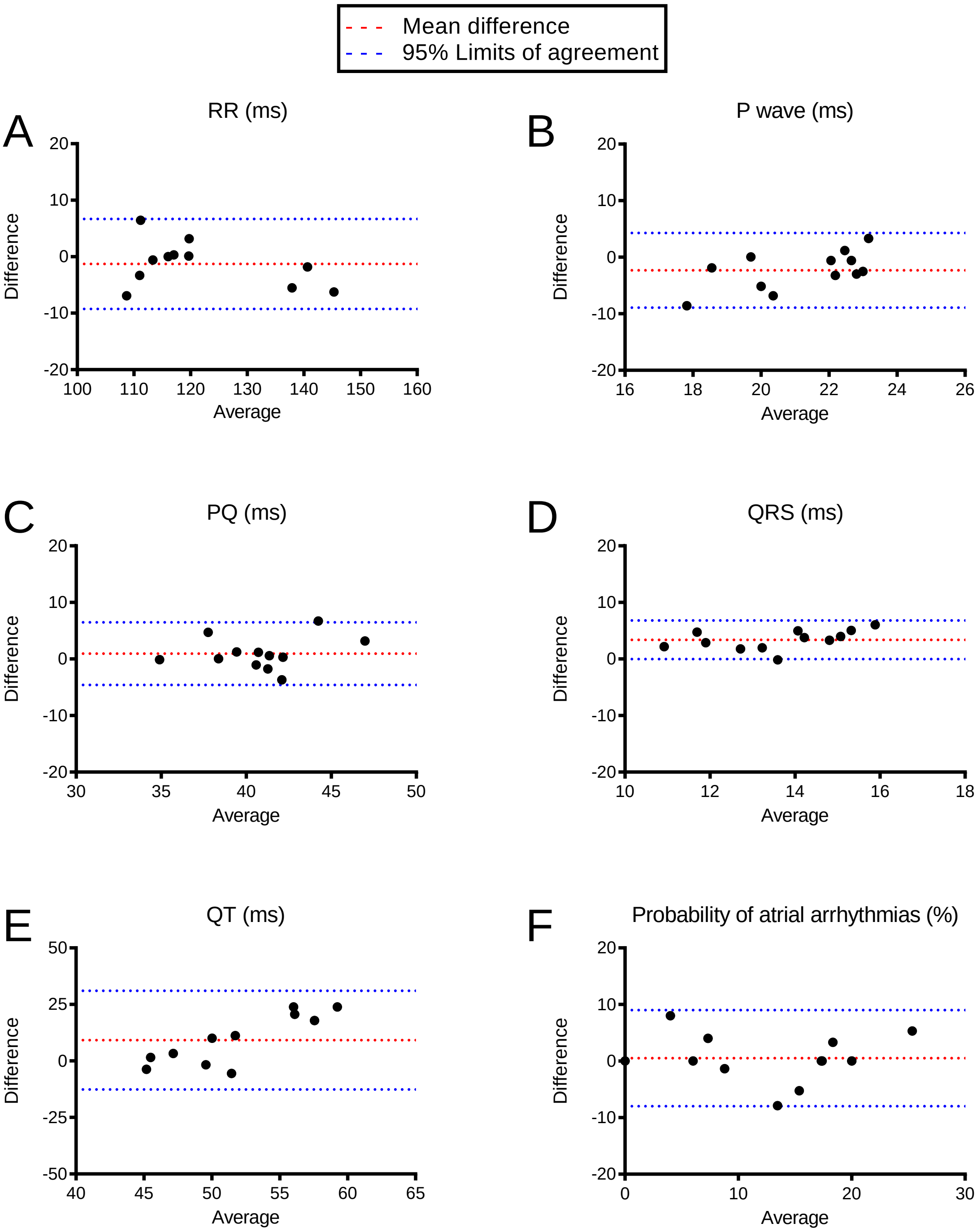

Figure 2-13. Bland-Altman plots of the basal surface electrocardiogram (ECG) parameters (A-E) and the probability of atrial arrhythmias (F) measured by two different observers. Red dotted line – the mean difference between the two operators, blue dotted lines – 95% limits of agreement.

DIET MODIFICATIONS (TETRAHYDROBIOPTERIN)

The tetrahydrobiopterin (BH4) supplementation study was carried out in 12-14 week old C57BL/6J males. As described above, mice received intraperitoneal injections of low dose STZ (50 mg/kg) or vehicle (citrate buffer) over five consecutive days. Six weeks after the last injection, mice were put either on a handmade BH4 supplemented diet (BH4 dose: 200 mg/kg/day) or on a handmade placebo diet for the next 6 weeks. During the study, mouse body weight, plasma glucose levels, and food consumption were regularly monitored. At the end of the study, after 12 weeks of diabetes, cardiac function was assessed using echocardiography. Two days later all mice underwent transoesophageal atrial pacing study. After the pacing experiments mice were either sacrificed to collect tissue or recovered and used for optical mapping of isolated atria three to five days later.

The BH4-supplemented diet was prepared by mixing 720 g of rodent diet mash (Teklad global 16% protein diet, Harlan Laboratories) with 1000 mg of BH4 (Schirks Laboratories) dissolved in approximately 350 ml of water. Small balls of this mixture were rolled out on a flat and clean surface until a compact and ~1cm thick disc-like shape were obtained. The mixture was then cut into smaller pieces and left to dry overnight at 32-34ºC (*Figure 2-14*). The placebo diet was made in a similar way but BH4 was omitted. Dried food pieces were stored in a clean plastic container at -20°C for up to one month.

BH4 concentration in the diet was calculated from the results of a previous pilot study where we measured body weight and daily food consumption of our handmade diet in order to achieve a daily BH4 dose of 200 mg/kg. During the study, we continuously monitored daily food consumption to confirm that mice consumed the targeted daily dose of BH4.

Figure 2-14. Preparation, storage, and dispensing of tetrahydrobiopterin (BH4) supplemented diet.

Optical mapping of isolated atria

The mouse was humanely killed using a cervical dislocation, an approved method listed in the United Kingdom Home Office Schedule 1 to the Animals (Scientific Procedures) Act 1986. Following a cervical dislocation, the skin and abdominal wall below xiphoid were incised. Afterwards, the clamshell thoracotomy was performed and the heart immediately excised and placed into Tyrode's solution (35 °C) as specified in *Table 2-5*. The heart was then pinned to the bottom of a clear Sylgard-coated (Dow Corning Sylgard 184 Silicone Elastomer) petri dish to reveal the dorsal atrioventricular connective tissue.

The lungs, thymus, and ventricles were carefully dissected, leaving a preparation consisting of the interconnected left and right atria. Lastly, the superior and inferior vena cavae were cut open and the atrial tissue was stretched and pinned to the bottom of the Sylgard-coated superfusion chamber (a 35 mm plastic petri dish) using size 0 insect pins so that the crista terminalis and interatrial septum were visible.

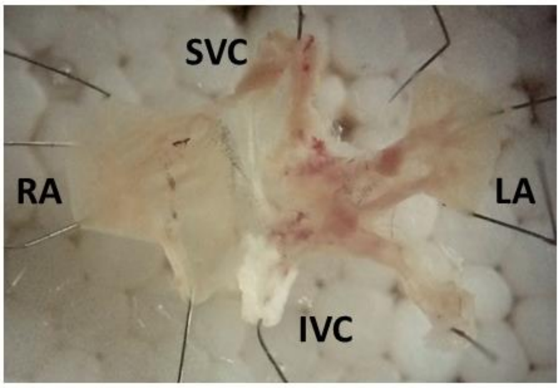

Figure 2-15. A picture of pinned down isolated mouse atria prepared for optical mapping recordings. RA – right atrium, LA – left atrium, SVC – superior vena cava, IVC – inferior vena cava.

Tyrode solution	MW	c (mM)	m (g) for 500 ml
NaCl	58.40	130	3.798
KCl	74.55	5.6	0.201
$MgCl_2$ x 6H2O	203.30	3.5	0.356
HEPES	238.30	5.0	0.596
Na_2HPO_4	141.96	0.4	0.031
Glucose	180.16	10	0.90
Taurine	125.15	20	1.25
Ca^{2+} (1M solution)	110.98	1.4	700µl of 1M
→ pH to 7.4 using NaOH			

Table 2-5. Specifications of the Tyrode solution used in the electrophysiological experiments. The concentrated 10X Tyrode stock solution containing everything apart from glucose, taurine and calcium was prepared in advance and stored at 4°C for up to one month. On the day of the experiment, the final Tyrode solution was freshly prepared from the stock solution. MW – molecular weight, c – final concentration of the solution.

Atria were incubated with the voltage-sensitive dye di-4-ANNEPS (20 µM) for 30 minutes at 37°C. The staining solution was then removed and preparations were superfused with (95% O_2/5% CO_2) Krebs solution containing 5 µM blebbistatin to prevent motion artefacts, as specified in *Table 2-6*. The temperature in the perfusion chamber was regularly controlled and maintained at 37°C by adjusting the flow rate of the heated buffer in the chamber. Experiments were performed in spontaneous sinus rhythm conditions therefore it was critical to maintain the temperature constant in the physiological range.

Krebs solution	MW	c (mM)	m (g) for 1L
NaCl	58.40	118	6.90
KCl	74.55	4.2	0.313
KH_2PO_4	136.02	1.2	0.163
$MgSO_4$	120.37	1.2	0.144
$NaHCO_3$	84.01	25	2.1
Glucose	180.16	11	2.0
Na-pyruvate	110.04	2.0	0.22
$CaCl_2$	110.98	1.5	0.166
→ pH to 7.4			

Table 2-6. Specifications of the Krebs solution used in the electrophysiological experiments. MW – molecular weight, c – final concentration of the solution.

Illuminating light, provided by a LED source (MacroLED, Cairn Research) was passed through a selection filter and reflected off a dichroic mirror (565 nm, Chroma) onto the preparation. For imaging transmembrane voltage (Vm) kinetics, the emitted light was passed through a long-pass filter (>700 nm) and captured using a high-speed CMOS camera (NeuroCMOS-DW128-II, Cairn Research) with 250x250 pixel resolution. The camera was mounted on an Olympus MVX10 Macroview fluorescent microscope and images were acquired at 1000 frames/s using the GView optical mapping software (courtesy of Professor Gil Bub, University of Oxford). Electrogram recordings of isolated atria were obtained simultaneously with optical mapping by placing custom-made platinum bipolar electrodes directly on the atrial tissue. Electrical signals were then amplified using the Iso-DAM8A amplifier system (World Precision Instruments), acquired using the Power1401 data acquisition device (Cambridge Electronic Design) at a sampling rate of 2000 Hz, and visualized using the Spike 7 analysis software (Cambridge Electronic Design).

Figure 2-16. Setup of the optical mapping equipment. The perfusion chamber was perfused with Krebs buffer and was maintained at 37°C by adjusting the flow rate of the heated perfusion buffer.

Optical action potential duration (APD) was computed offline from inverted fluorescence data from several small regions (6x6 pixel squares) of interest (ROI) using a script that was written in MATLAB (MATLAB R2017a, Mathworks, Natick, MA) (*see Appendix*). Raw action potentials (AP) were first filtered (5th order Butterworth filter, 100 Hz cut-off) and the filtered traces analysed to identify activation and repolarization times. Activation time of the AP was determined as the time of the maximum of the first derivative of the fluorescence signal (dF/dt) corresponding to the maximum slope of the action potential upstroke. Repolarization time was measured as the time when a specified level of repolarization (30%, 50%, and 80%) is reached during the repolarization phase of the AP. The APD was then calculated as the difference between the activation and repolarization time. Finally, the average APD was calculated from several ROIs from LA and RA.

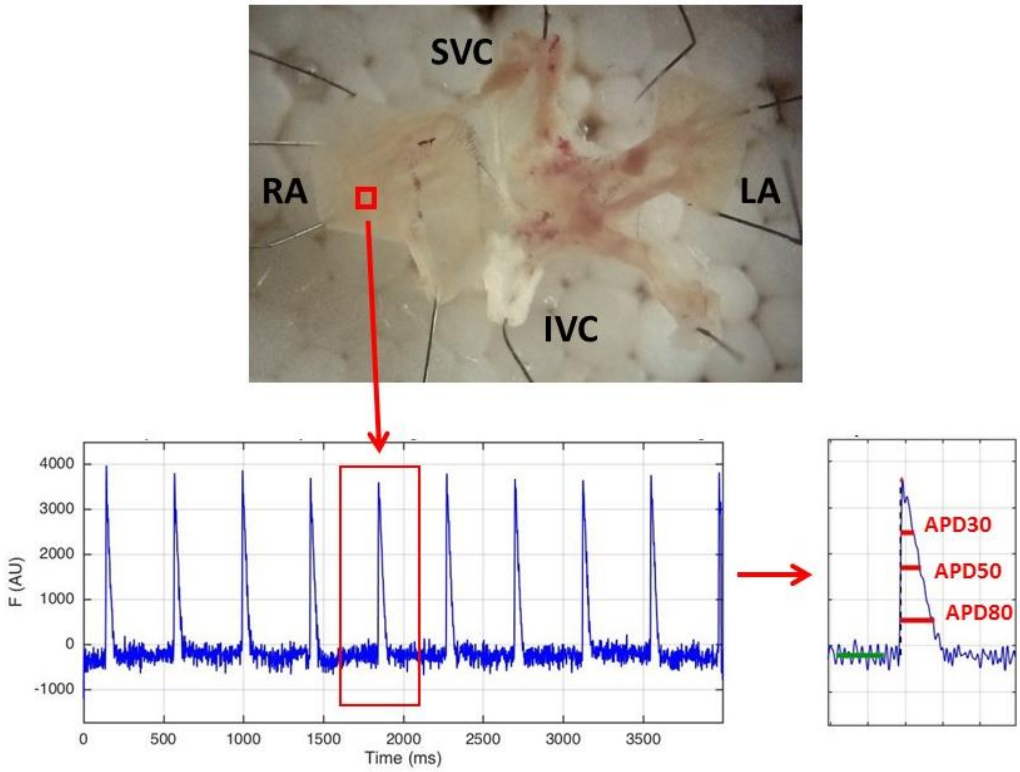

Figure 2-17. A representative fluorescence signal (F) obtained from a single region of interest (red square) and the corresponding automatic calculation of action potential duration (APD). APD30/APD50/APD80 – action potential duration at 30%, 50%, and 80% repolarization respectively.

Regional atrial conduction velocity is another important feature that was calculated from the optical mapping recordings. Firstly, the atrial region was outlined and masked from the bright field image obtained after every fluorescence recording. A MATLAB script was written to automatically detect the atrial region (*see Appendix*) using a series of Gaussian filters and edge detection algorithms followed by dilation and hole filling to obtain a closed mask area (*Figure 2-18*). Secondly, the masked image was then cut to quarters by width to roughly divide the whole atria into four regions: lateral-LA, mid-LA, mid-RA, and lateral-RA (*Figure 2-19A*). Finally, the fluorescence recordings from those individual regions were then analysed using the Ccoffinn (Cardiomyocyte Cultures Optically-mapped: Fast Feature extractIoN and tracking) toolkit written by Jakub Tomek

(240). The software detects electrically active areas in every frame and then segments those areas into the leading wavefront edge area (depolarization), the area within the wave, and the end of the wave area (repolarization area). This approach is somewhat different from a conventional approach where first an activation map is created and then multiple vectors are fitted on based on the whole activation map to calculate conduction velocity. While a majority of conduction velocity analysis software in previously published papers is proprietary, there is now finally a trend to publish the analysis software in an open-source repositories (240, 241). The movement of areas is then tracked frame by frame to allow the extraction of several different electrical conduction features such as wavefront speed (conduction velocity) and wavefront roughness. Wavefront roughness is calculated as a mean perimeter-to-area ratio of the wavefront. Wavefront roughness represents how smoothly and uniformly the electrical signal moves through the tissue.

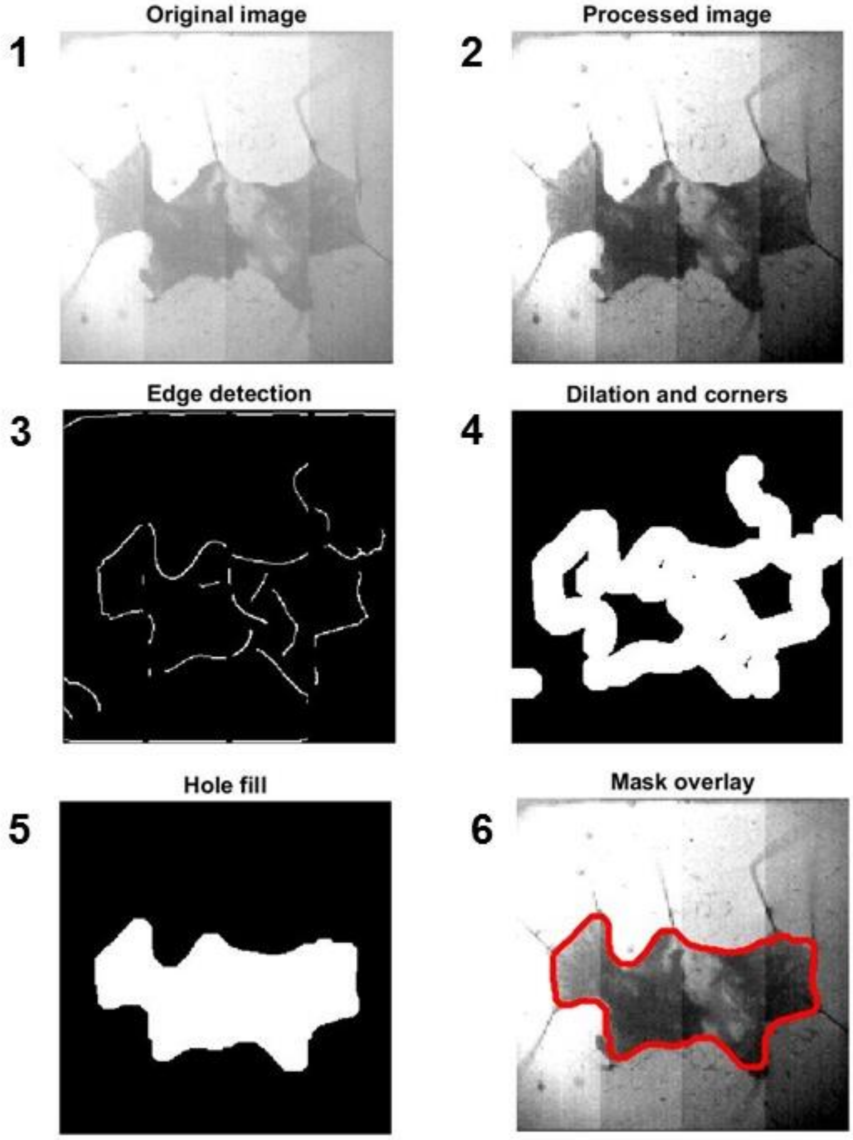

Figure 2-18. Main steps in automatic outlining of the atrial region. Original image (1) was first adjusted to increase the contrast (2), then the edge detection algorithm was applied to the image (3), followed by dilation of lines to create an enclosed area (4), which was then filled to form one object (5). The final mask was checked for accuracy by overlaying it on the original image (6).

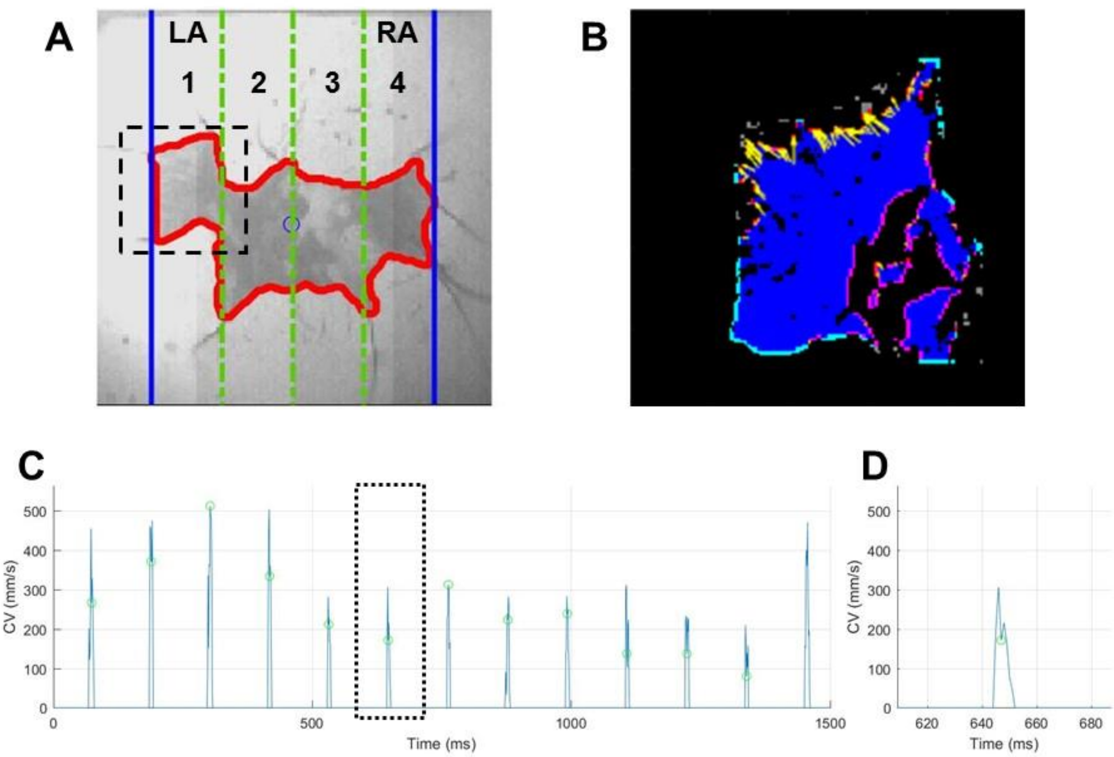

Figure 2-19. (A) For the conduction velocity analysis, the whole atria were divided into four regions. (B) An enlarged image of the boxed region in (A) presenting the Ccoffinn analysis of conduction: yellow arrows – conduction vectors representing the movement of the leading wavefront edge area (depolarization), blue area – area within the wave, purple – end of the wave area representing the repolarization. (C-D) Plots of the average length of conduction vectors per frame over the whole length of the recording of one atrial region.

31P magnetic resonance spectroscopy

Cardiac ^{31}P magnetic resonance spectroscopy (MRS) experiments were performed, as described previously (242-244). Mice were euthanized with an intraperitoneal injection of pentobarbitone (140mg/kg) and anticoagulated with an intraperitoneal injection of heparin (150 IU). Afterwards, the clam-shell thoracotomy was performed and the heart was rapidly excised, cannulated and retrogradely perfused with the Krebs solution using the constant pressure (80mmHg) Langendorff setup. After the cannulation, the hearts were put into the centre of a ^{1}H/^{31}P coil (Rapid Biomedical, Wurzburg, Germany) with an inner diameter of 10 mm for the MRS in an 11.7 T magnetic resonance scanner (Magnex Scientific, Oxford, UK). The precise position of the heart was finely adjusted by taking 3-slice ^{1}H magnetic resonance images. After shimming, the water resonance line-width was less than 70 Hz for all the measurements. The ^{31}P spectra of the heart were acquired at 202.4 MHz using a 90° flip angle, repetition time (TR) 15 seconds and 80 averages. The spectra were analysed using the AMARES algorithm in the jMRUI software package (245, 246). The phosphocreatine (PCr) resonance was set to 0.0 ppm and the chemical shifts of other metabolites were referenced to the PCr. The PCr to ATP ratio was calculated from the areas under the fitted γ-ATP and PCr peaks.

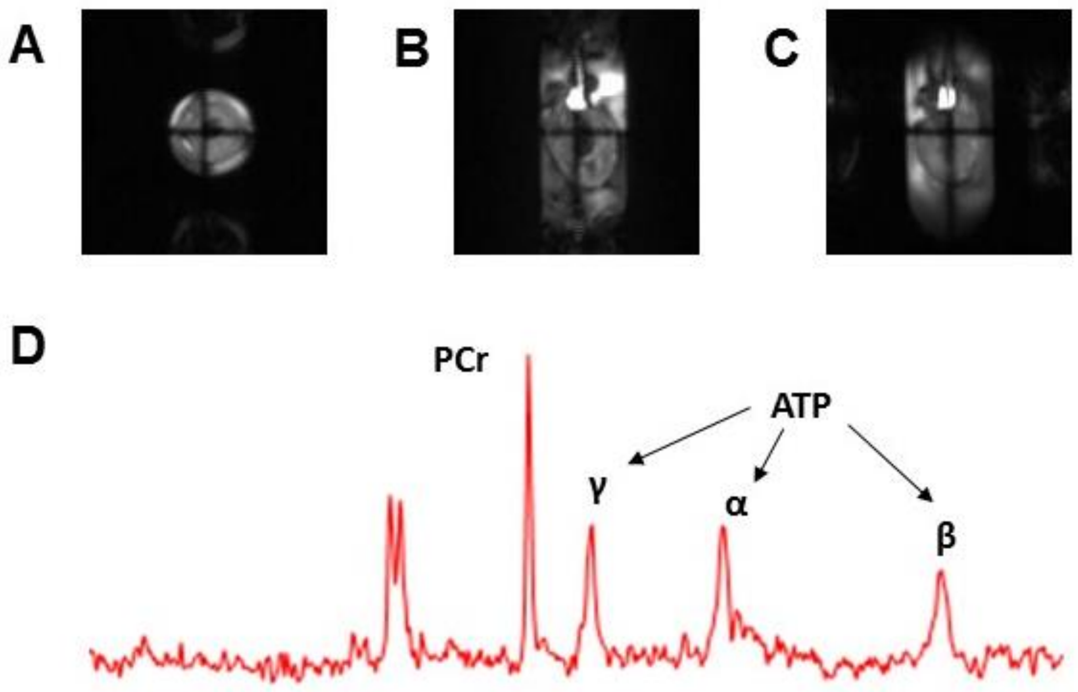

Figure 2-20. (A-C) Axial, sagittal, and coronal plane localisation of the isolated perfused heart in the coil during ^{31}P magnetic resonance spectroscopy (MRS) recordings. (D) Representative spectral trace from ^{31}P-MRS in isolated perfused hearts illustrating phosphocreatine (PCr) and ATP peaks.

Cell shortening experiments

Cell shortening experiments were performed as described previously (185). The mouse was sacrificed using a cervical dislocation, an approved method listed in the United Kingdom Home Office Schedule 1 to the Animals (Scientific Procedures) Act 1986. Following a cervical dislocation, the skin and abdominal wall below xiphoid were incised. Afterwards, the clamshell thoracotomy was performed. The heart was cannulated in situ, excised, and placed on the Langendorff perfusion system. Hearts were perfused with Ca^{2+}-free isolation solution for 3 minutes, followed by perfusion with a solution containing collagenase type I for 9 minutes. Afterwards, the hearts were removed from the Langendorff perfusion system, LV was excised, and placed in the digestion solution containing collagenase type II. Afterwards, the solution was centrifuged and resuspended in storage solution. Experiments on isolated LV cardiomyocytes were performed within 6 hours of the isolation.

Cell shortening experiments were performed in a continuously perfused and field-stimulated (at 3 Hz) chamber. The cardiomyocyte contraction and relaxation were recorded using a video-edge detection system (IonOptix). Cardiomyocyte fractional shortening and relaxation constant (characterised by t_{50}) were measured and averaged from at-least 10 steady-state contractions.

Tissue collection

The mouse was humanely killed using a cervical dislocation, an approved method listed in the United Kingdom Home Office Schedule 1 to the Animals (Scientific Procedures)

Act 1986. Following a cervical dislocation, the skin and abdominal wall below xiphoid were firstly transversely incised. Then the abdominal wall was incised longitudinally and large intestines pushed laterally until the inferior vena cava was clearly visualised. The inferior vena cava was then cut. Afterwards, the clamshell thoracotomy was performed and the cardiac pericardium was removed. The heart was then slowly perfused with approximately 10-15 ml ice-cold phosphate-buffered saline (PBS) using a 25G needle firstly from the right ventricle (RV) and then from the LV until the whole circulation system was cleared of blood (as noted by clear liquid coming out of the incised inferior vena cava). At this stage the RA and LA were cut, quickly dried of excess fluid on a paper tissue, put into a cryotube, which was then put into a container with liquid nitrogen (-196°C) for rapid freezing. Then the whole heart was incised and put into a container with cold PBS. The base of the heart with all the valves was removed and then the RV was cut away from the LV. The LV tissue was longitudinally cut into four small pieces, and then, as before, quickly dried of excess fluid on a paper tissue, put into a cryotube, which was then put into a container with liquid nitrogen for rapid freezing. If needed, other organs such as lung, liver, kidney, pancreas, spleen, skeletal muscle and brain were collected afterwards. In the end, the cryotubes were collected and stored at alarm-monitored freezer at -80°C until used for later assays.

Tissue processing

In order to use samples for any molecular assay, the frozen tissue needs to be homogenized. A chunk of frozen tissue (e.g. a quarter of LV or whole atria) was weighed and then moved into a new cold tube. An ice-cold homogenizing buffer was added according to the weight of the tissue (10µl for every mg of tissue, a minimum volume of

100 μl). Different homogenizing buffers were used depending on the final molecular assay used: e.g. RIPA buffer (Thermo Fisher), Krebs buffer or PBS. Tissue was then homogenised either with the handheld glass homogenizer on ice or using the TissueLyser (Qiagen) with pre-cooled (on dry-ice) 5 mm stainless steel beads for 2 minutes at 50 Hz. The homogenate was then centrifuged at 17,000g at 4°C for 10 minutes. Finally, the supernatant was moved into a new tube and used for further analysis. An aliquot of the supernatant was used for the determination of the protein concentration.

Tissue extract protein quantification

Protein concentration in a tissue extract was assessed using a Pierce BCA Protein Assay Kit (Thermo Scientific). The kit uses a bicinchoninic acid (BCA) for the colourimetric quantification of total protein in the sample (247). Peptide bonds in proteins in alkaline environment reduce the Cu^{2+} to Cu^{+}. This reduction reaction is proportional to the amount of protein. The BCA then chelates the Cu^{+} ion to form a purple coloured complex. The whole reaction can be quantified by measuring the absorbance at 562 nm.

An aliquot of the homogenized tissue extract was diluted so that the protein concentration was in the working range of the assay kit (0.1 – 2.0 mg/ml). A series of standard protein (bovine serum albumin - BSA, 2.0 mg/ml) dilutions were prepared ranging from 0 to 2.0 mg/ml. Then the standards and sample dilutions were incubated with an equal volume of 0.1M iodoacetamide in 0.1M NaOH solution for 15 min at 37°C. Afterwards, the working reagent (a mixture of the kit's BCA reagent A and B in 50:1 ratio) was added to all the standards and samples. The tubes were then incubated for 3- min at 37°C. Finally, the standards and samples were then pipetted (in duplicates) into a flat bottom 96-well plate and the absorbance in the wells was measured at 562 nm. The average of the duplicates was used for the analysis. The standard curve was created by fitting a linear line to the values of the standards. The standard curve was then used to calculate the protein concentration of the samples.

Western blot

The tissue samples were firstly homogenised in the RIPA buffer containing protease inhibitors (cOmplete protease inhibitor cocktail, Roche) as described above. The protein concentration of every sample was measured using the BCA assay as described above. The proteins were separated by the gel electrophoresis using the Criterion 4-15% gradient gel in the Tris-Gly-SDS running buffer. The full-range Rainbow protein marker (Fischer Scientific) was loaded in the first well of the gel to allow the visualization of different protein weights. An equal amount of isolated protein (20 µg) of every sample was then loaded in the remaining wells. The electrophoresis was firstly run for 10 minutes at a 90V (constant voltage setting) at the room temperature to line up all the proteins in different gels. Afterwards, the electrophoresis was run at 150V (constant voltage setting) for around 40-50 minutes until the marker for the lowest protein weight was just about to reach the bottom part of the gel.

After the proteins were separated in the gel, we prepared the cassette for the protein transfer from the gel to the PVDF membrane. The PVDF membrane was pre-activated in 100% methanol for 1 minute and then washed in the water. The transfer sandwich constituted of sponge, blotting filter paper (Criterion), PVDF membrane, gel, blotting filter paper, and another sponge. The sandwich was closed in a dedicated Criterion transfer cassette and allow to equilibrate in the ice-cold transfer buffer (Tris-Gly buffer with 20% methanol). The cassette was secured in the Criterion transfer tank and placed in the cold room (4°C). The transfer was run at 35V (constant voltage) for 90 minutes.

After the transfer of the proteins to the membrane was completed, the membrane was trimmed to the right size. The membrane was stained with the Ponceau S acid red to confirm the successful protein transfer all across the membrane. Afterwards, the membrane was washed in the blotting Tris-buffered saline containing 10% Tween (TBS-T). The membrane was then blocked in 5% milk dissolved in TBS-T for 60 minutes at the room temperature. Afterwards, the membrane was incubated in the primary antibody solution (diluted in 5% milk TBS-T) overnight at (4°C). The primary antibodies used in the results presented in this thesis are as follows: GAPDH (Millipore AB516, 1:50000 dilution), TnI (Millipore MAB1691, 1:2000 dilution), UCP3 (Thermo Scientific, 1:1000 dilution), GLUT1 (Millipore 07-1401, 1:1000 dilution), GLUT4 (Millipore, 1:5000 dilution).

After the overnight incubation of the membrane with the primary antibodies, the membranes were washed to remove non-specifically bound primary antibodies. Afterwards, the membrane was placed in the solution containing the secondary antibodies conjugated with the horseradish peroxidase (HRP) of the appropriate host to target the primary antibody (anti-rabbit from Promega 1:5000 dilution, anti-goat from Promega 1:5000 dilution) for 1 hour at the room temperature. The membrane was then incubated with the Pierce enhanced chemiluminescence (ECL) substrate solution (Thermo Fischer) and imaged with the ChemiDoc MP imaging system (BioRad). The appropriate protein bands were then quantified densitometrically and normalized to the housekeeping proteins (e.g. GAPDH or TnI).

Biopterin measurements

The concentration of tetrahydrobiopterin (BH4), dihydrobiopterin (BH2) and biopterin (B) in the sample was measured using the high-performance liquid chromatography (HPLC) method (185, 248). The compounds were separated using the reverse phase HPLC separation (*Figure 2-21*). The BH4 was measured using the electrochemical detector (Coulochem III, ESA Inc.), which firstly oxidized the BH4 into quinonoid dihydrobiopterin (qBH2) and then reduced it back to the BH4. The generated current is used to determine the BH4 concentration. The BH2 and B were measured using the fluorescence detector (Jasco FP2020).

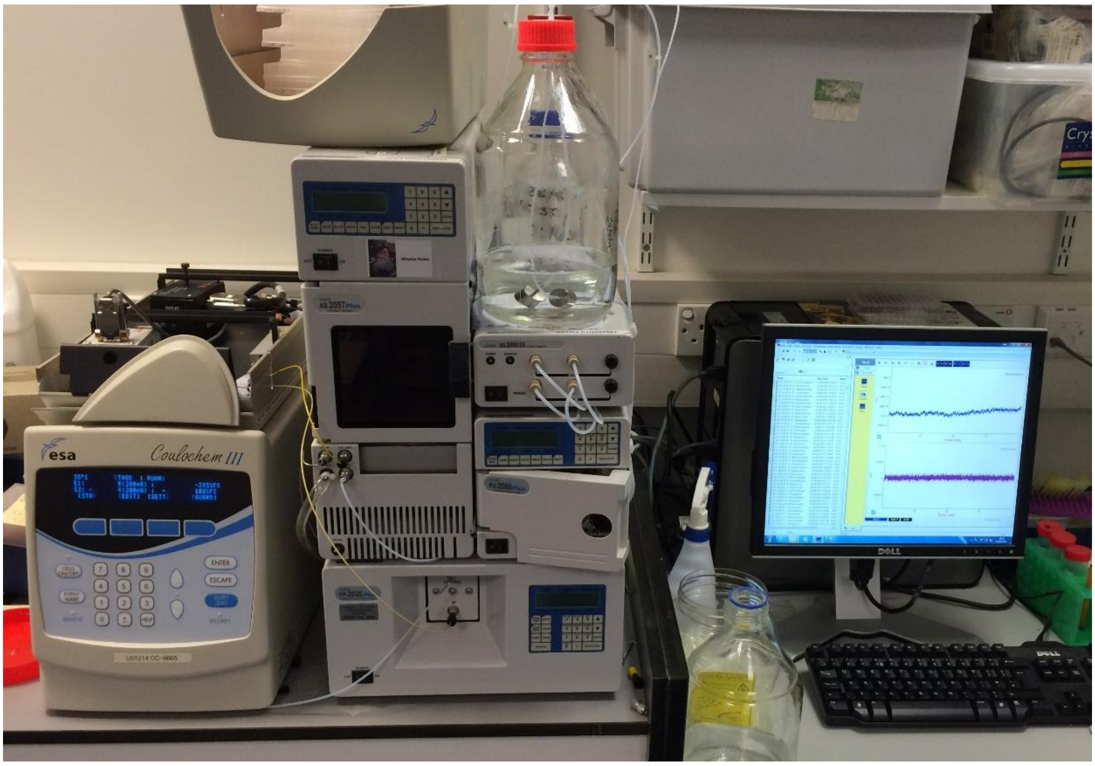

Figure 2-21. A high-performance liquid chromatography (HPLC) setup to sequentially measure the concentrations of tetrahydrobiopterin (using the electrochemical detector), dihydrobiopterin and biopterin (using the fluorescence detector).

The tissue sample was firstly homogenized in ice-cold PBS (50 mM, pH 7.4) containing dithioerythritol (DTE, 1 mM) and ethylenediaminetetraacetic acid (EDTA, 100 µM). The homogenate was then centrifuged at 17,000g at 4°C for 15 minutes, the supernatant was collected and centrifuged again at 17,000g at 4°C for 15 minutes. Afterwards, an aliquot of the supernatant was collected for the sample's protein concentration measurement. The remaining supernatant was then treated with phosphoric acid (final concentration 1M), trichloroacetic acid (final concentration 2M), and DTE (final concentration 1mM) to precipitate all the proteins. The treated supernatant was centrifuged at 17,000g at 4°C for 5 minutes. The clear supernatant was then loaded into the 96-well plate from which the autosampler collected the liquid and injected into the HPLC column. The HPLC separation was performed using a 250 mm ACE C-18 column (Hichrom) and a mobile phase containing sodium acetate (50 mM), citric acid (5 mM), EDTA (48 µM), DTE (160 µM), pH 5.22 and a flow rate of 1.3 ml/min.

All the biopterins (BH4, BH2, and B) were quantified as the area under the curve (AUC) from the signal obtained from the sequential electrochemical and fluorescence detection (*Figure 2-22*). The values were compared to the externally validated standards of BH4, BH2, and B that were also run at the same time as the samples. The final concentration was normalized to the sample's protein content.

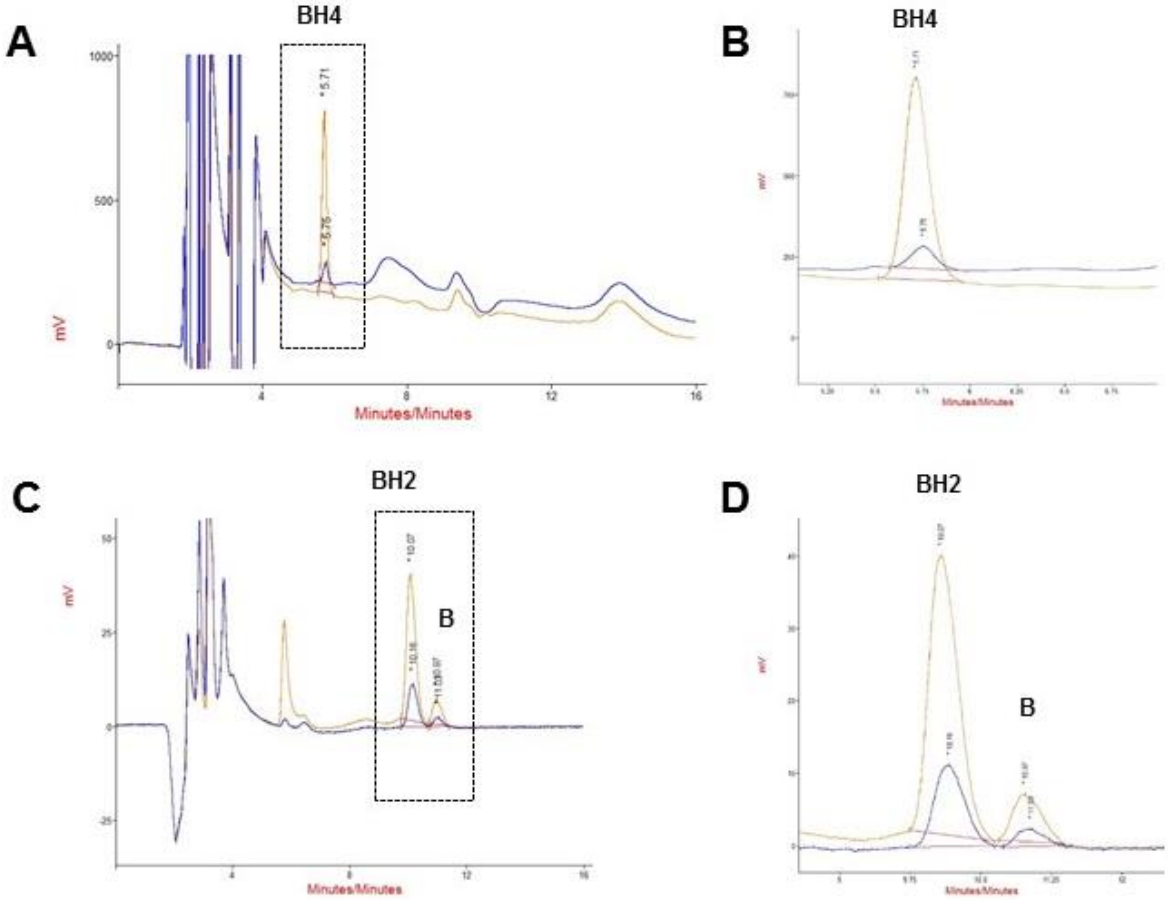

Figure 2-22. Representative HPLC detector traces of the standard sample in orange (containing a known concentration of tetrahydrobiopterin - BH4, dihydrobiopterin - BH2, and biopterin - B) and a tissue sample trace in blue. (A-B) Electrochemical detector trace used to detect and quantify the BH4 concentration. (C-D) Fluorescence detector trace used to detect and quantify the concentrations of BH2 and B.

NOS activity measurements

Nitric oxide synthase (NOS) activity was measured by quantifying the conversion rate of the radioactively labelled arginine to the citrulline. However, NOS is not the only enzyme that metabolizes arginine. Arginase is an enzyme that converts arginine to urea and ornithine and competes with NOS for the availability of the arginine (*Figure 2-23*). In addition, ornithine can also be converted to citrulline (primarily in hepatocytes, to a smaller degree in other cells) by ornithine transcarbamylase (OTC). Therefore it was important to assess the NOS activity in the presence of arginase inhibitor (Nω-hydroxy-nor-Arginine, nor-NOHA) to eliminate non-NOS mediated conversion to citrulline. Also, every sample was processed in the presence or absence of the NOS inhibitor (Nω-Nitro-L-arginine methyl ester hydrochloride, L-NAME) to specifically measure only the NOS activity. Radioactively labelled arginine and its metabolic products citrulline and ornithine were separated using the HPLC and quantified by scintillation detector (249).

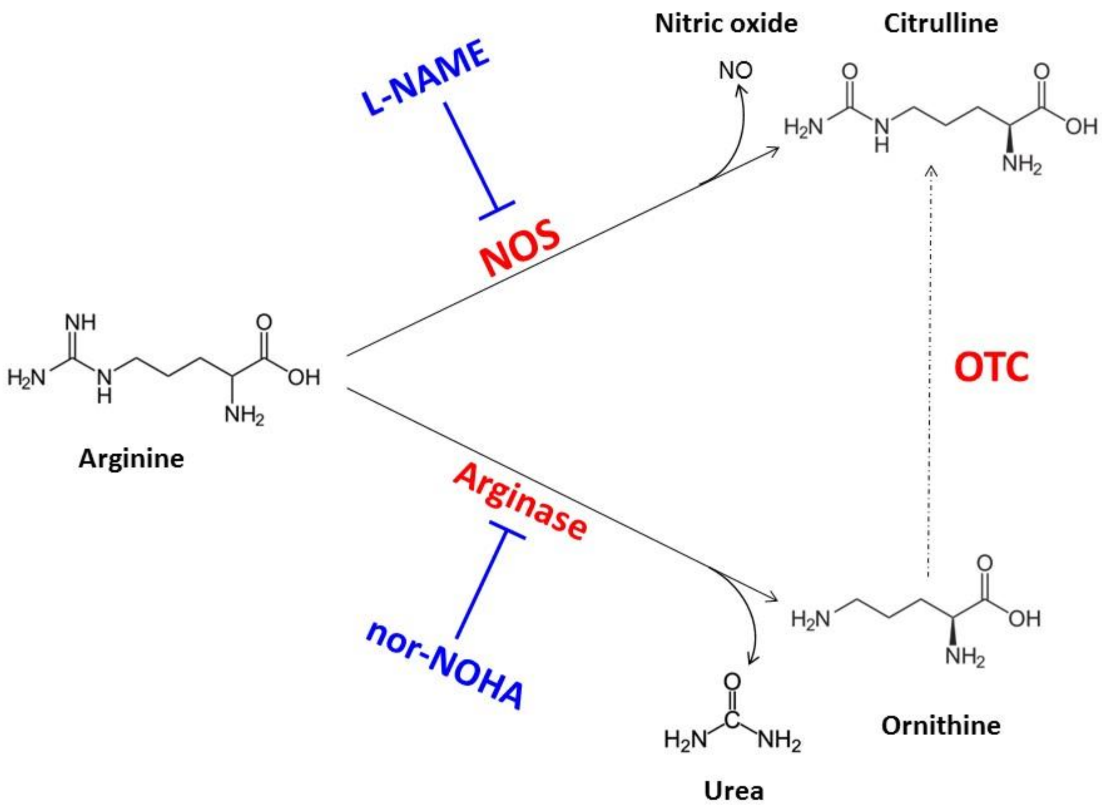

Figure 2-23. Metabolic pathways of arginine: nitric oxide synthase (NOS) converts arginine to citrulline and nitric oxide (NO), arginase converts arginine to ornithine and urea, and ornithine transcarbamylase (OTC) converts ornithine to citrulline. Nω-Nitro-L-arginine methyl ester hydrochloride (L-NAME) is an inhibitor of NOS, Nω-hydroxy-nor-Arginine (nor-NOHA) is an inhibitor of arginase.

Tissue samples (approximately 40 mg of LV, 4 combined atria) were homogenized in the Krebs-HEPES buffer (*Table 2-7*) containing 5 µM nor-NOHA (CAY10566, Cayman Chemical), 1 µM DTE, and EDTA-free protease inhibitor (cOmplete Mini, Roche) using the TissueLyser (Qiagen) with pre-cooled (on dry-ice) 5 mm stainless steel beads for 2 minutes at 50 Hz. The homogenate was then centrifuged at 17,000g at 4°C for 10 minutes. The supernatant was centrifuged again at 17,000g at 4°C for 10 minutes. Finally, the supernatant was moved into a new tube and used for further analysis. An aliquot of the supernatant was used for the determination of the protein concentration.

Krebs-HEPES	MW	c (mM)	m (g) for 500 ml
NaCl	58.40	118	3.45
KCl	74.55	4.7	0.175
KH_2PO_4	136.02	1.2	0.081
$MgSO_4$	120.37	1.1	0.066
$NaHCO_3$	84.01	25	1.05
Glucose	180.16	5.6	0.5
Hepes	238.30	10	1.192
Ca^{2+} (1M solution)	110.98	1.4	700µl of 1M
→ pH to 7.4			

Table 2-7. Specifications of the Krebs-HEPES solution used in the nitric oxide synthase activity measurements. MW – molecular weight, c – final concentration of the solution.

Every reaction tube for the NOS activity assay contained 500 µg of protein (in 200 µl) and was incubated for 30 minutes on ice with NOS cofactors (except BH4): 10 µM riboflavin 5′-monophosphate (FMN, Sigma F2253), 10 µM flavin adenine dinucleotide (FAD, Sigma F6625), 1 µM β-nicotinamide adenine dinucleotide 2'-phosphate (NADPH, Sigma N1630) in the presence or absence of NOS inhibitor L-NAME (Sigma N5751).

Afterwards, 1.5 µl of ^{14}C L-arginine (1.85 MBq/ml, Amersham Biosciences UK Ltd.) was added into every reaction tube. Tubes were then incubated for 4 hours at 37°C. After the incubation, the proteins were precipitated by adding 60 µl of 10% trichloroacetic acid (TCA) and sample centrifuged at 17,000g for 20 minutes. The 220 µl of supernatant was then transferred to the plastic HPLC vials containing 100 µl of 10% TCA and 450 µl of H_2O. The vials were then placed in the autosampler rack and 700 µl of the solution was injected into the HPLC column. The HPLC separation of the arginine metabolism products was obtained by ion-exchange chromatography using a Supelcosil LC-SCX column (Sigma) using the gradient elution with the following conditions (elution rate 1 ml/min): 100% buffer A (distilled water) for 5 minutes, then linear gradient from 100% buffer A to 100% buffer B (200 mM sodium citrate, pH 3) over 10 minutes, followed by 100% buffer B for 15 minutes (*Figure 2-24*). At the end of every sample, the column was washed with 100% buffer A for 3 minutes before injecting the next one. Separated products were detected using a continuous flow liquid scintillation detector (Lablogic β-RAM Model 3).

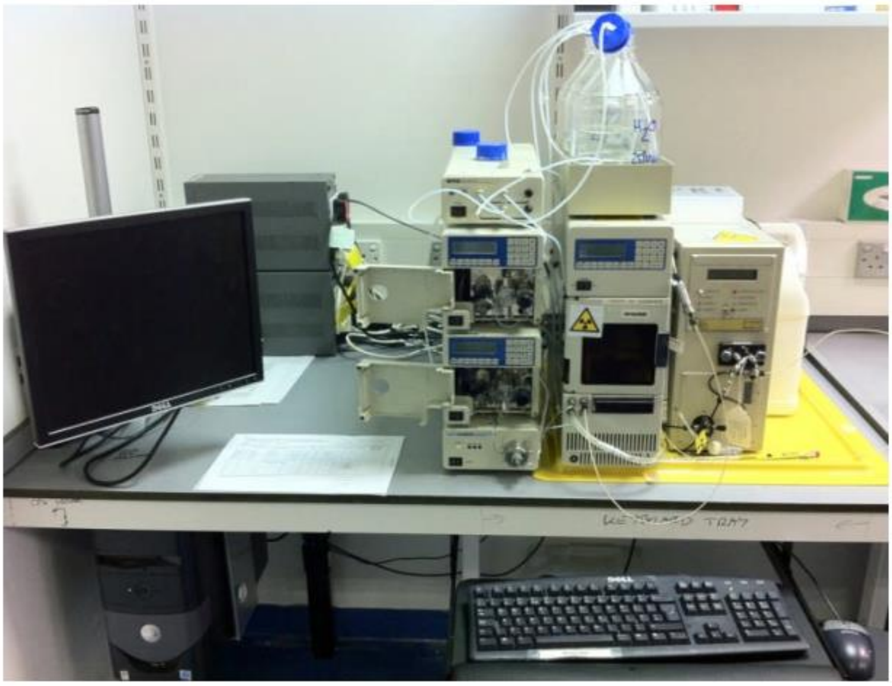

Figure 2-24. A high-performance liquid chromatography (HPLC) setup to separate the ^{14}C radiolabelled products of arginine metabolism (arginine, citrulline, ornithine) by using gradient flow ion-exchange chromatography and measure its concentration using a liquid scintillation detector.

Arginine and citrulline were quantified as the area under the curve (AUC) from the scintillation detector signal and expressed as the relative proportion of the total ^{14}C count (*Figure 2-25*). A MATLAB script was written to automatically detect the peaks and integrate the signal to obtain the AUC (*see Appendix*). Finally, the NOS activity was calculated as the proportion of arginine to citrulline conversion that was inhibitable by L-NAME.

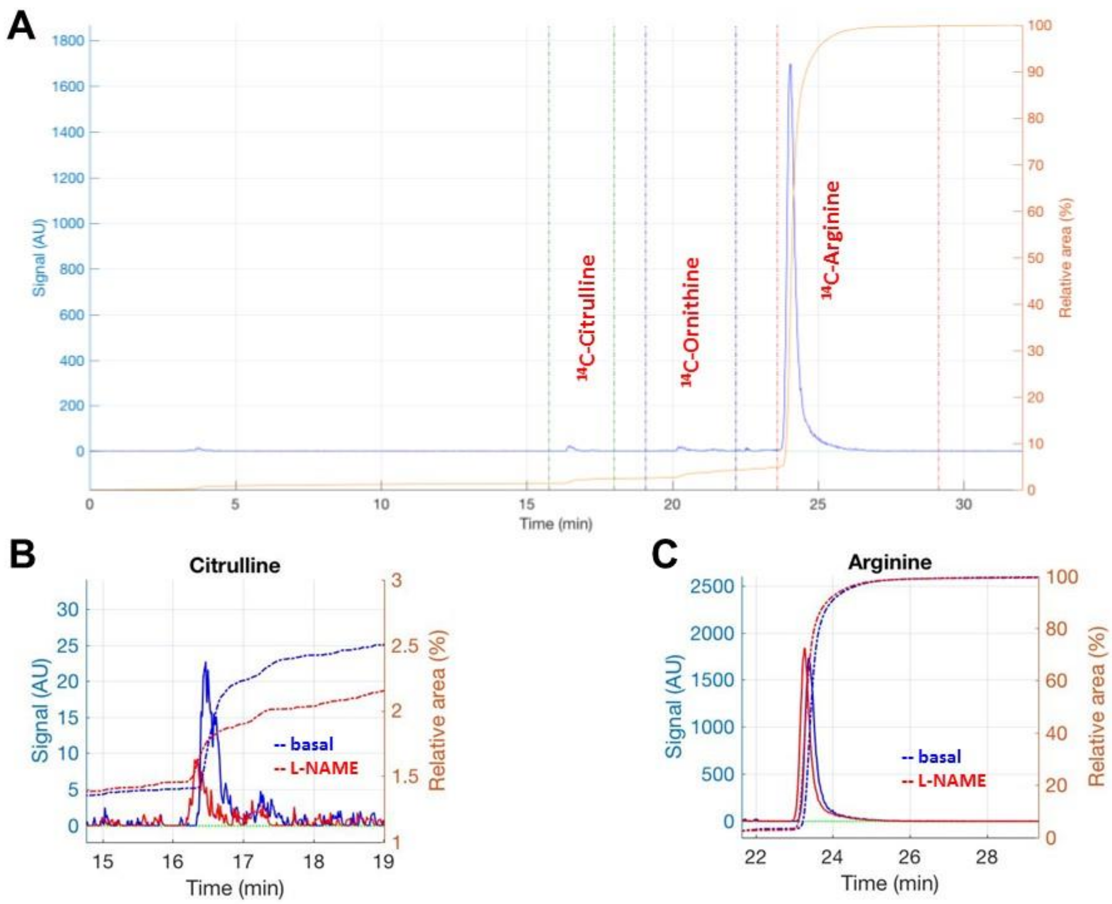

Figure 2-25. (A) A full-length scintillation detector trace of a sample with separated peaks for ^{14}C-citrulline, ^{14}C-ornithine, and ^{14}C-arginine. (B) An enlarged section focusing on the citrulline peak of two paired samples with or without the presence of nitric oxide synthase (NOS) inhibitor L-NAME. (C) An enlarged section focusing on the arginine peak of two paired samples with or without the presence of nitric oxide synthase (NOS) inhibitor L-NAME.

Creatine kinase activity measurements

Creatine kinase (CK) is an enzyme that reversibly produces phosphocreatine (PCr) by catalysing the reaction between creatine and ATP. Phosphocreatine is used as energy storage and is particularly important in tissues with rapid ATP consumption. Phosphocreatine can be easily transported from subcellular parts producing energy to areas with high energy consumption and to renew the ATP levels. In the myocardium, there are two main CK isoenzymes: dimeric cytosolic CK and octameric mitochondrial CK located in the mitochondrial cristae and intermembrane space (250). All CK isoenzymes are highly susceptible to oxidative stress damage and impairment of CK is detrimental for intracellular metabolic balance.

CK activity measurements were performed by Hannah Whittington as described previously (251-253). The frozen LV samples were homogenised in ice-cold buffer (K_2HPO_4 0.08mM, KH_2PO_4 0.02 mM, EGTA 1mM, and β-mercaptoethanol 1mM). Aliquots of the homogenates were taken for the protein quantification. Afterwards, the Triton-X 100 (final v/v 0.1%) was added to fully permeabilize the membranes in the homogenates. The homogenate samples were stored on ice for 30 min to allow the precipitation of the debris and the supernatant was used for further measurements.

The total CK activity was quantified by spectrophotometrically measuring the downstream products using a coupled enzyme reactions kit (Helena Laboratories, UK). The CK catalysed the reversible reaction of where PCr and ADP were catalysed to creatine and ATP. In the next step, the glucose-6-phosphate was produced from glucose and ATP. Finally, glucose-6-phosphate and NADP reacted to produce 6-phosphogluconate and NADPH. The increase in the NADPH can be measured as an increase in the absorbance at 340 nm. The rate of increase in the absorbance was proportional to the CK activity. The sample's CK activity was normalised to the total protein level and the total citrate synthase activity, which was a measure of the sample's total oxidative capacity.

The CK isoenzyme activity was quantified by firstly separating the isoenzymes according to their isoelectric point using a rapid gel electrophoresis kit (Helena Laboratories, UK). The CK isoenzymes were visualized by adding the CK reagent chromogen and its relative activity quantified by densitometry of the band corresponding to the specific CK isoenzyme. The absolute CK isoenzyme activity was obtained by multiplying the relative activity with the measured (and normalised) total CK activity.

Total collagen assay

The mouse atrial tissue is very thin which makes histological quantification (a gold standard technique) of fibrosis more challenging, even though it can be performed as described here (254). For our atrial measurements, the total collagen in content was determined using the hydroxyproline assay provided as a kit (QuickZyme Biosciences). Hydroxyproline is a non-proteinogenic amino acid and is in mammals present only in the collagen. The measurement of hydroxyproline concentration in the sample was used to assess the total collagen concentration. The tissue sample was completely hydrolysed in the 6M hydrochloric acid (HCl) at a high temperature (95°C). The hydroxyproline was then oxidized to pyrrole-2-carboxylic acid, which then formed a chromophore with p-dimethylaminobenzaldehyde (255). The final product was quantified by measuring the absorbance at 570 nm.

Frozen tissue samples (non-homogenized) were firstly weighed and then moved into the screw-capped tubes. A fixed amount of 6M HCl (250 µl for 20-30 mg of LV tissue; 100 µl for RA and LA) was then added to tubes. A standard collagen dilution was prepared by mixing a 125 µl of externally validated collagen standard (1200 µg/ml) with an equal volume of 12M HCl. Samples and standards were incubated in an oven at 95°C for 20 hours. All tubes were then centrifuged at 13,000 g for 10 minutes and the supernatant was moved into new tubes. Serial dilutions of the hydrolysed collagen standard were prepared to cover the range of 0-300 µg/ml as described in *Table 2-8*. Hydrolysed tissue samples were diluted with water and 4M HCl to achieve the final HCl concentration of 4M and to bring the collagen concentration in the working range of the assay (we used the dilution factor of 5 for LV samples and dilution factor of 2 for atria) as described in *Table 2-9*.

Label	Sample from	4M HCl	H_2O	Collagen concentration (µg/ml)
S1	125 µl hydr. std.	62.5 µl	62.5 µl	300
S2	120 µl S1	60 µl	x	200
S3	90 µl S2	90 µl	x	100
S4	90 µl S3	90 µl	x	50
S5	90 µl S4	90 µl	x	25
S6	90 µl S5	90 µl	x	12
S7	90 µl S6	90 µl	x	6.25
S8	0	90 µl	x	0

Table 2-8. Preparation of standard collagen dilutions from the hydrolysed collagen standard (hydr. std.) for use with the total collagen assay.

Tissue	Sample from	4M HCl	H_2O	Dilution factor
LA	80 µl of SN	40 µl	40 µl	2
RA	80 µl of SN	40 µl	40 µl	2
LV	40 µl of SN	140 µl	20 µl	5

Table 2-9. An example of the tissue sample dilution preparation for use with the total collagen assay.

The hydroxyproline assay was performed in a 96-well flat-bottom plastic plate. Diluted standards and samples were pipetted in duplicates (35 µl/well) into wells. Then the 75 µl of assay buffer was added into every well. The plate was placed on a plate shaker for 20 minutes at room temperature. Afterwards, 75 µl of detection reagent (a mixture of kit's reagent A and reagent B in 2:3 ratio) was pipetted into every well. The plate was shaken on a plate shaker for one minute and then incubated in an oven at 60°C for 60 minutes. Standards and samples turned into a brown liquid proportionally to the amount of collagen present (*Figure 2-26*). The plate was cooled on ice and then the absorbance in the wells was measured at 570 nm.

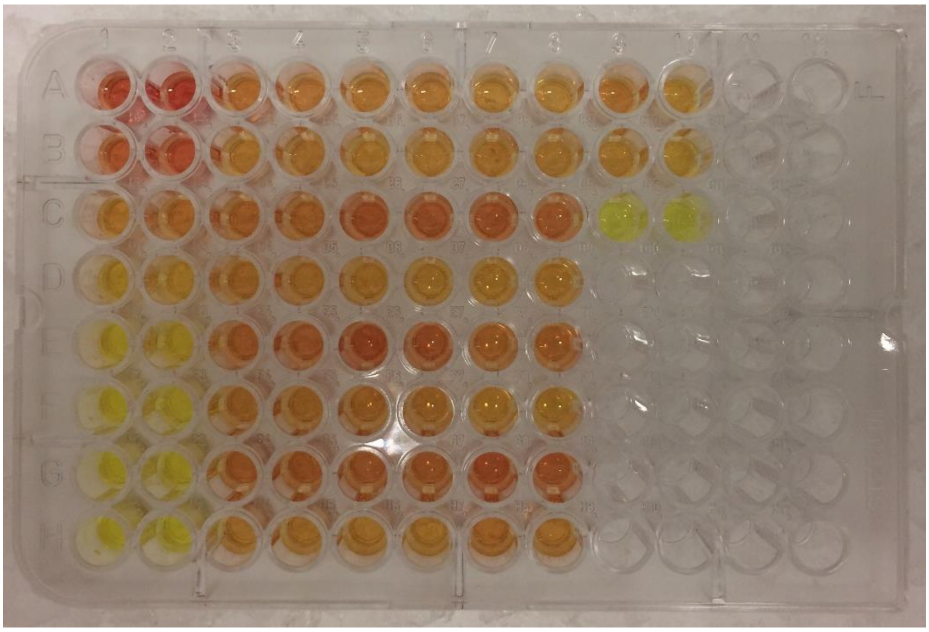

Figure 2-26. An example of a 96-well plate used for the total collagen assay. The amount of collagen in wells is proportional to the brown colour of the liquid.

The average of the absorbance of the duplicates was used for the analysis. The standard curve was created by fitting a linear line to the values of collagen standards. The standard curve was then used to calculate the collagen concentration in the wells (*Figure 2-27*).

From there the total collagen of the sample was calculated by adjusting for the dilution factor and the initial volume of 6M HCl in which the sample was hydrolysed. Finally, data were normalised to the weight of the tissue and were presented as µg of collagen per mg of tissue.

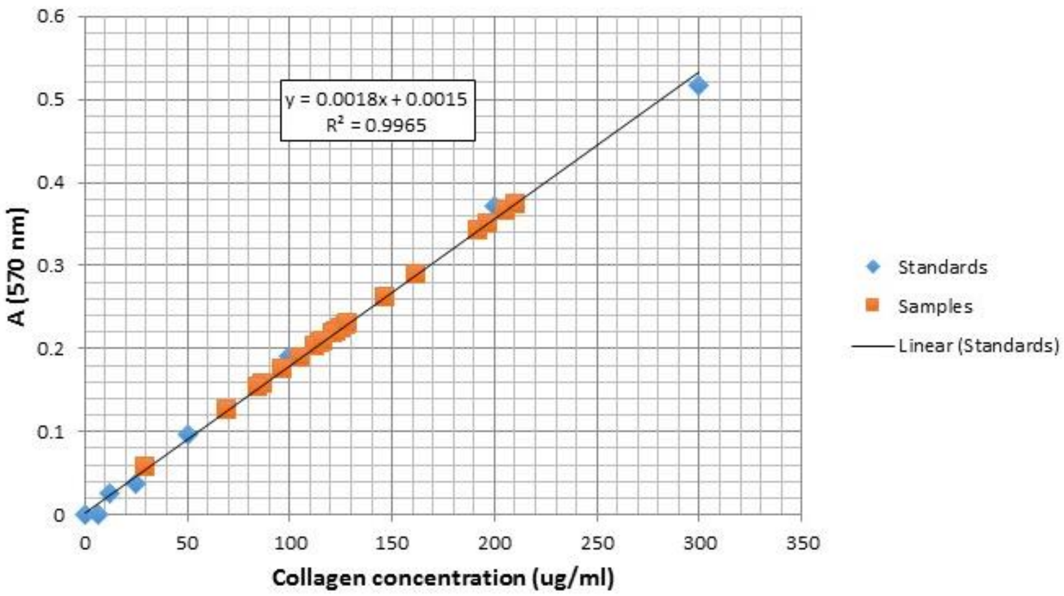

Figure 2-27. An example of the collagen standard curve with superimposed values for the samples. Blue diamonds – absorbance measurements at 570 nm of collagen standards, orange squares – absorbance measurements at 570 nm for tissue samples.

Statistics

Mice in the diabetic and BH4 supplemented studies were randomly assigned to their corresponding groups before the STZ-induction protocol was started. The *in vivo* procedures were not performed blindly, however the analysis of echocardiographic and electrophysiological recordings were done blindly. The optical mapping, 31P MRS, cell shortening experiments, and all molecular biology measurements were performed blindly with a second investigator performing the blinding (e.g. by picking the mouse from the cage in case of the optical mapping and 31P MRS, or by labelling the tubes in case of cell shortening experiments and all molecular biology measurements). Furthermore, the optical mapping and histological fibrosis analysis was performed semi-automatically using a custom-made software analysis tools. The unblinding was done only after the *a priori* determined number of measurements in every group was obtained. The outliers were not removed in the studies presented here unless explicitly stated (e.g. echocardiographic measurements performed at the heart rate outside of the pre-determined range).

All parametric data are expressed as mean ± standard error of the mean (SEM) and non-parametric data as median ± interquartile range (IQR). Statistical comparisons were made using unpaired Student's t-test, Mann-Whitney test, one-way analysis of variance (ANOVA) with Bonferroni's post hoc test, or two-way ANOVA to test the interaction, as appropriate.

CHAPTER 3:

The development of diabetic cardiomyopathy is prevented in mGCH1 transgenic mice with high myocardial levels of tetrahydrobiopterin

Introduction

Diabetic cardiomyopathy is a term used to describe cardiac dysfunction in the absence of coronary artery disease, hypertension, and significant valvular disease in patients with diabetes mellitus (DM) (24, 25). This distinct form of cardiac dysfunction was first described in a small case series report based on autopsy findings and further corroborated by epidemiological studies identifying that DM was an independent risk factor for heart failure (HF) even after adjusting for other known risk factors (26, 27, 256). From a clinical perspective, diabetic cardiomyopathy is considered to be initially asymptomatic with an early subtle left ventricular (LV) diastolic dysfunction (16, 29). The condition then progresses to the state with a clear LV diastolic dysfunction with or without LV hypertrophy, which is then followed by the symptomatic heart failure with LV systolic dysfunction and LV dilatation (16, 29).

Underlying pathophysiological mechanisms of diabetic cardiomyopathy also remains to be elucidated. Hyperglycaemia and impaired insulin signalling result in cardiac metabolic disturbances (e.g. decreased glucose oxidation, increased free fatty acid utilization, lipotoxicity), dysfunction of cardiomyocytes (e.g. impaired calcium handling, mitochondrial dysfunction, increased oxidative stress, hypertrophy), cardiac structural changes (e.g. fibrosis, AGE deposition), activation of the inflammatory response, microvascular dysfunction, and cardiac autonomic neuropathy (13, 29, 31, 257). As presented in the general introduction chapter, multiple signalling pathways are implicated in the diabetic cardiomyopathy each causing a distinct phenotype with no consensus on the relative importance of each of them.

It is important to stress that there is no specific and effective prevention or treatment for diabetic cardiomyopathy beyond the standard glucose-lowering medications and classical HF medications (renin-angiotensin-aldosterone and neprilysin inhibitors, beta-blockers, and diuretics) (13, 25). Considering that the cardiovascular mortality of diabetic patients with HF is 50-90% higher compared to the non-DM patients (13), further research is warranted to investigate novel medical options targeting specifically the diabetic cardiomyopathy.

One novel approach to target diabetic cardiomyopathy is use of the tetrahydrobiopterin (BH4). BH4 is an essential cofactor for several aromatic amino acid hydroxylases, alkylglycerol monooxygenases, and, importantly, nitric oxide synthases (NOS) (194). Impaired NO signalling and reduced BH4 availability have been reported in the vasculature of diabetic animal models as well as in patients with type 2 DM (202, 258). However, it is not known whether impaired NO signalling and/or reduced BH4 availability is also present in the cardiomyocytes of diabetic patients. Furthermore, overexpression of GTP cyclohydrolase 1 (GCH1) in endothelial cells prevented the development of vascular dysfunction in diabetic mice (202). A small study in patients with type 2 DM also showed that intra-arterial infusion of BH4 acutely improved the coronary vascular function (204). Importantly, it has not been yet investigated whether BH4 treatment prevents the development of cardiac dysfunction.

Therefore, the aim of this part of the study was to investigate whether impaired BH4 availability and NO signalling promote the development of diabetic cardiomyopathy. Furthermore, we also tested whether increasing myocardial BH4 levels and thus augmenting the NOS activity prevented the development of the diabetic cardiomyopathy.

Methods

All methods are described in greater detail in the general methods chapter.

ANIMAL MODELS

We used a genetically modified mouse (CBA strain backcrossed to the C57BL/6JOlaHsd background for three generation) with a myocardial specific overexpression of the human GTP cyclohydrolase 1 gene (mGCH1-Tg), which was created in our Department at the University of Oxford (185). Mice were housed in individually ventilated cages in a temperature-controlled environment (20-22°C) with a 12-hour light-dark cycle. Mice had ad libitum access to food and water. Sentinel animals were kept in the same racks and regularly underwent health monitoring to ensure and confirm specific pathogen-free environment.

All animal procedures were performed in accordance with the United Kingdom Home Office Animals (Scientific Procedures) Act of 1986. They were carried out under the authority of the project licence number PPL 30/2804 (project licence holder: Prof Barbara Casadei) until 25.1.2016, and after this date, under PPL 30/3374 (project licence holder: Dr Ricardo Carnicer Hijazo).

STREPTOZOTOCIN INDUCED DIABETES MELLITUS

Males, aged 14-16 weeks, received intraperitoneal injections of low-dose streptozotocin (STZ) (42-45 mg/kg) or intraperitoneal injections of vehicle (citrate buffer) over five consecutive days. During the study, mouse body weight (BW) and plasma glucose levels were regularly monitored. A mouse was classified as diabetic if the plasma glucose level was greater than 16 mM. After 12 weeks of the last injection, mice cardiac function was assessed using echocardiography. After that the mice were euthanized, hearts either excised for further experiments on Langendorff perfusion system, or used to isolate cardiomyocytes, or the tissue was frozen and used for later molecular experiments.

ECHOCARDIOGRAPHY IN MICE

Echocardiography was performed using a Vevo 2100 (VisualSonics) ultrasound imaging system with an ultra-high frequency MS400 cardiovascular transducer (18-38 MHz) under the isoflurane general anaesthesia (1.0-2.0% isoflurane). LV systolic function was assessed by the ejection fraction (EF) calculated from the motion-mode recordings of the LV short-axis view, at the papillary muscle level. LV diastolic function was assessed by tissue Doppler imaging (TDI) and mitral valve flow parameters recorded with the pulsed-wave Doppler mode.

CARDIAC 31P MAGNETIC RESONANCE SPECTROSCOPY

Cardiac ^{31}P magnetic resonance spectroscopy (MRS) experiments were performed, as described previously (242-244). Mice were euthanized and anticoagulated before the heart was rapidly excised, cannulated and retrogradely perfused with the Krebs solution using the constant pressure Langendorff setup. After the cannulation, the hearts were put into the centre of a ^{1}H/^{31}P coil (Rapid Biomedical, Wurzburg, Germany) with an inner diameter of 10 mm for the MRS in an 11.7 T magnetic resonance scanner (Magnex Scientific, Oxford, UK). After shimming, the water resonance linewidth was less than 70

Hz for all the measurements. The ^{31}P spectra of the heart were acquired at 202.4 MHz using a 90° flip angle, repetition time (TR) 15 seconds and 80 averages. The spectra were analysed using the AMARES algorithm in the jMRUI software package (245, 246). The phosphocreatine (PCr) resonance was set to 0.0 ppm and the chemical shifts of other metabolites were referenced to the PCr. The PCr to ATP ratio was calculated from the areas under the fitted γ-ATP and PCr peaks.

CELL SHORTENING EXPERIMENTS

Cell shortening experiments were performed as described previously (185). The mouse was sacrificed and the heart was rapidly cannulated, excised, and placed on the Langendorff perfusion system. Hearts were initially perfused with Ca^{2+}-free isolation solution, followed by perfusion with a solution containing collagenase type II. Afterwards, the LV was excised, and placed in the digestion solution containing collagenase type II. After the digestion, the isolated cardiomyocytes were centrifuged and resuspended in the storage solution. Cell shortening experiments were performed in a continuously perfused and field-stimulated (at 3 Hz) chamber. The cardiomyocyte contraction and relaxation were recorded using a video-edge detection system (IonOptix). Cardiomyocyte fractional shortening and relaxation constant (characterised by t_{50}) were measured and averaged from at-least 10 steady-state contractions.

HUMAN SAMPLES

Samples of the right atrial appendage were collected from patients undergoing on-pump cardiac surgery for coronary revascularization and stored at -80°C. Investigations were approved by the Research Ethics Committee. All patients gave informed written consent. The human atrial samples were analysed by Dr Ricardo Carnicer.

MOLECULAR BIOLOGY MEASUREMENTS

The concentration of tetrahydrobiopterin (BH4), dihydrobiopterin (BH2) and biopterin (B) in the tissue samples were measured using the high-performance liquid chromatography (HPLC) method as detailed here (185, 248). Nitric oxide synthase (NOS) activity was measured by quantifying the conversion rate of the radioactively labelled arginine to the citrulline using the continuous flow liquid scintillation detector (Lablogic β-RAM Model 3) recording of HPLC separated compounds. The insulin concentration in plasma was determined using an ELISA kit (Millipore).

The superoxide production in mice LV homogenates was measured by lucigenin-enhanced chemiluminescence with a single-tube luminometer (FB12, Berthold, Germany). The superoxide production in human atrial myocardial tissue was assessed by measuring the dihydroethidium (DHE) conversion to 2-hydroxyethidium using the HPLC and the fluorescence detector (excitation at 510 nm, emission at 595 nm). All superoxide measurement experiments were performed in the presence of the NOS inhibitor (L-NAME) and the absence of the NOS inhibitor (incubation with the D-NAME – an inactive isomer). All results were expressed at the tiron-inhibitable fraction.

The quantification of the interstitial fibrosis was performed on the histological sections of the LV stained with the Picrosirius Red (Polysciences Inc.) and imaged using the inverted microscope (Nikon Eclipse TE2000). Images were analysed using the ImageJ and the interstitial fibrosis quantified as the relative area of the LV myocardial interstitial connective tissue divided by the total tissue area. The total collagen content in the LV was assessed using the hydroxyproline colourimetric detection kit (QuickZyme Biosciences). The sample's collagen was calculated by comparison to the collagen standard curve and expressed as the collagen content per tissue weight.

The total creatine kinase (CK) activity was measured by spectrophotometrically quantifying the downstream product (NADPH) of enzymatically coupled CK reaction using the kit (Helena Laboratories, UK) as described previously (251-253). The specific CK isoenzyme activity was quantified by firstly separating the isoenzymes using rapid gel electrophoresis followed by densitometric quantification of individual bands after addition of CK reagent chromogen. The CK isoenzyme activity was normalised to the total protein and total citrate synthase activity, which was a measure of the sample's total oxidative capacity.

The tissue protein levels were determined using the western blot technique. The proteins in the homogenized tissue samples were separated using the gel electrophoresis and were then transferred to the PVDF membrane. The membrane was then incubated with the primary antibodies targeting the desired proteins. The primary antibodies used in this chapter were as follows: TnI (Millipore MAB1691), VDAC (Abcam), UCP3 (Thermo Scientific), GLUT1 (Millipore 07-1401), GLUT4 (Millipore). Afterwards, the membrane was incubated in the solution containing secondary antibodies conjugated with the horseradish peroxidase targeting the primary antibodies of the appropriate host. Finally, the membrane was stained with the chemiluminescence substrate and imaged using the ChemiDoc MP imaging system (BioRad). The appropriate protein bands were then quantified densitometrically and normalized to the housekeeping protein (e.g. TnI).

STATISTICS

All parametric data are expressed as mean ± standard error of the mean (SEM) and non-parametric data as median ± interquartile range (IQR). Statistical comparisons were made using unpaired Student's t-test, Mann-Whitney test, one-way analysis of variance (ANOVA) with Bonferroni's post hoc multiple comparison test, or two-way ANOVA to test the interaction, as appropriate.

Results

STREPTOZOTOCIN INJECTED MICE DEVELOPED HYPERGLYCEMIA

Streptozotocin injected (diabetic) mice developed hyperglycaemia two weeks after the last injection and hyperglycaemia persisted over the 12 weeks. After 12 weeks both the diabetic wild-type (WT DM) and diabetic mice with myocardial specific GCH1 overexpression (Tg DM) had lower body weight compared to the non-diabetic control littermates regardless of the genotype ($p < 0.001$) (*Figure 3-1A*). The plasma glucose concentration was elevated in both WT DM and Tg DM groups compared to the non-diabetic groups ($p < 0.001$) (*Figure 3-1B*). Importantly, there was no difference in the glucose level or body weight between the WT DM and Tg DM mice. Similarly, there was no difference in the plasma glucose or body weight of non-diabetic mice of either genotype.

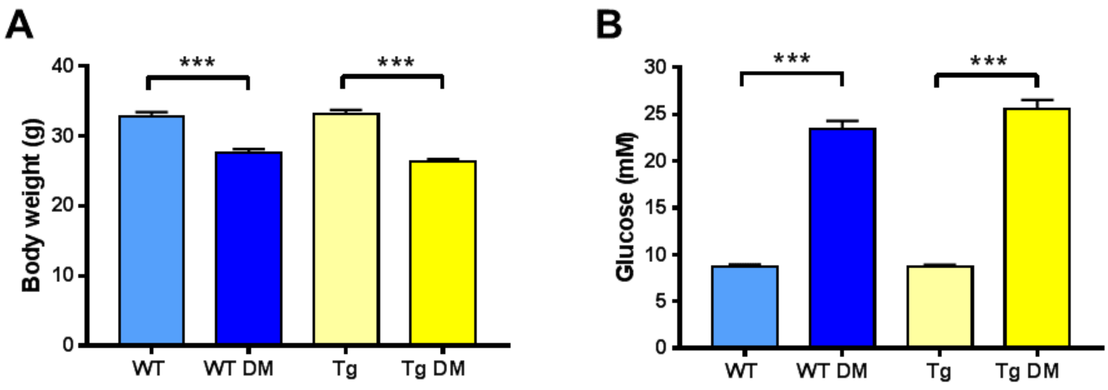

*Figure 3-1. (A) Body weight at the end of the protocol (week 12) for wild-type (WT) mice, wild-type diabetic (WT DM) mice, mice with myocardial specific GCH1 overexpression (Tg), and Tg diabetic mice (Tg DM) (n = 16-20/group, one-way ANOVA with Bonferroni's multiple comparisons test). (B) Non-fasting plasma glucose at the end of the protocol (week 12) for WT, WT DM, Tg, and Tg DM mice (n = 16-20/group, one-way ANOVA with Bonferroni's multiple comparisons test). *** - $p < 0.001$.*

We measured plasma insulin levels for our diabetic and non-diabetic mice of both genotypes (*Figure 3-2*). WT DM and Tg DM had lower insulin plasma concentration compared to the non-diabetic WT and Tg controls ($p < 0.001$ for all comparisons). There was also no difference in the plasma insulin concentration between the WT DM and Tg DM mice ($p = 0.98$) and no difference in the insulin concentration of the non-diabetic controls of either genotype ($p = 0.61$).

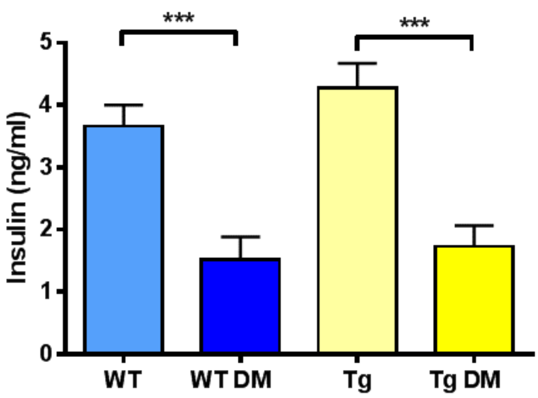

*Figure 3-2. Plasma insulin concentration at the end of the diabetic protocol (week 12) for wild-type (WT) mice, wild-type diabetic (WT DM) mice, mice with myocardial specific GCH1 overexpression (Tg), and Tg diabetic mice (Tg DM) (n = 16-20/group, one-way ANOVA with Bonferroni's multiple comparisons test), *** - p<0.001*

MYOCARDIAL GCH1 OVEREXPRESSION PREVENTED THE DEVELOPMENT OF LEFT VENTRICULAR DIASTOLIC DYSFUNCTION

We used echocardiography to assess the *in vivo* LV systolic and diastolic function (*Table 3-1*). The main finding of this part of the study was that the WT DM mice developed diastolic dysfunction as indicated by the decrease in the tissue Doppler E'/A' ratio and an increase in the combined E/E' ratio (*Figure 3-3 A-C*). Importantly, the Tg DM mice did not develop any significant changes in these echocardiographic parameters suggesting that the GCH1 overexpression prevented the development of LV diastolic dysfunction. Also, there was no statistically significant difference in echocardiographic LV systolic function parameters between any of the groups (*Figure 3-3 D-E*). Furthermore, the Tg controls and Tg DM mice had a lower heart rate during the echocardiographic investigations compared to the WT controls and WT DM mice.

Echocardiographic measurements	*WT (n = 11)*	*WT DM (n = 10)*	*Tg (n = 9)*	*Tg DM (n = 8)*
Heart rate				
Baseline HR (bpm)	478 ± 9	476 ± 7	**413 ± 8***	**413 ± 6***
Diastolic func. HR (bpm)	356 ± 12	377 ± 12	**330 ± 7***	**300 ± 7***
LV dimensions				
LV anterior wall (mm)	1.01 ± 0.03	0.95 ± 0.03	0.99 ± 0.04	0.96 ± 0.03
LV EDD (mm)	3.71 ± 0.09	3.71 ± 0.08	3.46 ± 0.08	3.69 ± 0.09
LV ESD (mm)	1.67 ± 0.05	**1.47 ± 0.04**$^{\#}$	1.55 ± 0.06	1.54 ± 0.06
LV diastolic volume (µl)	59.2 ± 3.5	60.8 ± 3.2	49.9 ± 3.7	58.1 ± 3.4
LV systolic volume (µl)	13.6 ± 1.1	17.6 ± 1.5	10.8 ± 0.9	10.8 ± 1.1
LV systolic function				
LV EF (%)	77 ± 2	71 ± 3	80 ± 2	77 ± 3
LV diastolic function				
Mitral valve E/A ratio	1.88 ± 0.06	1.79 ± 0.12	2.22 ± 0.12	**2.61 ± 0.18***
Tissue Doppler E'/A' ratio	1.61 ± 0.04	**1.10 ± 0.08**$^{\$}$	1.85 ± 0.08	2.03 ± 0.15
Combined E/E' ratio	29.9 ± 1.5	**37.6 ± 2.0**$^{\#}$	30.1 ± 1.2	30.0 ± 1.3

*Table 3-1. Mean echocardiographic measurements evaluating left ventricular (LV) size, LV systolic function, and LV diastolic function of wild-type (WT) mice, wild-type diabetic (WT DM) mice, mice with myocardial specific GCH1 overexpression (Tg), and Tg diabetic mice (Tg DM) (n = 8-11/group, two-way ANOVA followed by Bonferroni's multiple comparison tests, all values are mean ± SEM). HR – heart rate, LV – left ventricle, EDD – end-diastolic diameter, ESD – end-systolic diameter, E – early mitral valve inflow velocity, A – late mitral valve inflow velocity, E' – early tissue Doppler mitral valve annulus velocity, A' – late tissue Doppler mitral valve annulus velocity. * - p < 0.05 vs WT and WT DM, # - p < 0.05 vs WT, $ - p < 0.05 vs WT, Tg, and Tg DM.*

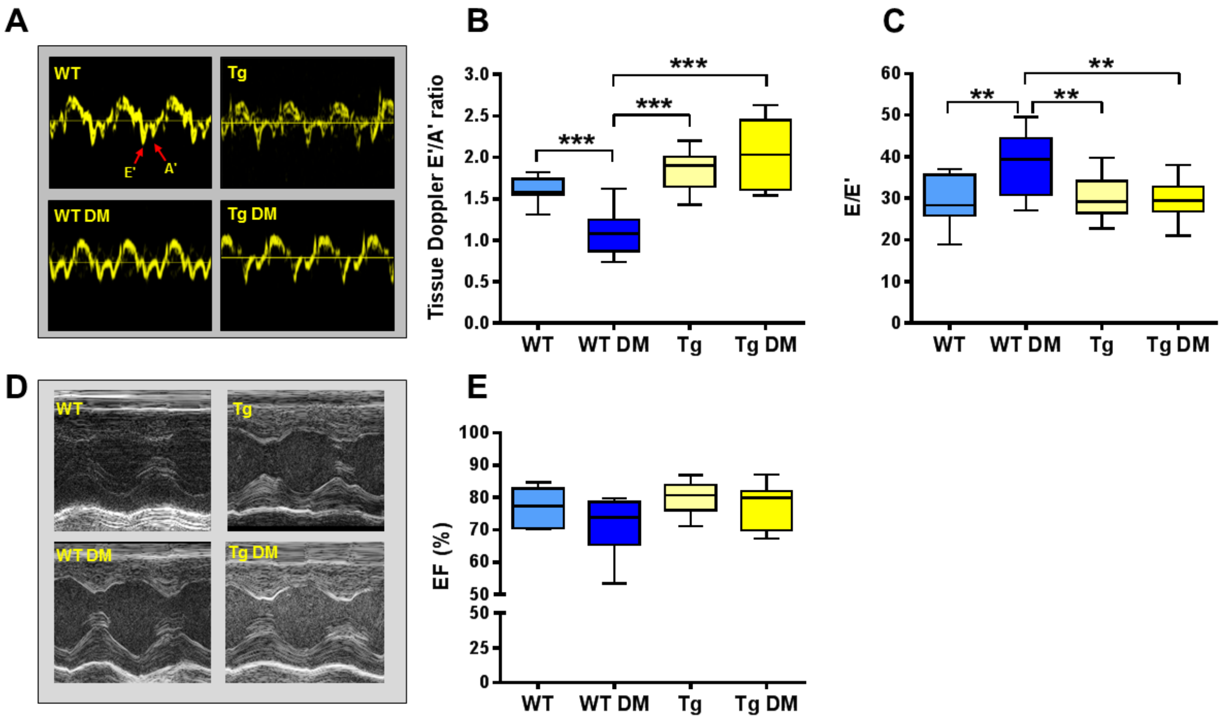

*Figure 3-3. Echocardiographic assessment of LV diastolic and LV systolic function of wild-type (WT) mice, wild-type diabetic (WT DM) mice, mice with myocardial specific GCH1 overexpression (Tg), and Tg diabetic mice (Tg DM). (A) Representative tissue Doppler traces representing mitral annulus motion velocity. (B) The ratio of tissue Doppler early (E') vs late (A') mitral annulus velocities (n = 8-11/group, one-way ANOVA followed by Bonferroni's multiple comparison tests). (C) Combined early mitral blood flow velocity (E) vs. early tissue Doppler mitral annulus velocity (E') ratio (n = 8-11/group, one-way ANOVA followed by Bonferroni's multiple comparison tests) (D) Representative LV short-axis M-mode echocardiographic recording used to assess the LV dimensions and calculate LV ejection fraction (EF). (E) LV EF calculated from the echocardiographic measurements of LV dimensions from short-axis view (n = 8-11/group, one-way ANOVA followed by Bonferroni's multiple comparison tests). ** - $p < 0.01$, *** - $p < 0.001$.*

We also assessed contractility and relaxation of LV cardiomyocytes isolated from these mice. Similarly to the *in vivo* echocardiographic diastolic function measurements, WT DM cardiomyocytes showed impaired relaxation (prolonged time to 50% relaxation, t_{50}) compared to all other groups (*Figure 3-4B*). Isolated cardiomyocytes from Tg DM ventricles did not showed significant changes in t_{50} suggesting that the myocardial GCH1 overexpression prevented the development of impaired relaxation. Furthermore, there was no difference in contractility, measured as a fractional shortening, in any of the groups (*Figure 3-4C*). The differences between the groups remained the same regardless whether the statistics was performed using individual cell measurements or averaged for every heart.

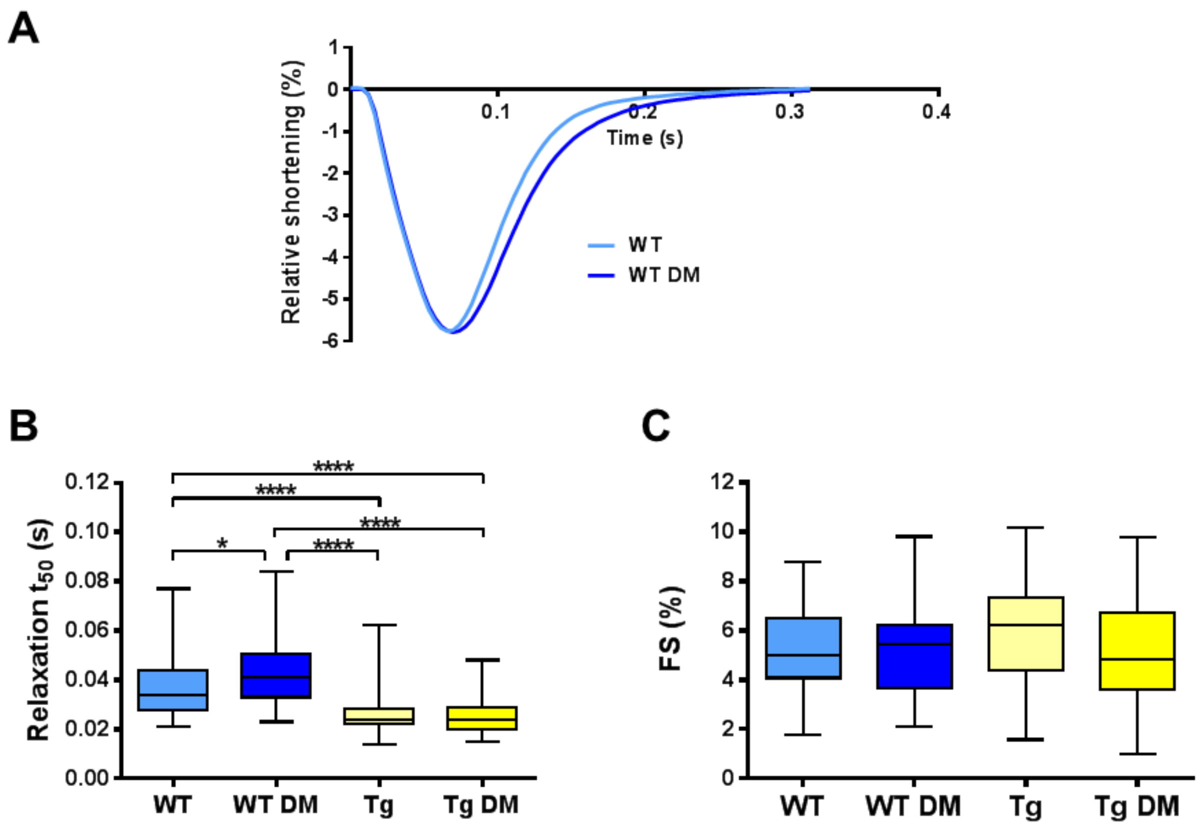

*Figure 3-4. Cardiomyocyte shortening of wild-type (WT) mice, wild-type diabetic (WT DM) mice, mice with myocardial specific GCH1 overexpression (Tg), and Tg diabetic mice (Tg DM). (A) Representative averaged traces of isolated cardiomyocyte shortening. (B) Relaxation rate measured as time to 50% relaxation (t_{50}) (n=57-69 cells/group from 4-5 hearts/group, two-way ANOVA followed by Bonferroni's multiple comparison test, * - p<0.05, **** - p<0.0001). (C) Fractional cell shortening (FS) measurements (n=61-84 cells/group from 4-5 hearts/group, two-way ANOVA followed by Bonferroni's multiple comparison test).*

DIABETIC MICE DID NOT HAVE INCREASED MYOCARDIAL OXIDATION OF BH4 OR INCREASED SUPEROXIDE PRODUCTION

Diabetic WT mice hearts did not have a reduced amount of the BH4 compared to the non-diabetic WT controls ($p = 0.99$) (*Figure 3-5A*). Similarly, the ratio of BH4 to BH2 and B was not altered between the WT and WT DM hearts ($p = 0.99$) (*Figure 3-5B*). As expected, both the Tg control and Tg DM hearts had increased myocardial BH4 concentration compared to the WT hearts ($p < 0.001$ for comparisons for both groups). The ratio of BH4 to BH2 and B was not changed between the Tg and Tg DM groups, nor it was changed compared to any other groups. Myocardial NOS activity was not changed due to hyperglycaemia ($p = 0.99$) (*Figure 3-5C*) but Tg and Tg DM hearts showed a 2 fold increase when compared to the WT controls ($p = 0.02$ and $p = 0.01$).

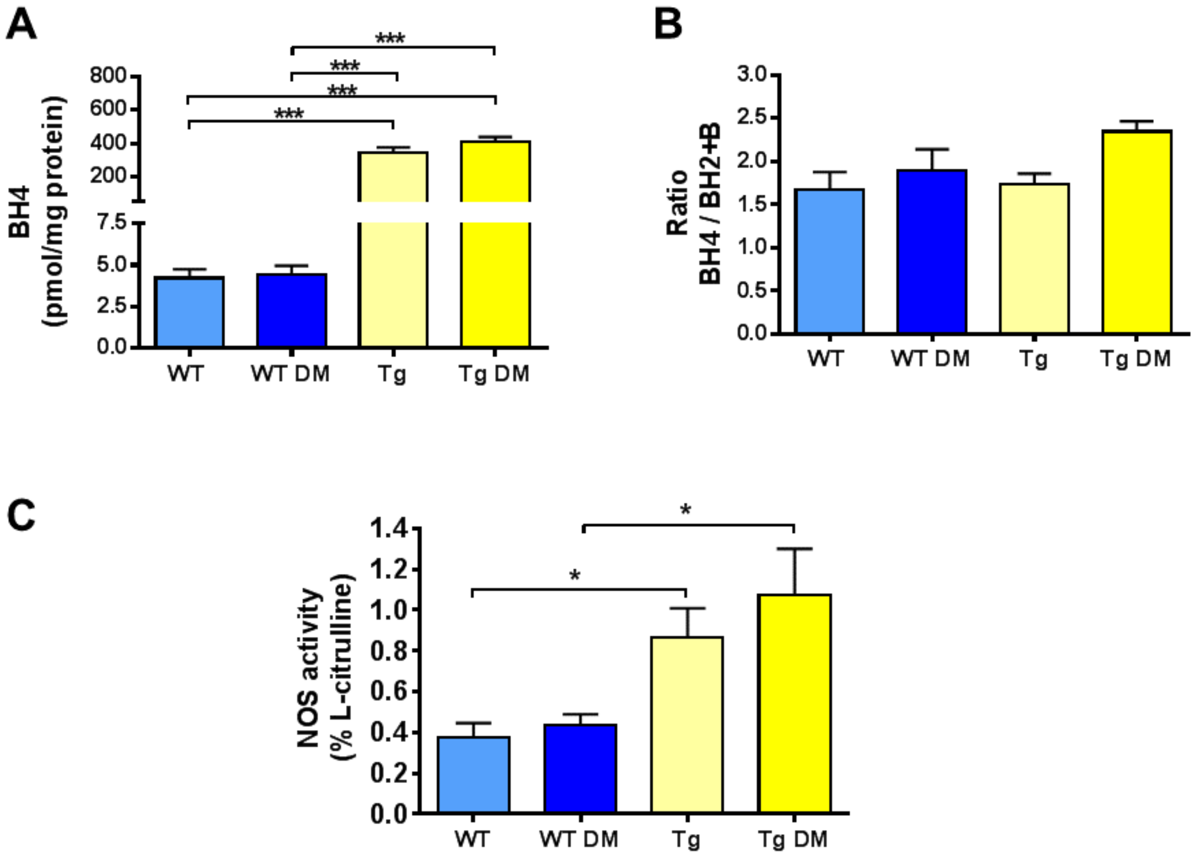

*Figure 3-5. (A) Quantification of left ventricular (LV) tetrahydrobiopterin (BH4) levels by HPLC in wild-type (WT) mice, wild-type diabetic (WT DM) mice, mice with myocardial specific GCH1 overexpression (Tg), and Tg diabetic mice (Tg DM) (n=9-15 hearts/group, one-way ANOVA followed by Bonferroni's multiple comparisons test, *** - p<0.001). (B) The ratio of BH4 to dihydrobiopterin (BH2) and biopterin (B) of WT, WT DM, Tg, and Tg DM mice (n = 9-15 hearts/group, one-way ANOVA followed by Bonferroni's multiple comparisons test). (C) Total nitric oxide synthase (NOS) activity in LV myocardium of WT, WT DM, Tg, and Tg DM mice measured using radiochemical detection of L-arginine to L-citrulline conversion (n = 7 hearts/group, one-way ANOVA followed by Bonferroni's multiple comparisons test, * - p<0.05).*

Next, we measured the myocardial total superoxide production and the NOS derived superoxide production (assessed as the difference between the total superoxide production using inactive isomer D-NAME and the superoxide production in the presence of the NOS inhibitor L-NAME). Importantly, there was no difference in the total superoxide production between the WT and WT DM hearts nor any difference in the uncoupled-NOS derived superoxide (*Figure 3-6*). Furthermore, there was no difference in either the myocardial total superoxide production or the uncoupled-NOS derived superoxide production in any of the investigated groups.

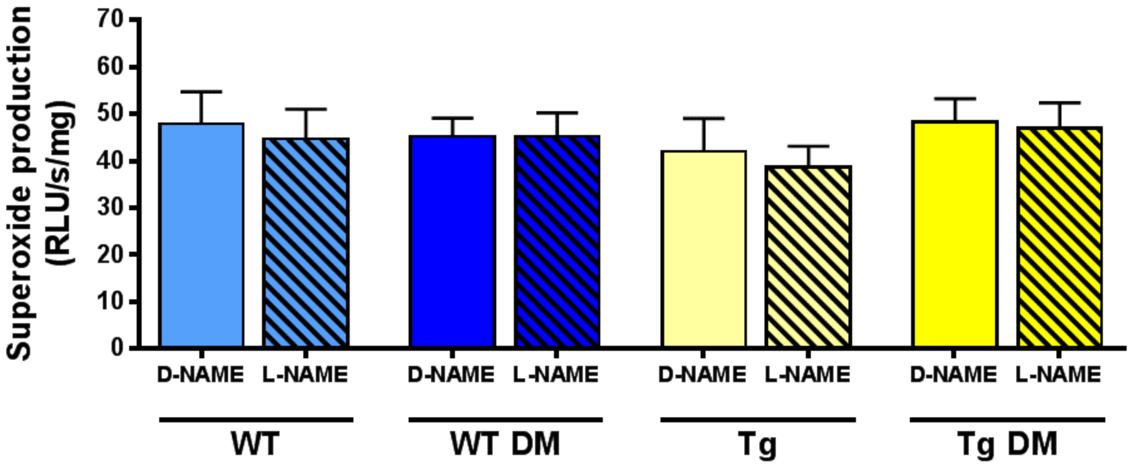

Figure 3-6. Superoxide production measured by the lucigenin-enhanced chemiluminescence in left ventricular (LV) homogenates of wild-type (WT) mice, wild-type diabetic (WT DM) mice, mice with myocardial specific GCH1 overexpression (Tg), and Tg diabetic mice (Tg DM) in the presence of the NOS inhibitor (L-NAME) and the absence of the NOS inhibitor (D-NAME – an inactive isomer) (n=11-13 hearts/group, one-way ANOVA followed by Bonferroni's multiple comparisons test). Measurements courtesy of Dr Drew Duglan.

MYOCARDIUM OF DIABETIC PATIENTS DID NOT HAVE REDUCED BH4 AVAILABILITY OR INCREASED SUPEROXIDE PRODUCTION

We wanted to explore whether patients with DM had reduced BH4 availability, NOS uncoupling or greater total superoxide production compared with matched non-DM controls. Apart from insulin medication, there were no significant differences in any other patient characteristics, cardiac risk factors, or prescribed medications between the DM and non-DM patients (*Table 3-2*). The myocardium of patients with DM did not have a reduced BH4 availability compared to the non-DM matched controls (t-test, $p = 0.74$) (*Figure 3-7A*). Similarly, the ratio of BH4 to BH2 and B was also unaltered between the DM and the non-DM groups (t-test, $p = 0.87$) (*Figure 3-7B*). Furthermore, there was no difference in the uncoupled-NOS derived superoxide production in the myocardium of the DM and the non-DM patients (t-test, nominal $p = 0.49$) (*Figure 3-8*). Finally, there was no difference in total superoxide production between the DM and the non-DM groups (t-test, nominal $p = 0.78$).

	Non-DM ***(n = 19)***	***DM*** ***(n = 17)***	***p-value***
Characteristics			
Males	15 (79%)	12 (71%)	0.72
Age (years)	62.4 ± 7.7	64.4 ± 5.9	0.39
BMI (kg/m^2)	26.3 ± 3.1	25.3 ± 2.5	0.30
Risk factors			
Current smoker	2 (11%)	7 (41%)	0.25
EF (%)	64 ± 6	60 ± 6	0.06
LV hypertrophy	1 (5%)	2 (12%)	0.83
Heart failure	0	0	0.93
Hypertension	14 (74%)	11 (65%)	0.65
Previous MI	7 (37%)	8 (47%)	0.25
Previous stroke	2 (11%)	2 (12%)	0.91
PAD	0	1 (6%)	0.85
CKD	0	0	0.93
Medications			
Insulin	0	17 (100%)	-
Statins	0	3 (18%)	0.67
Beta-blockers	18 (95%)	17 (100%)	1.00
Ca-channel blocker	8 (42%)	7 (42%)	1.00
ACE inhibitors	10 (53%)	6 (35%)	0.25
Diuretics	1 (5%)	2 (12%)	0.83

Table 3-2. Patient characteristics of diabetic (DM) patients and matched non-diabetic (non-DM) patients that underwent cardiac surgery, where the atrial appendage tissue was collected for further analysis (data presented as mean ± SD, p-value calculated using Fisher's exact test or t-test as appropriate). BMI – body mass index, EF – echocardiographic ejection fraction measured pre-surgery, LV – left ventricle, MI – myocardial infarction, PAD – peripheral arterial disease, CKD – chronic kidney disease, ACE – angiotensin-converting enzyme.

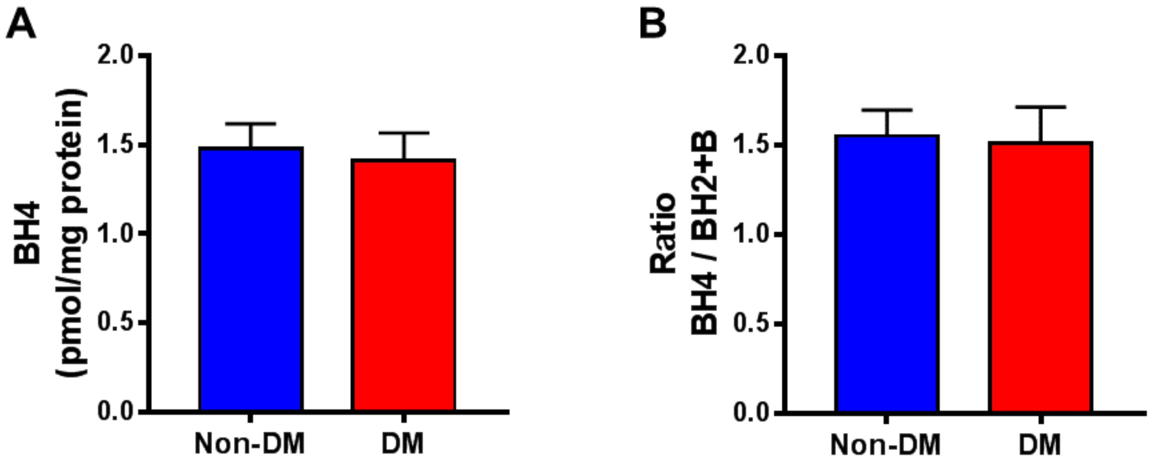

Figure 3-7. (A) The tetrahydrobiopterin (BH4) and the (B) ratio of BH4 to dihydrobiopterin (BH2) and biopterin are not compromised in the atrial myocardium of diabetic mellitus (DM) patients (n=17-19 patients/group, t-test).

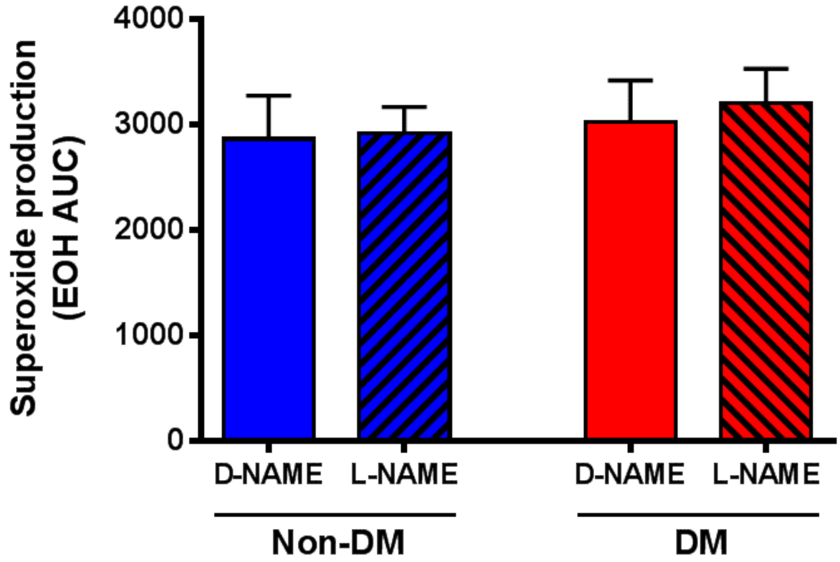

Figure 3-8. Superoxide production measured as the amount of the 2-hydroxyethidium (EOH) produced from the dihydroethidium (DHE) in the presence of the NOS inhibitor (L-NAME) and the absence of the NOS inhibitor (D-NAME – an inactive isomer) in the atrial myocardium of patients with the diabetes mellitus (DM) and matched controls (non-DM) (n=9-10/group, one-way ANOVA followed by Bonferroni's multiple comparisons test).

MYOCARDIAL GCH1 OVEREXPRESSION DID NOT PREVENT THE DIABETES-INDUCED MYOCARDIAL FIBROSIS

The LV of WT DM mice and Tg DM had an increase in myocardial fibrosis compared to the non-DM WT and Tg controls. This observation was confirmed in the histological analysis of the myocardial interstitial fibrosis (*Figure 3-9 A-B*) as well as by measuring the total collagen content in LVs using the hydroxyproline kit (*Figure 3-9C*). However, there was no difference in the interstitial fibrosis or total collagen content between the WT DM and Tg DM group ($p = 0.99$ for both measurements). There was also no difference in the interstitial fibrosis or total collagen content between the WT and Tg controls ($p = 0.99$ for both measurements).

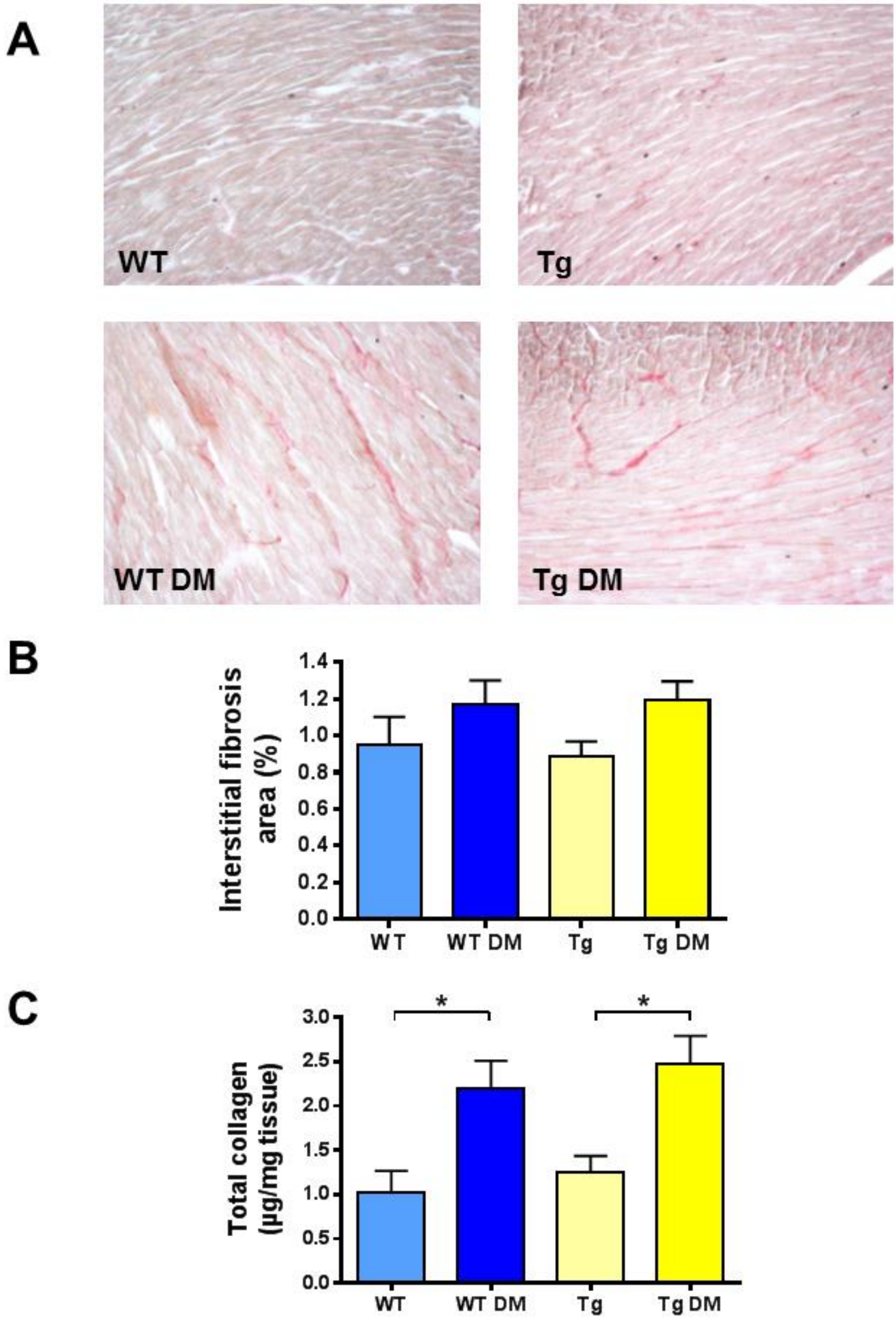

Figure 3-9. (A) Representative histological images of left ventricles (LV) of wild-type (WT) mice, wild-type diabetic (WT DM) mice, mice with myocardial specific GCH1 overexpression (Tg), and Tg diabetic mice (Tg DM) stained with Picrosirius Red. Histology study courtesy of Dr Simona Mafrici. (B) Interstitial fibrosis assessed as the

*relative area of the LV myocardial interstitial connective tissue divided by the total tissue area (n = 6-8 hearts/group, one-way ANOVA followed by Bonferroni's multiple comparisons test). (C) Total collagen content in the LV homogenates (n = 8-10 hearts/group, one-way ANOVA followed by Bonferroni's multiple comparisons test, * - p < 0.05).*

MYOCARDIAL GCH1 OVERXPRESSION PREVENTED THE DECLINE IN THE CARDIAC ENERGY AVAILABILITY

To evaluate whether myocardial energetics differed between genotypes, we performed ^{31}P magnetic resonance spectroscopy in isolated perfused hearts. The main finding was that the WT DM hearts had a decreased PCr/ATP ratio compared to the WT controls ($p = 0.04$). On the other hand, Tg DM hearts did not have a decreased PCr/ATP ratio compared to WT hearts ($p = 0.99$) and the Tg DM PCr/ATP ratio was significantly greater compared to the WT DM hearts ($p = 0.005$) (*Figure 3-10*). The differences in the PCr/ATP ratios between the other comparisons (WT vs. Tg, WT vs. Tg DM, and Tg vs. Tg DM) were not statistically significantly different ($p = 0.99$, $p = 0.99$, and $p = 0.43$ respectively).

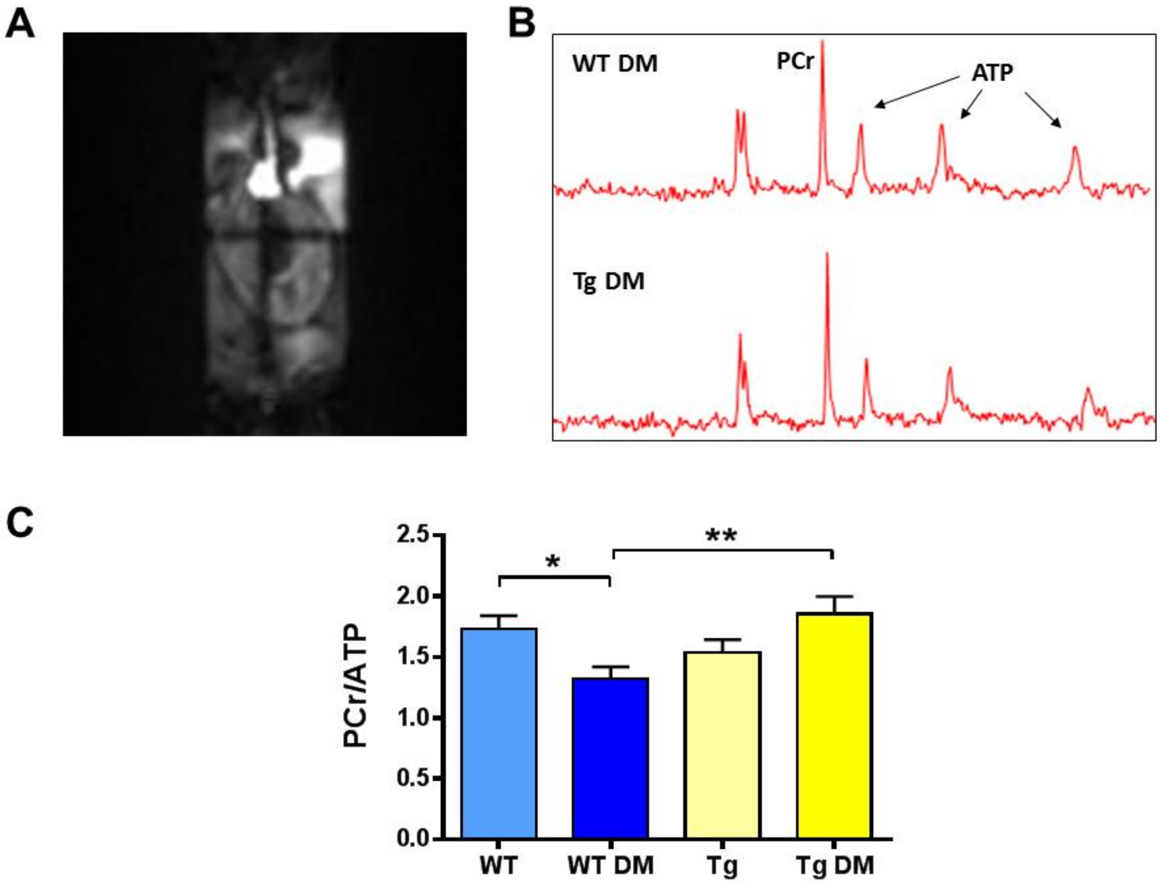

*Figure 3-10. (A) The localisation of the isolated perfused heart in the coil during the ^{31}P-MRS recordings. (B) Representative spectral traces from ^{31}P-MRS in isolated perfused hearts illustrating phosphocreatine (PCr) and ATP peaks in wild-type diabetic (WT DM) mice and diabetic mice with the myocardial specific GCH1 overexpression (Tg DM). (C) PCr to ATP ratio in isolated perfused hearts of wild-type (WT) mice, wild-type diabetic (WT DM) mice, mice with myocardial specific GCH1 overexpression (Tg), and Tg diabetic mice (Tg DM) (n=9-11 hearts/group, two-way ANOVA followed by Bonferroni's multiple comparisons test, * - $p<0.05$, ** - $p<0.01$).*

We further investigated the difference in the cardiac energy availability by assessing the activity of the mitochondrial creatine kinase (CK), the activity of the cytosolic CK, and the activity of the citric synthase (a measurement of the cell's total oxidative capacity). While there was no difference in the activity of the CS between any of the investigated groups (*Figure 3-11A*), the activity of the mitochondrial CK was significantly lower in the WT DM hearts compared to the WT, Tg, and Tg DM hearts (*Figure 3-11B*). The mitochondrial CK activity was not statistically significantly different between other comparisons. Finally, the cytosolic CK activity was not different between any of the investigated groups (*Figure 3-11C*).

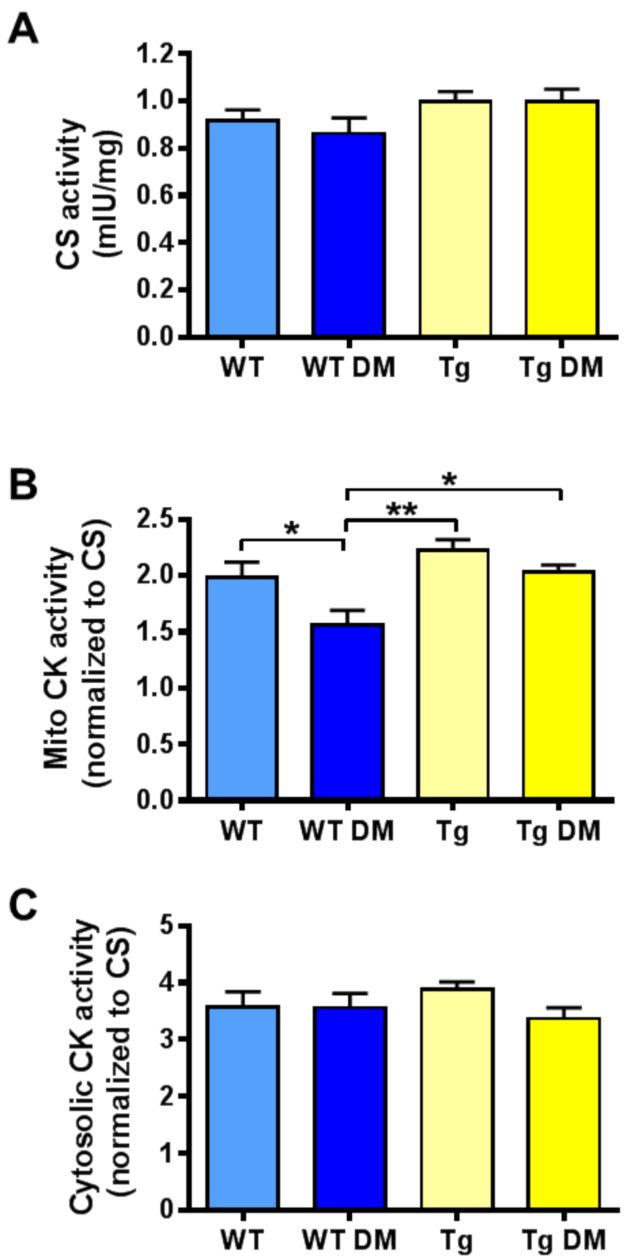

*Figure 3-11. (A) Myocardial activity of the Krebs cycle enzyme citric synthase (CS) in wild-type (WT) mice, wild-type diabetic (WT DM) mice, mice with myocardial specific GCH1 overexpression (Tg), and Tg diabetic mice (Tg DM) (n= 6-10 hearts/group, two-way ANOVA followed by Bonferroni's multiple comparison test). (B) The activity of the mitochondrial isoform of creatine kinase (mito CK) normalized to the CS activity (n=6-10 hearts/group, two-way ANOVA followed by Bonferroni's multiple comparison test, * - $p<0.05$, ** $p<0.01$). (C) The activity of the cytosolic isoform of CK normalized to the CS activity (n=6-10 hearts/group, two-way ANOVA followed by Bonferroni's multiple comparison test).*

The cardiac energy dysfunction measured in the WT DM hearts above was not due to the difference in the number of mitochondria, as the amount of the voltage-dependent anion-selective channel (VDAC – a mitochondrial housekeeping protein) was not different between any of the investigated groups (*Figure 3-12A*). On the other hand, the mitochondrial uncoupling protein 3 (UCP3) was significantly increased in the WT DM hearts compared to the all other groups, whereas the Tg DM hearts were protected from this increase (*Figure 3-12B*). There was no difference in the amount of the UCP3 between the WT, Tg, and Tg DM groups.

Furthermore, the hearts of the Tg and Tg DM had an almost two-fold increase in the amount of the glucose transporter 1 (GLUT-1, an insulin-independent glucose transporter) compared to the WT and WT DM hearts (*Figure 3-12C*). There was no difference in the amount of the GLUT-1 between the WT and WT DM hearts ($p = 0.83$) as well as no difference between the Tg and Tg DM hearts ($p = 0.50$). Finally, there was no difference in the amount of glucose transporter 4 (GLUT-4, an insulin-regulated glucose transporter) between any of the groups (*Figure 3-12D*).

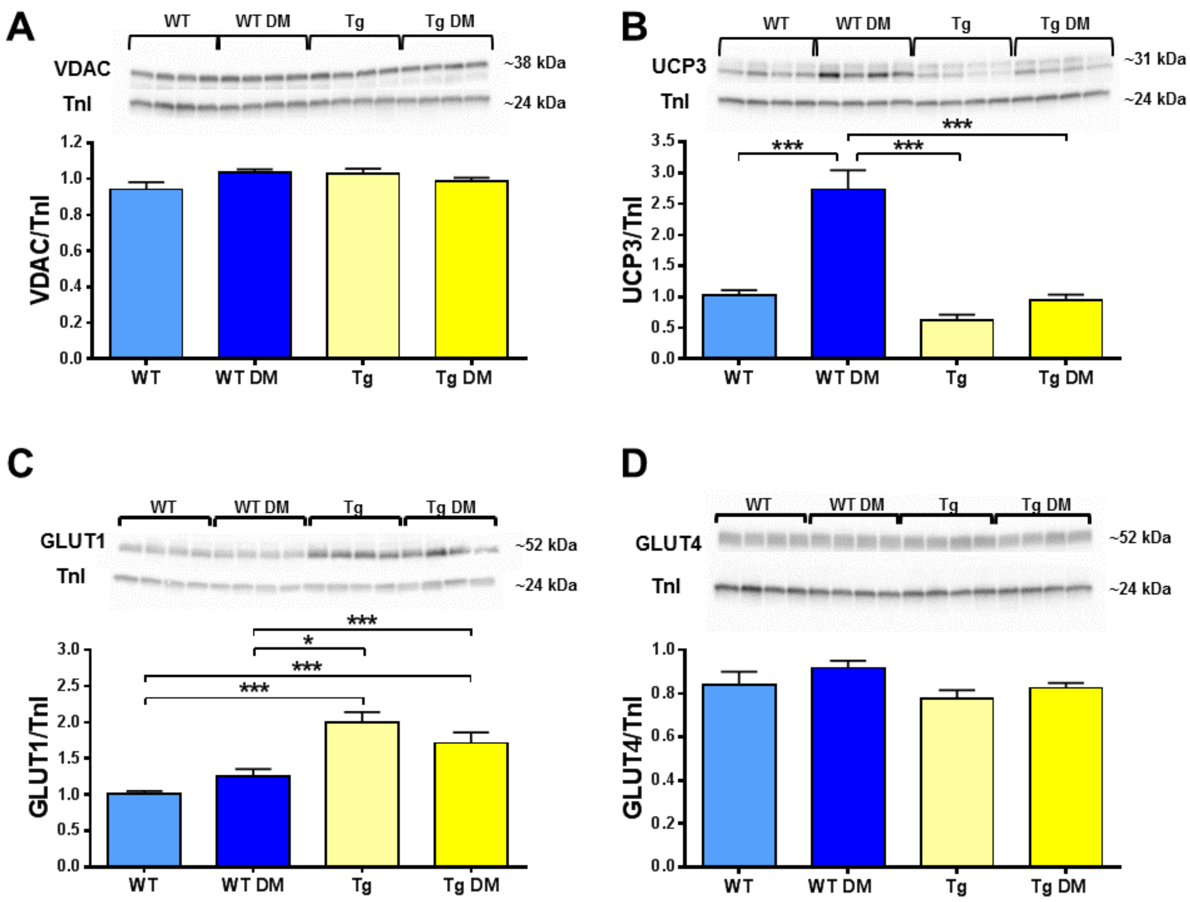

*Figure 3-12. (A) Representative immunoblots and quantification of the voltage-dependent anion-selective channel (VDAC) mitochondrial housekeeping protein in left ventricular (LV) homogenates of wild-type (WT) mice, wild-type diabetic (WT DM) mice, mice with myocardial specific GCH1 overexpression (Tg), and Tg diabetic mice (Tg DM) (n=7 hearts/group, two-way ANOVA followed by Bonferroni's multiple comparison test). (B) Representative immunoblots and quantification of the mitochondrial uncoupling protein 3 (UCP3) in LV homogenates of WT, WT DM, Tg, and Tg DM mice (n=11-12 hearts/group, two-way ANOVA followed by Bonferroni's multiple comparison test, *** - p<0.001). (C) Representative immunoblots and quantification of the glucose transporter 1 (GLUT-1) in LV homogenates of WT, WT DM, Tg, and Tg DM mice (n=11-12 hearts/group, two-way ANOVA followed by Bonferroni's multiple comparison test, * - p<0.05, *** - p<0.001). (D) Representative immunoblots and quantification of the glucose transporter 4 (GLUT-4) in LV homogenates of WT, WT DM, Tg, and Tg DM mice (n=4 hearts/group, two-way ANOVA followed by Bonferroni's multiple comparison test). TnI – troponin I isoform. WB courtesy of Dr Drew Duglan.*

Discussion

The main finding of this study was that the myocardial GCH1 overexpression prevented the development of the diastolic dysfunction in diabetic mice. The protective effects of the GCH1-Tg on diabetes-induced diastolic dysfunction were demonstrated by both *in vivo* echocardiographic measurements as well as *in vitro* in isolated cardiomyocytes. Those results are in agreement with a study where myocardial overexpression of the GCH1 ameliorated the severe LV systolic dysfunction and LV diastolic dysfunction in a similar STZ mouse model of diabetes (259). However, the underlying molecular mechanisms of protection, as discussed below, differ significantly between our diabetic model and the model reported in this study.

Importantly, it has to be noted that the heart rate of the GCH1-Tg mice (both DM and non-DM) was somewhat lower compared to the WT and WT DM, which could affect the echocardiographic diastolic function parameters. However, studies investigating the relationship of heart rate and echocardiographic diastolic function parameters note that the early (passive) filling of LV (measured using parameters E and E') are not affected by the heart rate, while the atrial (active) contraction (measured using parameters A and A') is smaller with lower heart rates (233, 234). Thus the diastolic function parameters E/A and E'/A' in the Tg and Tg-DM mice would be higher as a result of the lower heart rate, which might to some extent explain the improvement of the measured diastolic function in the Tg DM group.

A unique feature of our STZ-induced mouse model of diabetes was that the diabetic hearts only developed the diastolic dysfunction with no significant systolic dysfunction, no LV hypertrophy or LV dilation. This is in contrast to other studies using STZ diabetic rodents, where a more severe cardiac phenotype is described and incorporates both LV diastolic and LV systolic function (31, 32). Two potential reasons for this distinct characteristic is that we used a slightly lower dose of STZ (42-45mg/kg vs. 50-60mg/kg in other studies) as well as we started the diabetes induction in older fully matured mice (aged 14-16 weeks vs. 6-8 weeks in other studies). As a result, our STZ diabetic mice had a slightly less severe phenotype with no excess mortality during the course of the study and milder cardiac phenotype (only LV diastolic dysfunction, with no LV systolic dysfunction) despite having a similar level of plasma hyperglycaemia (23-26 mM). Therefore our diabetic mice could be considered as a model of an intermediary stage in the progression of the diabetic cardiomyopathy (29).

There was no difference in the level of hyperglycaemia, body weight, and plasma insulin levels between the WT DM and Tg DM mice. Those results were expected considering that the transgenic mice had a myocardial specific overexpression of the GCH1 with no leakage of BH4 out of cardiomyocytes and therefore BH4 should not affect any non-cardiac systems (185). However, both the Tg and Tg DM mice had lower heart rates compared to the WT and WT DM mice. This interesting electrophysiological observation has been further explored in a later chapter of the thesis.

On the other hand, the Tg and Tg DM mice had, as expected and previously reported, significantly increased cardiac BH4 levels and increased cardiac NOS activity (185). The majority of previous studies investigating the BH4 and NOS in DM focused on the vasculature and in particular to the endothelial cells. Multiple studies have now established that various diabetic animal models, as well as patients with DM, have impaired NO-mediated vascular relaxation, uncoupled NOS, and reduced endothelial BH4 levels with reduced BH4 to BH2 ratio (194, 202, 260). However, the role of BH4 availability and NOS activity in cardiomyocytes has not been investigated in great detail. One study using the STZ diabetic mice reported reduced cardiac BH4 levels and impaired cardiac nNOS signalling, which is different from observations in our diabetic mice (259). It is important to note, that in that study mice already developed severe LV systolic dysfunction and those discrepancies in the cardiac BH4 levels and NOS activity might represent different stages in the progressing of diabetic cardiomyopathy. Importantly, our findings show that the WT DM hearts did not have reduced BH4 levels, nor did they have reduced ratio of BH4 to BH2 and B. Also, WT DM mice did not have a reduced cardiac NOS activity suggesting that at early stages the myocardium is less affected than the vasculature in the presence of hyperglycaemia. In line with these results, there was no difference in BH4 availability or BH4 to BH2 and B ratio in human myocardium of patients with DM compared to the matched non-diabetic controls. These human samples were collected from a specific subset of patients with long-standing DM (all of them receiving insulin treatment), undergoing CABG or aortic valve cardiac surgery, but without a previous clinical diagnosis of HF and normal LV systolic function (even though the EF of patients with DM was lower (60% vs 64% in controls), those are still considered normal values overall). Based on the results from our diabetic mouse hearts and human myocardium of patients with DM we concluded that reduced BH4 availability is not the culprit for diabetic cardiomyopathy in earlier stages (i.e. stage without severe LV systolic dysfunction).

Oxidative stress is another mechanism often reported and implicated in the pathogenesis of the diabetic cardiomyopathy. However, in the hearts of our diabetic mouse model, there was no measurable increase in the total superoxide production when compared to the non-diabetic controls. There were also no differences between any of the transgenic groups in the amount of superoxide production. Results from other studies in diabetic animal have been inconsistent regarding the production of cardiac reactive oxygen species (ROS). Some studies in STZ and Akita diabetic model did not detect any increase in superoxide, hydrogen peroxide, or any other ROS (150, 261). On the other hand, other studies in STZ and OVE26 diabetic models showed a significant increase in the production of superoxide and other ROS (49, 259, 262). As discussed above, those discrepancies in the cardiac ROS production were likely due to different stages and severities of the underlying diabetic cardiomyopathy. A significant and global increase in the ROS production in cardiomyocytes was present only in more severe and late stages of diabetic cardiomyopathy.

We also measured the superoxide production in human myocardium in a cohort of patients with DM undergoing cardiac surgery. Similarly to the results in the myocardium of our diabetic mouse model, we did not detect any increase in the total myocardial superoxide production nor in the uncoupled NOS-derived superoxide production in myocardial of patients with DM. This result is indicating that a significant global increase in the oxidative stress is only present in late stages of severe HF and is absent in the earlier stages of diabetic cardiomyopathy. Nevertheless, it is still possible that changes in the relative redox state in different localized cellular compartments can still regulate important signalling pathways in cardiomyocytes from patients with DM, even in the absence of global increase of ROS (50). For example, a study in patients with type 2 DM without LV systolic dysfunction showed increased localized hydrogen peroxide emission from mitochondria in isolated cardiomyocytes confirming the notion that only localized (if any at all) redox-changes are present in the early stages of diabetic cardiomyopathy (36).

Impaired calcium handling has been an important element in the pathophysiology of heart failure and has thus been also implicated in the development of the diabetic cardiomyopathy. However, while cardiomyocytes from our diabetic mice had slower rate of the decay of the Ca^{2+} transients compared to the non-diabetic controls, they did not show any changes in the amplitude of the Ca^{2+} transients, nor any changes in the SERCA2a and phospholamban (PLB) protein levels, or PLB-Ser^{16} and PLB-Thr^{17} phosphorylation between the DM and non-DM mice (results not presented in this chapter). The unchanged properties of the calcium handling apparatus in our diabetic mouse model was in contrast with some other studies in STZ, OVE26, db/db, and ob/ob diabetic animal models, where they described significant changes in the calcium handling proteins (76, 259, 263-265). All those studies also reported increased levels of myocardial ROS, which is in agreement with the notion that the impaired calcium regulation and oxidative stress is an important feature in late-stage diabetic cardiomyopathy with developed HF, whereas in earlier stages of the diabetic cardiomyopathy those changes are absent.

Cardiac interstitial fibrosis is another characteristic feature described in the pathogenesis of the diabetic cardiomyopathy (16, 28, 29). Our results were in an agreement with previous studies as we also detected an increased area of interstitial fibrosis and an increased total collagen content in LV. However, there was no difference in the amount of fibrosis between the Tg DM and the WT DM hearts. Therefore the myocardial interstitial fibrosis, while an important element in the pathogenesis of diabetic cardiomyopathy, was not the mechanisms by which GCH1 overexpression and this increased myocardial BH4 prevented the development of the diastolic dysfunction in the Tg DM hearts.

One of the earliest events in the setting of DM is the impaired myocardial energetics (266). Impaired myocardial energetics was measured even prior to the development of any diabetes-related microvascular complications in patients with type 1 DM and type 2 DM (267, 268). In line with these results we detected impaired myocardial energetics characterised by the decreased cardiac PCr/ATP ratio in our diabetic mouse model compared to the non-diabetic controls. Furthermore, the diabetic hearts had a significantly increased level of the mitochondrial uncoupling protein 3 (UCP3), which is a sign of mitochondrial dysfunction and characterises the myocardial substrate switch to using predominantly fatty acids (FA) as a source of energy (150, 269). As reported in previous studies, UCP3 levels are consistently increased in diabetic animal models (28, 266). The mitochondrial dysfunction in our diabetic mice hearts was further corroborated by decreased activity of the mitochondrial isoform of the CK with the unchanged activity of the cytosolic CK, unchanged activity of the CS, and the unchanged number of mitochondria (measured as the amount of the VDAC – a mitochondrial housekeeping protein). The reduction in mitochondrial CK indicates reduced capacity for high-energy phosphate shuttling out of the mitochondria, which could affect overall myocyte ATP availability (270).

In healthy hearts, it has been estimated that around 30% of ATP production comes from glucose and lactate, whereas around 70% of ATP is made by FA oxidation (266). Glucose uptake in diabetic hearts is decreased either due to the lack of insulin (e.g. in type 1 DM) or due to insulin resistance (e.g. in type 2 DM) and as a result, the heart switches to FA oxidation as the predominant source of energy. This metabolic switch starts an undesired positive feedback loop as increased FA oxidation directly inhibits glycolysis and glucose oxidation further shifting the cardiomyocyte to increased FA oxidation as the source of the energy. A disproportionate increase in the FA oxidation results in up to 30% decrease in cardiac metabolic efficiency due to oxygen wasting (more oxygen is required to produce ATP from FA compared to the glucose) (271). A high rate of FA oxidation also leads to increased mitochondrial ROS production, lipotoxicity, and mitochondrial dysfunction (272).

The main novel finding of this part of the study was that the myocardial GCH1 overexpression and thus increased myocardial BH4 level prevented the impairment of myocardial energetics in diabetic mice. Tg DM hearts were able to maintain the unchanged PCr/ATP ratio compared to the non-diabetic controls. In addition, Tg DM hearts did not have impaired mitochondrial CK activity and they also did not have elevated UCP3 levels. Those results suggested that the myocardial GCH1 overexpression prevented the metabolic shift to using FA oxidation as the sole source of energy and thus prevented the mitochondrial dysfunction. The increase in the insulin independent GLUT1 transporter could prevent the harmful positive feedback loop when cardiomyocytes use FA as the only source of energy. We are now in the process of investigating whether glucose uptake and glucose utilisation is upregulated in these Tg cardiomyocytes. The effect of BH4 and NO signalling on the regulation of GLUT1 in cardiomyocytes has not been studied yet. Nevertheless, results from studies on other cell types could provide a plausible mechanistic link between the NOS and GLUT1 regulation. For example, primary skeletal muscle cells from Zucker diabetic rats had a significant increase in the glucose uptake after incubation with sodium nitroprusside (NO-donor) irrespectively of the presence or absence of insulin. Similarly, another study demonstrated an upregulation of the GLUT1 in endothelial cells in the presence of the NO donors (273). In addition, a study in diabetic thioredoxin-interacting protein (TXNIP) knockout mice showed that they have increased cardiac GLUT1 protein levels, greater glucose uptake in cardiomyocytes and thus greater functional energetic reserve compared to the WT diabetic hearts (274).

Furthermore, increased glucose uptake might particularly aid with the function of ion-transporters that rely on a constant supply of ATP to maintain the function and are therefore very susceptible to impaired myocardial energetics associated with DM. For example, studies reported that Ca^{2+}-ATPase SERCA2a and Na^{+}/Ca^{2+} exchanger transporters localise near glycolytic enzymes and they mainly dependent on glycolysis as a source of ATP for their function (275-277). Inhibition of glycolysis by FA impaired the function of SERCA2a and Na^{+}/Ca^{2+} exchanger without changing their gene expression or protein levels in STZ diabetic rats (278, 279). Therefore this is a possible unifying explanation for the dysfunction seen in the hearts of our diabetic mice: impaired myocardial energetics resulted in decreased function of SERCA2a and Na^{+}/Ca^{2+} exchanger (without altering their total protein levels), which in turn caused slower Ca^{2+} uptake resulting in cardiac diastolic dysfunction. Further studies are needed to confirm whether the protective effects of GCH1 overexpression are mediated by this mechanism.

In conclusion, we demonstrated that in our animal model of early diabetic cardiomyopathy the myocardial overexpression of the GCH1 and thus increased myocardial BH4 levels prevented the development of diastolic dysfunction. The protective mechanism was not related to the reduction of the oxidative stress, NOS uncoupling or fibrosis, but was related to improving the myocardial energetics by enhancing glucose uptake through upregulated GLUT1 transporter. While the cardiac protection in GCH1 transgenic mice has been here clearly demonstrated, it is still unknown whether oral BH4 supplementation can result in similar protection from diabetic cardiomyopathy.

CHAPTER 4:

Atrial electrophysiological disturbances in diabetes mellitus

Introduction

Atrial fibrillation (AF) is the most common heart rhythm disorder. AF is associated with considerable morbidity, decreased quality of life, and increased mortality as a consequence of abnormal hemodynamics, atrioventricular dyssynchrony, atrial and ventricular mechanical dysfunction, and thromboembolic events (82). Prevalence of AF in the general population is 1-2% and continues to rise. It is estimated that by 2060 the number of patients with AF will double compared to the year 2010 and will thus be an even greater health problem (280).

Rather than being a primary electrophysiological condition – AF is usually the final manifestation of various underlying pathological mechanisms. Risk factors such as age, hypertension, coronary artery disease, valvular heart disease, chronic heart failure (HF), smoking, obstructive sleep apnoea, obesity, and diabetes mellitus (DM) all independently increase the risk for AF (82, 85). Studying the underlying mechanisms of each distinct risk factor is challenging as patients often have multiple risk factors simultaneously, and is therefore, difficult to depict the relative contribution of individual disorder.

As presented in more detail in the general introduction chapter, multiple disturbances have been reported in atrial myocardium of patients with DM. Altered cardiac metabolism, mitochondrial dysfunction, increased oxidative stress, inflammation, and fibrosis have all been observed in atria of patients with DM, but their role in the pathogenesis of AF remains uncertain (112, 139, 281).

The aim of this project was firstly to determine whether chronic hyperglycaemia alone (without concomitant risk factors such as obesity, hypertension, and significant HF) is sufficient to increase the risk for atrial fibrillation using an animal model of type 1 DM. Secondly, the project then explored different pathophysiological mechanisms that could explain the electrophysiological phenotype in diabetic mouse atria.

Methods

All methods are described in greater detail in the general methods chapter.

ANIMAL MODELS

Experiments were performed on the males of the C57BL/6JOlaHsd strain purchased directly from Envigo (main United Kingdom distributor of animal models). Mice were housed in individually ventilated cages in a temperature-controlled environment (20-22°C) with a 12-hour light-dark cycle. Mice had ad libitum access to food and water. Sentinel animals were kept in the same racks and regularly underwent health monitoring to ensure and confirm specific pathogen-free environment.

All animal procedures were performed in accordance with the United Kingdom Home Office Animals (Scientific Procedures) Act of 1986. They were carried out under the authority of the project licence number PPL 30/2804 (project licence holder: Prof Barbara Casadei) until 25.1.2016, and after this date, under PPL 30/3374 (project licence holder: Dr Ricardo Carnicer Hijazo).

STREPTOZOTOCIN INDUCED DIABETES MELLITUS

Males, aged 12-14 weeks, received intraperitoneal injections of low-dose streptozotocin (STZ) (50 mg/kg) or intraperitoneal injections of vehicle (citrate buffer) over five consecutive days. During the study, mouse body weight (BW) and plasma glucose levels were regularly monitored. After 12 weeks of the last injection, cardiac function was assessed non-invasively using echocardiography. Two days later mice underwent transoesophageal atrial pacing study. After the pacing experiments mice were either sacrificed to collect tissue or recovered and used for optical mapping of isolated atria three to five days later.

IN VIVO ATRIAL ELECTROPHYSIOLOGY IN MICE

Electrocardiogram recordings and transoesophageal atrial pacing were performed under isoflurane general anaesthesia (1.5-2.0% isoflurane), as previously described (236, 237). Surface electrocardiogram (ECG) was obtained by placing electrodes subcutaneously in all four limbs. Afterwards, an octapolar electrophysiological catheter (NuMED CIBER mouse electrophysiology catheter) was introduced on the oesophagus and used to pace the atria. Burst atrial pacing with reduced cycle length (CL) periods was used to measure the inducibility of atrial arrhythmias. Atrial arrhythmias were defined as an induced episode of irregular atrial rhythm lasting longer than 2 seconds. The number of arrhythmic episodes and their duration were measured.

ECHOCARDIOGRAPHY IN MICE

Echocardiography was performed using a Vevo 2100 (VisualSonics) ultrasound imaging system with an ultra-high frequency MS400 cardiovascular transducer (18-38 MHz) under the isoflurane general anaesthesia (1.0-2.0% isoflurane). LV diastolic function was assessed by tissue Doppler imaging (TDI) and mitral valve flow parameters recorded with the pulsed-wave Doppler mode. Left atrial (LA) size was measured from the LA recordings from the apical 4-chamber view at the end of LV systole – at the point of largest LA size.

OPTICAL MAPPING OF ISOLATED ATRIA

Mouse atria were isolated, superfused in Tyrode solution, and pinned to the Sylgard-coated petri dish in orientation to make crista terminalis and interatrial septum visible. Atria were then incubated with the voltage-sensitive dye di-4-ANNEPS (20 µM) for 30 minutes at 37°C. Afterwards, the atria were superfused with Krebs solution containing 5 µM blebbistatin to prevent motion artefacts. To inhibit the NOS we incubated atria with 10µM N-[(4S)-4-Amino-5-[(2-aminoethyl](amino]pentyl]-N’-nitroguanidine (AAAN) for 20 min (and then continuously throughout the experiment) before starting any optical mapping recordings. Images of atria were acquired by a high-speed CMOS camera (NeuroCMOS-DW128-II, Cairn Research) at 1000 frames/s using the GView optical mapping software (courtesy of Professor Gil Bub, University of Oxford). Optical action potential duration (APD) and conduction velocity were obtained from the analysis of the recordings using a custom-made analysis program written in MATLAB (*full source code in Appendix*).

MOLECULAR BIOLOGY MEASUREMENTS

The total collagen content in the LV was assessed using the hydroxyproline colourimetric detection kit (QuickZyme Biosciences). The sample's collagen was calculated by comparison to the collagen standard curve and expressed as the collagen content per tissue weight.

Results

MULTIPLE LOW DOSE STREPTOZOTOCIN INJECTIONS RESULT IN STABLE HYPERGLYCAEMIA WITHOUT SEVERE ADVERSE SIDE-EFFECTS

The first step was to confirm the hyperglycaemic profile of the STZ induced DM in C57BL/6 mice and to monitor for any adverse severe side-effects. As seen in *Figure 4-1*, compared to the control mice, the STZ mice had higher glucose levels already at the end of the five-day-long injection protocol. The plasma glucose levels in diabetic mice reached the plateau levels after 4 weeks and then the glucose level did not significantly increase in the 12 weeks follow up period. On the other hand, the control mice injected only with the citrate buffer remained normoglycaemic for the whole duration of the study. Body weight was another physiological parameter we regularly measured to ensure the wellbeing of mice. Control mice continued to gain body weight throughout the study. STZ injected diabetic mice had lower body weight compared to the control mice. Most importantly, the diabetic mice were not losing body weight throughout the study. We did not detect any severe adverse side effects or severe health problems in diabetic mice.

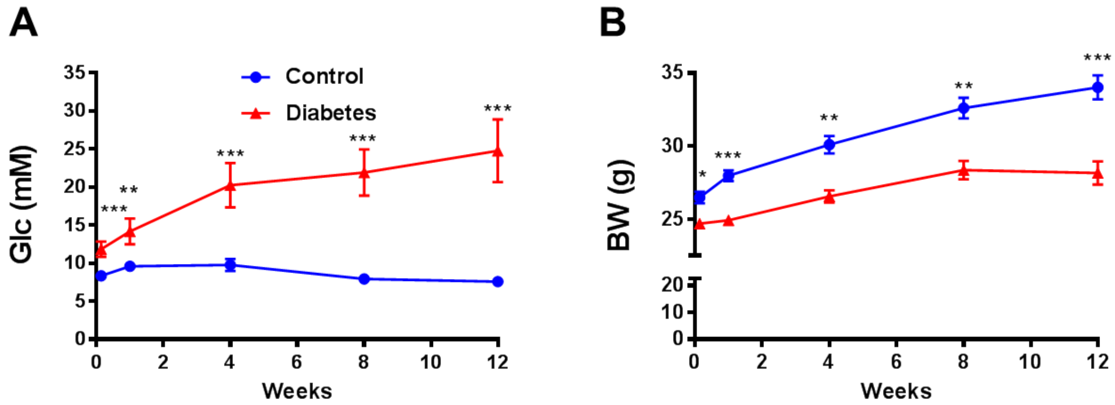

*Figure 4-1. (A) Plasma glucose (Glc) levels of streptozotocin injected mice (diabetes) and control mice throughout the study (n = 12/group). (B) Body weight (BW) of streptozotocin injected mice (diabetes) and control mice throughout the study (n = 12/group, t-test). * - p < 0.05, ** - p < 0.01, *** - p < 0.001.*

ELECTROPHYSIOLOGY AND PACING INDUCED ARRHYTHMIAS

The main finding of the study was that a higher proportion of diabetic mice developed at least one pacing induced atrial arrhythmia when compared to the control mice (92% vs. 63%, p = 0.007, n = 24-26/group) (*Figure 4-2A*). Furthermore, diabetic mice had a higher probability of pacing induced arrhythmias (measured as the proportion of burst pacing episodes resulting in atrial arrhythmia) compared to the control mice (12±16% vs. 3±12% [median ± IQR], p=0.004, n=24-26/group) (*Figure 4-2B*). On the other hand, there was no difference in duration of pacing induced atrial arrhythmias between diabetic and control mice (15±31s vs. 9±44s [median ± IQR], p=0.66, n=24-26/group) (*Figure 4-2C*).

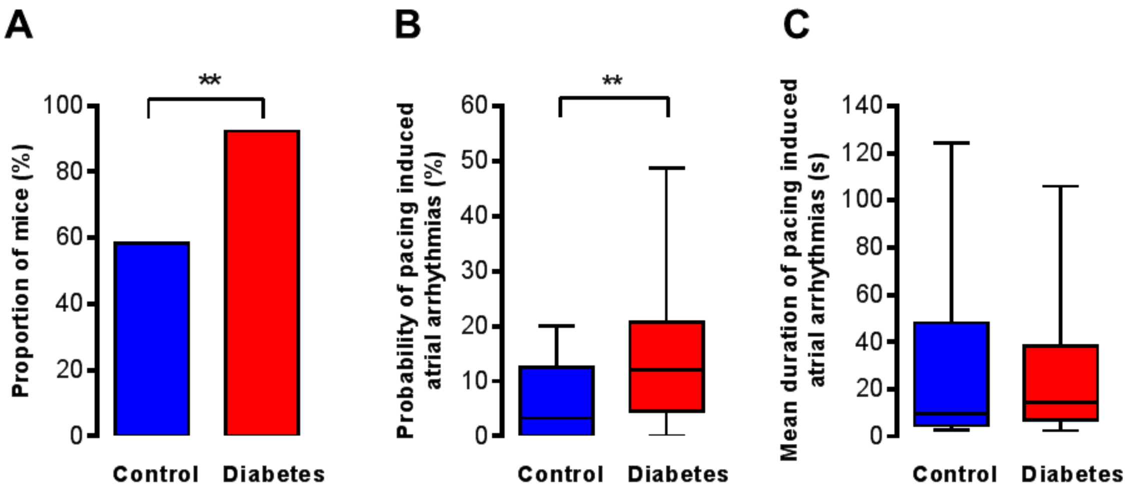

*Figure 4-2. (A) The proportion of mice that had at least one pacing inducible episode of atrial arrhythmia (n = 24-26 per group, Fisher's exact test). (B) Probability of pacing-induced atrial arrhythmias (n = 24-26 per group, Mann-Whitney test). (C) Mean duration of pacing-induced atrial arrhythmias (n = 24-26 per group, Mann-Whitney test). ** - $p < 0.01$*

We analysed the baseline electrocardiogram intervals of diabetic and control mice. The main difference between the two groups was prolonged PQ interval in diabetic mice (43.5±0.1 ms vs. 39.4±0.6 ms, p = 0.001) and longer duration of the P wave (21.7±0.7 ms vs. 20.5±0.5 ms, p = 0.18). There was no difference in baseline RR interval, QRS interval or QTc interval between the two groups (*Table 4-1*).

	Control (n = 24)	***Diabetes (n = 26)***	***p-value***
ECG intervals			
RR (ms)	130.5 ± 3.5	131.6 ± 3.6	0.81
P wave duration (ms)	20.5 ± 0.5	21.7 ± 0.7	0.18
PQ (ms)	39.4 ± 0.6	43.5 ± 0.1	**0.001 ****
QRS (ms)	17.6 ± 0.7	18.3 ± 0.6	0.43
QTc (ms)	52.5 ± 1.4	52.9 ± 1.5	0.84

*Table 4-1. Electrophysiological properties of anaesthetized diabetic mice compared to their control littermates (n = 24-26/group, t-test, all values are mean ± SEM), ** - p<0.01*

DIABETIC MICE HAVE MODEST LEFT VENTRICULAR DIASTOLIC DYSFUNCTION, RELATIVE LEFT ATRIAL ENLARGEMENT, BUT NO LEFT VENTRICULAR SYSTOLIC DYSFUNCTION

We assessed the diabetic cardiac *in vivo* mechanical function using the echocardiography performed under general anaesthesia. Summary of main results is presented in *Table 4-2*. Briefly, hearts of diabetic mice were smaller compared to the control mice: the LV diastolic volume (p = 0.002) and LV systolic volume (p = 0.09) were smaller in the diabetic group (*Figure 4-3 A-B*). However, the indexed (normalised to body weight) LV diastolic and systolic volumes were not different between the two groups (*Figure 4-3 C-D*). Similarly, the calculated mean LV mass was also smaller in the diabetic group compared to the control group (p = 0.001), however, the indexed LV mass was not different between the groups (*Figure 4-4*).

There was no difference in the LV systolic function between the diabetic and control mice: both the ejection fraction and cardiac index (calculated cardiac output normalised to body weight) was not different between the two groups ($p = 1.00$ and $p = 0.26$ respectively) (*Figure 4-5*). On the other hand, diabetic mice showed a degree of LV diastolic dysfunction. The tissue Doppler early to late mitral valve annulus velocity ratio (E'/A') was smaller in the diabetic group compared to the control group ($p = 0.04$) (*Figure 4-6B*). Furthermore, the mitral valve early to late inflow velocity ratio was higher in the diabetic group compared to the control group ($p = 0.08$) (*Figure 4-6A*). However, there was no difference in the combined E/E' ratio between the two groups (*Figure 4-6C*). Also, there was no difference in any of the characteristic cardiac times: isovolumetric contraction time, ejection time, and isovolumetric relaxation time between the two groups. Finally, there was no difference in the calculated myocardial performance index (Tei index) between the diabetic and control group (T*able 4-2*).

Another important echocardiographic finding was that the diabetic mice have relative enlargement of left atria (LA). There was no difference in the absolute LA dimensions (long axis, short axis, and total area), however, the indexed (normalised to body weight) LA area is significantly larger in the diabetic mice compared to control mice ($p = 0.001$) (*Figure 4-7*).

Echocardiographic measurements	*Control (n = 11)*	*Diabetes (n = 12)*	*p-value*
Body weight (g)	35.5 ± 1.0	29.0 ± 0.6	**0.0001 *** **
Heart rate			
Baseline HR (bpm)	499 ± 3	501 ± 5	0.70
HR for diastolic measurements (bpm)	333 ± 14	318 ± 8	0.37
LV dimensions			
LV anterior wall (mm)	1.01 ± 0.05	0.96 ± 0.02	0.26
LV posterior wall (mm)	0.93 ± 0.03	0.87 ± 0.02	0.13
LV diastolic internal diam. (mm)	3.71 ± 0.07	3.31 ± 0.09	**0.002 ** **
LV systolic internal diam. (mm)	1.81 ± 0.06	1.62 ± 0.07	0.07
LV diastolic volume (µl)	58.9 ± 2.6	44.9 ± 2.8	**0.002 ** **
LV systolic volume (µl)	10.1 ± 0.9	7.8 ± 0.9	0.09
Indexed LV diastolic volume (µl/g)	1.67 ± 0.09	1.54 ± 0.08	0.26
Indexed LV systolic volume (µl/g)	0.29 ± 0.03	0.26 ± 0.03	0.56
LV mass			
LV mass (mg)	110 ± 5	84.2 ± 3.6	**0.001 *** **
Indexed LV mass (mg/g)	3.09 ± 0.10	2.89 ± 0.09	0.14
LV systolic function			
LV ejection fraction (EF, %)	83.1 ± 1	83.1 ± 1.1	1.00
Cardiac index (µl/min/g)	691 ± 31	640 ± 31	0.26
LV diastolic function			
Mitral valve E/A ratio	1.49 ± 0.04	1.68 ± 0.09	0.08
Tissue Doppler E'/A' ratio	1.20 ± 0.06	1.02 ± 0.05	**0.04 * **
Combined E/E' ratio	35.8 ± 1.8	35.8 ± 1.8	0.99
Cardiac times			
IVCT (ms)	21.7 ± 1.8	23.0 ± 1.4	0.60
ET (ms)	59.8 ± 1.6	64.3 ± 1.5	0.06
IVRT (ms)	24.6 ± 2.1	23.4 ± 1.7	0.64
Tei Index	0.78 ± 0.06	0.72 ± 0.04	0.48
LA dimensions			
LA long axis (mm)	4.44 ± 0.09	4.47 ± 0.1	0.83
LA short axis (mm)	1.80 ± 0.07	1.92 ± 0.06	0.18
LA area (mm^2)	8.24 ± 0.21	8.04 ± 0.25	0.55
Indexed LA area (mm^2/g)	0.234 ± 0.007	0.278 ± 0.009	**0.001 ** **

Table 4-2. Main echocardiographic measurements evaluating left ventricular (LV) size, mass, systolic and diastolic function, cardiac times, and left atrial (LA) dimensions of anaesthetized diabetic mice compared to their control littermates (n = 11-12/group, t-test, all values are mean ± SEM). HR – heart rate, LV – left ventricle, LA – left atrium,

*BW – body weight, E – early mitral valve inflow velocity, A – late mitral valve inflow velocity, E' – early tissue Doppler mitral valve annulus velocity, A' – late tissue Doppler mitral valve annulus velocity, IVCT – isovolumetric contraction time, ET – ejection time, IVRT – isovolumetric relaxation time, * - p<0.05, ** - p<0.01, *** - p < 0.001*

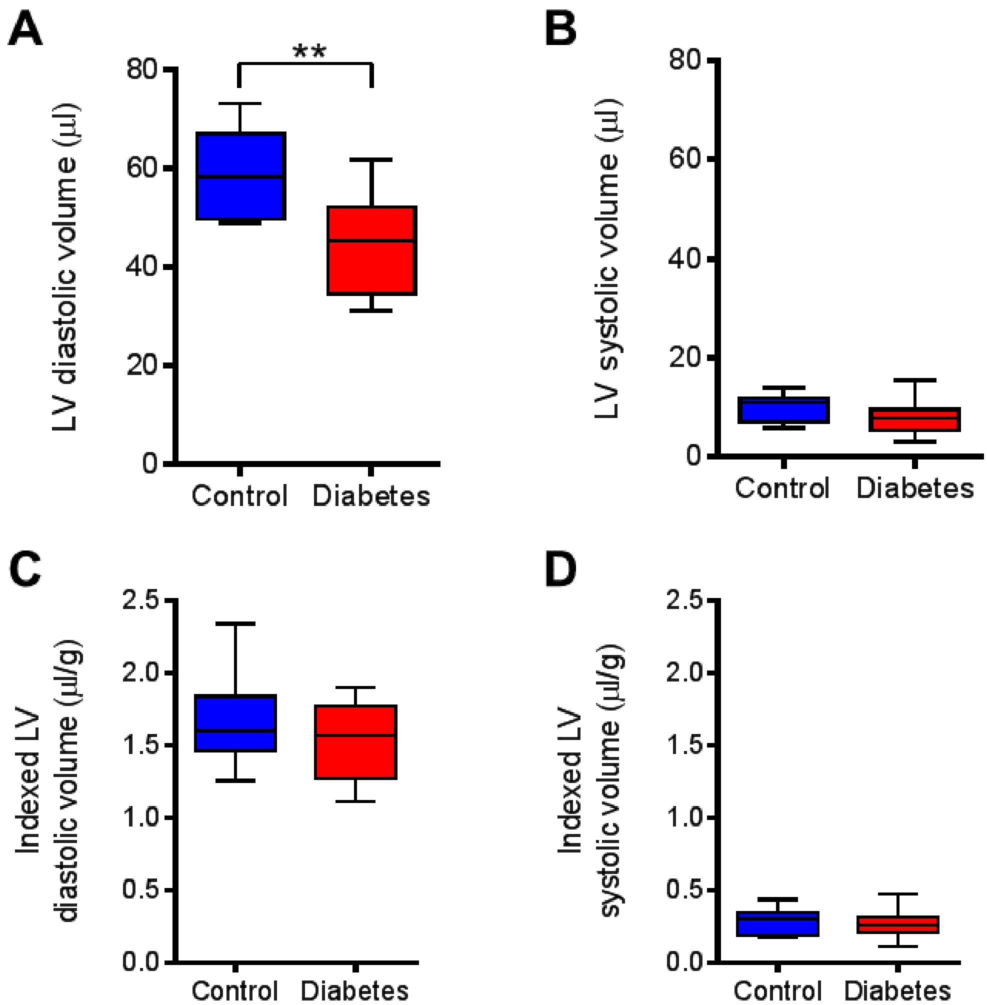

*Figure 4-3. (A-B) Left ventricular (LV) diastolic and systolic volumes of diabetic mice compared to the control mice calculated from echocardiographic measurements of LV dimensions from short-axis view. (C-D) Indexed (normalised to the body weight) LV diastolic and systolic volume of diabetic mice compared to the control mice (n = 11-12/group, t-test, all values are mean ± SEM). ** - p<0.01*

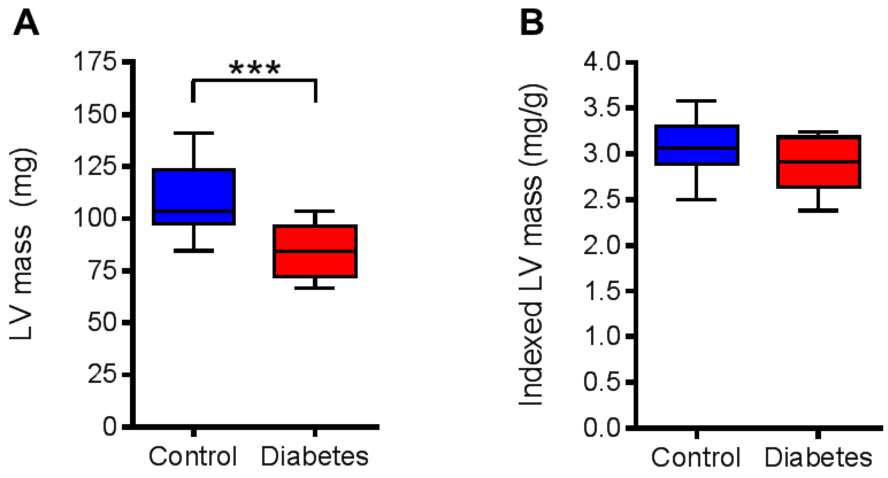

*Figure 4-4. (A) Left ventricular (LV) mass and (B) indexed LV mass (normalised to the body weight) of diabetic mice compared to the control mice calculated from echocardiographic measurements of LV dimensions from short-axis view (n = 11-12/group, t-test, all values are mean ± SEM). *** - p<0.001*

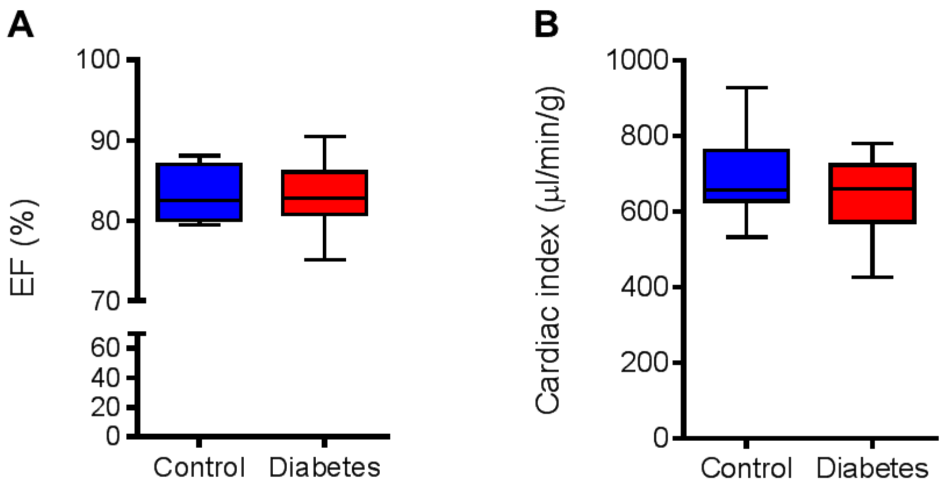

Figure 4-5. Echocardiographic assessment of left ventricular (LV) systolic function. (A) LV ejection fraction (EF) of diabetic mice compared to the control mice calculated from echocardiographic measurements of LV dimensions from short-axis view (n = 11-12/group, t-test, all values are mean ± SEM). (B) LV cardiac index (cardiac output normalised to body weight) of diabetic mice compared to the control mice (n = 11-12/group, t-test, all values are mean ± SEM).

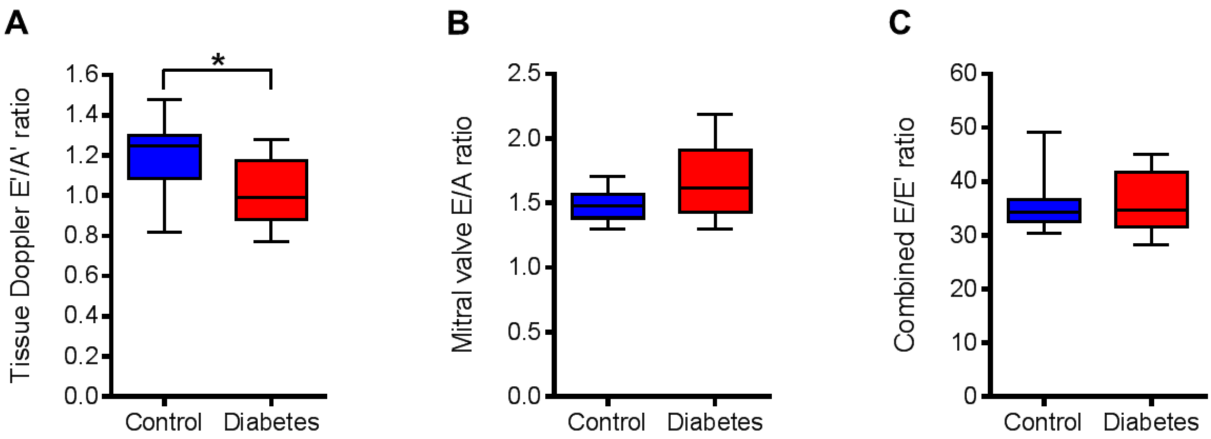

*Figure 4-6. Echocardiographic assessment of left ventricular (LV) diastolic function of diabetic mice compared to the control mice. (A) The ratio of early (E) vs late (A) blood flow velocity through the mitral valve (n = 11-12/group, t-test, all values are mean ± SEM). (B) The ratio of tissue Doppler early (E') vs late (A') mitral annulus velocities (n = 11-12/group, t-test, all values are mean ± SEM). (C) Combined early mitral blood flow velocity (E) vs. early tissue Doppler mitral annulus velocity (E') ratio (n = 11-12/group, t-test, all values are mean ± SEM). * - p<0.05*

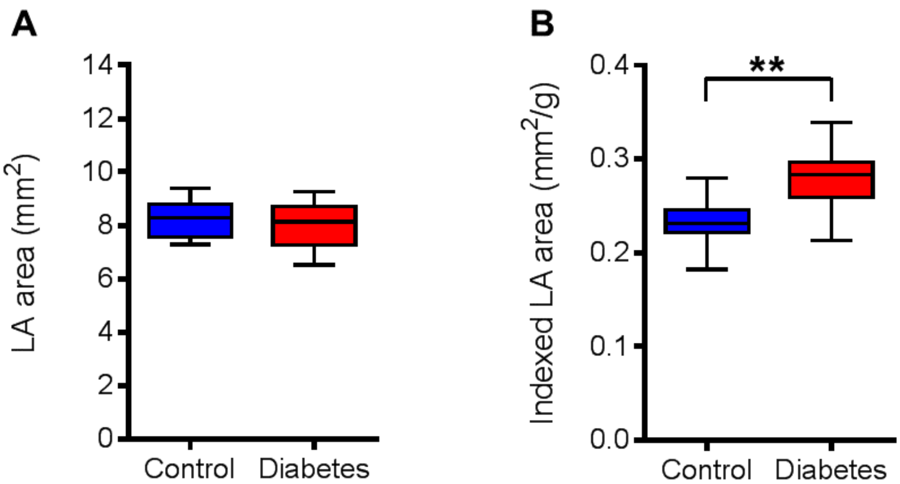

*Figure 4-7. (A) Echocardiographic assessment of left atrial (LA) dimensions obtained from apical four-chamber view (n = 11-12/group, t-test, all values are mean ± SEM). (B) Indexed (normalised to body weight) LA dimensions obtained from apical four-chamber view (n = 11-12/group, t-test, all values are mean ± SEM). ** - p<0.01*

We also investigated the relationship between the pacing induced atrial arrhythmias, diastolic function, and relative LA size relative to the degree of hyperglycaemia (*Figure 4-8*). We found a positive correlation between the probability of pacing induced atrial arrhythmias and a plasma glucose levels ($p = 0.002$), a negative correlation between the tissue Doppler E'/A' ratio and plasma glucose levels ($p = 0.06$), and a positive correlation between the indexed LA area and plasma glucose levels ($p = 0.03$).

In an attempt to explore the main physiological mechanisms connecting the increased pacing induced atrial arrhythmias with baseline underlying electrophysiological and mechanical properties, we plotted multiple correlations between characteristic variables (*Figure 4-9*). We found the positive correlation between the probability of pacing induced arrhythmias and PQ interval ($p = 0.03$) and the probability of pacing induced arrhythmias and indexed LA area ($p = 0.09$). There was no correlation between the pacing induced arrhythmias and tissue Doppler E'/A' ratio as well as no correlation between the pacing induced arrhythmias and P wave duration. Furthermore, there was a positive correlation between the PQ interval and indexed LA area ($p = 0.002$) as well as a negative correlation between the PQ interval and the tissue Doppler E'/A' ratio.

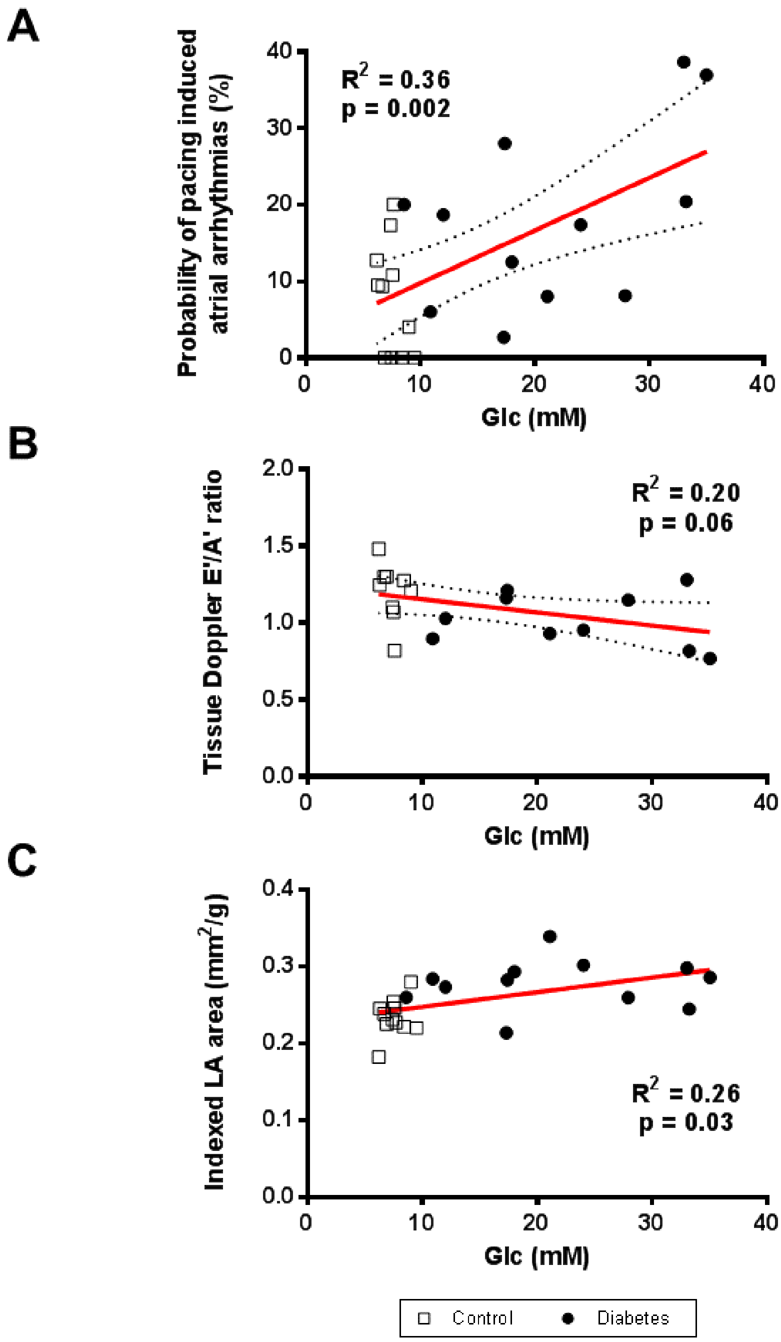

Figure 4-8. (A) Linear correlation between the probability of pacing-induced atrial arrhythmias and plasma glucose (Glc) levels. (B) Linear correlation between the left ventricular diastolic function as measured by tissue Doppler E'/A' ratio and plasma glucose levels. (C) Linear correlation between the indexed left atrial (LA) size and plasma glucose levels.

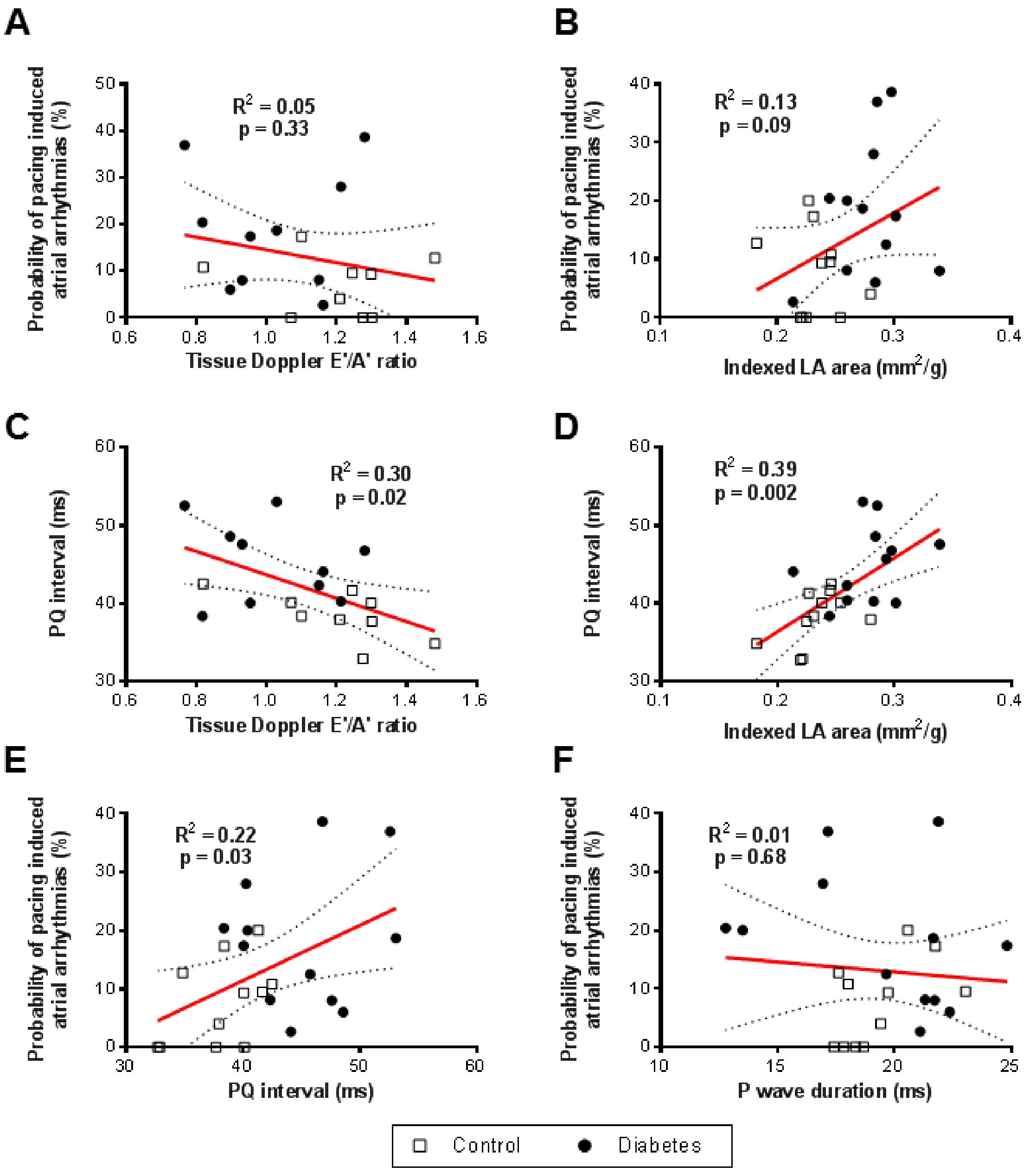

Figure 4-9. (A) Linear correlation between the probability of pacing-induced atrial arrhythmias and left ventricular diastolic function as measured by tissue Doppler E'/A' ratio. (B) Linear correlation between the probability of pacing-induced atrial arrhythmias and indexed left atrial (LA) size. (C) Linear correlation between PQ interval and left ventricular diastolic function as measured by tissue Doppler E'/A' ratio. (D) Linear correlation between PQ interval and indexed left atrial (LA) size. (E) Linear correlation between the probability of pacing-induced atrial arrhythmias and PQ interval. (F) Linear correlation between the probability of pacing-induced atrial arrhythmias and P wave duration.

Increased susceptibility of pacing-induced AF can be explained by changes promoting the re-entry of the electrical conduction in the atria. The main determinants favouring this re-entry are decreased refractory period and decreased conduction velocity (100, 104). Therefore the next investigations were focused on studying the electrical properties of diabetic myocardium using the optical mapping of isolated perfused atrial preparations.

Tissue refractoriness can be assessed by measuring the action potential duration (APD) in different parts of the tissue. APD trended towards an increase in the diabetic left atrium (LA) (APD80 21±2 ms vs. 17±2 ms in controls, p = 0.14), without any differences in the right atrium (RA) (APD80 18±2 ms vs. 19±1 ms in controls, p = 0.73) (*Figure 4-10*).

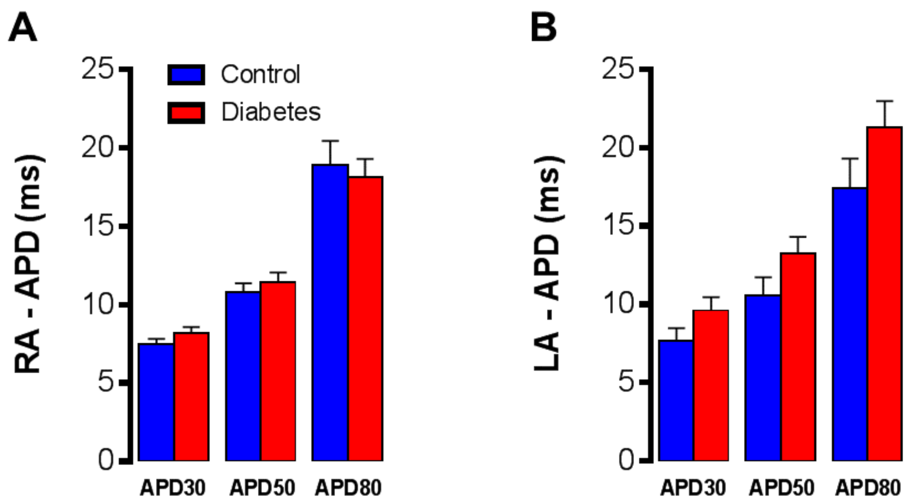

Figure 4-10. Action potential duration (APD) measured from spontaneously beating isolated atrial preparations (n = 6-7 per group, t-test). RA – right atrium, LA – left atrium, APD30 – APD at 30% repolarization, APD50 – APD at 50% repolarization, APD80 – APD at 80% repolarization.

To assess the global conduction, we measured the time needed for electrical activation of spontaneously beating atria to reach the outermost edge of either RA or LA assessed by creating activation maps of spontaneous electrical beats (*Figure 4-11*). The conduction time to the edge of the LA was almost two-fold greater in diabetic atria compared to controls (39±3 ms vs. 22±2 ms in controls, p = 0.0006, n = 6/group), without differences in the conduction time to the edge of the RA (12±1 ms vs. 12±1 ms in controls, p = 0.93, n = 6/group) (*Figure 4-12*). Importantly, there was no difference in the isolated atrial long axis length (p = 0.45) and total atrial area (p = 0.81) between the diabetic and the control group (*Figure 4-13*). Those measurement combined indicate that the average electrical conduction velocity is lower in diabetic atria compared to the control ones.

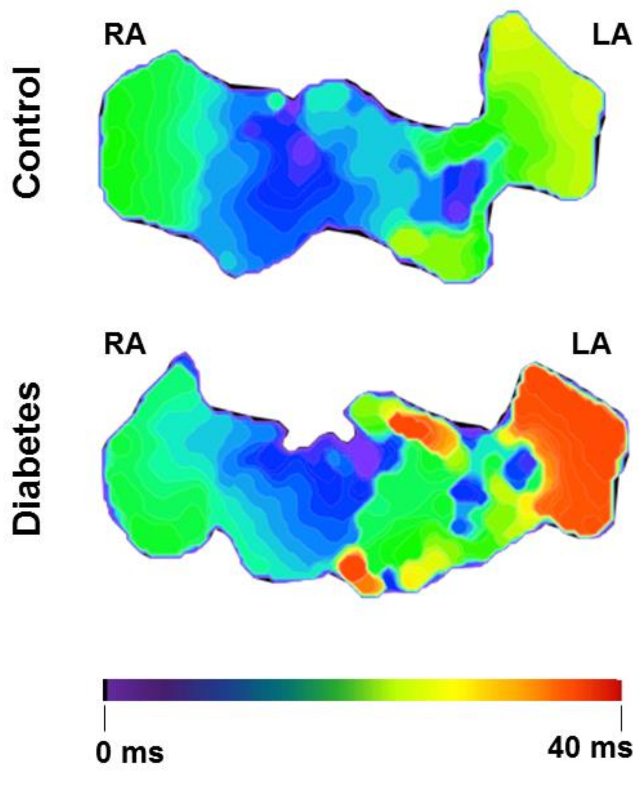

Figure 4-11. A representative activation map of the isolated perfused atrial preparation created using optical mapping recordings. RA – right atrium, LA – left atrium

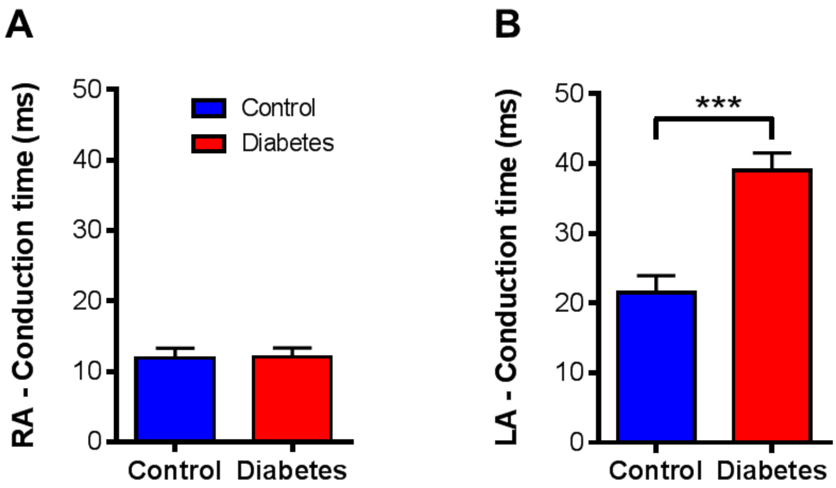

*Figure 4-12. Conduction time defined as the time of electrical propagation from the sinoatrial node to the edge of (A) right atrium (RA) or (B) left atrium (LA) (n = 6/group, t-test). *** - p < 0.001*

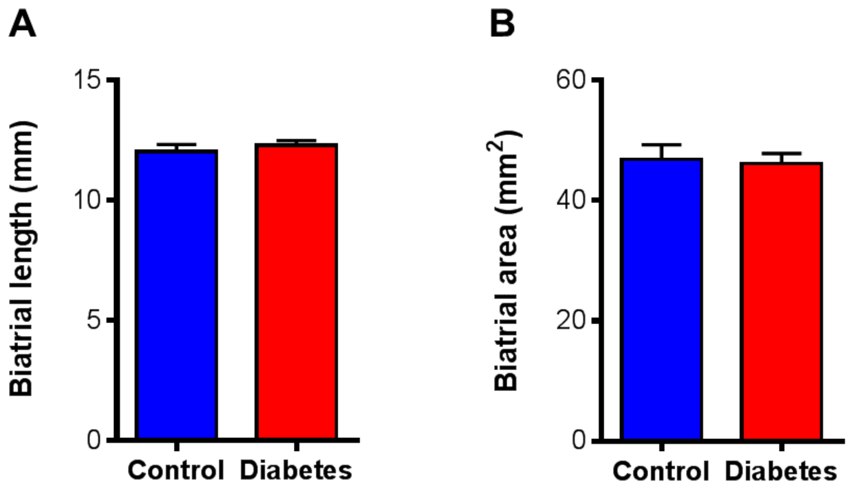

Figure 4-13. (A) Long axis dimensions of isolated atrial preparations measured from optical mapping recordings (n = 6-7/group, t-test). (B) Area of isolated atrial preparations measured from optical mapping recordings (n = 6-7/group, t-test).

To study the electrical propagation within the atria in greater detail, we used the Ccoffinn (Cardiomyocyte Cultures Optically-mapped: Fast Feature extractIoN and tracking) toolkit developed by our collaborators Jakub Tomek and Bob Gil (Department of Physiology, University of Oxford). As detailed in the methods section, this novel analytical approach allows quantification the wavefront propagation velocity frame-by-frame (in their actual propagation direction) and the wavefront propagation roughness (quantified as a perimeter-to-area ratio).

The averaged (across multiple spontaneous beats and multiple recordings) mean conduction velocity (CV) of one whole spontaneous beat was significantly lower in diabetic atria compared to the control group ($p = 0.009$) (*Figure 4-14A*). Similarly, the averaged maximum CV of one spontaneous beat was also lower in diabetic atria compared to the control atria ($p = 0.04$) (*Figure 4-14A*). Furthermore, the averaged mean perimeter-to-area (P/A) ratio (a measure of wavefront roughness) and averaged maximum P/A ratio was greater in the diabetic atria compared to the control atria ($p = 0.04$ and $p = 0.03$ respectively) (*Figure 4-14B*).

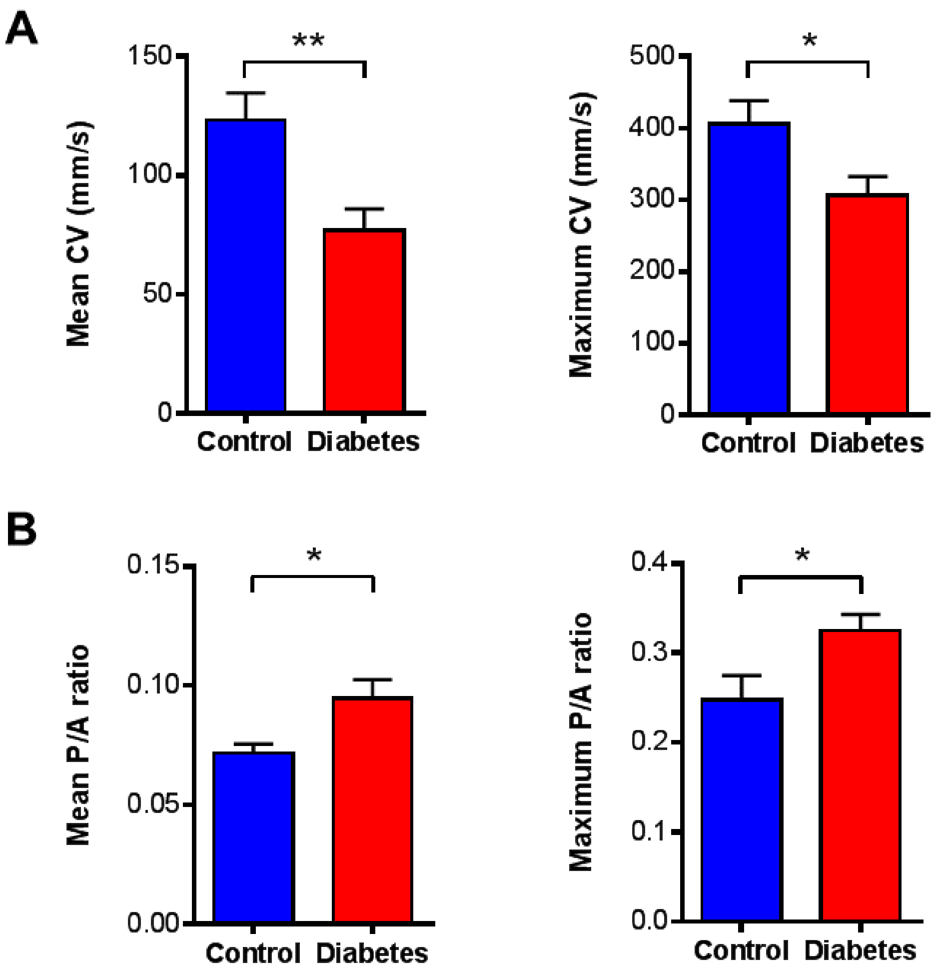

*Figure 4-14. Electrical wave conduction and organizational properties obtained using automated wave tracking analysis of optical mapping recordings in whole perfused isolated atria. (A) Mean and maximum electrical conduction velocity (CV) (n = 5-7/group, t-test). (B) Mean and maximum perimeter-to-area (P/A) ratio of analysed electrical conduction waves (n = 5-7/group, t-test). * - p < 0.05, ** - p < 0.01*

Furthermore, we analysed the regional differences in the conduction velocity and the wavefront roughness between the atria of the diabetic and the control group. During the analysis, the atria were split into four zones of equal widths labelled I – IV across the long axis spreading from RA to LA (*Figure 4-15A*). Averaged mean CV and averaged maximum CV were significantly different in zone II (medial half of the RA) between the diabetic and control atria ($p = 0.04$ and $p = 0.007$ respectively) (*Figure 4-15B*). There was no significant difference in the averaged mean CV and averaged maximum CV between diabetic and control atria in other zones. The averaged mean P/A ratio (a measure of wavefront roughness) was significantly greater in the zone IV (lateral half of the LA) ($p = 0.01$) but was also greater in zone II ($p = 0.09$) and zone III ($p = 0.14$) (*Figure 4-15C*). Similarly, the averaged maximum P/A ratio was greater in zone II ($p = 0.06$) and zone III (medial part of the LA) ($p = 0.04$).

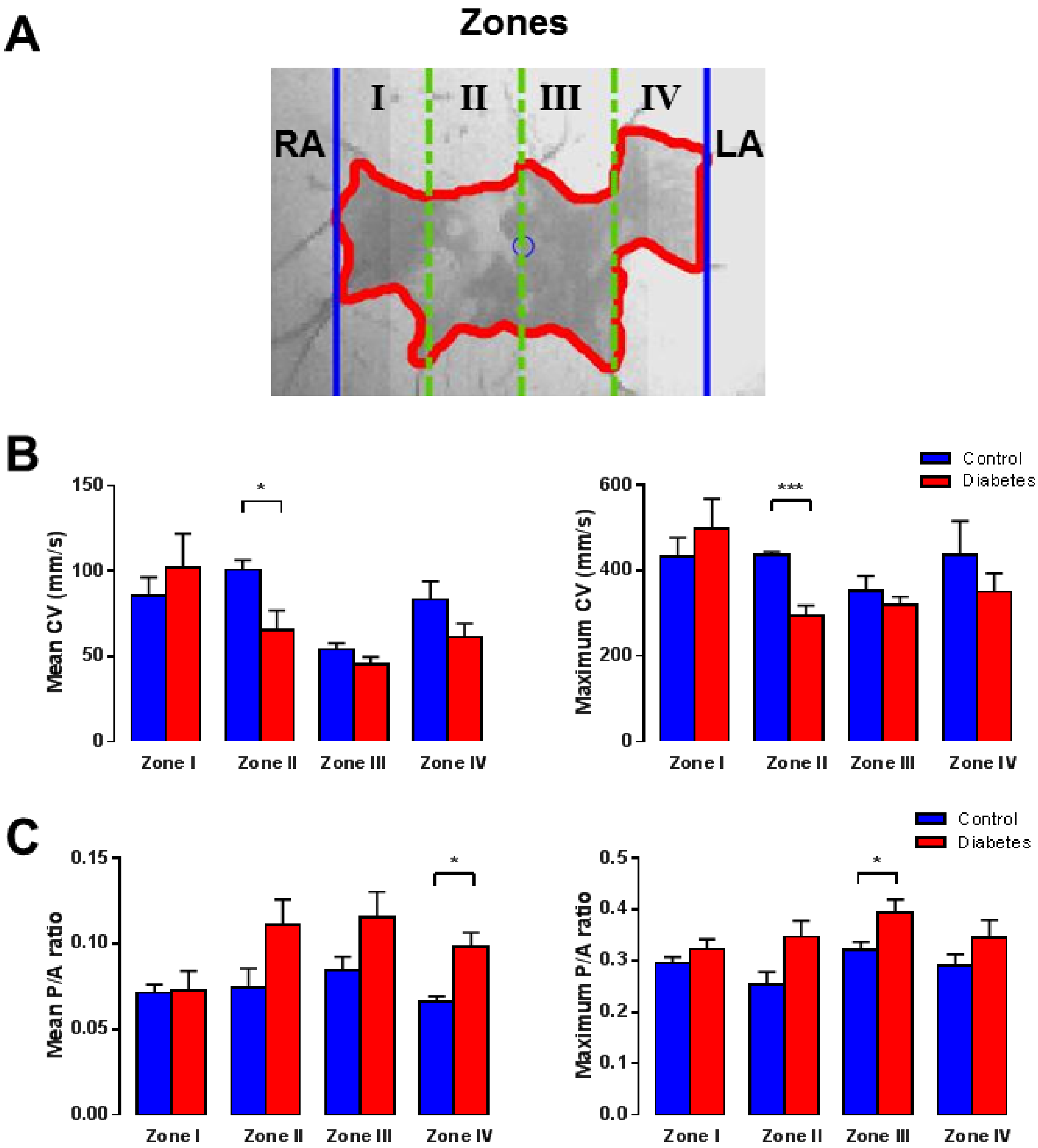

*Figure 4-15. Regional variation of electrical wave conduction and organizational properties obtained using automated wave tracking analysis of optical mapping recordings in whole perfused isolated atria. (A) Division of atria in four zones of equal width (1/4 of the whole width). (B) Mean and maximum electrical conduction velocity (CV) in different atrial zones (n = 5-7/group, t-test comparing each zone independently). (B) Mean and maximum perimeter-to-area (P/A) ratio of analysed electrical conduction waves in different atrial zones (n = 5-7/group, t-test comparing each zone independently). * - p < 0.05, *** - p < 0.001*

TOTAL COLLAGEN CONTENT OF RIGHT AND LEFT ATRIA

We measured the total mass of frozen RA and LA and there was no difference in atrial mass between the diabetic and control mice (*Figure 4-16*). Then we measured the total collagen content in different regions of atria (corresponding to results from the conduction velocity analysis) to quantify the amount of the connective tissue and to assess for any excess global tissue fibrosis. The total collagen content was significantly greater in zone II of diabetic atria compared to the control atria (p = 0.0002) (*Figure 4-17B*). The total collagen content in other regions was only slightly greater in diabetic mice compared to the control mice (the difference between the groups was not statistically significant in any other region).

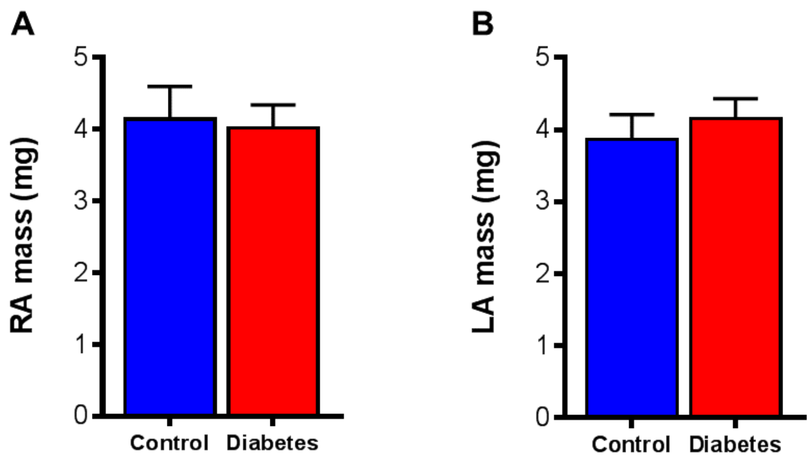

Figure 4-16. Mass of frozen (A) right atrium (RA) and (B) left atrium (LA) tissue after tissue collection. (n = 11-13/group, t-test).

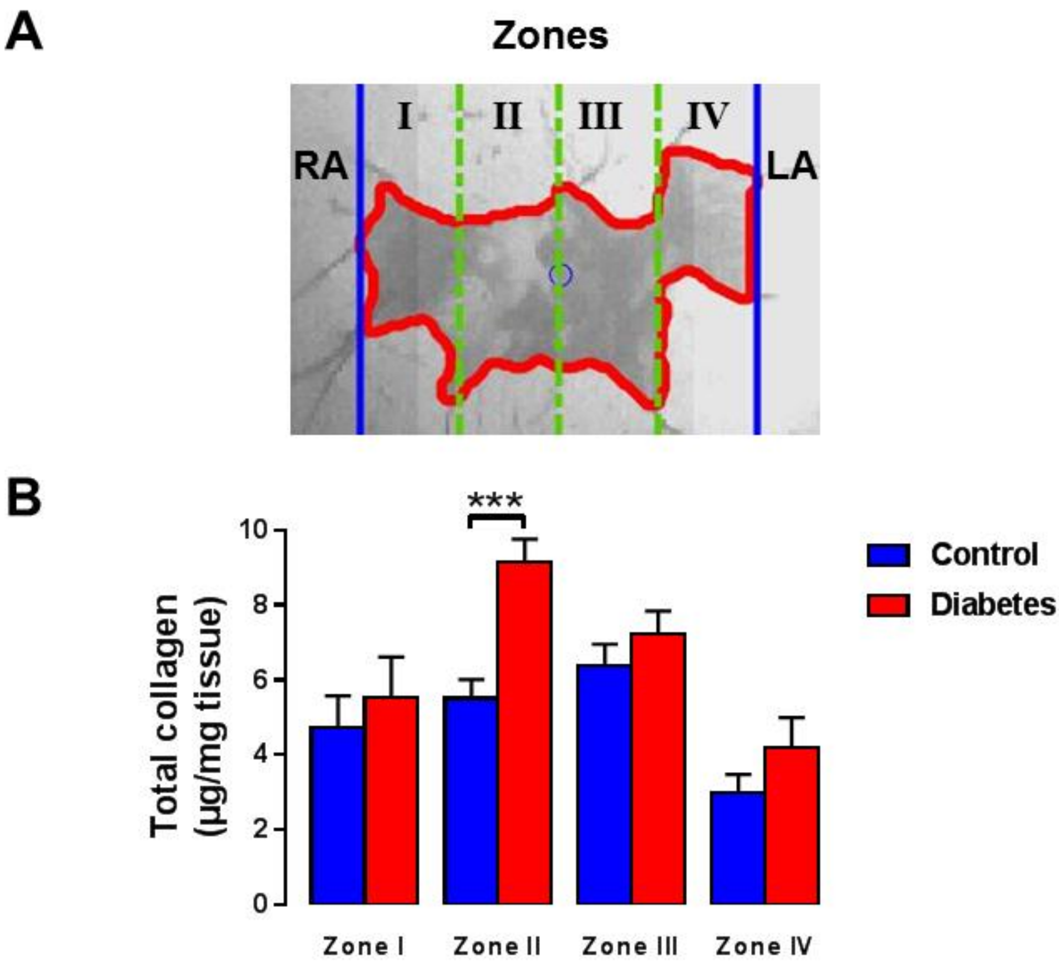

*Figure 4-17. Regional variation of total collagen content. (A) A representative image of how atria were divided into four zones of equal width for total collagen measurement. (B) The total collagen content in different regions of atria (n = 9-11/group, t-test). RA – right atrium, LA – left atrium, *** - p < 0.001*

Discussion

This is the first study that demonstrated an increased risk for *in vivo* pacing induced atrial arrhythmias in a diabetic animal model. Previously, it has been demonstrated that there is a higher rate of pacing induced atrial arrhythmias in isolated and Langendorff-perfused whole hearts of STZ-induced DM rats (97, 282), diabetic Goto-Kakizaki rats (125), and alloxan-induced DM rabbits (126), but it has not been demonstrated before that those electrophysiological characteristics can be reproduced *in vivo* as well.

Even though this study was designed to only measure the pacing induced atrial arrhythmias (not detecting any spontaneous arrhythmias), it is important to highlight that pacing induced AF in human patients have indistinguishable electrophysiological characteristics compared to the spontaneously initiated AF. This notion was explored in a study that enrolled 85 patients referred for ablation of paroxysmal AF where they compared the spatial distribution of atrial activation frequencies between spontaneously initiated AF and pacing-induced AF (283). The study reported no significant differences in the dominant frequency, the frequency gradient between RA and LA, the number of maximal frequency sites, and the spatial distribution of maximal dominant frequency sites between the pacing-induced AF and spontaneously initiated AF. Interestingly, the analysis in this study did not reveal any differences in those features between induced AF from rapid pacing from different sites (RA, coronary sinus, LA). Results of this study imply that pacing-induced atrial arrhythmias adequately reveal characteristic electrophysiological properties that are present in spontaneous AF.

Previous studies have shown that in *ex vivo* isolated and perfused hearts of rat model of STZ-induced DM there is an increased incidence of burst-pacing induced atrial arrhythmias compared to the control non-diabetic rats (97, 282). On the other hand, a study using a similar model of STZ-induced DM in rats did not find any difference in burst pacing induced atrial arrhythmias in isolated perfused hearts between the two groups but were able to elicit differences after either sympathetic or parasympathetic nerve stimulation (146). Diabetic rats in those studies had comparable plasma glucose levels (25-28 mM), which in turn are comparable to our mouse model of STZ-induced DM.

Similar findings of increased AF inducibility in isolated perfused diabetic hearts have been also demonstrated in the model of alloxan-induced DM in rabbits as well as in Goto-Kakizaki rats, which are genetic non-overweight model of type 2 DM with characteristic defects such as hyperinsulinemia, peripheral insulin resistance, impaired glucose-stimulated insulin secretion and hyperglycaemia (125, 126). All those results obtained from different models of DM and different species strongly suggest that an underlying pathological mechanism is intrinsic to diabetes rather than secondary to side effects and limitations of different animal diabetes models.

All the above-mentioned studies in diabetic animal models aim to enhance the understanding of the role of DM in patients. It has been known since the Framingham Heart Study that DM is one of the independent risk factors for developing AF (87). This epidemiological finding was further confirmed with several other studies and meta-analysis (88-91). However, the mechanism underlying this association is not known. There are only a few studies that looked into the potential electrophysiological mechanisms that could explain this connection.

One of the possible mechanisms of increased risk of AF in patients with DM is impaired electrical conduction within the atria. In our study, we found out that the PQ interval in the ECG recordings was significantly longer in the diabetic mice compared to the controls. In addition, our data suggest that also the P wave duration might be longer in diabetic mice. However, the difference was not statistically significant, likely due to greater relative variability of the measurements due to technical limitations of the recordings and inability to precisely determine the end of the P wave in the ECG trace. Even though it is known that abnormal atrial conduction assessed by surface ECG parameters such as P-wave duration and P-wave dispersion are predictors for AF (284, 285), the importance of the ECG parameters in patients with DM has not been studied in great detail. Still, findings from the published studies are generally in agreement with our results in diabetic mice. For example, a study with 426 participants found a positive correlation between fasting blood glucose levels and the PR interval (286). Also, a study comparing 88 T2DM patients with 49 case-matched controls found a prolonged P wave duration and greater P-wave dispersion in diabetic patients (287).

Another important finding of our study was that the diabetic mice have larger LA (relative to the heart size), modest LV diastolic dysfunction with no LV systolic dysfunction. The indexed cardiac chamber sizes were only normalized to either their own relative sizes (LA vs. LV) or to the body weight. A further improvement could be made by incorporating the size of the mouse by normalizing the sizes to either tibia length or mouth-to-anus length. In studies assessing the cardiac function in diabetic animal models, there is a lot of variability in the reported parameters. Comparing the echocardiographic results to the previous studies in diabetic animal models there is a lot of variability in reported cardiac function parameters. In particular, studies that used high dose STZ regimens in mice and rats report LV systolic and diastolic dysfunction (288-290). On the other hand, several studies report findings similar to our measurements where diabetic animals did not have any systolic dysfunction, but they had diastolic dysfunction as well as an enlarged LA (126, 289-291). All of those observations in diabetic animal models very well mirror with the established landmark findings of the diabetic cardiomyopathy in humans. Diabetic cardiomyopathy in humans starts with diastolic dysfunction followed by mild systolic dysfunction and LV hypertrophy, which over time results in severe systolic dysfunction and severe symptoms of heart failure (NYHA IV) (292, 293).

To better understand the underlying mechanism of increased inducibility of atrial arrhythmias in our diabetic mice model, we used the optical mapping of isolated perfused atrial preparations to directly measure some of the characteristic electrophysiological properties of the atria. One of the main electrophysiological characteristics is APD. In our study there was no difference in the APD in the isolated RA between diabetic and control atria, however, there was a small APD prolongation in the LA of diabetic mice. Results from other studies using diabetic animal models indicate that diabetic atria have longer APD. For example, in a study on isolated and perfused STZ-induced diabetic rat atria, there was a prolongation of the APD in all regions of the RA (no measurements were done on LA) (282). Furthermore, isolated atrial cardiomyocytes from alloxan-induced diabetic rabbit hearts also show APD prolongations when measured using whole-cell patch-clamp approach (126).

The next characteristic electrophysiological parameter that is very important in the maintenance of atrial fibrillation is tissue electrical conduction velocity. In our study, we assessed electrical conduction using a few different approaches. Using a simple measurement of the conduction time defined as the time needed for the activation signal to travel from sinoatrial node to the outer edge of the RA or LA we found out that the conduction in the LA was significantly prolonged in diabetic mice compared to the controls. On the other hand, there was no difference in the conduction time in the RA between the two groups. There was no difference in absolute length or total area of atria between the diabetic and control groups. This finding suggested that the conduction velocity was not diffusely and globally impaired in diabetic mice, but instead, there might be a focal conduction defect.

To detect localised conduction abnormalities in isolated atria, we used wavefront propagation analysis tool. This approach allowed us to measure the conduction velocity and the wavefront roughness in different parts of the atria. Using this approach we found out that the averaged (across the atria) mean and maximum conduction velocity was lower in diabetic atria compared to the controls. In addition, the wavefront's perimeter-to-area ratio was higher in diabetic atria indicating that the electrical conduction was less smooth in diabetic atria. Furthermore, the most intriguing findings of this analysis were obtained when we investigated the regional differences in electrical conduction. The most significant decrease in the electrical conduction velocity in diabetic atria occurred in the medial region of the RA – the area that contains the sinoatrial node as well as the inter-atrial bundles electrically connecting RA and LA. A decrease in the conduction velocity in this specific area explains the inter-atrial block, as well as the AV block, noted as prolongation in the surface ECG's PR interval.

Our findings corroborate the idea that diabetes causes pathological atrial remodelling. Our result of increased atrial conduction time to the edge of the LA is consistent with the observations in other diabetic animal models. The inter-atrial conduction time (measured with directly with electrodes placed in RA and LA in isolated and perfused hearts) was prolonged in the diabetic Goto-Kakizaki rats and alloxan-induced DM rabbits (125, 126). Furthermore, a study that used optical mapping to assess the atria also measured a decreased conduction velocity in STZ-induced DM rats (282). In addition, they noticed greater heterogeneity of conduction velocity vectors, however, they did not further quantify this observation. In contrast to our analysis, this study did not assess the anatomical localisation of any focal conduction defects.

The connection between diabetes and atrial conduction disorders is true not only for diabetic animal models but also exists in human patients with DM. In a study involving 228 patients undergoing catheter ablation procedure for paroxysmal AF investigators compared different electrophysiological characteristics between patients with and without type 2 DM (294). Patients with DM compared to the non-DM patient had increased total activation time in RA and LA and decreased bipolar voltage in RA and LA (both measured during the electrophysiological study). Patients with DM also had increased LA size and higher AF recurrence during the follow-up phase. In addition, a smaller study (110 participants) comparing patients with type 2 DM and their case-matched controls without DM also found that the intra-RA, intra-LA, and inter-atrial electromechanical delays were longer in the diabetes group (295).

Furthermore, a recent study provided a more detailed insight into the presence of atrial conduction disorders by using the high-resolution epicardial mapping of atria in 164 patients undergoing open-chest cardiac surgery (296). The key finding of their study was that premature ectopic atrial beat results in significantly more conduction abnormalities (defined as the sum of the number of conduction delays and conduction blocks detected in epicardial mapping) compared to the beats during the regular sinus rhythm. This aberrant conduction was present in an even greater degree in patients with diabetes mellitus (OR = 2.5) and patients with LA dilatation (OR = 4.6), while on the other hand variables such as age above 76 years, hypertension, and hypercholesterolemia were not associated with a greater degree of conduction abnormalities. Importantly, diabetes mellitus resulted in a greater degree of atrial conduction abnormalities even during the normal sinus rhythm conduction pattern (OR = 3.2). The outcomes of this study support the notion that diabetes mellitus alone causes a significant atrial remodelling and in particular affects the normal electrical conduction patterns.

Multiple pathological biochemical processes have been implicated in the diabetes mellitus related atrial remodelling, however, the relative importance of each of those mechanisms have not been fully elucidated. The first and presumed main mechanism in the relationship between DM and AF is increased interstitial atrial fibrosis. Results in our diabetic model suggest that the localised rather than the global fibrosis might be the culprit in the DM-related AF. Only the region in the medial RA of diabetic mice had a significant increase in the total collagen content compared to the control mice. Importantly, the fibrosis in this medial RA region corresponds well to a significant decrease in the measured regional CV in diabetic atria. This provides integrated physiological evidence of why diabetic atria are more prone to pacing-induced AF. Several previous studies have measured the interstitial fibrosis in diabetic myocardium, however, none of them looked at the regional variability of the fibrosis. For example, studies using GK rats, alloxan-induced DM in rabbits, and STZ-induced DM in rats have all reported an increased atrial interstitial fibrosis (97, 125, 126, 282, 297, 298). Similar results of increased interstitial fibrosis have also been obtained in human right atrial appendage tissues of type 2 DM patients undergoing CABG surgery (299). Our results on regional fibrosis raise an interesting question: is fibrosis in a critical area resulting in a focal conduction defect more important than global diffuse interstitial fibrosis? Our results suggest that a focal conduction defect as a result of the fibrosis in the medial region of the RA is sufficient to make the atria more prone for AF.

Other mechanisms, apart from fibrosis, have also been implicated in the pathogenesis of DM-related AF. Electrical remodelling, autonomic remodelling, oxidative stress, and derailed cardiac metabolism have all been proposed and investigated as the potential culprits in the pathogenesis of diabetes-related AF (139, 140), however, we have not explored them in this study.

In conclusion, the main finding of this part of the study is that *in vivo* the diabetes mellitus causes atrial dysfunction in mice making them more prone for AF. Our animal model of DM also recapitulates several landmark findings of human diabetic cardiomyopathy. This particular animal model, therefore, has great potential for testing new therapeutical interventions targeting diabetes-induced arrhythmias and other cardiac dysfunctions. Furthermore, our experiments exploring the underlying pathological mechanisms demonstrate that localized atrial fibrosis in a critical area causes a focal conduction defect, which is sufficient to make the atria more prone to AF. Future research is needed to explore the exact mechanisms involved in diabetes mediated dysfunction in atria. In particular, future experimental work might focus on regional changes in cell type distribution as well as regional-specific modulations of ion channels, metabolic alterations and other characteristic signalling pathways.

CHAPTER 5:

The effect of increased levels of tetrahydrobiopterin on atrial electrophysiology and potential role in the treatment of diabetes-induced atrial fibrillation BH4 electrophysiology

Introduction

Nitric oxide synthase (NOS) and NO are involved in multiple signalling and regulatory pathways in various tissues, including the cardiac tissue. The role of constitutive NO production in myocardial calcium handling and excitation-contraction coupling, both in physiological conditions and in disease states, is well established (300). On the other hand, the precise role of NOS on atrial electrophysiology has yet to be studied in greater detail. Studies, so far, have demonstrated that a decrease in the NO signalling results in shorter action potential duration (APD), increase in I_{to}, I_{Kur} and I_{K1} currents, and a decrease in the late Na^+ current (178, 187, 188). Furthermore, NO also modulates Ca^{2+} handling proteins, for example, an increase in the NOS activity results in a decreased Ca^{2+} current density, faster Ca^{2+} transient decay but no changes in SR Ca^{2+} load or Ca^{2+} transient amplitude (185). In addition, NO also increases the S-nitrosylation of the ryanodine receptors (RyR) and phospholamban phosphorylation (PLB) resulting in increased Ca^{2+} diastolic leak (184, 185, 301). However, it is unknown what kind of *in vivo* electrophysiological phenotype results from all those changes at the cellular level.

Tetrahydrobiopterin (BH4) is an essential cofactor of for several aromatic amino acid hydroxylases, alkylglycerol monooxygenases, and, importantly, NOS (192, 193). Interestingly, increased concentration of BH4 increases the activity of NOS thus making it a useful agent to modulate NO signalling pathways. Multiple studies reported that increased BH4 levels improve endothelial dysfunction, improve diastolic dysfunction in an animal model of hypertension, reduce myocardial fibrosis in a model of left ventricular (LV) pressure overload by suppressing the immune response, and (as presented in the previous chapter) improve myocardial energetics in a diabetic animal model (198, 200-202, 212, 213, 220, 221). In addition, the BH4 is already regularly used for the treatment of phenylketonuria (a genetic metabolic disease) in clinical practice making it even more appealing as a potential treatment, as it has already passed the rigorous drug safety trials (302).

The aim of this part of our study was to explore the electrophysiological changes in mice with high levels of intra-myocardial BH4 and to test whether the oral BH4 supplementation can reduce the probability of pacing-induced AF and improve the diastolic dysfunction in diabetic mice.

Methods

All methods are described in greater detail in the general methods chapter.

ANIMAL MODELS

In experiments investigating the effects of increased myocardial BH4 levels, we used a genetically modified mouse strain with a myocardial specific overexpression of the human GTP cyclohydrolase 1 gene (mGCH1-Tg), which was created in our Department at the University of Oxford (185). Experiments investigating the oral BH4 supplementation were performed on the males of the C57BL/6JOlaHsd strain purchased directly from Envigo (main United Kingdom distributor of animal models). Mice were housed in individually ventilated cages in a temperature-controlled environment (20-22°C) with a 12-hour light-dark cycle. Mice had ad libitum access to food and water. Sentinel animals were kept in the same racks and regularly underwent health monitoring to ensure and confirm specific pathogen-free environment.

All animal procedures were performed in accordance with the United Kingdom Home Office Animals (Scientific Procedures) Act of 1986. They were carried out under the authority of the project licence number PPL 30/2804 (project licence holder: Prof Barbara Casadei) until 25.1.2016, and after this date, under PPL 30/3374 (project licence holder: Dr Ricardo Carnicer Hijazo).

STREPTOZOTOCIN INDUCED DIABETES MELLITUS

Males, aged 12-14 weeks, received intraperitoneal injections of low-dose streptozotocin (STZ) (50 mg/kg) or intraperitoneal injections of vehicle (citrate buffer) over five consecutive days. During the study, mouse body weight (BW) and plasma glucose levels were regularly monitored. Mice used for the BH4 supplementation study had their diet changed (BH4 supplemented cookies or placebo cookies) after 6 weeks of diabetes (*Figure 5-1*). The BH4-supplemented diet was prepared by mixing rodent diet mash (Teklad global 16% protein diet, Harlan Laboratories) with BH4 (Schirks Laboratories) in a ratio to achieve an estimated daily BH4 dose 200 mg/kg. After 12 weeks of the last injection, cardiac function was assessed non-invasively using echocardiography. Two days later, all mice underwent transoesophageal atrial pacing study. After the pacing experiments mice were either immediately sacrificed to collect tissue or recovered and sacrificed three to five days later for optical mapping of isolated atria.

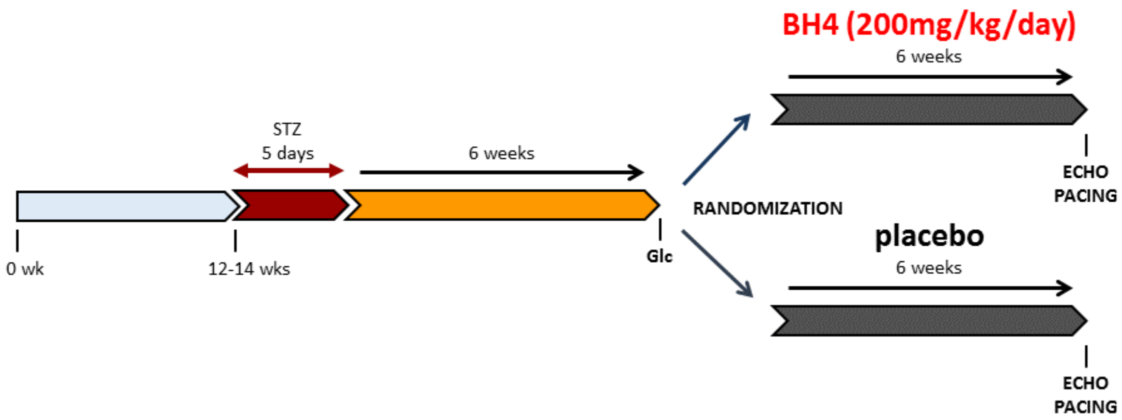

Figure 5-1. A timeline of the BH4 supplementation study in diabetic mice protocol. STZ – streptozotocin, BH4 – tetrahydrobiopterin, Glc – glucose.

ECHOCARDIOGRAPHY IN MICE

Echocardiography was performed using a Vevo 2100 (VisualSonics) ultrasound imaging system with an ultra-high frequency MS400 cardiovascular transducer (18-38 MHz) under the isoflurane general anaesthesia (1.0-2.0% isoflurane). LV diastolic function was assessed by tissue Doppler imaging (TDI) and mitral valve flow parameters recorded with the pulsed-wave Doppler mode. Left atrial (LA) size was measured from the LA recordings from the apical 4-chamber view at the end of LV systole – at the point of largest LA size.

IN VIVO ATRIAL ELECTROPHYSIOLOGY IN MICE

Electrocardiogram recordings and transoesophageal atrial pacing were performed under isoflurane general anaesthesia (1.5-2.0% isoflurane), as previously described (236, 237). (12, 13). Surface electrocardiogram (ECG) was obtained by placing electrodes subcutaneously in all four limbs. Afterwards, an octapolar electrophysiological catheter (NuMED CIBER mouse electrophysiology catheter) was introduced on the oesophagus and used to pace the atria. Burst atrial pacing with reduced cycle length (CL) periods was used to measure the inducibility of atrial arrhythmias. Atrial arrhythmias were defined as an induced episode of irregular atrial rhythm lasting longer than 2 seconds. The number of arrhythmic episodes and their duration were measured. Afterwards, the additional electrophysiological parameters such as sinus-node recovery time (SNRT), Wenckebach cycle length, and AV node effective refractory period (AV ERP) were measured. The analysis of the heart rate variability (HRV) was performed on the long (5 minutes) uninterrupted baseline ECG recording of the anaesthetised mice. We compared the standard deviation (SD) of the RR intervals and the SD of ΔRR intervals between the groups.

MOLECULAR BIOLOGY MEASUREMENTS

The concentration of tetrahydrobiopterin (BH4), dihydrobiopterin (BH2) and biopterin (B) in the tissue samples were measured using the high-performance liquid chromatography (HPLC) method as detailed here (185, 248). Nitric oxide synthase (NOS) activity was measured by quantifying the conversion rate of the radioactively labelled arginine to the citrulline using the continuous flow liquid scintillation detector (Lablogic β-RAM Model 3) recording of HPLC separated compounds.

OPTICAL MAPPING OF ISOLATED ATRIA

Mouse atria were isolated, superfused in Tyrode solution, and pinned to the Sylgard-coated petri dish in orientation to make crista terminalis and interatrial septum visible. Atria were then incubated with the voltage-sensitive dye di-4-ANNEPS (20 µM) for 30 minutes at 37°C. Afterwards, the atria were superfused with Krebs solution containing

5 µM blebbistatin to prevent motion artefacts. To inhibit (predominantly) nNOS activity we incubated atria with 10µM N-[(4S)-4-Amino-5-[(2-aminoethyl](amino]pentyl]-N'-nitroguanidine (AAAN) for 20 min (and then continuously throughout the experiment) before starting any optical mapping recordings. Images of atria were acquired by a high-speed CMOS camera (NeuroCMOS-DW128-II, Cairn Research) at 1000 frames/s using the GView optical mapping software (courtesy of Professor Gil Bub, University of Oxford). Optical action potential duration (APD) and conduction velocity were obtained from the analysis of the recordings using a custom-made analysis program written in MATLAB (*full source code in Appendix*).

STATISTICS

All parametric data are expressed as mean ± standard error of the mean (SEM) and non-parametric data as median ± interquartile range (IQR). Statistical comparisons were made using unpaired Student's t-test, Mann-Whitney u-test, or one-way analysis of variance (ANOVA) with Bonferroni's post hoc test, as appropriate (the type of test is included in each figure legend).

Results

MYOCARDIAL GCH1 OVEREXPRESSION INCREASES THE ATRIAL BH4 CONCENTRATION AND INCREASES THE MYOCARDIAL NOS ACTIVITY

Firstly we measured the biopterin levels of mGCH1-Tg mice in atria. Compared to the wild-type (WT) mice, the mGCH1-Tg atria had a 50-fold increase in the total biopterin concentration ($p < 0.0001$) (*Figure 5-2 A-B*). All forms – tetrahydrobiopterin (BH4), dihydrobiopterin (BH2), and oxidised biopterin (B) – were increased in similar proportion. The ratio of reduced BH4 compared to oxidised forms (BH2 + B) was slightly, but not significantly, decreased (*Figure 5-2C*). The increase in the myocardial BH4 levels resulted in a 2-fold increase in total NOS activity ($p < 0.001$) (*Figure 5-2D*).

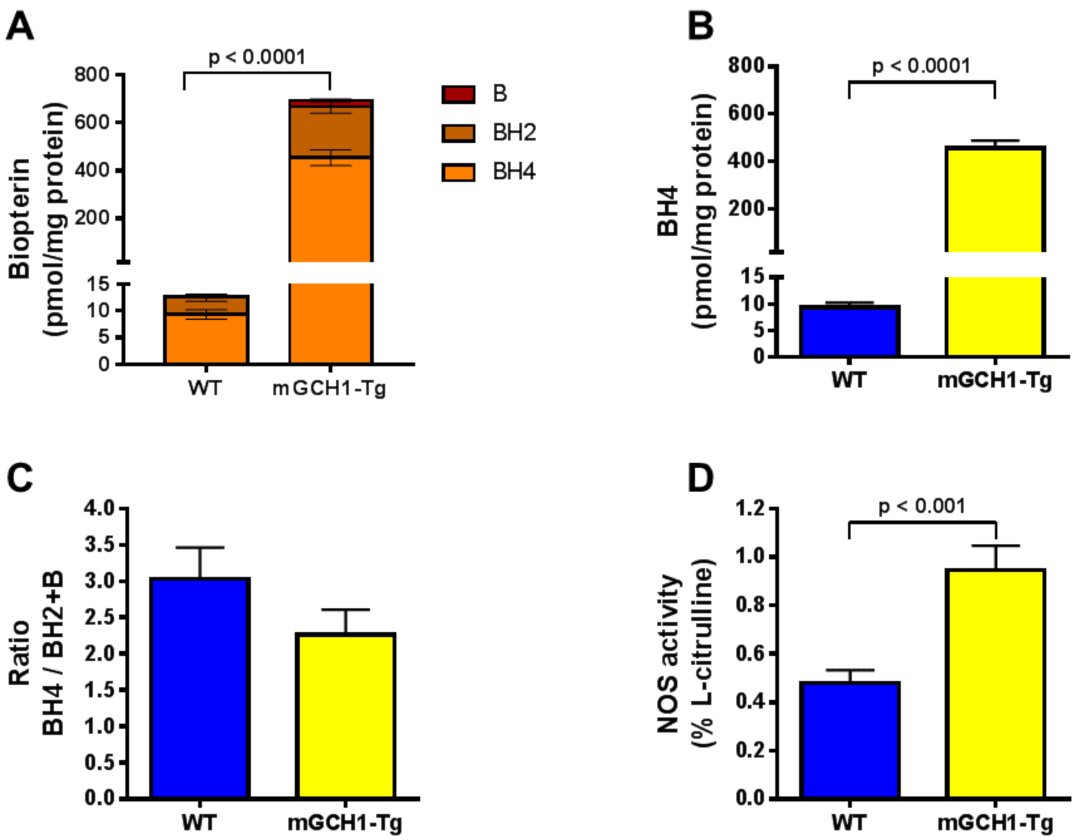

Figure 5-2. Myocardial overexpression of GCH1 results in an increase in the tetrahydrobiopterin (BH4) concentration in atria and in an increase in the NOS activity. (A) Levels of all detected biopterin forms in atria as measured by HPLC (n=11-14, t-test for total biopterin levels, p<0.0001). (B) Tetrahydrobiopterin (BH4) concentration in atria measured by HPLC (n=11-14 atria/group, t-test, p<0.0001). (C) Ratio of BH4 to dihydrobiopterin (BH2) and biopterin (B) (n=11-14 atria/group, t-test, p=0.25). (D) Total NOS activity in myocardium measured using radiochemical detection of L-arginine to L-citrulline conversion (n=7-8 hearts/group, t-test, p<0.001). B – biopterin, BH2 – dihydrobiopterin, BH4 – tetrahydrobiopterin.

MICE WITH MYOCARDIAL GCH1 OVEREXPRESSION HAVE SLOWER HEART RATE AND LONGER QT INTERVAL

We assessed the basic electrophysiological profile of mGCH1-Tg mice by measuring the ECG intervals. The mGCH1-Tg mice had a significantly lower heart rate as indicated by longer RR interval ($p < 0.01$) compared to the WT mice. The mGCH1-Tg mice also had a longer QT interval ($p < 0.01$), and a longer QT interval corrected for the heart rate using the Bazett's formula ($p < 0.05$). The QRS interval in the mGCH1-Tg was almost 10% longer compared to the WT mice, but this difference was not statistically significant ($p = 0.16$). The P wave duration and PQ interval were not different between the two groups.

ECG intervals	***WT (n = 11)***	***mGCH1-Tg (n = 19)***	***p-value***
RR (ms)	130.8 ± 4.2	144.9 ± 2.8	**0.008 ****
P wave duration (ms)	20.4 ± 1.2	21.0 ± 0.6	0.64
PQ (ms)	38.7 ± 0.7	38.0 ± 1.4	0.74
QRS (ms)	18.1 ± 0.8	19.8 ± 0.8	0.16
QT (ms)	58.5 ± 2.7	68.8 ± 2.3	**0.009 ****
QTc (ms)	56.0 ± 2.1	62.5 ± 1.8	**0.03 ***

*Table 5-1. Electrophysiological properties of anaesthetized mice with myocardial GCH1 overexpression (mGCH1-Tg) compared to the wild-type (WT) littermates (n = 11-19/group, t-test, all values are mean ± SEM), QTc – QT interval corrected for the RR interval using the Bazett's formula, * - p<0.05, ** - p<0.01.*

As both the RR interval and the QT interval were longer in the mGCH1-Tg mice (*Figure 5-3*) we explored whether the measured prolongation in the QT interval was independent of the elongated RR interval. As routinely used in humans, the studies in mice report the corrected QT interval using a simple mathematical correction such as Bazett's correction (303). However, the use of this correction formula has been heavily criticised as being inaccurate (304, 305). Furthermore, it is also unknown whether a similar QT-RR relationship even exists in mice (306, 307).

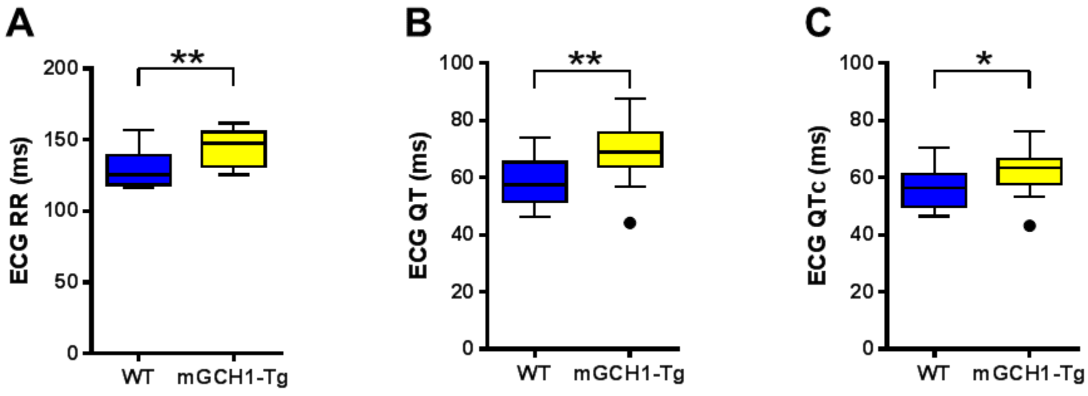

*Figure 5-3. Comparison of the (A) RR interval, (B) QT interval, and (C) the QT interval corrected for the RR interval using the Bazett's formula (QTc) of the mice with myocardial GCH1 overexpression (mGCH1-Tg) compared to the wild-type (WT) littermates (n = 11-19/group, t-test). * - p<0.05, ** - p<0.01*

Our measurements of averaged QT interval plotted against averaged RR interval indicate that there is a significant positive correlation between the intervals for both groups: mGCH1-Tg and WT controls (*Figure 5-4A*). In our measurements, the simple Bazett's formula corrected the QT-RR relationship to the extent that the linear correlations were not significantly different from the zero-line for both groups (*Figure 5-4B*). Importantly, the QT-RR regression line of the mGCH1-Tg mice was above the regression line of the WT control group regardless of whether the correction was used or not. The QT interval of the mGCH1-Tg mice is thus longer independently of the RR interval elongation.

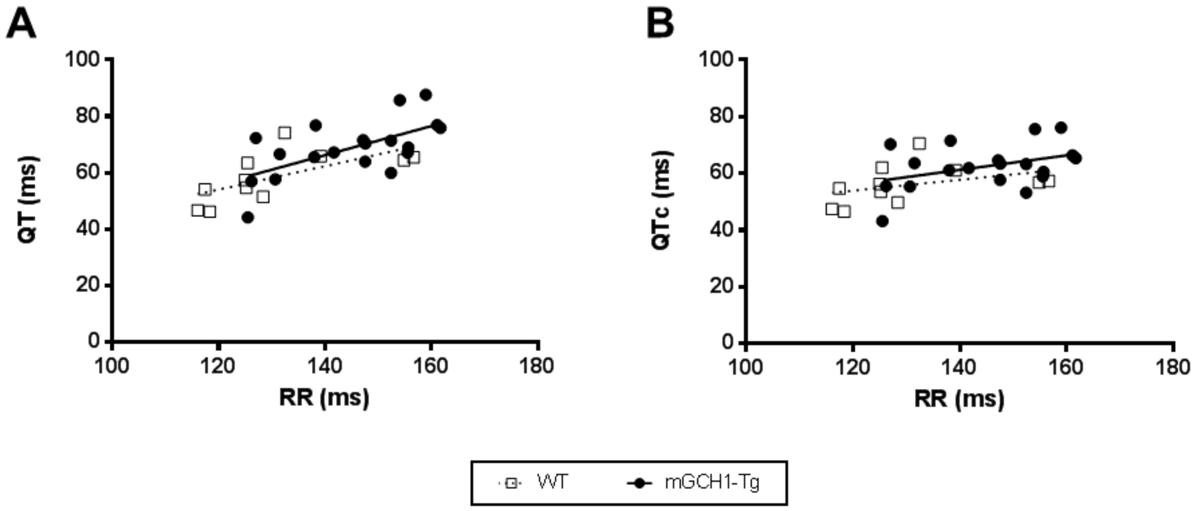

Figure 5-4. (A) Comparison of the uncorrected QT interval and the corresponding RR interval between the mice with myocardial specific over-expression of GCH1 (mGCH1-Tg) and their wild-type (WT) controls. The linear correlation between QT and RR was significantly non-zero for both groups (mGCH1-Tg p = 0.004, WT p = 0.03). (B) Comparison of the Bazett's formula corrected QT interval (QTc) and the corresponding RR interval between the mGCH1-Tg and WT mice. The linear correlation between QT and RR was not significantly non-zero for both groups (mGCH1-Tg p = 0.09, WT p = 0.25).

MICE WITH MYOCARDIAL GCH1 OVEREXPRESSION HAVE FREQUENT EPISODES OF AV NODAL ESCAPE RHYTHM

I annotated all arrhythmias and other ECG abnormalities during the electrophysiological recording of anaesthetised mice (*Figure 5-5*). The main difference was the increase in the frequency of the AV nodal escape rhythm in mGCH1-Tg mice when comparted to WT mice. This arrhythmia was recorded in 64% of mGCH1-Tg and only in 9% of the WT littermates (p = 0.01). There was no difference in the frequency of premature ventricular contractions (PVC) between the two groups. Ventricular tachycardia (VT) was not observed in any of the WT mice. On the other hand, one mouse from the mGCH1-Tg group had several episodes of non-sustained VT, however, the overall difference between the groups was not statistically significant.

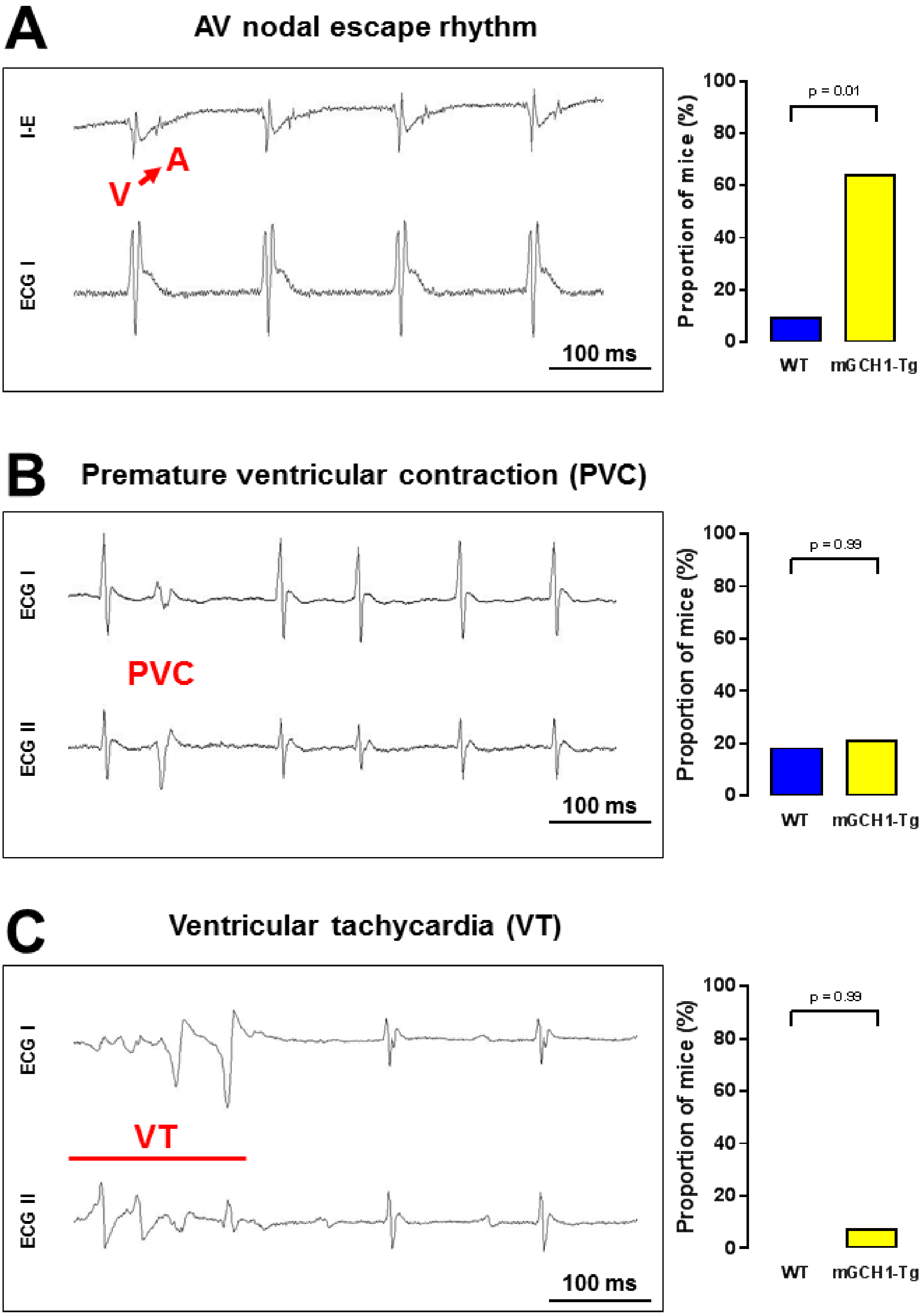

Figure 5-5. (A) An example of spontaneous AV nodal rhythm recording in mice with an intra-oesophageal (I-E) electrogram demonstrating retrograde ventricular (V) to atrial (A) electrical propagation. AV nodal escape rhythm was more frequent in mice with myocardial specific over-expression of GCH1 (mGCH1-Tg) compared to their wild-type (WT) controls (n = 11-14/group, Fisher's exact test). (B) An ECG example of premature ventricular contraction (PVC) in mice. There was no difference in the proportion of mice with at least one PVC between mGCH1-Tg and WT controls (n = 11-14/group, Fisher's exact test). (C) An ECG example of non-sustained ventricular tachycardia (VT) in mice. VT was defined as three or more consecutive beats arising from the ventricle. One mouse in the mGCH1-Tg group had several episodes of non-sustained VT. VT was not observed in any of the WT mice.

MICE WITH MYOCARDIAL GCH1 OVEREXPRESSION DO NOT HAVE HIGHER PROBABILITY OF PACING INDUCED ATRIAL ARRHYTHMIAS

There was no significant difference in the inducibility of atrial arrhythmias between WT and mGCH1-Tg mice. The proportion of mice that had at least one episode of burst-pacing induced atrial arrhythmia was not different between the mGCH1-Tg and WT group (57% vs 55%, p = 0.99, n = 11-14/group) (*Figure 5-6A*). Similarly, the median probability of pacing-induced arrhythmias (quantified as the proportion of burst pacing episodes resulting in atrial arrhythmia) was not significantly different between the genotypes (median 2.0% vs 1.3, p = 0.33, n = 11-14/group) (*Figure 5-6B*). However, the variability in the probability of pacing-induced arrhythmias between the individual mice was significantly greater in the mGCH1-Tg group (IQR 19% vs 3%, p = 0.04, n = 11-14/group, Brown-Forsythe test). On the other hand, the mean duration of pacing-induced atrial arrhythmias tended to be shorter in the mGCH1-Tg group compared to the WT littermates (5±11 s vs 17±22 s [median ± IQR], p = 0.09, n = 11-14/group) (*Figure 5-6C*).

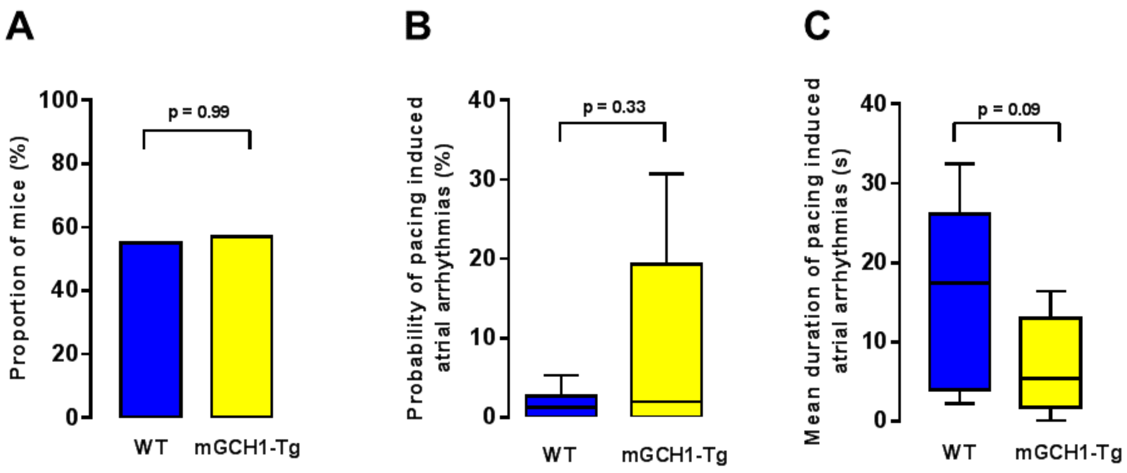

Figure 5-6. (A) The proportion of mice that had at least one pacing inducible episode of atrial arrhythmia (n = 11-14/group, Fisher's exact test). (B) Probability of pacing-induced atrial arrhythmias (n = 11-14/group, Mann-Whitney test). (C) Mean duration of pacing-induced atrial arrhythmias (n = 11-14/group, Mann-Whitney test).

MICE WITH MYOCARDIAL GCH1 OVEREXPRESSION HAVE SLOWER AV NODE CONDUCTION

We measured additional atrial electrophysiological properties such as SNRT, Wenckebach cycle length, AVERP, and HRV parameters. The main finding was that the Wenckebach cycle length was significantly higher in the mGCH1-Tg mice (83±2 ms vs. 76±2 ms in WT, p = 0.02) (*Table 5-2*) increasing the likelihood for the AV block. There were no differences in the SNRT and AVERP between the mGCH1-Tg and WT mice.

Atrial EP parameters	***WT*** ***(n = 8)***	***mGCH1-Tg*** ***(n = 9)***	***p-value***
SNRT (ms)	39 ± 11	35 ± 6	0.74
WAVB (ms)	76 ± 2	83 ± 2	**0.02 ***
AVERP (ms)	46 ± 2	48 ± 5	0.69

*Table 5-2. In vivo atrial electrophysiological characteristics of wild-type mice (WT) and mice with myocardial specific GCH1 overexpression (mGCH1-Tg) mice (n=8-9 mice/group, t-test, all values are mean ± SEM). SNRT – sinus node recovery time, WAVB – Wenckebach AV block cycle length, AVERP – combined atrial and AV node effective refractory period, * - p < 0.05.*

Additionally, we measured HRV (during the sinus rhythm), which primarily depends on the balance of the parasympathetic and sympathetic autonomic nervous system. There were no differences in the distribution of the individual RR intervals between the mGCH1-Tg and WT groups measured as SD of all individual RR intervals in the long baseline ECG recording (2.2±2.5 ms vs. 2.6±1.6 ms, p = 0.97) (*Figure 5-7A*). There were also no differences in the distribution of individual beat-to-beat differences measured as SD of all ΔRR intervals in the long baseline ECG recording between the mGCH1-Tg and WT groups (2.2±1.3 ms vs. 3.2±2.3 ms, p = 0.38) (*Figure 5-7B*).

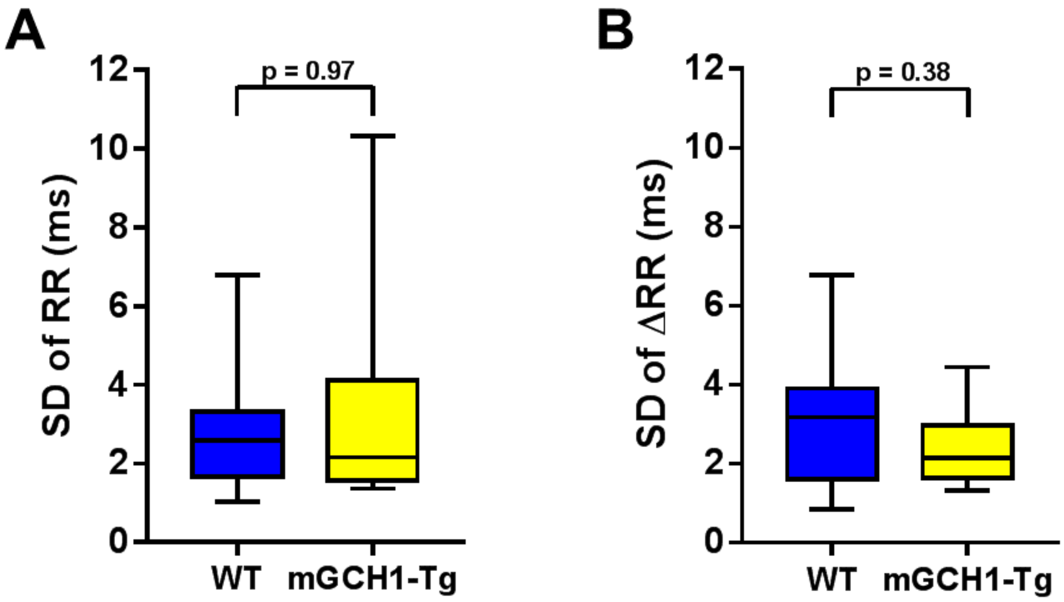

Figure 5-7. Heart rate variability (HRV) analysis of the long baseline ECG recording comparing wild-type mice (WT) and mice with myocardial specific GCH1 overexpression (mGCH1-Tg). (A) Standard deviation (SD) of all the individual RR intervals per mouse (n = 9-12/group, Mann-Whitney test). (B) Standard deviation (SD) of all the differences between individual RR (ΔRR) intervals per mouse (n = 9-12/group, Mann-Whitney test).

MICE WITH MYOCARDIAL GCH1 OVEREXPRESSION HAVE LONGER ACTION POTENTIAL DURATION AND SLOWER CONDUCTION VELOCITY

Mice with overexpression of GCH1 and high myocardial BH4 levels had a distinct *in vivo* electrophysiological phenotype. The mGCH1-Tg mice had a slower heart rate, prolonged QT interval, slowed AV node conduction, and they had spontaneous episodes of AV nodal escape rhythm. In order to explore the electrophysiological characteristics of mGCH1-Tg atria in greater detail, I used optical mapping of isolated perfused atrial preparations and assessed the action potential and conduction properties.

We measured the action potential duration (APD) separately for the right atrium (RA) and left atrium (LA). In both atria, the APD was longer in the mGCH1-Tg compared to the WT littermates (*Figure 5-8*). The difference in the APD between the genotypes was most pronounced at the APD30 interval in both the RA (10.0±0.4 ms vs. 7.9±0.3 ms in WT, p = 0.0003) and the LA (11.0±0.7 ms vs. 8.9±0.4 ms in WT, p = 0.006).

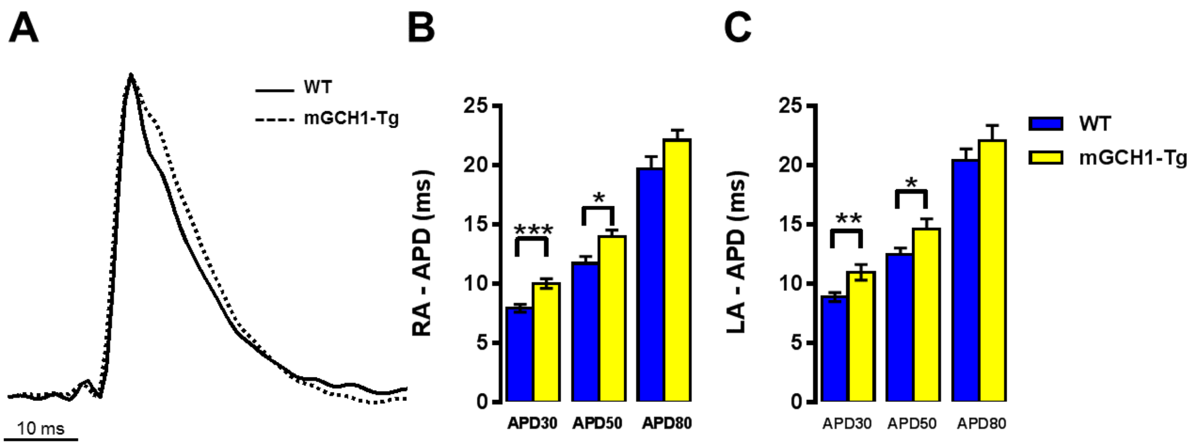

Figure 5-8. (A) Representative optical mapping recording of an action potential in isolated mouse atria of wild-types (WT) and mice with myocardial specific GCH1 overexpression (mGCH1-Tg). (B) Right atrial (RA) action potential duration is longer in mGCH1-Tg isolated atria compared to WT atria (n=18-21/group, t-test, p_{APD30}=0.0003, p_{APD50}=0.01, p_{APD80}=0.09). (C) Left atrial (LA) action potential duration is longer in mGCH1-Tg isolated atria compared to WT atria (n=18-21/group, t-test, p_{APD30}=0.007, p_{APD50}=0.04, p_{APD80}=0.29).

We also measured the atrial tissue APD in RA and LA in the presence (or absence) of nNOS inhibitor (AAAN). In the RA, there was a significant interaction between the mouse genotype and the nNOS inhibition (*Figure 5-9*). The nNOS inhibition in the mGCH1-Tg atria tended to reduce the APD compared to the control mGCH1-Tg atria whereas APD tended to increase in WT atria in response to AAAN. We did not measure the effect of AAAN on the NOS activity in the atrial tissue.

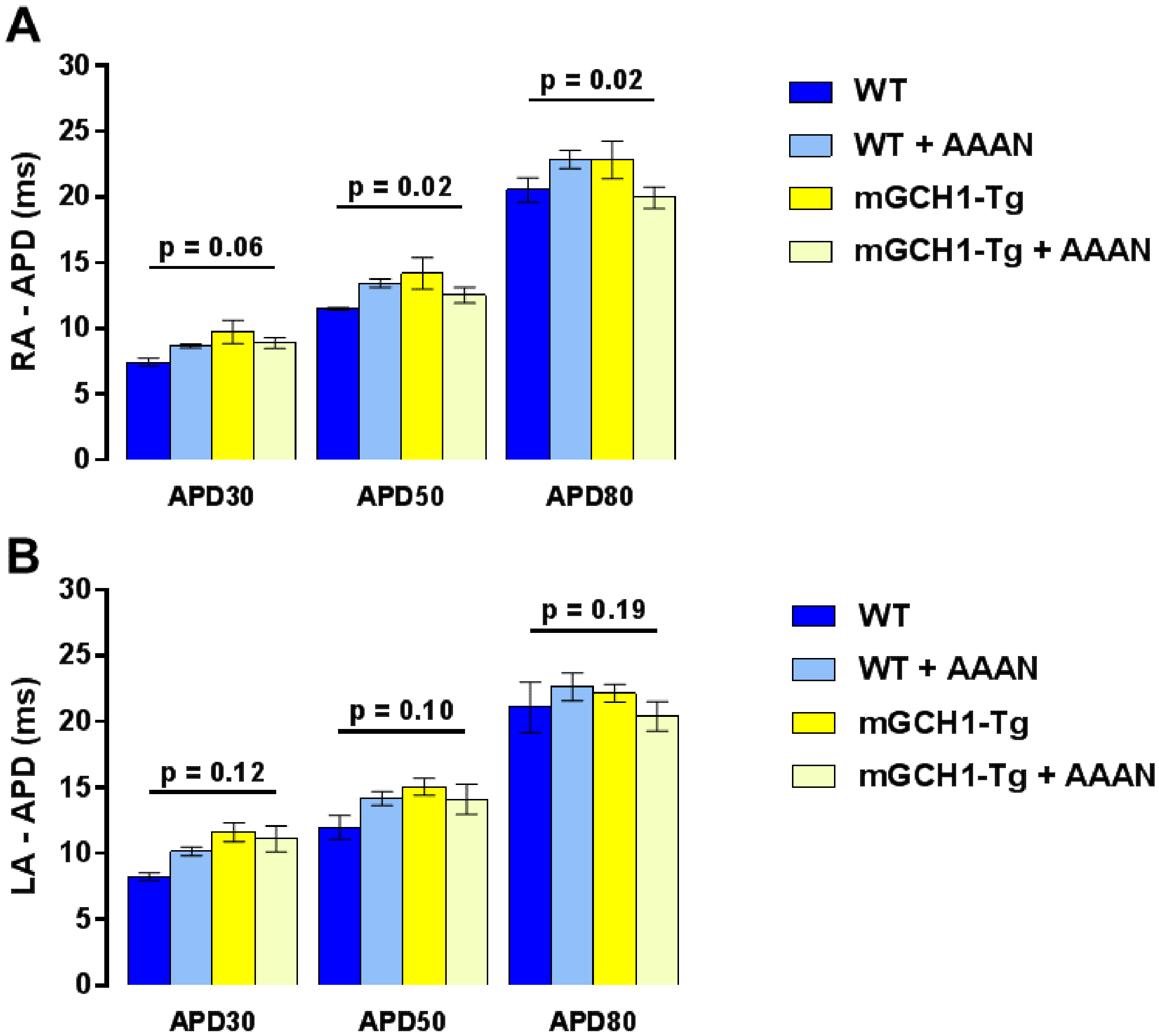

Figure 5-9. (A) Right atrial (RA) action potential duration (APD) in wild-type (WT) mice and mice with myocardial specific GCH1 overexpression (mGCH1-Tg) with or without the N-[(4S)-4-Amino-5-[(2-aminoethyl](amino]pentyl]-N'-nitroguanidine (AAAN – nNOS inhibitor) (n = 4-6/group, two-way ANOVA, p-value for the interaction between the genotype and the NOS inhibition). (B) Left atrial (LA) APD in WT and mGCH1-Tg mice with or without the AAAN (nNOS inhibitor) (n = 4-6/group, two-way ANOVA, the p-value is the interaction between the genotype and nNOS inhibition).

I measured the global conduction speed by measuring the time needed for electrical activation of spontaneously beating atria to reach the outermost edge of either RA or LA. The conduction time to the RA and LA was assessed by creating the activation maps of spontaneous electrical beats (*Figure 5-10*). The conduction time to the edge of the RA was 36% longer in the mGCH1-Tg group compared to the WT group (20±4 ms vs. 15±2 ms, p = 0.23) (*Figure 5-11A*). An even greater difference was observed in the conduction time to the edge of the LA (*Figure 5-11B*), where the conduction time was 52% longer (35±3 ms vs. 23±3 ms, p = 0.01). As there was no difference in the size of atria between the two groups, I can conclude that the average global electrical conduction velocity was lower in the mGCH1-Tg groups. Furthermore, the conduction time was relatively uniformly prolonged in both the RA and LA, suggesting a globally diffused underlying change.

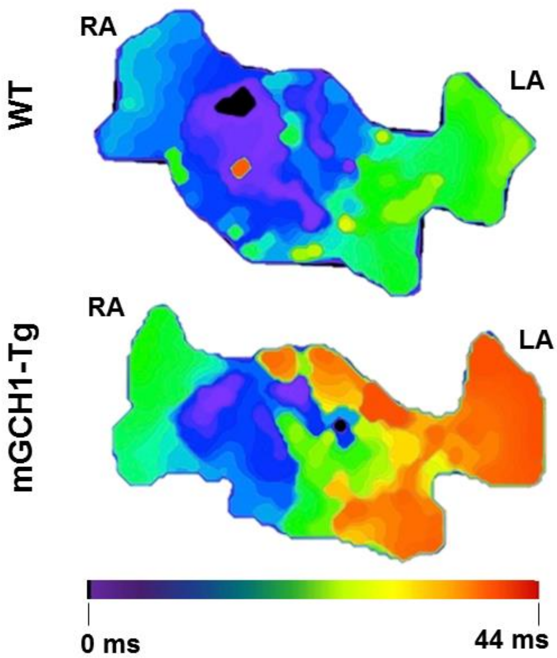

Figure 5-10. (A) A representative activation map of the isolated perfused atrial preparation created using optical mapping recordings for wild-type (WT) and myocardial specific GCH1 overexpression (mGCH1-Tg) isolated mouse atria.

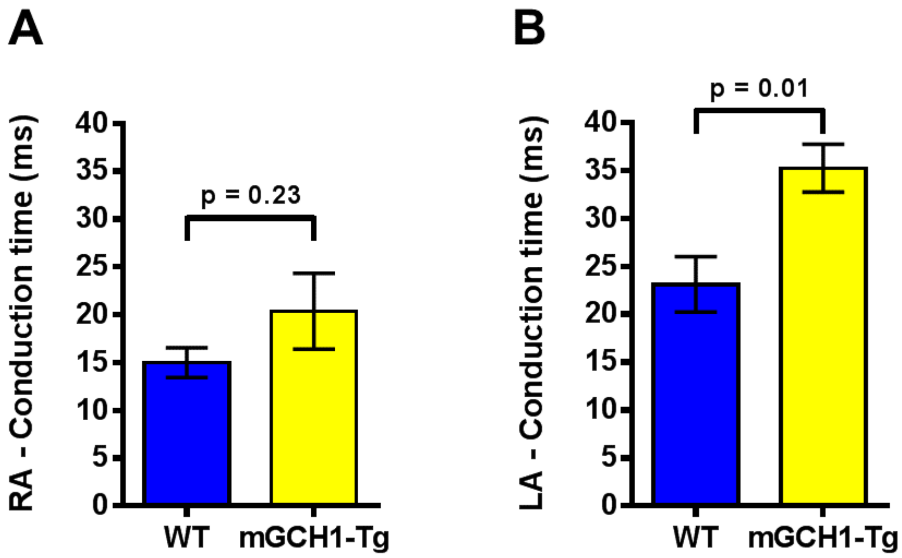

Figure 5-11. Conduction time defined as the time of electrical propagation from the sinoatrial node to the edge of (A) right atrium (RA) or (B) left atrium (LA) comparing the wild-type (WT) and myocardial specific GCH1 overexpression (mGCH1-Tg) atria (n = 6/group, t-test).

ORAL BH4 SUPPLEMENTATION INCREASES THE ATRIAL BH4 LEVELS AND INCREASES THE NOS ACTIVITY

I wanted to examine whether oral BH4 intake could increase the atrial myocardial BH4 levels. Unpublished data from our group (courtesy of Dr Svetlana Reilly) obtained from the analysis of biopterins of patients participating in the OXBIO clinical study (www.clinicaltrials.gov; identifier, NCT00423280) showed a trend towards an increase in atrial BH4 levels in a small group of patients treated with oral BH4 in whom a sample of the right atrial appendage was retrieved at the time of the surgery.

I tested whether BH4 supplementation (at a dose of 200mg/kg/day) for 6 weeks could increase cardiac BH4 levels in diabetic mice. I confirmed that the total biopterin levels in the atrial tissue of mice supplemented with BH4 were increased by around 55-60% compared to the placebo-treated controls and placebo-treated diabetic mice ($p_{corrected} = 0.002$ and $p_{corrected} = 0.005$ respectively) (*Figure 5-12A*). Similarly, atrial BH4 levels were also increased by 50-60% in the mice supplemented with BH4 compared to the placebo-treated controls and placebo-treated diabetic mice ($p_{corrected} = 0.04$ and $p_{corrected} = 0.12$ respectively) (*Figure 5-12B*). The ratio of BH4 to BH2 and B was decreased in the atria of BH4 supplemented mice compared to the placebo-treated controls and placebo-treated diabetic mice ($p_{corrected} = 0.06$ and $p_{corrected} = 0.26$ respectively) (*Figure 5-12C*). Finally, NOS activity in the atria of mice supplemented with BH4 was also increased 2.0-2.5 fold compared to the placebo-treated controls and placebo-treated diabetic mice ($p_{corrected} = 0.03$ and $p_{corrected} = 0.02$ respectively) (*Figure 5-12D*). Importantly, in placebo-treated diabetic mice total biopterin levels ($p = 0.76$), BH4 levels ($p = 0.63$), the ratio of BH4 to BH2+B ($p = 0.52$), and atrial NOS activity ($p = 0.83$) were not different compared to the placebo-treated non-diabetic controls (*Figure 5-12*).

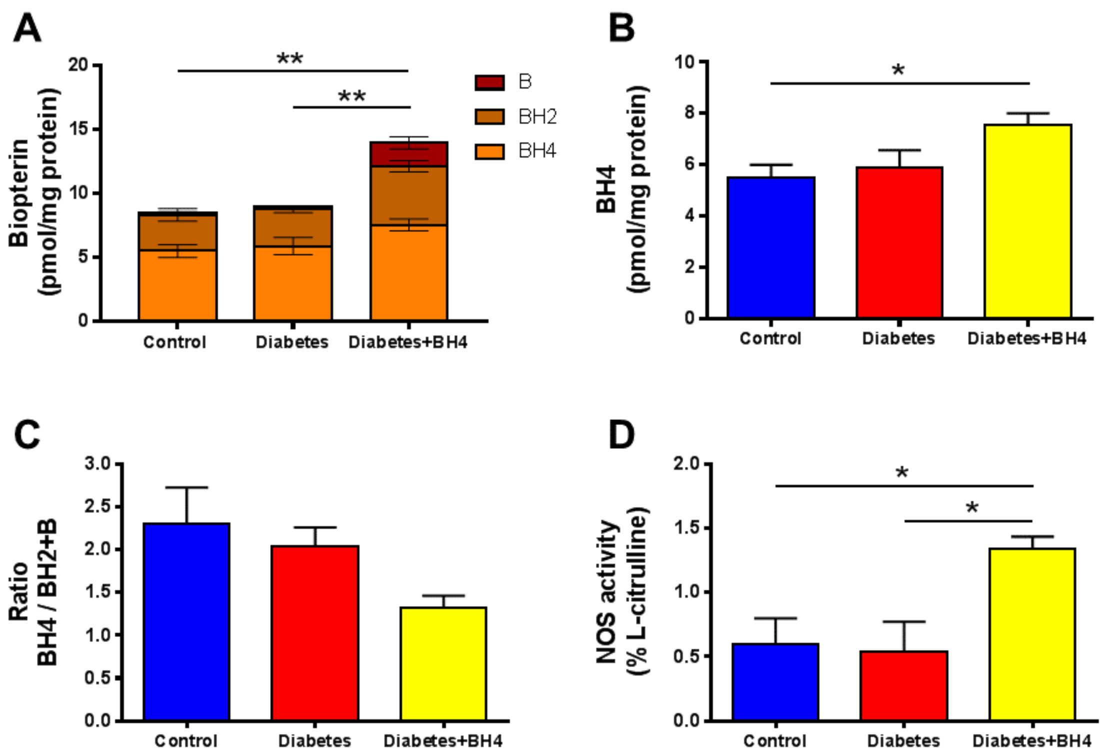

Figure 5-12. Comparison of atrial biopterin levels and nitric oxide synthase (NOS) activity between control mice, placebo-treated diabetic mice and diabetic mice treated with tetrahydrobiopterin (BH4). (A) Levels of all detected biopterin forms in atria as measured by HPLC (n = 10-11/group, one-way ANOVA with Bonferroni post-hoc test). (B) Tetrahydrobiopterin (BH4) concentration in atria measured by HPLC (n = 10-11/group, one-way ANOVA with Bonferroni post-hoc test). (C) The ratio of BH4 to dihydrobiopterin (BH2) and biopterin (B) (n = 10-11/group, one-way ANOVA with Bonferroni post-hoc test). (D) Total NOS activity in atria measured using radiochemical detection of L-arginine to L-citrulline conversion (n = 9 pooled atria/group, one-way ANOVA with Bonferroni post-hoc test). B – biopterin, BH2 – dihydrobiopterin, BH4 – tetrahydrobiopterin. P-values were adjusted for multiple comparisons using Bonferroni correction: * - $p_{corrected} < 0.05$, ** - $p_{corrected} < 0.01$.

ORAL BH4 SUPPLEMENTATION DOES NOT AFFECT PLASMA GLUCOSE LEVELS OR BODY WEIGHT IN DIABETIC MICE

During the course of the BH4 supplementation study in diabetic mice, we regularly monitored body weight (BW) and plasma glucose levels. There was no difference in the body weight of BH4-treated diabetic mice compared to the placebo-treated diabetic mice at any of the monitored time points (*Table 5-3*). Similarly, there was no difference in the plasma glucose levels of BH4-treated diabetic mice compared to the placebo-treated diabetic mice at any of the monitored time points.

	Diabetes (n = 16)	***Diabetes+BH4 (n = 18)***	***p-value***
Body weight (g)			
baseline	24.5 ± 0.4	24.3 ± 0.4	0.68
mid-point (6 weeks)	25.0 ± 0.6	24.8 ± 0.6	0.81
end-point (12 weeks)	25.5 ± 0.7	25.7 ± 0.7	0.84
Plasma glucose (mM)			
mid-point (6 weeks)	28.1 ± 1.7	27.2 ± 1.4	0.69
end-point (12 weeks)	29.4 ± 1.6	29.5 ± 1.7	0.94

Table 5-3. Body weight and plasma glucose over the course of the tetrahydrobiopterin (BH4) supplementation study in diabetic mice. (n = 16-18/group, t-test, all values are mean ± SEM).

BH4 SUPPLEMENTATION DOES NOT REVERSE THE DIABETES INDUCED ELECTROPHYSIOLOGICAL DISTURBANCES

In this part of the study, I investigated whether oral BH4 supplementation could reverse the diabetes-induced cardiac dysfunction reported in the previous chapter. In particular, we tested whether the BH4 supplementation could decrease the probability of pacing-induced atrial arrhythmias and improve the *in vivo* atrial conduction measured as the ECG PQ interval. At the same time, I wanted to monitor whether oral BH4 supplementation can cause any negative electrophysiological side effects as seen in the mGCH1-Tg mice, specifically an increase in the ECG QT interval and an increase in the frequency of AV nodal escape rhythm.

The main finding of this part of the study is that the BH4 supplementation did not decrease the proportion of diabetic mice showing at least one episode of pacing-induced atrial arrhythmia (94% vs. 94%, $p = 0.93$) (*Figure 5-13A*). Similarly, BH4-supplemented diabetic mice did not have a lower probability of pacing-induced arrhythmias (measured as the proportion of burst pacing episodes resulting in atrial arrhythmia) compared to the placebo-treated diabetic mice (18±17% vs. 17±17% [median ± IQR], $p = 0.60$) (*Figure 5-13B*). Finally, even though the spread (measured as IQR) of the mean duration of pacing-induced atrial arrhythmias was lower in the BH4-supplemented group of diabetic mice, the median pacing-induced duration of atrial arrhythmia was not different between the groups (12±9s vs. 15±14s, $p = 0.51$) (*Figure 5-13C*).

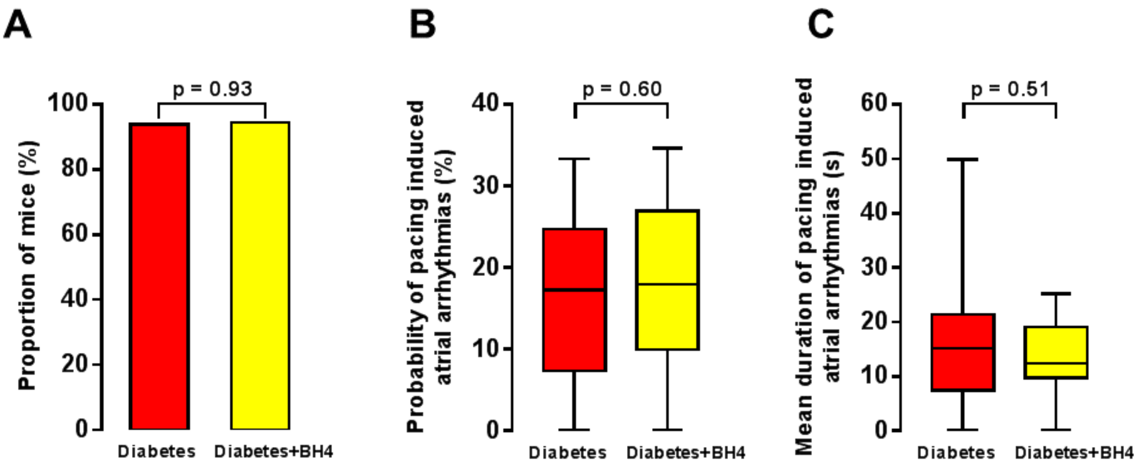

Figure 5-13. Comparison of the pacing-induced atrial arrhythmias between the placebo-treated diabetic mice and diabetic mice treated with tetrahydrobiopterin (BH4). (A) The proportion of mice that had at least one pacing inducible episode of atrial arrhythmia (n = 16-18/group, Fisher's exact test). (B) Probability of pacing-induced atrial arrhythmias (n = 16-18/group, Mann-Whitney test). (C) Mean duration of pacing-induced atrial arrhythmias (n = 16-18/group, Mann-Whitney test).

I also compared the baseline ECG parameters of BH4-supplemented diabetic mice with those of the placebo-treated diabetic mice. There was no difference in any of the measured ECG parameters between the two groups (*Table 5-4*). Finally, we also counted any spontaneous arrhythmias over the course of the *in vivo* electrophysiological investigations. Importantly, BH4-supplementation of diabetic mice compared to the placebo-treated diabetic mice did not increase the incidence of AV nodal escape rhythm (22% vs. 25%, p = 0.99) (*Figure 5-14A*). While we recorded higher incidence of PVCs and VT episodes in BH4-supplemented group compared to the placebo-treated group (PVC: 3/18 (17%) vs. 0/16 (0%), p = 0.23, VT: 1/18 (6%) vs. 0/16 (0%), p = 0.99), the overall incidence was low and differences between the groups were not statistically significantly different (*Figure 5-14B-C*).

ECG intervals	*Diabetes (n = 16)*	*Diabetes+BH4 (n = 18)*	*p-value*
RR (ms)	149.2 ± 5.9	154.5 ± 5.1	0.50
P wave duration (ms)	20.0 ± 0.8	20.1 ± 0.8	0.88
PQ (ms)	44.7 ± 1.0	45.5 ± 0.8	0.61
QRS (ms)	21.8 ± 0.64	21.3 ± 0.5	0.59
QT (ms)	56.3 ± 1.8	55.0 ± 1.2	0.57
QTc (ms)	46.1 ± 0.8	44.4 ± 0.7	0.12

Table 5-4. Comparison of electrophysiological properties of anaesthetized placebo-treated diabetic mice and diabetic mice treated with tetrahydrobiopterin (BH4) (n = 16-18/group, t-test, all values are mean ± SEM), QTc – QT interval corrected for the RR interval using the Bazett's formula.

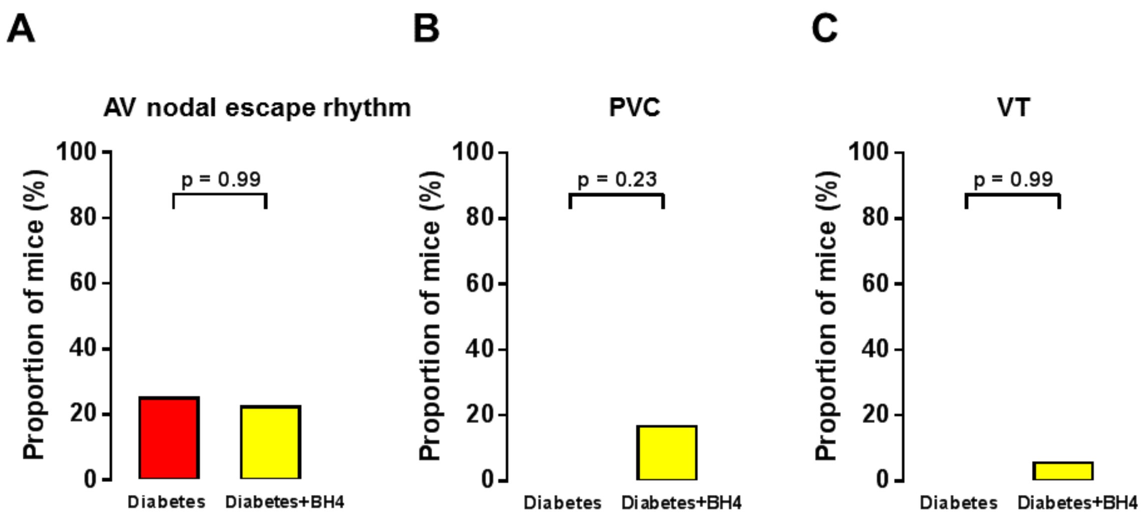

Figure 5-14. Frequency of different spontaneous arrhythmias observed in the ECG recordings. (A) There was no difference in the AV nodal escape rhythm between the placebo-treated diabetic mice and diabetic mice treated with tetrahydrobiopterin (BH4) (n = 16-18/group, Fisher's exact test). (B) There was no statistically significant difference in the proportion of mice with at least one premature ventricular contraction (PVC) between the placebo-treated diabetic mice and diabetic mice treated with BH4 (n = 16-18/group, Fisher's exact test). (C) Ventricular tachycardia (VT) was defined as three or more consecutive beats arising from the ventricle. There was no statistically

significant difference in the proportion of mice with at least one episode of VT between the placebo-treated diabetic mice and diabetic mice treated with BH4 (n = 16-18/group, Fisher's exact test).

BH4 SUPPLEMENTATION DOES NOT REVERSE THE DIABETES INDUCED DIASTOLIC DYSFUNCTION

We have reported in the previous chapter that diabetic mice develop LV diastolic dysfunction and relative LA enlargement compared to the non-diabetic littermates. Based on those findings, we designed the BH4 supplementation study to test whether BH4 could improve those *in vivo* cardiac parameters, as assessed using echocardiography. The main finding of this part of the study is that there was no significant difference in any of the measured LV diastolic function parameters between the BH4-treated diabetic mice and placebo-treated diabetic mice (*Figure 5-15*). Furthermore, there was no difference in the absolute LA area and no difference in the indexed LA area between the BH4-treated diabetic mice and placebo-treated diabetic mice (*Figure 5-16*).

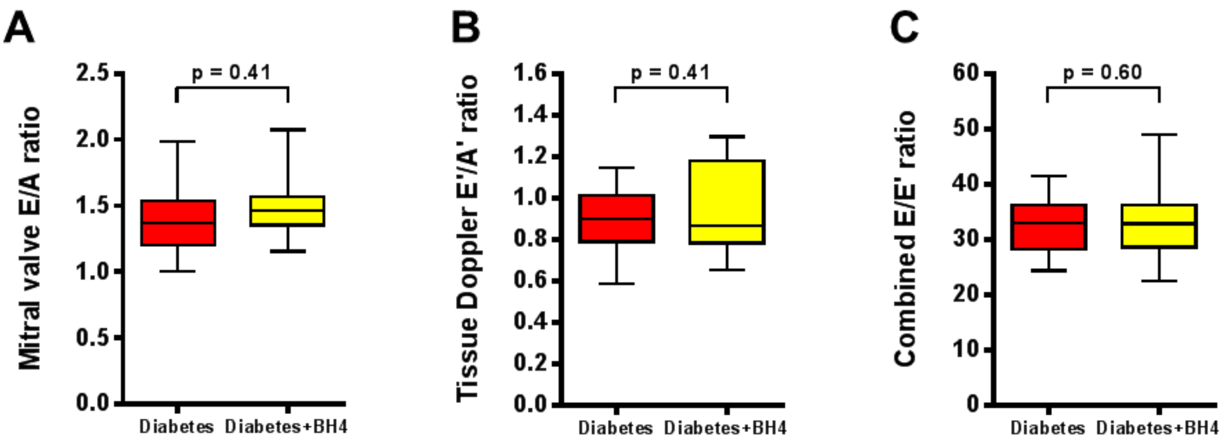

Figure 5-15. Echocardiographic assessment of left ventricular (LV) diastolic function of placebo-treated diabetic mice and BH4-treated diabetic mice. (A) The ratio of early (E) vs. late (A) blood flow velocity through the mitral valve (n = 16-18/group, t-test). (B) The ratio of tissue Doppler early (E') vs. late (A') mitral annulus velocities (n = 16-18/group, t-test). (C) Combined early mitral blood flow velocity (E) vs. early tissue Doppler mitral annulus velocity ratio (n = 16-18/group, t-test).

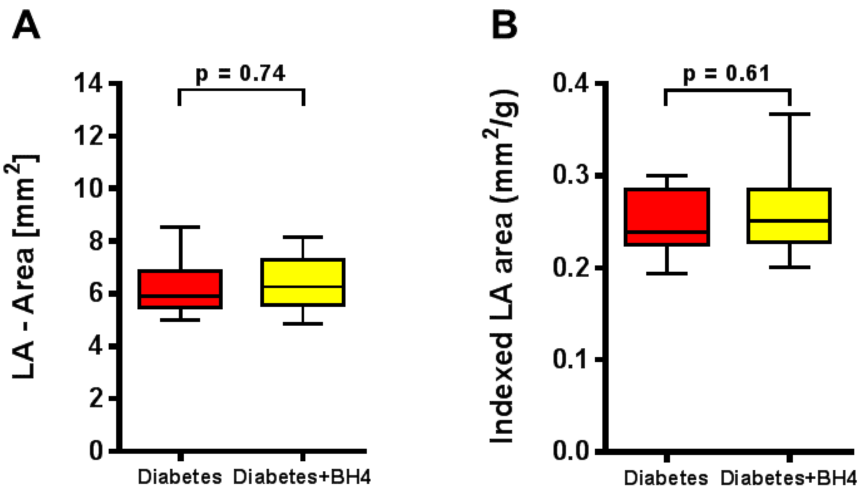

Figure 5-16. (A) Echocardiographic assessment of left atrial (LA) dimensions obtained from apical four-chamber view (n = 16-18/group, t-test). (B) Indexed (normalised to body weight) LA dimensions obtained from apical four-chamber view (n = 16-18/group, t-test).

Discussion

The first part of this study demonstrated that the atrial myocardium of mGCH1-Tg mice had significantly higher levels of BH4. BH4 levels in atria were increased around 50-fold, which is an even greater increase than we measured in the ventricular myocardium (185). Similarly, as in the ventricular myocardium, NOS activity in the atrial myocardium of mGCH1-Tg mice was significantly higher. Importantly, this increase in the NOS activity (predominantly nNOS-derived) in atrial and ventricular myocardium occurred despite unchanged (or even slightly reduced) ratio of reduced-to-oxidised biopterins (BH4:BH2+B ratio). This is in contrast with eNOS in the vascular endothelium, where the ratio BH4:BH2+B, rather than the total BH4 levels, is the main determinant of NOS function (194, 211). This further emphasizes the functional differences of distinct NOS isoforms in specific tissues and cell types.

The second part of this study explored the electrophysiological phenotype of the mGCH1-Tg mice. The first significant difference observed was a lower heart rate in the mGCH1-Tg group. The RR interval in the baseline ECG was around 10% longer in the mGCH1-Tg but the resulting decrease in the heart rate was not severe enough to cause major cardiovascular complications, as no increased intra-uterine deaths were noticed (mGCH1-Tg pups were born in the correct 1:1 Mendelian ratio) and no premature deaths were observed. Still, the mechanisms for the decrease in the heart rate are not entirely clear.

Known factors controlling the heart rate can be grouped into external and internal ones. The main external factor (if drugs are not used) controlling the heart rate is the autonomic nervous system (308, 309). A recent study reported that hph-1 mice – a model of BH4 deficiency – have increased resting heart rate, and the increase was due to increased β-adrenergic sensitivity (310). We measured the heart-rate variability (HRV) as a surrogate assessment for the imbalance between the sympathetic and parasympathetic nervous system (239). None of the HRV parameters were different in the mGCH1-Tg group in our analysis. Therefore, at least under our experimental conditions involving mild general anaesthesia, the autonomic nervous system imbalance cannot explain the differences in the heart rate between the mGCH1-Tg and WT groups. In order to fully explore the potential effect of the autonomic nervous system on *in vivo* cardiac electrophysiology, we should perform ECG telemetry measurements in awake mice over longer periods of time.

The main internal factors controlling the heart rate involve the different pathways regulating the pacemaker's diastolic membrane potential in cardiomyocytes in the sinoatrial node (308, 309). The depolarization rate of the pacemaker membrane potential between two action potentials determines the heart rate. This slow depolarization is achieved by sarcolemmal ion currents, such as the outward rectifier K^+ current I_{K1}, non-specific mixed inward cation current – "funny current" I_f, and membrane calcium currents I_{CaL} and I_{CaT}. Furthermore, the membrane depolarization can also be achieved by spontaneous Ca^{2+} release from the sarcoplasmic reticulum through the RyR2 channels, which activates the NaCa exchanger resulting in a strong depolarizing I_{NCX} current.

The potential role of BH4 and/or NO signalling on the regulation of the pacemaker clock in the sinoatrial node described above has not been studied great detail. Some insight into the role of NO signalling in heart rate regulation can be obtained from studies that used *in vivo* systemic NOS inhibitors. Animals in those studies developed hypertension and likely secondary (reflex) bradycardia when subjected to systemic NOS inhibitors (311-313). On the other hand, no significant changes in heart rate and blood pressure were observed when NOS inhibitors were administered directly in the coronary arteries of human subjects (314). Based on those *in vivo* studies with NOS inhibitors is very difficult to reach any conclusions regarding the effect of NO signalling on the automaticity of the sinoatrial node.

On the other hand, from studies on isolated atrial and ventricular cardiomyocytes, we know that NO signalling is an important modulator of various sarcolemmal ion channels and is also involved in the regulation of calcium currents and transporters (178, 185, 187-190, 200, 216). Therefore it is very plausible that the similar mechanisms are involved in the regulation of pacemaker activity. In order to study the role of BH4 and NOS on cardiac pacemaker cells, new experiments have been planned to perform detailed optical mapping analysis of isolated atria focusing specifically on the sinoatrial region as well as studying the isolated cardiomyocytes from that region both combined with NOS inhibitor experiments.

Another striking electrophysiological feature of the mGCH1-Tg mice was the significantly higher incidence of AV nodal escape rhythm. More than 60% of mGCH1-Tg mice had at least one episode of AV nodal escape rhythm, compared to only 10% in the WT control group. There are several potential reasons for this difference, such as sinoatrial node dysfunction, impaired conduction of electrical impulses to the AV node, or changes in the AV node itself. As discussed above, the mGCH1-Tg mice have lower heart rate, however, the analysis of ECG traces did not reveal severe bradycardia or even sinus arrest immediately prior to the occurrence of the AV nodal escape rhythm.

Furthermore, we also assessed the function of the sinoatrial node, by measuring the SNRT after pacing suppression (315, 316). Prolonged SNRT is a good indicator of the sinoatrial node dysfunction (317, 318). There was no difference in the SNRT between the mGCH1-Tg and WT controls. All aforementioned findings make the sinoatrial node dysfunction a less likely explanation for the increased probability of AV nodal escape rhythm in mGCH1-Tg mice.

We also analysed the propagation of the electrical signal through the atria and the AV node. There was no difference in the *in vivo* PQ interval in the baseline ECG between the mGCH1-Tg and WT controls, which suggest that there is no large atrial conduction delay. On the other hand, in the isolated atria the conduction time (measured with optical mapping system) from the sinoatrial node to the edge of the RA and LA was prolonged, which suggests that there are differences in tissue conduction. Furthermore, the *in vivo* Wenckebach AV block cycle length (WAVB) was significantly increased in the mGCH1-Tg mice, which could also suggest that there is not only a difference in the tissue conduction but perhaps even a change in the AV node function itself (319). Again, the underlying mechanisms for those changes are not known and the role of NO signalling within the cardiomyocytes in the AV node has not been studied.

Based on the open chest *in vivo* studies of AV node in anaesthetised dogs we know that NOS inhibition enhances the effect of the sympathetic nervous system and the response to the isoproterenol infusion, but with no changes to the spontaneous heart rate or changes to intra-atrial conduction time (320). Observations from our mGCH1-Tg model of increased cardiac NOS activity would be in an agreement with the conclusions of those studies that NO acts as a partial inhibitor of the sympathetic regulation of the AV node thus resulting in decreased heart rate and decreased conduction through the AV node. Further studies are needed to depict the exact role and intracellular mechanisms of increased NO signalling on the atrial cardiac tissue and more specifically to the cardiac pacemaker regions.

Another important electrophysiological difference of the mGCH1-Tg mice was the significantly longer QT interval by almost 20% compared to the WT control mice. The mGCH1-Tg mice had a lower heart rate, which might affect the QT interval. In humans and larger animals, there is a strong physiological relationship between the RR interval and the QT interval. The QT interval shortens with shortening of the RR interval as a result of several physiological processes such as accumulation of the slow potassium current (I_{KS}) in the open state and activation of the Ca^{2+} dependent Cl-current (I_{TO2}) both resulting in shortening of the APD (304-306).

Several correction formulas were introduced to correct the QT interval for the RR interval to enable the comparison of the QT intervals. The oldest and most widely used correction formulas are Bazett's and Fridericia's correction formulas (303, 321), with many new ones developed over the decades. All correction formulas have limitations particularly because the relationship between the QT and RR interval is highly individual (i.e. every person has a fairly unique QT-RR relationship) and thus making the use of any correction formula very imprecise (305). The usage of human QT correction formula has been widely used to evaluate the QT prolongation also in mice despite the fact that the QT-RR relationship has not been carefully examined in mice. Recent studies designed to evaluate the QT-RR relationship in mice have demonstrated that there is very weak or even no shortening of the QT interval with shortening of the RR interval – this observation is true for both the anaesthetised and awake mice (306, 307). In that case, the use of QT correction formulas in mice might actually introduce a bias in the QT interval measurements.

In the case of the mGCH1-Tg mice, the QT interval was longer even after the conventional correction formula was used, which means that the QT interval was prolonged independently of the RR interval elongation. The QT prolongation is an indication of longer repolarization phase of the ventricular tissue. While in this study we have not studied the ventricular myocardial tissue in further detail, we have measured the repolarization features of atrial tissue. The *in vivo* measurement of combined atrial and AV node effective refractory period was not prolonged in the mGCH1-Tg mice. On the other hand, the APD in isolated perfused atria measured with optical mapping technique was significantly longer in the mGCH1-Tg mice. The difference in the APD was present in both the RA and LA and was relatively the largest in the early repolarization phase (APD30 and APD50).

Atrial APD differences in mGCH1-Tg mice are in agreement with studies investigating the role of NO in isolated cardiomyocytes (300). Experiments on isolated cardiomyocytes from nNOS knock-out mice ($nNOS^{-/-}$) have a shorter atrial APD and, similarly, the inhibition of nNOS in human atrial myocytes leads to an increase in I_{to}, I_{Kur} and I_{K1} also decreasing APD (187). Furthermore, activation of nNOS has been reported to induce S-nitrosylation of $Na_v1.5$, which in turn increases late Na current resulting in longer APD (178, 188). Nitric oxide also affects APD by modulating repolarizing potassium currents. For example, NO donors prolong APD by inhibiting $K_v1.5$ and $K_v4.3$ channels via cGMP and cAMP-dependent mechanisms, as well as by S-nitrosylating cysteine residues (189, 190). However, some studies report opposite effects of NO on APD, for example, a study on isolated human cardiomyocytes showed that NO donors can increase the I_{K1} current by activating Kir2.1 via selective S-nitrosylation of cysteine residues, which results in shorted APD and hyperpolarization of the resting membrane potential (216). In summary, the observed longer APD duration and longer QT interval in our mGCH1-Tg mice can be explained by increased activation of NO signalling affecting predominantly sarcolemmal ion channels.

Our protocol of burst pacing-induced atrial arrhythmias is a measure of atrial tissue susceptibility to maintain the arrhythmia. The mGCH1-Tg mice did not have a higher probability of pacing-induced atrial arrhythmias compared to the WT mice. There were no significant differences in either the proportion of mice with inducible atrial arrhythmia nor in the proportion of all burst pacing episodes resulting in the atrial arrhythmias between the mGCH1-Tg and WT controls. There was, however, statistically significantly greater variability of in the probability of pacing-induced arrhythmias in the mGCH1-Tg mice, while the mean duration of arrhythmia was shorter in the mGCH1-Tg group. All of those observations together suggest that the tissue substrate of mGCH1-Tg atria is not more susceptible for maintenance of atrial arrhythmias. Conceptually, the tissue is more likely to maintain the arrhythmia, when there are conditions that favour the electrical "re-entry" mechanism. The two main determinants of the "re-entry" electrical conduction are refractory period primarily determined by the APD and tissue decreased conduction velocity (104, 281). The mGCH1-Tg atria have around 25% longer APD, which increases the tissue refractory period and thus decreases the ability of the tissue to maintain an arrhythmia. On the other hand, the mGCH1-Tg have around 25-35% lower tissue conduction velocity, which would increase the tissue's probability to sustain the arrhythmia. Since the probability of pacing-induced arrhythmias did not change between the mGCH1-Tg and the WT controls, we can conclude that the increase in the APD was sufficiently protective against a decrease in the electrical conduction by the same proportion in the atrial tissue.

The interplay of those two opposing tissue characteristics, where one increases the ability to maintain the arrhythmia with the other one having the opposite effect might also explain the greater variability in the probability of pacing-induced atrial arrhythmias in the mGCH1-Tg mice. A small inter-subject variability in either the mechanisms increasing the APD or mechanisms decreasing the CV can significantly alter the functional electrophysiological balance resulting in the tissue that is very prone for arrhythmias or, on the other hand, in the highly stable electrical tissue.

One mouse in the mGCH1-Tg group had a recorded spontaneous (not pacing-induced) episode of short non-sustained VT. The significance of this observation is unknown as this was a single and isolated event. Nonetheless, the longer ECG QT interval is associated with an increased risk for ventricular arrhythmias (322, 323). Furthermore, cardiomyocytes with longer APD are more prone for early afterdepolarizations (EADs) and delayed afterdepolarizations (DADs), which can act as a trigger for the arrhythmia (281, 324). Further experiments using ECG telemetry in the awake mice would be needed to detect the presence of arrhythmias during the longer observation period. As mGCH1-Tg mice have those features it would be therefore prudent to carefully monitor any animal experiments and particularly any human studies that will test drugs that result in increased BH4 levels or increased NOS activity. Even short ventricular arrhythmias have a potential to turn into sustained VT or even ventricular fibrillation with fatal outcomes.

In this part of the study, we used an established mouse model of a myocardial specific increase in the NOS activity (185, 213). We described the *in vivo* and tissue level electrophysiological properties of this animal model in great detail, however, we cannot firmly conclude that those changes are a direct consequence of increased NO signalling within the cardiomyocyte. Hearts of mGCH1-Tg mice have a 50-fold increase in the BH4 levels, which can also result in NO-independent changes. For example, BH4 is a cofactor in several aromatic amino acid hydroxylases and alkylglycerol monooxygenases producing serotonin, tyrosine, and L-DOPA and changes in those neurotransmitters can potentially cause electrophysiological changes as well (194). Furthermore, BH4 also acts as a direct antioxidant by being able to be oxidized to BH2 and can, therefore, change the redox state in the cardiomyocyte and thus potentially modulate the sarcolemmal ion channels (50, 325).

We used AAAN as a preferential nNOS inhibitor, which has a good tissue penetration and has been used previously to inhibit the NOS within the isolated hearts (326, 327). Using optical mapping of the isolated perfused atrial tissue, nNOS inhibition, as expected, slightly shortened right atrial APD prolongation in mGCH1-Tg mice. Surprisingly, however, nNOS inhibition resulted in unexpected slight prolongation of right atrial APD in WT mice. It should be noted that, due to unavailability of suitable equipment, we were not able to measure the effect of the AAAN at the experimental concentration and incubation time on atrial NOS activity.

Even in the experiments in isolated cardiomyocytes, there is always a concern whether a NOS inhibitor has sufficiently penetrated into the cell. Experiments using patch-clamping combine the NOS inhibitor in the pipette solution in addition to the perfusion buffer to improve the intracellular inhibition of the NOS (185, 191). The inhibitor penetration problem is even greater in tissues that are only superfused compared to the Langendorff perfused isolated hearts that use the native coronary vessels for perfusion. In order to study the intracellular molecular mechanisms responsible for electrophysiological changes seen in the mGCH1-Tg mice, we would first need to optimize and confirm that the NOS inhibitor of choice can evenly reach cardiomyocytes within the whole atria and that the dose of the inhibitor is sufficient to inhibit the NOS activity while at the same time not causing significant off-target side effects (328, 329). In addition, an even more elegant experiment would be to study the effects of increased myocardial BH4 using the mGCH1-Tg mice with the simultaneous deletion of nNOS. This new transgenic mouse model has now been created by our group.

In addition, a control experiment using only alpha myosin heavy chain (αMHC) transgenic mouse would be needed to confirm that all the cardiac electrophysiological changes are solely due to the GCH1 overexpression. A recent study has pointed out that the overexpression of αMHC in the αMHC-Cre$^{+/-}$ mouse line results in mild inflammation, fibrosis, and DNA-damage in myocardium (330). This potential cardiac toxicity might be further emphasized in the atria, where the αMHC is predominantly expressed.

In this part of the study, we described in great detail the *in vivo* and atrial tissue electrophysiological properties of a mouse model with increased myocardial BH4 levels and enhanced myocardial NOS activity. Even though we did not examine the underlying molecular mechanisms this investigation is still important as a screening of desired and also negative effects of any potential therapy that will target either BH4 or NOS activity. Therefore, as a safety precaution, patients enrolled in any clinical study using BH4 as a therapeutical intervention will have to be monitored for any changes in the heart rate as well as have several ECG recordings to assess any potential QT prolongation. In addition, they may have to undertake a longer 24h ECG recording to assess for any atrial or AV conduction block and to detect any increase in the frequency of PVCs or short episodes of VT. However, as mice receiving oral BH4 (which better mimic potential clinical applications) did not have any of those electrophysiological side effects, this safety precaution will only realistically be needed until confirmed that BH4 does not cause electrophysiological disturbances in humans.

In then examined the effects of oral BH4 supplementation in diabetic mice. In the previous chapter, we have shown that diabetes increases the risk for pacing-induced atrial arrhythmias and causes LV diastolic dysfunction with LA enlargement. We have also shown that diabetic mGCH1-Tg mice do not develop LV diastolic dysfunction due to improved myocardial energetics. In addition, BH4 supplementation has also been shown to modulate the inflammatory response, which is another common mechanism involved in diabetic cardiomyopathies (213). Based on those findings we hypothesized that BH4 supplementation would prevent the diabetes-induced increase in the risk of atrial arrhythmias and improve LV diastolic dysfunction.

We presented here that oral BH4 supplementation (rather than multiple intravenous injections as an alternative) is sufficient to increase myocardial BH4 levels. Furthermore, this increase in the myocardial BH4 levels was sufficient to increase the myocardial NOS activity by more than two-fold. Those results are encouraging because it allows a simple and efficient approach to testing BH4-based therapeutical interventions in various animal models as well as in human participants.

We then tested whether oral BH4 supplementation could prevent the development of diabetes-induced cardiac phenotype. BH4 supplementation did not reverse the increase in the probability for pacing-induced atrial arrhythmias in diabetic mice nor changed any other ECG parameter compared to the placebo-treated diabetic mice. Furthermore, the BH4 supplementation did not significantly improve LV diastolic dysfunction nor did it decrease the relative enlargement of LA characterized in diabetic mice.

Our study was the first to test whether BH4 supplementation can improve electrophysiological and atrial tissue disturbances seen in diabetic animal models. However, there are other published studies that investigated the potential use of BH4 in treating the vascular dysfunction in various disease states as well as improving cardiac function in animal models of LV pressure overload and severe ischemia (198, 200, 203-213, 220, 221). None of those studies specifically looked or described any potential electrophysiological effects of BH4 treatment. The transgenic mouse model of increased myocardial BH4 levels had several potentially dangerous electrophysiological features such as bradycardia, long QT interval, and increased incidence of spontaneous AV nodal rhythm. Mice treated with oral BH4 had only around a 50% increase in the myocardial BH4 and biopterin levels, compared to the 50-fold increase measured in the mGCH1-Tg hearts. Both the mGCH1-Tg and oral BH4 treated mice had a similar two-fold increase in the NOS activity within the myocardium. Importantly, the BH4 treated diabetic mice only had a statistically non-significant 4% increase in the ECG RR interval compared to the placebo-treated mice, whereas the mGCH1-Tg mice had an 11% increase in ECG RR interval compared to the WT controls. Furthermore, the BH4 treated mice did not have a longer QT interval and had no increase in the proportion of AV nodal escape rhythm compared to the placebo-treated mice. On the other hand, the BH4 treated diabetic mice had a higher number of recorded PVC and VT episodes compared to the placebo-treated mice where none of PVCs or VTs were noted. The overall incidence of those ventricular arrhythmias was low and therefore the difference between the groups was not statistically significant.

The reason why the oral BH4 treatment did not improve any of the diabetes-induced cardiac dysfunctions described in the previous chapters was unclear, considering the fact that the mGCH1-Tg successfully prevented the development of the diastolic dysfunction. Hearts of BH4 treated diabetic mice only had a 50% increase in the myocardial BH4 concentration compared to a 50-fold increase in the mGCH1-Tg hearts, therefore one possible explanation could be the dose of oral BH4 was too low. However, the fact there was no major difference in the increase in the NOS activity between the mGCH1-Tg and BH4-treated hearts, made this explanation less probable. A more plausible explanation could be the timing of oral BH4 treatment. The oral BH4 treatment commenced after 6 weeks of hyperglycaemia and lasted for another 6 weeks. Therefore the duration of the oral BH4 treatment might not be long enough to reverse the diabetes-induced changes or, on the other hand, diabetes might have already caused irreversible changes after 6 weeks and therefore increased myocardial BH4 levels could only prevent the development of diabetic complications but was not able to treat them or reverse them.

In conclusion, the oral BH4 supplementation at the dose we used is a safe way to increase the myocardial BH4 levels and increase the myocardial NOS activity without causing severe or harmful electrophysiological changes. However, if this kind of treatment is used in human subjects it may still be prudent to ensure regular ECG monitoring to ascertain that the BH4 treatment does not cause electrophysiological disturbances.

CHAPTER 6:

Conclusions and general discussion

Key findings and implications

The need for better understanding of the pathophysiology of the diabetes mellitus (DM) and diabetes-related complications is now more important than ever as the incidence and prevalence of the DM are rising rapidly (1). Only in the last decade the global prevalence of DM has increased by 62% and is estimated that by 2045 around 11% of the global population will have DM (3). Furthermore, the prevalence of heart failure (HF) in patients with DM range from 19% to 26% and the total number of DM patients with HF will only increase with time (16). The prevalence of atrial fibrillation (AF) is 2%, but the prevalence rises to 9% in patients older than 80 years (82, 85, 86). The risk for the AF is further increased by around 40% in the presence of DM (91). Importantly, the AF and HF frequently occur together and there is also a bidirectional epidemiological association with one condition predisposes the other (331). Taking into account all those epidemiological data we can conclude that there is a rising concern affecting a particular subpopulation of patients with DM who will likely develop diabetic cardiomyopathy and HF, as well as simultaneously (or independently of HF) having AF.

The general approach to the treatment of patients with DM is the management of main risk factors (e.g. obesity, smoking, hypertension, dyslipidaemia) followed by glucose-lowering medications (13). Currently, there are no medications used to specifically target DM-related AF or diabetic cardiomyopathy. The management of DM is therefore primarily focused on reaching the target glycaemic control. It has been demonstrated that tight glucose control targeting normal HbA1c levels (i.e. <7.0%) significantly decrease the incidence of microvascular complications (e.g. retinopathy, neuropathy, and nephropathy), however, the ideal HbA1c level for prevention of cardiovascular disease and in particular the HF and AF is not entirely clear (13). While an older study showed that each 1% increase in HbA1c is associated with an 8% increased risk of HF (332), some newer studies investigating intensified glucose control did not confirm this correlation (333), and some studies even showed an increased mortality in the intensive glucose control group (13, 334-336). Similarly, there was no difference in the incidence of AF between the intensive glucose control group and the standard treatment group (94). Therefore the optimal target glucose levels in DM patients with HF or AF is still unknown and requires further research.

The research on novel and more targeted therapeutical options for the diabetic cardiomyopathy and DM-related AF is complicated by the fact that those patients often have a lot of associated comorbidities, such as obesity, hypertension, and dyslipidaemia – and is, therefore, hard to isolate distinct pathological pathways associated solely with diabetes mellitus. On the other hand, animal models can provide a clearer insight into complications caused by an isolated abnormality such as plasma hyperglycaemia, lack of insulin, obesity etc.

We have chosen to investigate the effects of hyperglycaemia on the left ventricular (LV) and atrial function and therefore we used the streptozotocin (STZ) induced diabetes mouse animal model. STZ is a toxic alkylating agent that is preferentially up-taken by the glucose transporter 2 (GLUT2) of beta cells in the pancreas. The destruction of beta cells causes a decrease in insulin secretion and plasma hyperglycaemia (31, 32). The STZ mice are not obese and do not have hypertension and can, therefore, be used to answer questions such as whether hyperglycaemia and insulin deficiency are sufficient to cause myocardial dysfunction.

The first key finding of this research thesis is that our STZ diabetic mice recapitulated several of the key pathological changes of the intermediate stage of the diabetic cardiomyopathy – they developed LV diastolic dysfunction without LV systolic dysfunction, LV hypertrophy, or LV dilatation (29). In contrast to other studies investigating diabetic cardiomyopathy in STZ mice, where they develop more severe phenotype with severe LV systolic dysfunction and even increased mortality, our slightly milder model of diabetic cardiomyopathy might provide insight into the important pathological mechanism at the earlier stages, prior to the development of irreversible changes (31, 32).

One important insight from our diabetic mouse model is that the diabetic myocardium does not have an increase in the global cytosolic superoxide production, they do not have reduced levels of tetrahydrobiopterin (BH4), and have no signs of NOS dysfunction. This is an important distinction compared to studies investigating vascular dysfunction in STZ diabetic mice. Vascular dysfunction characterized by impaired NO-mediated vascular relaxation, reduced endothelial BH4 availability, NOS uncoupling and increased superoxide production occurs already after several weeks after induction of diabetes by STZ (194, 202, 260). Vascular dysfunction is, therefore, one of the early signs of complications by DM, whereas myocardium is initially protected or more resilient and thus do not develop NOS dysfunction and it also does not have signs of global oxidative stress. This interpretation is further confirmed by the results of a study where STZ diabetic mice already developed a more severe phenotype with LV systolic dysfunction and at that time they already had decreased myocardial BH4 levels and impaired cardiac nNOS signalling (259). Furthermore, our analysis of the human myocardial tissue of patients with DM undergoing cardiac surgery also demonstrated no increase in the superoxide production and no decrease in the myocardial BH4 levels (compared to the matched non-DM controls). Those diabetic patients did not have LV systolic dysfunction, did not have documented diagnosis of heart failure, and were overall fit enough for cardiac surgery. Results from the human tissue are in agreement with the interpretation of results from STZ diabetic mice, where global oxidative stress and reduced myocardial BH4 levels are not early changes and occur only later in the progression of diabetic cardiomyopathy with the development of severe LV systolic dysfunction.

Even though our STZ diabetic mice did not have a decrease in the myocardial BH4 levels or signs of impaired myocardial NOS signalling, overexpression of the GTP cyclohydrolase 1 (GCH1) resulting in above-normal myocardial BH4 levels and thus increased NOS activity prevented the development of the LV diastolic dysfunction in diabetic mice. The underlying mechanism of this protection in the mGCH1-Tg mice was the improvement in the myocardial energetics by increasing the glucose uptake as a result of the increased expression of the myocardial glucose transporter 1 (GLUT-1) in diabetic hearts.

This novel finding of a significant *in vivo* improvement of diabetic cardiomyopathy has several important implications. Firstly, those results directly suggest further investigation of whether a systemic intake of BH4 (e.g. by supplementing BH4 in the diet) could also prevent the development of diastolic dysfunction in diabetic mice. Furthermore, the mechanistic insight that improving the myocardial glucose uptake is sufficient to prevent the diastolic dysfunction in DM also opens the door for research of any other pharmacological agents that could augment glucose uptake selectively in cardiomyocytes. Finally, our results further emphasize the crucial role of efficient myocardial energetics and how essential is the availability of all different sources of energy (i.e. glucose and fatty acids) for the energetic flexibility and normal function of the cardiomyocyte.

Another pivotal finding of this research thesis is that our STZ mice have increased risk for *in vivo* pacing-induced AF. Importantly, the increase in the AF risk in this diabetic mouse model occurs without concomitant obesity, hypertension or LV systolic dysfunction. This important conclusion confirms the observations from large population-based studies, where DM has been identified statistically as one of the independent risk factors for AF (88-92). Furthermore, this finding also has important implications for the future clinical management of AF in patients with DM. Currently, the clinical guidelines do not provide any specific recommendations for this subgroup of patients beyond the general advice for anticoagulation, rate/rhythm control, and management of other known risk factors (13, 337). Considering that the intensive glycaemic control does not decrease the risk for AF (94) and that DM causes an increased risk for AF independently of other common risk factors, I strongly believe there is an untapped potential for the discovery of new treatment options for this subgroup of patients.

The main approach to finding novel targeted therapies is a better understanding of the underlying pathological mechanisms in a particular disease. Indeed, this is another area where our diabetic mouse model proves to be fruitful. Our diabetic mice have enlarged relative atrial size and impaired *in vivo* atrial conduction as indicated by prolonged ECG PQ interval. Furthermore, experiments in isolated whole atria demonstrate a significant focal increase in fibrosis in the medial part of the right atrium, which results in a significant decrease in the conduction velocity in the same area followed by an increase in the conduction wave-front heterogeneity in the left atrium. This finding has several important implications. Firstly, compared to other diabetic animal models with a more severe phenotype where they describe global diffuse atrial fibrosis (97, 125, 126, 282, 297, 298), our model of the earlier stage of diabetes-related dysfunction provides insight in where the atrial interstitial fibrosis starts in the first place. This finding also challenges the current understanding where the atrial structural remodelling is a relatively uniform process affecting myocardium globally (112, 140), instead, our results suggest that a focal conduction defect caused by the regional fibrosis in a critical area is sufficient to cause a substrate vulnerable for AF. Furthermore, focal fibrosis in a critical area within the atria measured using the late gadolinium enhancement magnetic resonance imaging technique (designed specifically to image atrial fibrosis in patients) might serve as an early clinical biomarker for predicting, which patients are at the highest risk for developing AF (338, 339). Finally, results from our diabetic mice model suggest that investigations of novel therapeutic options to decrease the risk for AF in patients with DM should focus on agents that modulate fibroblasts and formation of the connective tissue, as well as on agents targeting other factors that promote fibrosis, such as inflammation and chronic ischemia. Considering that the establishment of the myocardial interstitial fibrosis is a relatively irreversible process, all studies testing new pharmacological substances for this specific condition have to carefully plan the timing of the pharmacological intervention. The aim of the intervention should focus on the prevention of fibrosis or at least slowing down the creation fibrosis before it reaches an irreversible time point.

Considering we have shown that the mGCH1-Tg diabetic mice are protected from the development of LV diastolic dysfunction, we also wanted to explore if the increase in the myocardial BH4 levels protects from the development of the AF as well. However, the mGCH1-Tg mouse model proved to be unsuitable for studying the pacing-induced AF as around two-thirds of the transgenic mice spontaneously lose the sinus rhythm as it changes to the AV nodal escape rhythm. In addition, the mGCH1-Tg mice (compared to the WT) also had a large variability in the baseline AF inducibility, therefore making any experiments investigating the treatment potential to prevent the AF very difficult. On the other hand, the mGCH1-Tg mice provide important insight on any adverse electrophysiological effects if BH4-based therapies will ever be introduced to large long-term clinical studies. The mGCH1-Tg mice have several important *in vivo* electrophysiological changes – they have lower heart rates, they often spontaneously develop AV nodal escape rhythm, and they also have prolonged ECG QT interval. The underlying mechanisms for those changes are a global decrease in the atrial conduction velocity, decrease in the conduction through the AV node, as well an increase in the action potential duration (APD). It is very important to note that the adverse electrophysiological side-effects occur in a transgenic mouse model with around a 50-fold increase in the myocardial BH4 concentration. Mice receiving oral BH4 treatment, on the other hand, only have a two-fold increase in the myocardial BH4 concentration and do not have any of the aforementioned adverse electrophysiological side effects. This suggests that the adverse effects of BH4 are likely dose-dependent and might never be seen by using a systemic (oral or intravenous) treatment using typical BH4 dosing regimens. Nonetheless, based on our findings it would be prudent to incorporate regular monitoring of the heart rate (to detect any bradycardias) and several ECG recordings (to detect AV block or QT prolongation) during the course of any clinical study using the BH4 as a safety precaution. In addition, it might be useful to avoid using the BH4 in a clinical trial in any patient with the long QT at baseline or any pre-existing AV block, at least in the early stages until it is confirmed that BH4 would not cause those changes at the dose used in the trials.

Finally, the last part of this research thesis explores the oral BH4 supplementation in our diabetic mice and in particular whether it can decrease the risk for AF and/or improve the LV diastolic dysfunction. Unfortunately, the BH4 supplementation, as used in this study, does not decrease the probability for pacing-induced AF and it does not improve the LV dysfunction. The mice receiving oral BH4 have a similar increase in the myocardial NOS activity as the mGCH1-Tg mice, where they are protected from the diabetes-induced diastolic dysfunction. Based on this, insufficient oral BH4 dose may not be the main reason for the negative treatment result. The more plausible explanation for the discrepancy between the oral BH4 treatment and the transgenic mouse model is the timing of the treatment. We started treating diabetic mice with BH4 after 6 weeks of DM – the protocol used in other animal studies investigating the protective effects of BH4 in various diseases (198, 200, 212, 213, 220, 221). However, it is possible that after 6 weeks of DM some of the myocardial changes are already irreversible (i.e. fibrosis in atria of diabetic mice). In order to investigate that, the BH4 treatment should start earlier in the diabetic stage or perhaps even before the induction of DM.

Future work

As it is usual with any research work, several questions remained unanswered and several new questions came to light as a result of our findings. In our research, we have not examined the underlying mechanisms for the increase in the interstitial fibrosis. While our mice did not have an increase in the myocardial cytosolic superoxide production, there are other mechanisms, apart from oxidative stress, that can also cause structural remodelling in diabetic hearts. Hyperglycaemia in T1DM and T2DM is associated with an increase in angiotensin II and TGF-β signalling pathways, which are both known to activate profibrotic signalling pathways (139). Furthermore, prolonged exposure to hyperglycaemia can result in the intracellular and extracellular accumulation of advanced glycation end-products (AGEs), which in turn can enhance formation of fibrotic tissue by crosslinking collagens and laminins as well as by activating the profibrotic signalling pathways by binding to the receptors for AGE (RAGE) located on the cardiac fibroblasts (130).

Diabetes also alters the secretion of various signalling molecules from adipocytes (adipokines) such as leptin, adiponectin, resistin and others (340-342). Adipokines are involved in multiple different pathways such as fibrosis, metabolic alterations, inflammation and calcium homeostasis, which are all mechanisms that can result in arrhythmogenic alterations of atria resulting in AF (139, 340). The role of adipokines such as leptin, adiponectin and resistin in human AF has been evaluated in multiple clinical studies with varying and sometimes opposite effects (343). This area requires further research before any firm conclusions can be made.

Furthermore, inflammation is another process that has been implicated in both the pathogenesis of AF as well as in the pathogenesis of diabetic cardiomyopathy (139). Metabolic alterations present in diabetes activate multiple signalling pathways such as high-mobility group box 1 (HMGB1), Jun NH2-terminal kinase (JNK), protein kinase C (PKC), and glycogen synthase kinase 3 beta (GSK-3β) that all trigger the inflammatory cascades regulated primarily by the mitogen-activated protein kinase (MAPK) and nuclear factor kappa-light-chain-enhancer of activated B cells (NF-κB) (344). Activation of those inflammatory signalling pathways can result in pathological changes within cardiomyocytes resulting in altered contractility and electrophysiological changes, hypertrophy, and apoptosis. Activated inflammatory signalling pathways also stimulate fibroblasts to produce more collagen resulting in tissue fibrosis, modulate the dormant population of cardiac tissue macrophages, and finally activate leukocytes resulting in chronic systemic inflammation.

A classical explanation of cardiac electrical conduction is that only specialized cardiomyocytes are firstly responsible for creating a regular heartbeat in the sinoatrial pacemaker region from where the signal then spreads again by specialized cardiomyocytes through atria to the atrioventricular node and from there to both ventricles. This conventional view on cardiac electrical conduction has been recently expanded with findings that not only cardiomyocytes but also other cells such as fibroblasts and even tissue macrophages are electrically coupled to cardiomyocytes and help to coordinate and regulate the complex cardiac function (345). In particular, tissue macrophages can be a novel link between diabetes mellitus and cardiac arrhythmias. An exciting study explored the role of tissue-resident macrophages in the heart and particularly its role in modulating the cardiac electrical conduction (346). The main findings were that tissue macrophages are coupled to cardiomyocytes via the connexin 43 gap junctions and that if this Cx43 connection is removed or if the population of tissue macrophages is depleted in mice this results in prolongation of the APD in cardiomyocytes and delayed cardiac conduction particularly in the AV node resulting in progressive AV block phenotype. Furthermore, a study used the STZ-induced DM in mice to demonstrate that diabetic mice are more vulnerable to caffeine and dobutamine induced ventricular arrhythmias (347). Importantly, the susceptibility to arrhythmias diminishes in IL-1 receptor knock-out mice and also by injecting the IL-1 receptor antagonist. Also, the arrhythmia vulnerability is decreased by blocking the toll-like receptor 2 (TLR2) and the nucleotide-binding domain and leucine-rich repeat-containing protein (NLPR) signalling pathways in macrophages. Taking all those findings together it is possible to hypothesize that diabetes causes cardiac macrophage dysfunction and activation of the inflammatory pathways resulting in direct (e.g. via gap junction proteins) or indirect (e.g. by releasing IL-1β) modulation of cardiomyocytes resulting in cardiac tissue substrate that is prone for atrial and ventricular arrhythmias. Further research is warranted to explore the underlying intertwined mechanisms in arrhythmia generation, as well as the efficacy of macrophage and inflammation oriented therapeutic approaches for treating the AF.

Finally, we have not examined the effect of diabetes on the modulation of various ion channels on cardiomyocytes. For example, some (but not all) studies showed decreased Na+ current (I_{Na}), increased late Na+ current ($I_{Na,L}$), reduction in atrial acetylcholine-activated K+ current (I_{KAch}), decreased transient outward K+ current (I_{to}), and reduced expression of small conductance Ca^{2+}-activated K+ channels (139). The changes of different ion channels in human patients with diabetes mellitus are unknown and warrant further exploration. Furthermore, myocardial gap junction proteins are another important determinant of tissue conduction velocity and its function is also considered to be altered in the presence of diabetes. The most important gap junction proteins in atria are connexin (Cx) 40 and Cx-43. Studies in STZ-induced diabetic atria showed a decrease in the total Cx-40 levels (123, 282). More inconsistent results are reported for changes of Cx-43 in diabetic atria with some studies reported decreased levels of total Cx-43, while others found no changes (123, 282, 348). However, while the total levels of Cx-43 might remain unchanged, the same study reported increased lateralization of Cx-43 in cardiomyocytes, which can explain decreased conduction velocity and increased conduction heterogeneity

(123). The potential changes of connexin levels and its tissue distribution has not been studied in human patients with diabetes mellitus and require further research.

Until 2008, the clinical trials of all new drugs for the management of DM were focusing solely on the efficacy of the plasma glucose-lowering profile (16). Randomized clinical trials were following the patients only for 6 months or less, enrolled patients were normally not on any previous medications, the total duration of DM was relatively short, and often the pre-existing renal or cardiovascular disease was one of the exclusion criteria (16, 349). Therefore it was not surprising that there was a lack of improvement in the management of DM patients that were more complex and suffering from cardiovascular complications. After numerous published reports that some new glucose-lowering medications have the excess risk for cardiovascular mortality (compared to other treatment modalities), the Food and Drug Administration (FDA) in the USA published new guidelines stating that the clinical trials of new glucose-lowering medications have to demonstrate the no-excess risk for cardiovascular complications (350). After this new guidance was introduced, several studies re-evaluated the cardiovascular risk and benefit of several glucose-lowering drugs. Currently, there is evidence that some glucose-lowering medications increase the risk for developing HF (e.g. thiazolidinediones and some DPP4 inhibitors), while others decrease the risk for the HF (e.g. metformin, SGLT2 inhibitors, GLP1 receptor agonists), while the majority of them have a neutral effect (13, 16, 351). Nonetheless, all those new medications are designed mainly to improve the glycaemic profile. There is no drug currently used that would primarily target any of the other mechanisms involved in causing the DM-related cardiovascular dysfunction. Considering that the overall reduction in the cardiovascular complications in patients with DM, even using the newest approaches, is nowhere near the reductions that were seen in preventing the diabetic microvascular complications (e.g. retinopathy, neuropathy, and nephropathy), there is an urgent demand for exploring novel targets and therapeutic agents (13, 16).

Main limitations of the study

The main limitation of the study is the use of the STZ mouse model. First of all, the STZ mouse model, in general, might have significant extra-pancreatic toxic effects of STZ. STZ is a potent alkylating agent and can cause DNA methylation, DNA strand breaks, chromosomal aberrations, and cell death (352). Intraperitoneal injections of STZ caused tumours in kidneys, liver, and pancreas (353). STZ also caused direct hepatic impairment prior to any changes in plasma glucose levels (354). Furthermore, acute STZ treatment causes also a direct cardiomyocyte contractile dysfunction due to activation of the stress signalling p38 MAP kinase pathway and increased oxidative stress (355). Those adverse extra-pancreatic effects of STZ have been decreased by switching from a single high-dose injection of STZ to multiple low-dose STZ injections (356). In addition, only males were used in our STZ-induced DM studies as females develop only mild hyperglycaemia (compared to males) after STZ injections. While excluding females from the study improved the homogeneity of plasma glucose levels in investigated animals, it might on the other hand, introduced gender specific bias. Therefore some of the findings of this study might not be fully generalizable. In our STZ mouse model, those extra-pancreatic effects were further minimized by using an even lower dose of STZ for induction of DM. On the other hand, STZ diabetic models (in contrast to other models of pancreatic beta cell dysfunction) have several practical advantages such as an ability to study DM in various genetic background strains as well as in genetically altered models without complicated and prolonged genetic cross-breading, an option to study DM at various animal ages, and also to be able to use both mice and rats to study the DM-related complications (31, 32).

Another relative limitation of the STZ model of diabetes that it is a model of T1DM, whereas the majority of the adult population have T2DM (1). There are several significant differences between the T1DM and T2DM. The T1DM is characterised by a dysfunction in the insulin production or secretion in beta cells of the pancreas, usually secondary to the autoimmune disease. The T2DM, on the other hand, characteristically starts with the insulin resistance in multiple organs, followed by compensatory hyperinsulinemia until insulin-secreting beta cells in pancreas fail, which then results in the decreased levels of plasma insulin (1). However, both the T1DM and T2DM share several similar underlying features described in the development of human diabetic cardiomyopathy, such as LV diastolic and systolic dysfunction, myocardial interstitial fibrosis, impaired cardiac energetics and substrate switch, mitochondrial dysfunction, etc. (31, 32). Therefore, while there are definitely several fundamental differences between using the T1DM and T2DM animal model, some of the mechanistic findings of pathophysiological processes in the myocardium of one model might still be generalizable (to some extent at least) to the other type of DM.

Another important limitation is the use of a mouse model to study human disease. This is particularly true for studying the electrophysiological characteristics and inducibility of the cardiac arrhythmias. Compared to human cardiomyocytes, mice cardiomyocytes have shorter APD, and several small differences in expression (both over- and under-expressed compared to humans) of multiple ion channels, calcium handling proteins, and gap junction proteins (357). However, the biggest difference is simply the issue of the size of the hearts. Any sustainable arrhythmia requires a larger area to maintain itself – and while we can certainly induce arrhythmia in smaller mice atria, the arrhythmia pattern complexity, as well as the total duration of arrhythmia, is lower in mice compared to humans.

Also, exploration and characterization of a phenotype in the experimental model is inherently associated with measuring multiple parameters. In our studies we measured several different electrophysiological parameters, multiple echocardiographic parameters and evaluated various different characteristics. Testing of multiple variables can result in false positive statistical findings – an effect we can completely rule out in our study. However, we have *a priori* defined the statistical tests with appropriate power calculations for every major experiment as well as adjusted the p-value for multiple comparisons for several key analyses.

Final conclusion

In the end, I hope that this discussion highlighted why further research in the multifactorial mechanisms underlying DM-related cardiovascular complications and various novel therapeutical interventions is important. The field has numerous intertwined components and its relative contribution is often difficult to depict. At the same time, this presents many challenges and opportunities to create a meaningful contribution to the area that is growing in importance as the global prevalence DM is increasing. Based on all encouraging studies on animal models as well as early clinical trials I believe the further research in this intriguing area will be fruitful and rewarding.

REFERENCES

1. International Diabetes Federation. IDF Diabetes Atlas. 9th ed2019.
2. Danaei G, Finucane MM, Lu Y, Singh GM, Cowan MJ, Paciorek CJ, et al. National, regional, and global trends in fasting plasma glucose and diabetes prevalence since 1980: systematic analysis of health examination surveys and epidemiological studies with 370 country-years and 2.7 million participants. Lancet. 2011;378(9785):31-40. doi: 10.1016/S0140-6736(11)60679-X. PubMed PMID: 21705069.
3. Saeedi P, Petersohn I, Salpea P, Malanda B, Karuranga S, Unwin N, et al. Global and regional diabetes prevalence estimates for 2019 and projections for 2030 and 2045: Results from the International Diabetes Federation Diabetes Atlas, 9(th) edition. Diabetes Res Clin Pract. 2019;157:107843. Epub 2019/09/14. doi: 10.1016/j.diabres.2019.107843. PubMed PMID: 31518657.
4. Forbes JM, Cooper ME. Mechanisms of diabetic complications. Physiological reviews. 2013;93(1):137-88. doi: 10.1152/physrev.00045.2011. PubMed PMID: 23303908.
5. Organization WH. TADDS: Tool for assessment of diabetes and diabetic retinopathy Geneva2015. Available from: https://www.who.int/blindness/publications/TADDS_ENG.pdf.
6. Adler AI, Stevens RJ, Manley SE, Bilous RW, Cull CA, Holman RR, et al. Development and progression of nephropathy in type 2 diabetes: the United Kingdom Prospective Diabetes Study (UKPDS 64). Kidney Int. 2003;63(1):225-32. Epub 2002/12/11. doi: 10.1046/j.1523-1755.2003.00712.x. PubMed PMID: 12472787.
7. National Institutes of Health. 2018 USRDS Annual Data Report: Epidemiology of Kidney Disease in the United States Bethesda: National Institutes of Health, National Institute of Diabetes and Digestive and Kidney Diseases; [cited 2019 31 October]. Available from: https://www.usrds.org/2018/view/Default.aspx.
8. Sobhani S, Asayesh H, Sharifi F, Djalalinia S, Baradaran HR, Arzaghi SM, et al. Prevalence of diabetic peripheral neuropathy in Iran: a systematic review and meta-analysis. J Diabetes Metab Disord. 2014;13(1):97. Epub 2014/11/05. doi: 10.1186/s40200-014-0097-y. PubMed PMID: 25364702; PubMed Central PMCID: PMCPMC4215018.
9. Einarson TR, Acs A, Ludwig C, Panton UH. Prevalence of cardiovascular disease in type 2 diabetes: a systematic literature review of scientific evidence from across the world in 2007-2017. Cardiovasc Diabetol. 2018;17(1):83. Epub 2018/06/10. doi: 10.1186/s12933-018-0728-6. PubMed PMID: 29884191; PubMed Central PMCID: PMCPMC5994068.
10. Scholtens DM, Kuang A, Lowe LP, Hamilton J, Lawrence JM, Lebenthal Y, et al. Hyperglycemia and Adverse Pregnancy Outcome Follow-up Study (HAPO FUS): Maternal Glycemia and Childhood Glucose Metabolism. Diabetes Care. 2019;42(3):381-92. Epub 2019/01/09. doi: 10.2337/dc18-2021. PubMed PMID: 30617141; PubMed Central PMCID: PMCPMC6385697.
11. Crowther CA, Hiller JE, Moss JR, McPhee AJ, Jeffries WS, Robinson JS, et al. Effect of treatment of gestational diabetes mellitus on pregnancy outcomes. N Engl J

Med. 2005;352(24):2477-86. Epub 2005/06/14. doi: 10.1056/NEJMoa042973. PubMed PMID: 15951574.
12. Rao Kondapally Seshasai S, Kaptoge S, Thompson A, Di Angelantonio E, Gao P, Sarwar N, et al. Diabetes mellitus, fasting glucose, and risk of cause-specific death. N Engl J Med. 2011;364(9):829-41. Epub 2011/03/04. doi: 10.1056/NEJMoa1008862. PubMed PMID: 21366474; PubMed Central PMCID: PMCPMC4109980.
13. Cosentino F, Grant PJ, Aboyans V, Bailey CJ, Ceriello A, Delgado V, et al. 2019 ESC Guidelines on diabetes, pre-diabetes, and cardiovascular diseases developed in collaboration with the EASD. European heart journal. 2019. Epub 2019/09/10. doi: 10.1093/eurheartj/ehz486. PubMed PMID: 31497854.
14. Emerging Risk Factors C, Sarwar N, Gao P, Seshasai SR, Gobin R, Kaptoge S, et al. Diabetes mellitus, fasting blood glucose concentration, and risk of vascular disease: a collaborative meta-analysis of 102 prospective studies. Lancet. 2010;375(9733):2215-22. Epub 2010/07/09. doi: 10.1016/S0140-6736(10)60484-9. PubMed PMID: 20609967; PubMed Central PMCID: PMCPMC2904878.
15. Sattar N, Rawshani A, Franzen S, Rawshani A, Svensson AM, Rosengren A, et al. Age at Diagnosis of Type 2 Diabetes Mellitus and Associations With Cardiovascular and Mortality Risks. Circulation. 2019;139(19):2228-37. Epub 2019/04/09. doi: 10.1161/CIRCULATIONAHA.118.037885. PubMed PMID: 30955347.
16. Low Wang CC, Hess CN, Hiatt WR, Goldfine AB. Clinical Update: Cardiovascular Disease in Diabetes Mellitus: Atherosclerotic Cardiovascular Disease and Heart Failure in Type 2 Diabetes Mellitus - Mechanisms, Management, and Clinical Considerations. Circulation. 2016;133(24):2459-502. doi: 10.1161/CIRCULATIONAHA.116.022194. PubMed PMID: 27297342; PubMed Central PMCID: PMC4910510.
17. Elley CR, Kenealy T, Robinson E, Drury PL. Glycated haemoglobin and cardiovascular outcomes in people with Type 2 diabetes: a large prospective cohort study. Diabet Med. 2008;25(11):1295-301. Epub 2008/12/03. doi: 10.1111/j.1464-5491.2008.02581.x. PubMed PMID: 19046219.
18. Stratton IM, Adler AI, Neil HA, Matthews DR, Manley SE, Cull CA, et al. Association of glycaemia with macrovascular and microvascular complications of type 2 diabetes (UKPDS 35): prospective observational study. BMJ. 2000;321(7258):405-12. Epub 2000/08/11. doi: 10.1136/bmj.321.7258.405. PubMed PMID: 10938048; PubMed Central PMCID: PMCPMC27454.
19. Williams SB, Goldfine AB, Timimi FK, Ting HH, Roddy MA, Simonson DC, et al. Acute hyperglycemia attenuates endothelium-dependent vasodilation in humans in vivo. Circulation. 1998;97(17):1695-701. Epub 1998/05/20. doi: 10.1161/01.cir.97.17.1695. PubMed PMID: 9591763.
20. Perkins JM, Joy NG, Tate DB, Davis SN. Acute effects of hyperinsulinemia and hyperglycemia on vascular inflammatory biomarkers and endothelial function in overweight and obese humans. Am J Physiol Endocrinol Metab. 2015;309(2):E168-76. Epub 2015/05/28. doi: 10.1152/ajpendo.00064.2015. PubMed PMID: 26015434; PubMed Central PMCID: PMCPMC4504937.
21. Zheng XL, Yuan SG, Peng DQ. Phenotype-specific inhibition of the vascular smooth muscle cell cycle by high glucose treatment. Diabetologia. 2007;50(4):881-90. Epub 2007/03/06. doi: 10.1007/s00125-006-0543-6. PubMed PMID: 17334654.
22. Nishizawa T, Bornfeldt KE. Diabetic vascular disease and the potential role of macrophage glucose metabolism. Ann Med. 2012;44(6):555-63. Epub 2011/06/18. doi: 10.3109/07853890.2011.585346. PubMed PMID: 21679104; PubMed Central PMCID: PMCPMC3430835.

23. Tate M, Grieve DJ, Ritchie RH. Are targeted therapies for diabetic cardiomyopathy on the horizon? Clinical science. 2017;131(10):897-915. Epub 2017/05/06. doi: 10.1042/CS20160491. PubMed PMID: 28473471.
24. Grant PJ, Cosentino F. The 2019 ESC Guidelines on diabetes, pre-diabetes, and cardiovascular diseases developed in collaboration with the EASD: New features and the 'Ten Commandments' of the 2019 Guidelines are discussed by Professor Peter J. Grant and Professor Francesco Cosentino, the Task Force chairmen. European heart journal. 2019;40(39):3215-7. Epub 2019/10/15. doi: 10.1093/eurheartj/ehz687. PubMed PMID: 31608951.
25. Writing Committee Members, Yancy CW, Jessup M, Bozkurt B, Butler J, Casey DE, Jr., et al. 2013 ACCF/AHA guideline for the management of heart failure: a report of the American College of Cardiology Foundation/American Heart Association Task Force on practice guidelines. Circulation. 2013;128(16):e240-327. Epub 2013/06/07. doi: 10.1161/CIR.0b013e31829e8776. PubMed PMID: 23741058.
26. Kannel WB, Hjortland M, Castelli WP. Role of diabetes in congestive heart failure: the Framingham study. The American journal of cardiology. 1974;34(1):29-34. Epub 1974/07/01. doi: 10.1016/0002-9149(74)90089-7. PubMed PMID: 4835750.
27. Klajda MD, Scott CG, Rodeheffer RJ, Chen HH. Diabetes Mellitus Is an Independent Predictor for the Development of Heart Failure: A Population Study. Mayo Clin Proc. 2020;95(1):124-33. Epub 2020/01/07. doi: 10.1016/j.mayocp.2019.07.008. PubMed PMID: 31902407.
28. Holscher ME, Bode C, Bugger H. Diabetic Cardiomyopathy: Does the Type of Diabetes Matter? Int J Mol Sci. 2016;17(12). Epub 2016/12/22. doi: 10.3390/ijms17122136. PubMed PMID: 27999359; PubMed Central PMCID: PMCPMC5187936.
29. Jia G, Hill MA, Sowers JR. Diabetic Cardiomyopathy: An Update of Mechanisms Contributing to This Clinical Entity. Circ Res. 2018;122(4):624-38. Epub 2018/02/17. doi: 10.1161/CIRCRESAHA.117.311586. PubMed PMID: 29449364; PubMed Central PMCID: PMCPMC5819359.
30. Bluemke DA, Kronmal RA, Lima JA, Liu K, Olson J, Burke GL, et al. The relationship of left ventricular mass and geometry to incident cardiovascular events: the MESA (Multi-Ethnic Study of Atherosclerosis) study. J Am Coll Cardiol. 2008;52(25):2148-55. Epub 2008/12/20. doi: 10.1016/j.jacc.2008.09.014. PubMed PMID: 19095132; PubMed Central PMCID: PMCPMC2706368.
31. Riehle C, Bauersachs J. Of mice and men: models and mechanisms of diabetic cardiomyopathy. Basic research in cardiology. 2018;114(1):2. Epub 2018/11/18. doi: 10.1007/s00395-018-0711-0. PubMed PMID: 30443826; PubMed Central PMCID: PMCPMC6244639.
32. Bugger H, Abel ED. Rodent models of diabetic cardiomyopathy. Dis Model Mech. 2009;2(9-10):454-66. Epub 2009/09/04. doi: 10.1242/dmm.001941. PubMed PMID: 19726805.
33. Seferovic PM, Paulus WJ. Clinical diabetic cardiomyopathy: a two-faced disease with restrictive and dilated phenotypes. European heart journal. 2015;36(27):1718-27, 27a-27c. Epub 2015/04/19. doi: 10.1093/eurheartj/ehv134. PubMed PMID: 25888006.
34. Levelt E, Gulsin G, Neubauer S, McCann GP. MECHANISMS IN ENDOCRINOLOGY: Diabetic cardiomyopathy: pathophysiology and potential metabolic interventions state of the art review. Eur J Endocrinol. 2018;178(4):R127-R39. Epub 2018/02/15. doi: 10.1530/EJE-17-0724. PubMed PMID: 29440374; PubMed Central PMCID: PMCPMC5863473.

35. McGavock JM, Lingvay I, Zib I, Tillery T, Salas N, Unger R, et al. Cardiac steatosis in diabetes mellitus: a 1H-magnetic resonance spectroscopy study. Circulation. 2007;116(10):1170-5. Epub 2007/08/19. doi: 10.1161/CIRCULATIONAHA.106.645614. PubMed PMID: 17698735.
36. Anderson EJ, Kypson AP, Rodriguez E, Anderson CA, Lehr EJ, Neufer PD. Substrate-specific derangements in mitochondrial metabolism and redox balance in the atrium of the type 2 diabetic human heart. Journal of the American College of Cardiology. 2009;54(20):1891-8. doi: 10.1016/j.jacc.2009.07.031. PubMed PMID: 19892241; PubMed Central PMCID: PMC2800130.
37. Anderson EJ, Rodriguez E, Anderson CA, Thayne K, Chitwood WR, Kypson AP. Increased propensity for cell death in diabetic human heart is mediated by mitochondrial-dependent pathways. American journal of physiology Heart and circulatory physiology. 2011;300(1):H118-24. doi: 10.1152/ajpheart.00932.2010. PubMed PMID: 21076025; PubMed Central PMCID: PMC3023249.
38. Cai L, Kang YJ. Oxidative stress and diabetic cardiomyopathy: a brief review. Cardiovasc Toxicol. 2001;1(3):181-93. Epub 2002/09/06. doi: 10.1385/ct:1:3:181. PubMed PMID: 12213971.
39. Kakkar R, Kalra J, Mantha SV, Prasad K. Lipid peroxidation and activity of antioxidant enzymes in diabetic rats. Mol Cell Biochem. 1995;151(2):113-9. Epub 1995/10/18. doi: 10.1007/bf01322333. PubMed PMID: 8569756.
40. Ohkuwa T, Sato Y, Naoi M. Hydroxyl radical formation in diabetic rats induced by streptozotocin. Life Sci. 1995;56(21):1789-98. Epub 1995/01/01. doi: 10.1016/0024-3205(95)00150-5. PubMed PMID: 7739353.
41. Serpillon S, Floyd BC, Gupte RS, George S, Kozicky M, Neito V, et al. Superoxide production by NAD(P)H oxidase and mitochondria is increased in genetically obese and hyperglycemic rat heart and aorta before the development of cardiac dysfunction. The role of glucose-6-phosphate dehydrogenase-derived NADPH. American journal of physiology Heart and circulatory physiology. 2009;297(1):H153-62. doi: 10.1152/ajpheart.01142.2008. PubMed PMID: 19429815; PubMed Central PMCID: PMC2711743.
42. Kajstura J, Fiordaliso F, Andreoli AM, Li B, Chimenti S, Medow MS, et al. IGF-1 overexpression inhibits the development of diabetic cardiomyopathy and angiotensin II-mediated oxidative stress. Diabetes. 2001;50(6):1414-24. Epub 2001/05/26. doi: 10.2337/diabetes.50.6.1414. PubMed PMID: 11375343.
43. Faria A, Persaud SJ. Cardiac oxidative stress in diabetes: Mechanisms and therapeutic potential. Pharmacology & therapeutics. 2017;172:50-62. Epub 2016/12/06. doi: 10.1016/j.pharmthera.2016.11.013. PubMed PMID: 27916650.
44. Elangovan V, Shohami E, Gati I, Kohen R. Increased hepatic lipid soluble antioxidant capacity as compared to other organs of streptozotocin-induced diabetic rats: a cyclic voltammetry study. Free Radic Res. 2000;32(2):125-34. Epub 2000/02/01. doi: 10.1080/10715760000300131. PubMed PMID: 10653483.
45. Wolff SP, Jiang ZY, Hunt JV. Protein glycation and oxidative stress in diabetes mellitus and ageing. Free Radic Biol Med. 1991;10(5):339-52. Epub 1991/01/01. doi: 10.1016/0891-5849(91)90040-a. PubMed PMID: 1855674.
46. Yeh CH, Sturgis L, Haidacher J, Zhang XN, Sherwood SJ, Bjercke RJ, et al. Requirement for p38 and p44/p42 mitogen-activated protein kinases in RAGE-mediated nuclear factor-kappaB transcriptional activation and cytokine secretion. Diabetes. 2001;50(6):1495-504. Epub 2001/05/26. doi: 10.2337/diabetes.50.6.1495. PubMed PMID: 11375353.

47. Volpe CMO, Villar-Delfino PH, Dos Anjos PMF, Nogueira-Machado JA. Cellular death, reactive oxygen species (ROS) and diabetic complications. Cell Death Dis. 2018;9(2):119. Epub 2018/01/27. doi: 10.1038/s41419-017-0135-z. PubMed PMID: 29371661; PubMed Central PMCID: PMCPMC5833737.
48. Teshima Y, Takahashi N, Nishio S, Saito S, Kondo H, Fukui A, et al. Production of reactive oxygen species in the diabetic heart. Roles of mitochondria and NADPH oxidase. Circ J. 2014;78(2):300-6. Epub 2013/12/18. doi: 10.1253/circj.cj-13-1187. PubMed PMID: 24334638.
49. Jo H, Otani H, Jo F, Shimazu T, Okazaki T, Yoshioka K, et al. Inhibition of nitric oxide synthase uncoupling by sepiapterin improves left ventricular function in streptozotocin-induced diabetic mice. Clin Exp Pharmacol Physiol. 2011;38(8):485-93. Epub 2011/05/11. doi: 10.1111/j.1440-1681.2011.05535.x. PubMed PMID: 21554376.
50. Simon JN, Ziberna K, Casadei B. Compromised redox homeostasis, altered nitroso-redox balance, and therapeutic possibilities in atrial fibrillation. Cardiovasc Res. 2016;109(4):510-8. Epub 2016/01/21. doi: 10.1093/cvr/cvw012. PubMed PMID: 26786158; PubMed Central PMCID: PMCPMC4777914.
51. Du X, Matsumura T, Edelstein D, Rossetti L, Zsengeller Z, Szabo C, et al. Inhibition of GAPDH activity by poly(ADP-ribose) polymerase activates three major pathways of hyperglycemic damage in endothelial cells. The Journal of clinical investigation. 2003;112(7):1049-57. Epub 2003/10/03. doi: 10.1172/JCI18127. PubMed PMID: 14523042; PubMed Central PMCID: PMCPMC198524.
52. Siwik DA, Pagano PJ, Colucci WS. Oxidative stress regulates collagen synthesis and matrix metalloproteinase activity in cardiac fibroblasts. Am J Physiol Cell Physiol. 2001;280(1):C53-60. Epub 2000/12/21. doi: 10.1152/ajpcell.2001.280.1.C53. PubMed PMID: 11121376.
53. Schilling JD, Mann DL. Diabetic cardiomyopathy: bench to bedside. Heart Fail Clin. 2012;8(4):619-31. Epub 2012/09/25. doi: 10.1016/j.hfc.2012.06.007. PubMed PMID: 22999244; PubMed Central PMCID: PMCPMC3457018.
54. Mann DL. Inflammatory mediators and the failing heart: past, present, and the foreseeable future. Circ Res. 2002;91(11):988-98. Epub 2002/11/29. doi: 10.1161/01.res.0000043825.01705.1b. PubMed PMID: 12456484.
55. Fuentes-Antras J, Ioan AM, Tunon J, Egido J, Lorenzo O. Activation of toll-like receptors and inflammasome complexes in the diabetic cardiomyopathy-associated inflammation. Int J Endocrinol. 2014;2014:847827. Epub 2014/04/20. doi: 10.1155/2014/847827. PubMed PMID: 24744784; PubMed Central PMCID: PMCPMC3972909.
56. Kuethe F, Sigusch HH, Bornstein SR, Hilbig K, Kamvissi V, Figulla HR. Apoptosis in patients with dilated cardiomyopathy and diabetes: a feature of diabetic cardiomyopathy? Horm Metab Res. 2007;39(9):672-6. Epub 2007/09/12. doi: 10.1055/s-2007-985823. PubMed PMID: 17846975.
57. Jia G, DeMarco VG, Sowers JR. Insulin resistance and hyperinsulinaemia in diabetic cardiomyopathy. Nature reviews Endocrinology. 2016;12(3):144-53. Epub 2015/12/19. doi: 10.1038/nrendo.2015.216. PubMed PMID: 26678809; PubMed Central PMCID: PMCPMC4753054.
58. Bugger H, Abel ED. Mitochondria in the diabetic heart. Cardiovascular research. 2010;88(2):229-40. doi: 10.1093/cvr/cvq239. PubMed PMID: 20639213; PubMed Central PMCID: PMC2952534.
59. Mandavia CH, Aroor AR, Demarco VG, Sowers JR. Molecular and metabolic mechanisms of cardiac dysfunction in diabetes. Life Sci. 2013;92(11):601-8. Epub

2012/11/14. doi: 10.1016/j.lfs.2012.10.028. PubMed PMID: 23147391; PubMed Central PMCID: PMCPMC3594135.
60. Shah RV, Abbasi SA, Kwong RY. Role of cardiac MRI in diabetes. Curr Cardiol Rep. 2014;16(2):449. Epub 2014/01/17. doi: 10.1007/s11886-013-0449-0. PubMed PMID: 24430012; PubMed Central PMCID: PMCPMC3965673.
61. Knuuti J, Takala TO, Nagren K, Sipila H, Turpeinen AK, Uusitupa MI, et al. Myocardial fatty acid oxidation in patients with impaired glucose tolerance. Diabetologia. 2001;44(2):184-7. Epub 2001/03/29. doi: 10.1007/s001250051597. PubMed PMID: 11270674.
62. Trueblood N, Ramasamy R. Aldose reductase inhibition improves altered glucose metabolism of isolated diabetic rat hearts. Am J Physiol. 1998;275(1):H75-83. Epub 1998/08/05. doi: 10.1152/ajpheart.1998.275.1.H75. PubMed PMID: 9688898.
63. Nishikawa T, Edelstein D, Du XL, Yamagishi S, Matsumura T, Kaneda Y, et al. Normalizing mitochondrial superoxide production blocks three pathways of hyperglycaemic damage. Nature. 2000;404(6779):787-90. Epub 2000/04/28. doi: 10.1038/35008121. PubMed PMID: 10783895.
64. D'Souza A, Howarth FC, Yanni J, Dobryznski H, Boyett MR, Adeghate E, et al. Left ventricle structural remodelling in the prediabetic Goto-Kakizaki rat. Exp Physiol. 2011;96(9):875-88. Epub 2011/05/31. doi: 10.1113/expphysiol.2011.058271. PubMed PMID: 21622965.
65. Mizushige K, Yao L, Noma T, Kiyomoto H, Yu Y, Hosomi N, et al. Alteration in left ventricular diastolic filling and accumulation of myocardial collagen at insulin-resistant prediabetic stage of a type II diabetic rat model. Circulation. 2000;101(8):899-907. Epub 2000/03/01. doi: 10.1161/01.cir.101.8.899. PubMed PMID: 10694530.
66. Westermann D, Rutschow S, Jager S, Linderer A, Anker S, Riad A, et al. Contributions of inflammation and cardiac matrix metalloproteinase activity to cardiac failure in diabetic cardiomyopathy: the role of angiotensin type 1 receptor antagonism. Diabetes. 2007;56(3):641-6. Epub 2007/03/01. doi: 10.2337/db06-1163. PubMed PMID: 17327431.
67. Aronson D. Cross-linking of glycated collagen in the pathogenesis of arterial and myocardial stiffening of aging and diabetes. J Hypertens. 2003;21(1):3-12. Epub 2003/01/25. doi: 10.1097/00004872-200301000-00002. PubMed PMID: 12544424.
68. Yamagishi S, Maeda S, Matsui T, Ueda S, Fukami K, Okuda S. Role of advanced glycation end products (AGEs) and oxidative stress in vascular complications in diabetes. Biochim Biophys Acta. 2012;1820(5):663-71. Epub 2011/03/29. doi: 10.1016/j.bbagen.2011.03.014. PubMed PMID: 21440603.
69. Candido R, Forbes JM, Thomas MC, Thallas V, Dean RG, Burns WC, et al. A breaker of advanced glycation end products attenuates diabetes-induced myocardial structural changes. Circ Res. 2003;92(7):785-92. Epub 2003/03/08. doi: 10.1161/01.RES.0000065620.39919.20. PubMed PMID: 12623881.
70. Li J, Ma W, Yue G, Tang Y, Kim IM, Weintraub NL, et al. Cardiac proteasome functional insufficiency plays a pathogenic role in diabetic cardiomyopathy. J Mol Cell Cardiol. 2017;102:53-60. Epub 2016/12/04. doi: 10.1016/j.yjmcc.2016.11.013. PubMed PMID: 27913284; PubMed Central PMCID: PMCPMC5316366.
71. Wang X, Li J, Zheng H, Su H, Powell SR. Proteasome functional insufficiency in cardiac pathogenesis. Am J Physiol Heart Circ Physiol. 2011;301(6):H2207-19. Epub 2011/09/29. doi: 10.1152/ajpheart.00714.2011. PubMed PMID: 21949118; PubMed Central PMCID: PMCPMC3233812.
72. Feng B, Chen S, Chiu J, George B, Chakrabarti S. Regulation of cardiomyocyte hypertrophy in diabetes at the transcriptional level. Am J Physiol Endocrinol Metab.

2008;294(6):E1119-26. Epub 2008/04/17. doi: 10.1152/ajpendo.00029.2008. PubMed PMID: 18413674.
73. Kumar R, Yong QC, Thomas CM, Baker KM. Intracardiac intracellular angiotensin system in diabetes. Am J Physiol Regul Integr Comp Physiol. 2012;302(5):R510-7. Epub 2011/12/16. doi: 10.1152/ajpregu.00512.2011. PubMed PMID: 22170614; PubMed Central PMCID: PMCPMC3311519.
74. Yaras N, Ugur M, Ozdemir S, Gurdal H, Purali N, Lacampagne A, et al. Effects of diabetes on ryanodine receptor Ca release channel (RyR2) and Ca2+ homeostasis in rat heart. Diabetes. 2005;54(11):3082-8. Epub 2005/10/27. doi: 10.2337/diabetes.54.11.3082. PubMed PMID: 16249429.
75. Chattou S, Diacono J, Feuvray D. Decrease in sodium-calcium exchange and calcium currents in diabetic rat ventricular myocytes. Acta Physiol Scand. 1999;166(2):137-44. Epub 1999/06/26. doi: 10.1046/j.1365-201x.1999.00547.x. PubMed PMID: 10383493.
76. Belke DD, Swanson EA, Dillmann WH. Decreased sarcoplasmic reticulum activity and contractility in diabetic db/db mouse heart. Diabetes. 2004;53(12):3201-8. Epub 2004/11/25. doi: 10.2337/diabetes.53.12.3201. PubMed PMID: 15561951.
77. Waddingham MT, Edgley AJ, Tsuchimochi H, Kelly DJ, Shirai M, Pearson JT. Contractile apparatus dysfunction early in the pathophysiology of diabetic cardiomyopathy. World J Diabetes. 2015;6(7):943-60. Epub 2015/07/18. doi: 10.4239/wjd.v6.i7.943. PubMed PMID: 26185602; PubMed Central PMCID: PMCPMC4499528.
78. Lebeche D, Davidoff AJ, Hajjar RJ. Interplay between impaired calcium regulation and insulin signaling abnormalities in diabetic cardiomyopathy. Nat Clin Pract Cardiovasc Med. 2008;5(11):715-24. Epub 2008/09/25. doi: 10.1038/ncpcardio1347. PubMed PMID: 18813212.
79. Serhiyenko VA, Serhiyenko AA. Cardiac autonomic neuropathy: Risk factors, diagnosis and treatment. World J Diabetes. 2018;9(1):1-24. Epub 2018/01/24. doi: 10.4239/wjd.v9.i1.1. PubMed PMID: 29359025; PubMed Central PMCID: PMCPMC5763036.
80. Pop-Busui R, Kirkwood I, Schmid H, Marinescu V, Schroeder J, Larkin D, et al. Sympathetic dysfunction in type 1 diabetes: association with impaired myocardial blood flow reserve and diastolic dysfunction. J Am Coll Cardiol. 2004;44(12):2368-74. Epub 2004/12/21. doi: 10.1016/j.jacc.2004.09.033. PubMed PMID: 15607400.
81. Bisognano JD, Weinberger HD, Bohlmeyer TJ, Pende A, Raynolds MV, Sastravaha A, et al. Myocardial-directed overexpression of the human beta(1)-adrenergic receptor in transgenic mice. J Mol Cell Cardiol. 2000;32(5):817-30. Epub 2000/04/25. doi: 10.1006/jmcc.2000.1123. PubMed PMID: 10775486.
82. Andrade J, Khairy P, Dobrev D, Nattel S. The Clinical Profile and Pathophysiology of Atrial Fibrillation: Relationships Among Clinical Features, Epidemiology, and Mechanisms. Circulation Research. 2014;114(9):1453-68. doi: 10.1161/circresaha.114.303211.
83. Marini C, De Santis F, Sacco S, Russo T, Olivieri L, Totaro R, et al. Contribution of atrial fibrillation to incidence and outcome of ischemic stroke: results from a population-based study. Stroke; a journal of cerebral circulation. 2005;36(6):1115-9. doi: 10.1161/01.STR.0000166053.83476.4a. PubMed PMID: 15879330.
84. Friberg L, Rosenqvist M, Lindgren A, Terent A, Norrving B, Asplund K. High prevalence of atrial fibrillation among patients with ischemic stroke. Stroke; a journal of

cerebral circulation. 2014;45(9):2599-605. doi: 10.1161/STROKEAHA.114.006070. PubMed PMID: 25034713.
85. Ball J, Carrington MJ, McMurray JJ, Stewart S. Atrial fibrillation: profile and burden of an evolving epidemic in the 21st century. International journal of cardiology. 2013;167(5):1807-24. doi: 10.1016/j.ijcard.2012.12.093. PubMed PMID: 23380698.
86. Go AS, Hylek EM, Phillips KA, Chang Y, Henault LE, Selby JV, et al. Prevalence of diagnosed atrial fibrillation in adults: national implications for rhythm management and stroke prevention: the AnTicoagulation and Risk Factors in Atrial Fibrillation (ATRIA) Study. Jama. 2001;285(18):2370-5. PubMed PMID: 11343485.
87. Benjamin EJ, Levy D, Vaziri SM, D'Agostino RB, Belanger AJ, Wolf PA. Independent risk factors for atrial fibrillation in a population-based cohort. The Framingham Heart Study. Jama. 1994;271(11):840-4. PubMed PMID: 8114238.
88. Watanabe H, Tanabe N, Watanabe T, Darbar D, Roden DM, Sasaki S, et al. Metabolic syndrome and risk of development of atrial fibrillation: the Niigata preventive medicine study. Circulation. 2008;117(10):1255-60. doi: 10.1161/CIRCULATIONAHA.107.744466. PubMed PMID: 18285562; PubMed Central PMCID: PMC2637133.
89. Dublin S, Glazer NL, Smith NL, Psaty BM, Lumley T, Wiggins KL, et al. Diabetes mellitus, glycemic control, and risk of atrial fibrillation. Journal of general internal medicine. 2010;25(8):853-8. doi: 10.1007/s11606-010-1340-y. PubMed PMID: 20405332; PubMed Central PMCID: PMC2896589.
90. Psaty BM, Manolio TA, Kuller LH, Kronmal RA, Cushman M, Fried LP, et al. Incidence of and risk factors for atrial fibrillation in older adults. Circulation. 1997;96(7):2455-61. PubMed PMID: 9337224.
91. Huxley RR, Filion KB, Konety S, Alonso A. Meta-analysis of cohort and case-control studies of type 2 diabetes mellitus and risk of atrial fibrillation. The American journal of cardiology. 2011;108(1):56-62. doi: 10.1016/j.amjcard.2011.03.004. PubMed PMID: 21529739; PubMed Central PMCID: PMC3181495.
92. Dahlqvist S, Rosengren A, Gudbjornsdottir S, Pivodic A, Wedel H, Kosiborod M, et al. Risk of atrial fibrillation in people with type 1 diabetes compared with matched controls from the general population: a prospective case-control study. Lancet Diabetes Endocrinol. 2017;5(10):799-807. Epub 2017/08/26. doi: 10.1016/S2213-8587(17)30262-0. PubMed PMID: 28838683.
93. Huxley RR, Alonso A, Lopez FL, Filion KB, Agarwal SK, Loehr LR, et al. Type 2 diabetes, glucose homeostasis and incident atrial fibrillation: the Atherosclerosis Risk in Communities study. Heart. 2012;98(2):133-8. doi: 10.1136/heartjnl-2011-300503. PubMed PMID: 21930722; PubMed Central PMCID: PMC3237721.
94. Fatemi O, Yuriditsky E, Tsioufis C, Tsachris D, Morgan T, Basile J, et al. Impact of intensive glycemic control on the incidence of atrial fibrillation and associated cardiovascular outcomes in patients with type 2 diabetes mellitus (from the Action to Control Cardiovascular Risk in Diabetes Study). Am J Cardiol. 2014;114(8):1217-22. Epub 2014/08/28. doi: 10.1016/j.amjcard.2014.07.045. PubMed PMID: 25159234; PubMed Central PMCID: PMCPMC4291278.
95. Ko SH, Park YM, Yun JS, Cha SA, Choi EK, Han K, et al. Severe hypoglycemia is a risk factor for atrial fibrillation in type 2 diabetes mellitus: Nationwide population-based cohort study. J Diabetes Complications. 2018;32(2):157-63. Epub 2017/12/03. doi: 10.1016/j.jdiacomp.2017.09.009. PubMed PMID: 29196120; PubMed Central PMCID: PMCPMC6278599.

96. Odeh M, Oliven A, Bassan H. Transient atrial fibrillation precipitated by hypoglycemia. Ann Emerg Med. 1990;19(5):565-7. Epub 1990/05/01. doi: 10.1016/s0196-0644(05)82191-2. PubMed PMID: 2331103.
97. Saito S, Teshima Y, Fukui A, Kondo H, Nishio S, Nakagawa M, et al. Glucose fluctuations increase the incidence of atrial fibrillation in diabetic rats. Cardiovascular research. 2014;104(1):5-14. doi: 10.1093/cvr/cvu176. PubMed PMID: 25082849.
98. Wang TJ, Parise H, Levy D, D'Agostino RB, Sr., Wolf PA, Vasan RS, et al. Obesity and the risk of new-onset atrial fibrillation. Jama. 2004;292(20):2471-7. doi: 10.1001/jama.292.20.2471. PubMed PMID: 15562125.
99. Dublin S, French B, Glazer NL, Wiggins KL, Lumley T, Psaty BM, et al. Risk of new-onset atrial fibrillation in relation to body mass index. Archives of internal medicine. 2006;166(21):2322-8. doi: 10.1001/archinte.166.21.2322. PubMed PMID: 17130384.
100. Wakili R, Voigt N, Kaab S, Dobrev D, Nattel S. Recent advances in the molecular pathophysiology of atrial fibrillation. The Journal of clinical investigation. 2011;121(8):2955-68. Epub 2011/08/02. doi: 10.1172/JCI46315. PubMed PMID: 21804195; PubMed Central PMCID: PMCPMC3148739.
101. Haissaguerre M, Jais P, Shah DC, Takahashi A, Hocini M, Quiniou G, et al. Spontaneous initiation of atrial fibrillation by ectopic beats originating in the pulmonary veins. The New England journal of medicine. 1998;339(10):659-66. Epub 1998/09/03. doi: 10.1056/NEJM199809033391003. PubMed PMID: 9725923.
102. Nerbonne JM, Kass RS. Molecular physiology of cardiac repolarization. Physiological reviews. 2005;85(4):1205-53. Epub 2005/09/27. doi: 10.1152/physrev.00002.2005. PubMed PMID: 16183911.
103. Nishida K, Michael G, Dobrev D, Nattel S. Animal models for atrial fibrillation: clinical insights and scientific opportunities. Europace : European pacing, arrhythmias, and cardiac electrophysiology : journal of the working groups on cardiac pacing, arrhythmias, and cardiac cellular electrophysiology of the European Society of Cardiology. 2010;12(2):160-72. Epub 2009/10/31. doi: 10.1093/europace/eup328. PubMed PMID: 19875395.
104. Schotten U, Verheule S, Kirchhof P, Goette A. Pathophysiological mechanisms of atrial fibrillation: a translational appraisal. Physiological reviews. 2011;91(1):265-325. Epub 2011/01/21. doi: 10.1152/physrev.00031.2009. PubMed PMID: 21248168.
105. Dobrev D, Wehrens XHT. Calcium-mediated cellular triggered activity in atrial fibrillation. The Journal of physiology. 2017;595(12):4001-8. Epub 2017/02/10. doi: 10.1113/JP273048. PubMed PMID: 28181690; PubMed Central PMCID: PMCPMC5471363.
106. Katra RP, Laurita KR. Cellular mechanism of calcium-mediated triggered activity in the heart. Circ Res. 2005;96(5):535-42. Epub 2005/02/19. doi: 10.1161/01.RES.0000159387.00749.3c. PubMed PMID: 15718502.
107. January CT, Riddle JM. Early afterdepolarizations: mechanism of induction and block. A role for L-type Ca2+ current. Circ Res. 1989;64(5):977-90. Epub 1989/05/01. doi: 10.1161/01.res.64.5.977. PubMed PMID: 2468430.
108. Mandapati R, Skanes A, Chen J, Berenfeld O, Jalife J. Stable microreentrant sources as a mechanism of atrial fibrillation in the isolated sheep heart. Circulation. 2000;101(2):194-9. Epub 2000/01/19. doi: 10.1161/01.cir.101.2.194. PubMed PMID: 10637208.
109. Pappone C, Rosanio S, Oreto G, Tocchi M, Gugliotta F, Vicedomini G, et al. Circumferential radiofrequency ablation of pulmonary vein ostia: A new anatomic

approach for curing atrial fibrillation. Circulation. 2000;102(21):2619-28. Epub 2000/11/22. doi: 10.1161/01.cir.102.21.2619. PubMed PMID: 11085966.
110. Miller JM, Kowal RC, Swarup V, Daubert JP, Daoud EG, Day JD, et al. Initial independent outcomes from focal impulse and rotor modulation ablation for atrial fibrillation: multicenter FIRM registry. Journal of cardiovascular electrophysiology. 2014;25(9):921-9. Epub 2014/06/21. doi: 10.1111/jce.12474. PubMed PMID: 24948520; PubMed Central PMCID: PMCPMC4282180.
111. Allessie MA, de Groot NM, Houben RP, Schotten U, Boersma E, Smeets JL, et al. Electropathological substrate of long-standing persistent atrial fibrillation in patients with structural heart disease: longitudinal dissociation. Circulation Arrhythmia and electrophysiology. 2010;3(6):606-15. Epub 2010/08/20. doi: 10.1161/CIRCEP.109.910125. PubMed PMID: 20719881.
112. Staerk L, Sherer JA, Ko D, Benjamin EJ, Helm RH. Atrial Fibrillation: Epidemiology, Pathophysiology, and Clinical Outcomes. Circ Res. 2017;120(9):1501-17. doi: 10.1161/CIRCRESAHA.117.309732. PubMed PMID: 28450367; PubMed Central PMCID: PMC5500874.
113. Wijffels MC, Kirchhof CJ, Dorland R, Allessie MA. Atrial fibrillation begets atrial fibrillation. A study in awake chronically instrumented goats. Circulation. 1995;92(7):1954-68. Epub 1995/10/01. doi: 10.1161/01.cir.92.7.1954. PubMed PMID: 7671380.
114. Shiroshita-Takeshita A, Mitamura H, Ogawa S, Nattel S. Rate-dependence of atrial tachycardia effects on atrial refractoriness and atrial fibrillation maintenance. Cardiovascular research. 2009;81(1):90-7. Epub 2008/09/20. doi: 10.1093/cvr/cvn249. PubMed PMID: 18801748.
115. Yue L, Feng J, Gaspo R, Li GR, Wang Z, Nattel S. Ionic remodeling underlying action potential changes in a canine model of atrial fibrillation. Circ Res. 1997;81(4):512-25. Epub 1997/10/07. doi: 10.1161/01.res.81.4.512. PubMed PMID: 9314832.
116. Sossalla S, Kallmeyer B, Wagner S, Mazur M, Maurer U, Toischer K, et al. Altered Na(+) currents in atrial fibrillation effects of ranolazine on arrhythmias and contractility in human atrial myocardium. Journal of the American College of Cardiology. 2010;55(21):2330-42. Epub 2010/05/22. doi: 10.1016/j.jacc.2009.12.055. PubMed PMID: 20488304.
117. Burstein B, Comtois P, Michael G, Nishida K, Villeneuve L, Yeh YH, et al. Changes in connexin expression and the atrial fibrillation substrate in congestive heart failure. Circ Res. 2009;105(12):1213-22. Epub 2009/10/31. doi: 10.1161/CIRCRESAHA.108.183400. PubMed PMID: 19875729.
118. Dhein S, Hagen A, Jozwiak J, Dietze A, Garbade J, Barten M, et al. Improving cardiac gap junction communication as a new antiarrhythmic mechanism: the action of antiarrhythmic peptides. Naunyn Schmiedebergs Arch Pharmacol. 2010;381(3):221-34. Epub 2009/11/28. doi: 10.1007/s00210-009-0473-1. PubMed PMID: 19943035.
119. Ausma J, van der Velden HM, Lenders MH, van Ankeren EP, Jongsma HJ, Ramaekers FC, et al. Reverse structural and gap-junctional remodeling after prolonged atrial fibrillation in the goat. Circulation. 2003;107(15):2051-8. Epub 2003/04/19. doi: 10.1161/01.CIR.0000062689.04037.3F. PubMed PMID: 12681996.
120. Gollob MH, Jones DL, Krahn AD, Danis L, Gong XQ, Shao Q, et al. Somatic mutations in the connexin 40 gene (GJA5) in atrial fibrillation. The New England journal of medicine. 2006;354(25):2677-88. Epub 2006/06/23. doi: 10.1056/NEJMoa052800. PubMed PMID: 16790700.

121. Sinno H, Derakhchan K, Libersan D, Merhi Y, Leung TK, Nattel S. Atrial ischemia promotes atrial fibrillation in dogs. Circulation. 2003;107(14):1930-6. Epub 2003/04/02. doi: 10.1161/01.CIR.0000058743.15215.03. PubMed PMID: 12668526.
122. Kato T, Yamashita T, Sekiguchi A, Tsuneda T, Sagara K, Takamura M, et al. AGEs-RAGE system mediates atrial structural remodeling in the diabetic rat. Journal of cardiovascular electrophysiology. 2008;19(4):415-20. doi: 10.1111/j.1540-8167.2007.01037.x. PubMed PMID: 18298515.
123. Li B, Pan Y, Li X. Type 2 Diabetes Induces Prolonged P-wave Duration without Left Atrial Enlargement. Journal of Korean medical science. 2016;31(4):525-34. doi: 10.3346/jkms.2016.31.4.525. PubMed PMID: 27051235; PubMed Central PMCID: PMC4810334.
124. Schotten U, Dobrev D, Platonov PG, Kottkamp H, Hindricks G. Current controversies in determining the main mechanisms of atrial fibrillation. J Intern Med. 2016;279(5):428-38. Epub 2016/03/19. doi: 10.1111/joim.12492. PubMed PMID: 26991914.
125. Kato T, Yamashita T, Sekiguchi A, Sagara K, Takamura M, Takata S, et al. What are arrhythmogenic substrates in diabetic rat atria? Journal of cardiovascular electrophysiology. 2006;17(8):890-4. doi: 10.1111/j.1540-8167.2006.00528.x. PubMed PMID: 16759295.
126. Liu C, Fu H, Li J, Yang W, Cheng L, Liu T, et al. Hyperglycemia aggravates atrial interstitial fibrosis, ionic remodeling and vulnerability to atrial fibrillation in diabetic rabbits. Anadolu Kardiyol Derg. 2012;12(7):543-50. Epub 2012/08/11. doi: 10.5152/akd.2012.188. PubMed PMID: 22877897.
127. Sedgwick B, Riches K, Bageghni SA, O'Regan DJ, Porter KE, Turner NA. Investigating inherent functional differences between human cardiac fibroblasts cultured from nondiabetic and Type 2 diabetic donors. Cardiovasc Pathol. 2014;23(4):204-10. Epub 2014/04/22. doi: 10.1016/j.carpath.2014.03.004. PubMed PMID: 24746387.
128. Singh VP, Baker KM, Kumar R. Activation of the intracellular renin-angiotensin system in cardiac fibroblasts by high glucose: role in extracellular matrix production. American Journal of Physiology-Heart and Circulatory Physiology. 2008;294(4):H1675-H84. doi: 10.1152/ajpheart.91493.2007. PubMed PMID: WOS:000254575000022.
129. Kato T, Yamashita T, Sekiguchi A, Tsuneda T, Sagara K, Takamura M, et al. AGEs-RAGE system mediates atrial structural remodeling in the diabetic rat. Journal of Cardiovascular Electrophysiology. 2008;19(4):415-20. doi: 10.1111/j.1540-8167.2007.01037.x. PubMed PMID: WOS:000254502000016.
130. Russo I, Frangogiannis NG. Diabetes-associated cardiac fibrosis: Cellular effectors, molecular mechanisms and therapeutic opportunities. J Mol Cell Cardiol. 2016;90:84-93. doi: 10.1016/j.yjmcc.2015.12.011. PubMed PMID: 26705059; PubMed Central PMCID: PMC4718740.
131. Rosito GA, Massaro JM, Hoffmann U, Ruberg FL, Mahabadi AA, Vasan RS, et al. Pericardial fat, visceral abdominal fat, cardiovascular disease risk factors, and vascular calcification in a community-based sample: the Framingham Heart Study. Circulation. 2008;117(5):605-13. Epub 2008/01/24. doi: 10.1161/CIRCULATIONAHA.107.743062. PubMed PMID: 18212276.
132. Levelt E, Pavlides M, Banerjee R, Mahmod M, Kelly C, Sellwood J, et al. Ectopic and Visceral Fat Deposition in Lean and Obese Patients With Type 2 Diabetes. J Am Coll Cardiol. 2016;68(1):53-63. Epub 2016/07/02. doi: 10.1016/j.jacc.2016.03.597. PubMed PMID: 27364051; PubMed Central PMCID: PMCPMC4925621.

133. Batal O, Schoenhagen P, Shao M, Ayyad AE, Van Wagoner DR, Halliburton SS, et al. Left atrial epicardial adiposity and atrial fibrillation. Circ Arrhythm Electrophysiol. 2010;3(3):230-6. Epub 2010/05/28. doi: 10.1161/CIRCEP.110.957241. PubMed PMID: 20504944; PubMed Central PMCID: PMCPMC2974566.
134. Al Chekakie MO, Welles CC, Metoyer R, Ibrahim A, Shapira AR, Cytron J, et al. Pericardial fat is independently associated with human atrial fibrillation. J Am Coll Cardiol. 2010;56(10):784-8. Epub 2010/08/28. doi: 10.1016/j.jacc.2010.03.071. PubMed PMID: 20797492.
135. Mahajan R, Lau DH, Brooks AG, Shipp NJ, Manavis J, Wood JP, et al. Electrophysiological, Electroanatomical, and Structural Remodeling of the Atria as Consequences of Sustained Obesity. J Am Coll Cardiol. 2015;66(1):1-11. Epub 2015/07/04. doi: 10.1016/j.jacc.2015.04.058. PubMed PMID: 26139051.
136. Haemers P, Hamdi H, Guedj K, Suffee N, Farahmand P, Popovic N, et al. Atrial fibrillation is associated with the fibrotic remodelling of adipose tissue in the subepicardium of human and sheep atria. Eur Heart J. 2017;38(1):53-61. Epub 2015/11/28. doi: 10.1093/eurheartj/ehv625. PubMed PMID: 26612579.
137. Venteclef N, Guglielmi V, Balse E, Gaborit B, Cotillard A, Atassi F, et al. Human epicardial adipose tissue induces fibrosis of the atrial myocardium through the secretion of adipo-fibrokines. Eur Heart J. 2015;36(13):795-805a. Epub 2013/03/26. doi: 10.1093/eurheartj/eht099. PubMed PMID: 23525094.
138. Abe I, Teshima Y, Kondo H, Kaku H, Kira S, Ikebe Y, et al. Association of fibrotic remodeling and cytokines/chemokines content in epicardial adipose tissue with atrial myocardial fibrosis in patients with atrial fibrillation. Heart Rhythm. 2018;15(11):1717-27. Epub 2018/06/17. doi: 10.1016/j.hrthm.2018.06.025. PubMed PMID: 29908372.
139. Bohne LJ, Johnson D, Rose RA, Wilton SB, Gillis AM. The Association Between Diabetes Mellitus and Atrial Fibrillation: Clinical and Mechanistic Insights. Frontiers in physiology. 2019;10:135. doi: 10.3389/fphys.2019.00135. PubMed PMID: 30863315; PubMed Central PMCID: PMC6399657.
140. Goudis CA, Korantzopoulos P, Ntalas IV, Kallergis EM, Liu T, Ketikoglou DG. Diabetes mellitus and atrial fibrillation: Pathophysiological mechanisms and potential upstream therapies. International journal of cardiology. 2015;184:617-22. doi: 10.1016/j.ijcard.2015.03.052. PubMed PMID: 25770841.
141. Vinik AI, Maser RE, Mitchell BD, Freeman R. Diabetic Autonomic Neuropathy. Diabetes Care. 2003;26(5):1553-79. doi: 10.2337/diacare.26.5.1553. PubMed PMID: WOS:000185505400038.
142. Grisanti LA. Diabetes and Arrhythmias: Pathophysiology, Mechanisms and Therapeutic Outcomes. Front Physiol. 2018;9:1669. Epub 2018/12/12. doi: 10.3389/fphys.2018.01669. PubMed PMID: 30534081; PubMed Central PMCID: PMCPMC6275303.
143. Singh JP, Larson MG, O'Donnell CJ, Wilson PF, Tsuji H, Lloyd-Jones DM, et al. Association of hyperglycemia with reduced heart rate variability (The Framingham Heart Study). Am J Cardiol. 2000;86(3):309-12. Epub 2000/08/03. doi: 10.1016/s0002-9149(00)00920-6. PubMed PMID: 10922439.
144. Rizzo MR, Sasso FC, Marfella R, Siniscalchi M, Paolisso P, Carbonara O, et al. Autonomic dysfunction is associated with brief episodes of atrial fibrillation in type 2 diabetes. J Diabetes Complications. 2015;29(1):88-92. Epub 2014/10/01. doi: 10.1016/j.jdiacomp.2014.09.002. PubMed PMID: 25266244.
145. Negishi K, Seicean S, Negishi T, Yingchoncharoen T, Aljaroudi W, Marwick TH. Relation of heart-rate recovery to new onset heart failure and atrial fibrillation in

patients with diabetes mellitus and preserved ejection fraction. Am J Cardiol. 2013;111(5):748-53. Epub 2013/01/01. doi: 10.1016/j.amjcard.2012.11.028. PubMed PMID: 23273718.
146. Otake H, Suzuki H, Honda T, Maruyama Y. Influences of autonomic nervous system on atrial arrhythmogenic substrates and the incidence of atrial fibrillation in diabetic heart. International heart journal. 2009;50(5):627-41. PubMed PMID: 19809211.
147. Thaung HP, Baldi JC, Wang HY, Hughes G, Cook RF, Bussey CT, et al. Increased Efferent Cardiac Sympathetic Nerve Activity and Defective Intrinsic Heart Rate Regulation in Type 2 Diabetes. Diabetes. 2015;64(8):2944-56. Epub 2015/03/19. doi: 10.2337/db14-0955. PubMed PMID: 25784543.
148. Reilly SN, Jayaram R, Nahar K, Antoniades C, Verheule S, Channon KM, et al. Atrial sources of reactive oxygen species vary with the duration and substrate of atrial fibrillation: implications for the antiarrhythmic effect of statins. Circulation. 2011;124(10):1107-17. doi: 10.1161/CIRCULATIONAHA.111.029223. PubMed PMID: 21844076.
149. Boudina S, Sena S, Theobald H, Sheng X, Wright JJ, Hu XX, et al. Mitochondrial energetics in the heart in obesity-related diabetes: direct evidence for increased uncoupled respiration and activation of uncoupling proteins. Diabetes. 2007;56(10):2457-66. doi: 10.2337/db07-0481. PubMed PMID: 17623815.
150. Bugger H, Boudina S, Hu XX, Tuinei J, Zaha VG, Theobald HA, et al. Type 1 diabetic akita mouse hearts are insulin sensitive but manifest structurally abnormal mitochondria that remain coupled despite increased uncoupling protein 3. Diabetes. 2008;57(11):2924-32. Epub 2008/08/06. doi: 10.2337/db08-0079. PubMed PMID: 18678617; PubMed Central PMCID: PMCPMC2570388.
151. Montaigne D, Marechal X, Lefebvre P, Modine T, Fayad G, Dehondt H, et al. Mitochondrial dysfunction as an arrhythmogenic substrate: a translational proof-of-concept study in patients with metabolic syndrome in whom post-operative atrial fibrillation develops. Journal of the American College of Cardiology. 2013;62(16):1466-73. doi: 10.1016/j.jacc.2013.03.061. PubMed PMID: 23644086.
152. Wolke C, Bukowska A, Goette A, Lendeckel U. Redox control of cardiac remodeling in atrial fibrillation. Biochimica et biophysica acta. 2015;1850(8):1555-65. doi: 10.1016/j.bbagen.2014.12.012. PubMed PMID: 25513966.
153. Ausma J, Coumans WA, Duimel H, Van der Vusse GJ, Allessie MA, Borgers M. Atrial high energy phosphate content and mitochondrial enzyme activity during chronic atrial fibrillation. Cardiovascular research. 2000;47(4):788-96. PubMed PMID: 10974227.
154. Mihm MJ, Yu F, Carnes CA, Reiser PJ, McCarthy PM, Van Wagoner DR, et al. Impaired myofibrillar energetics and oxidative injury during human atrial fibrillation. Circulation. 2001;104(2):174-80. PubMed PMID: 11447082.
155. Tu T, Zhou S, Liu Z, Li X, Liu Q. Quantitative proteomics of changes in energy metabolism-related proteins in atrial tissue from valvular disease patients with permanent atrial fibrillation. Circulation journal : official journal of the Japanese Circulation Society. 2014;78(4):993-1001. PubMed PMID: 24553264.
156. Modrego J, Maroto L, Tamargo J, Azcona L, Mateos-Caceres P, Segura A, et al. Comparative expression of proteins in left and right atrial appendages from patients with mitral valve disease at sinus rhythm and atrial fibrillation. Journal of cardiovascular electrophysiology. 2010;21(8):859-68. doi: 10.1111/j.1540-8167.2010.01718.x. PubMed PMID: 20132404.

157. Cha YM, Dzeja PP, Shen WK, Jahangir A, Hart CY, Terzic A, et al. Failing atrial myocardium: energetic deficits accompany structural remodeling and electrical instability. American journal of physiology Heart and circulatory physiology. 2003;284(4):H1313-20. doi: 10.1152/ajpheart.00337.2002. PubMed PMID: 12626329.
158. Sun DM, Yuan X, Wei H, Zhu SJ, Zhang P, Zhang SJ, et al. Impaired myocardium energetics associated with the risk for new-onset atrial fibrillation after isolated coronary artery bypass graft surgery. Coronary artery disease. 2014;25(3):224-9. doi: 10.1097/MCA.0000000000000081. PubMed PMID: 24463787.
159. Liu M, Liu H, Dudley SC, Jr. Reactive oxygen species originating from mitochondria regulate the cardiac sodium channel. Circ Res. 2010;107(8):967-74. doi: 10.1161/CIRCRESAHA.110.220673. PubMed PMID: 20724705; PubMed Central PMCID: PMC2955818.
160. Liu M, Sanyal S, Gao G, Gurung IS, Zhu X, Gaconnet G, et al. Cardiac Na+ current regulation by pyridine nucleotides. Circ Res. 2009;105(8):737-45. doi: 10.1161/CIRCRESAHA.109.197277. PubMed PMID: 19745168; PubMed Central PMCID: PMC2773656.
161. Yoshida H, Bao L, Kefaloyianni E, Taskin E, Okorie U, Hong M, et al. AMP-activated protein kinase connects cellular energy metabolism to KATP channel function. J Mol Cell Cardiol. 2012;52(2):410-8. doi: 10.1016/j.yjmcc.2011.08.013. PubMed PMID: 21888913; PubMed Central PMCID: PMC3248631.
162. Sasaki N, Sato T, Marban E, O'Rourke B. ATP consumption by uncoupled mitochondria activates sarcolemmal K(ATP) channels in cardiac myocytes. American journal of physiology Heart and circulatory physiology. 2001;280(4):H1882-8. PubMed PMID: 11247805.
163. Wagner S, Ruff HM, Weber SL, Bellmann S, Sowa T, Schulte T, et al. Reactive oxygen species-activated Ca/calmodulin kinase IIdelta is required for late I(Na) augmentation leading to cellular Na and Ca overload. Circ Res. 2011;108(5):555-65. doi: 10.1161/CIRCRESAHA.110.221911. PubMed PMID: 21252154; PubMed Central PMCID: PMC3065330.
164. Ares-Carrasco S, Picatoste B, Benito-Martin A, Zubiri I, Sanz AB, Sanchez-Nino MD, et al. Myocardial fibrosis and apoptosis, but not inflammation, are present in long-term experimental diabetes. American journal of physiology Heart and circulatory physiology. 2009;297(6):H2109-19. doi: 10.1152/ajpheart.00157.2009. PubMed PMID: 19820199.
165. Sinha K, Das J, Pal PB, Sil PC. Oxidative stress: the mitochondria-dependent and mitochondria-independent pathways of apoptosis. Archives of toxicology. 2013;87(7):1157-80. doi: 10.1007/s00204-013-1034-4. PubMed PMID: 23543009.
166. Carnicer R, Suffredini S, Liu X, Reilly S, Simon JN, Surdo NC, et al. The Subcellular Localisation of Neuronal Nitric Oxide Synthase Determines the Downstream Effects of NO on Myocardial Function. Cardiovascular research. 2017. doi: 10.1093/cvr/cvx002. PubMed PMID: 28158509; PubMed Central PMCID: PMC5408949.
167. Balligand JL, Cannon PJ. Nitric oxide synthases and cardiac muscle. Autocrine and paracrine influences. Arterioscler Thromb Vasc Biol. 1997;17(10):1846-58. Epub 1997/11/14. doi: 10.1161/01.atv.17.10.1846. PubMed PMID: 9351345.
168. Andrew PJ, Mayer B. Enzymatic function of nitric oxide synthases. Cardiovasc Res. 1999;43(3):521-31. Epub 2000/02/26. doi: 10.1016/s0008-6363(99)00115-7. PubMed PMID: 10690324.
169. Xu KY, Huso DL, Dawson TM, Bredt DS, Becker LC. Nitric oxide synthase in cardiac sarcoplasmic reticulum. Proc Natl Acad Sci U S A. 1999;96(2):657-62. Epub

1999/01/20. doi: 10.1073/pnas.96.2.657. PubMed PMID: 9892689; PubMed Central PMCID: PMCPMC15192.
170. Stoclet JC, Muller B, Gyorgy K, Andriantsiothaina R, Kleschyov AL. The inducible nitric oxide synthase in vascular and cardiac tissue. Eur J Pharmacol. 1999;375(1-3):139-55. Epub 1999/08/12. doi: 10.1016/s0014-2999(99)00221-6. PubMed PMID: 10443572.
171. Feron O, Belhassen L, Kobzik L, Smith TW, Kelly RA, Michel T. Endothelial nitric oxide synthase targeting to caveolae. Specific interactions with caveolin isoforms in cardiac myocytes and endothelial cells. J Biol Chem. 1996;271(37):22810-4. Epub 1996/09/13. doi: 10.1074/jbc.271.37.22810. PubMed PMID: 8798458.
172. Barouch LA, Harrison RW, Skaf MW, Rosas GO, Cappola TP, Kobeissi ZA, et al. Nitric oxide regulates the heart by spatial confinement of nitric oxide synthase isoforms. Nature. 2002;416(6878):337-9. Epub 2002/03/22. doi: 10.1038/416337a. PubMed PMID: 11907582.
173. Vaniotis G, Glazkova I, Merlen C, Smith C, Villeneuve LR, Chatenet D, et al. Regulation of cardiac nitric oxide signaling by nuclear beta-adrenergic and endothelin receptors. J Mol Cell Cardiol. 2013;62:58-68. Epub 2013/05/21. doi: 10.1016/j.yjmcc.2013.05.003. PubMed PMID: 23684854; PubMed Central PMCID: PMCPMC3735468.
174. Khan SA, Lee K, Minhas KM, Gonzalez DR, Raju SV, Tejani AD, et al. Neuronal nitric oxide synthase negatively regulates xanthine oxidoreductase inhibition of cardiac excitation-contraction coupling. Proc Natl Acad Sci U S A. 2004;101(45):15944-8. Epub 2004/10/16. doi: 10.1073/pnas.0404136101. PubMed PMID: 15486091; PubMed Central PMCID: PMCPMC528749.
175. Carnicer R, Crabtree MJ, Sivakumaran V, Casadei B, Kass DA. Nitric oxide synthases in heart failure. Antioxidants & redox signaling. 2013;18(9):1078-99. doi: 10.1089/ars.2012.4824. PubMed PMID: 22871241; PubMed Central PMCID: PMC3567782.
176. Oceandy D, Cartwright EJ, Emerson M, Prehar S, Baudoin FM, Zi M, et al. Neuronal nitric oxide synthase signaling in the heart is regulated by the sarcolemmal calcium pump 4b. Circulation. 2007;115(4):483-92. Epub 2007/01/24. doi: 10.1161/CIRCULATIONAHA.106.643791. PubMed PMID: 17242280.
177. Ueda K, Valdivia C, Medeiros-Domingo A, Tester DJ, Vatta M, Farrugia G, et al. Syntrophin mutation associated with long QT syndrome through activation of the nNOS-SCN5A macromolecular complex. Proceedings of the National Academy of Sciences of the United States of America. 2008;105(27):9355-60. Epub 2008/07/02. doi: 10.1073/pnas.0801294105. PubMed PMID: 18591664; PubMed Central PMCID: PMCPMC2442127.
178. Cheng J, Valdivia CR, Vaidyanathan R, Balijepalli RC, Ackerman MJ, Makielski JC. Caveolin-3 suppresses late sodium current by inhibiting nNOS-dependent S-nitrosylation of SCN5A. J Mol Cell Cardiol. 2013;61:102-10. Epub 2013/04/02. doi: 10.1016/j.yjmcc.2013.03.013. PubMed PMID: 23541953; PubMed Central PMCID: PMCPMC3720711.
179. Sun J, Picht E, Ginsburg KS, Bers DM, Steenbergen C, Murphy E. Hypercontractile female hearts exhibit increased S-nitrosylation of the L-type Ca2+ channel alpha1 subunit and reduced ischemia/reperfusion injury. Circ Res. 2006;98(3):403-11. Epub 2006/01/07. doi: 10.1161/01.RES.0000202707.79018.0a. PubMed PMID: 16397145.
180. Godecke A, Heinicke T, Kamkin A, Kiseleva I, Strasser RH, Decking UK, et al. Inotropic response to beta-adrenergic receptor stimulation and anti-adrenergic effect of

ACh in endothelial NO synthase-deficient mouse hearts. J Physiol. 2001;532(Pt 1):195-204. Epub 2001/05/23. doi: 10.1111/j.1469-7793.2001.0195g.x. PubMed PMID: 11368026; PubMed Central PMCID: PMCPMC2278534.
181. Ashley EA, Sears CE, Bryant SM, Watkins HC, Casadei B. Cardiac nitric oxide synthase 1 regulates basal and beta-adrenergic contractility in murine ventricular myocytes. Circulation. 2002;105(25):3011-6. PubMed PMID: 12081996.
182. Drexler H, Kastner S, Strobel A, Studer R, Brodde OE, Hasenfuss G. Expression, activity and functional significance of inducible nitric oxide synthase in the failing human heart. J Am Coll Cardiol. 1998;32(4):955-63. Epub 1998/10/13. doi: 10.1016/s0735-1097(98)00336-2. PubMed PMID: 9768717.
183. Gallo MP, Ghigo D, Bosia A, Alloatti G, Costamagna C, Penna C, et al. Modulation of guinea-pig cardiac L-type calcium current by nitric oxide synthase inhibitors. J Physiol. 1998;506 (Pt 3):639-51. Epub 1998/03/21. doi: 10.1111/j.1469-7793.1998.639bv.x. PubMed PMID: 9503327; PubMed Central PMCID: PMCPMC2230759.
184. Wang H, Viatchenko-Karpinski S, Sun J, Gyorke I, Benkusky NA, Kohr MJ, et al. Regulation of myocyte contraction via neuronal nitric oxide synthase: role of ryanodine receptor S-nitrosylation. The Journal of physiology. 2010;588(Pt 15):2905-17. doi: 10.1113/jphysiol.2010.192617. PubMed PMID: 20530114; PubMed Central PMCID: PMC2956906.
185. Carnicer R, Hale AB, Suffredini S, Liu X, Reilly S, Zhang MH, et al. Cardiomyocyte GTP cyclohydrolase 1 and tetrahydrobiopterin increase NOS1 activity and accelerate myocardial relaxation. Circ Res. 2012;111(6):718-27. doi: 10.1161/CIRCRESAHA.112.274464. PubMed PMID: 22798524.
186. Jin CZ, Jang JH, Kim HJ, Wang Y, Hwang IC, Sadayappan S, et al. Myofilament Ca2+ desensitization mediates positive lusitropic effect of neuronal nitric oxide synthase in left ventricular myocytes from murine hypertensive heart. J Mol Cell Cardiol. 2013;60:107-15. Epub 2013/04/30. doi: 10.1016/j.yjmcc.2013.04.017. PubMed PMID: 23624088.
187. Reilly S, Liu X, Carnicer R, Rajakumar T, Sayeed R, Krasopoulos G, et al. Evaluation of the role of miR-31-dependent reduction in dystrophin and nNOS on atrial-fibrillation-induced electrical remodelling in man. The Lancet. 2015;385, Supplement 1(0):S82. doi: http://dx.doi.org/10.1016/S0140-6736(15)60397-X.
188. Ahern GP, Hsu SF, Klyachko VA, Jackson MB. Induction of persistent sodium current by exogenous and endogenous nitric oxide. The Journal of biological chemistry. 2000;275(37):28810-5. doi: 10.1074/jbc.M003090200. PubMed PMID: 10833522.
189. Nunez L, Vaquero M, Gomez R, Caballero R, Mateos-Caceres P, Macaya C, et al. Nitric oxide blocks hKv1.5 channels by S-nitrosylation and by a cyclic GMP-dependent mechanism. Cardiovascular research. 2006;72(1):80-9. doi: 10.1016/j.cardiores.2006.06.021. PubMed PMID: 16876149.
190. Gomez R, Nunez L, Vaquero M, Amoros I, Barana A, de Prada T, et al. Nitric oxide inhibits Kv4.3 and human cardiac transient outward potassium current (Ito1). Cardiovascular research. 2008;80(3):375-84. doi: 10.1093/cvr/cvn205. PubMed PMID: 18678642.
191. Reilly SN, Liu X, Carnicer R, Recalde A, Muszkiewicz A, Jayaram R, et al. Up-regulation of miR-31 in human atrial fibrillation begets the arrhythmia by depleting dystrophin and neuronal nitric oxide synthase. Science translational medicine. 2016;8(340):340ra74. Epub 2016/05/27. doi: 10.1126/scitranslmed.aac4296. PubMed PMID: 27225184; PubMed Central PMCID: PMCPMC4993239.

192. Thony B, Auerbach G, Blau N. Tetrahydrobiopterin biosynthesis, regeneration and functions. The Biochemical journal. 2000;347 Pt 1:1-16. Epub 2000/03/23. PubMed PMID: 10727395; PubMed Central PMCID: PMCPMC1220924.
193. Werner ER, Blau N, Thony B. Tetrahydrobiopterin: biochemistry and pathophysiology. The Biochemical journal. 2011;438(3):397-414. Epub 2011/08/27. doi: 10.1042/BJ20110293. PubMed PMID: 21867484.
194. Bendall JK, Douglas G, McNeill E, Channon KM, Crabtree MJ. Tetrahydrobiopterin in cardiovascular health and disease. Antioxidants & redox signaling. 2014;20(18):3040-77. doi: 10.1089/ars.2013.5566. PubMed PMID: 24294830; PubMed Central PMCID: PMC4038990.
195. Luo S, Lei H, Qin H, Xia Y. Molecular mechanisms of endothelial NO synthase uncoupling. Current pharmaceutical design. 2014;20(22):3548-53. Epub 2013/11/05. doi: 10.2174/13816128113196660746. PubMed PMID: 24180388.
196. Alp NJ, McAteer MA, Khoo J, Choudhury RP, Channon KM. Increased endothelial tetrahydrobiopterin synthesis by targeted transgenic GTP-cyclohydrolase I overexpression reduces endothelial dysfunction and atherosclerosis in ApoE-knockout mice. Arteriosclerosis, thrombosis, and vascular biology. 2004;24(3):445-50. doi: 10.1161/01.ATV.0000115637.48689.77. PubMed PMID: 14707037.
197. Cosentino F, Patton S, d'Uscio LV, Werner ER, Werner-Felmayer G, Moreau P, et al. Tetrahydrobiopterin alters superoxide and nitric oxide release in prehypertensive rats. The Journal of clinical investigation. 1998;101(7):1530-7. doi: 10.1172/JCI650. PubMed PMID: 9525996; PubMed Central PMCID: PMC508731.
198. Landmesser U, Dikalov S, Price SR, McCann L, Fukai T, Holland SM, et al. Oxidation of tetrahydrobiopterin leads to uncoupling of endothelial cell nitric oxide synthase in hypertension. The Journal of clinical investigation. 2003;111(8):1201-9. doi: 10.1172/JCI14172. PubMed PMID: 12697739; PubMed Central PMCID: PMC152929.
199. Gimbrone MA, Jr., Garcia-Cardena G. Endothelial Cell Dysfunction and the Pathobiology of Atherosclerosis. Circ Res. 2016;118(4):620-36. Epub 2016/02/20. doi: 10.1161/CIRCRESAHA.115.306301. PubMed PMID: 26892962; PubMed Central PMCID: PMCPMC4762052.
200. Silberman GA, Fan TH, Liu H, Jiao Z, Xiao HD, Lovelock JD, et al. Uncoupled cardiac nitric oxide synthase mediates diastolic dysfunction. Circulation. 2010;121(4):519-28. doi: 10.1161/CIRCULATIONAHA.109.883777. PubMed PMID: 20083682; PubMed Central PMCID: PMC2819317.
201. Schmidt TS, McNeill E, Douglas G, Crabtree MJ, Hale AB, Khoo J, et al. Tetrahydrobiopterin supplementation reduces atherosclerosis and vascular inflammation in apolipoprotein E-knockout mice. Clinical science. 2010;119(3):131-42. doi: 10.1042/CS20090559. PubMed PMID: 20337596.
202. Alp NJ, Mussa S, Khoo J, Cai S, Guzik T, Jefferson A, et al. Tetrahydrobiopterin-dependent preservation of nitric oxide-mediated endothelial function in diabetes by targeted transgenic GTP-cyclohydrolase I overexpression. The Journal of clinical investigation. 2003;112(5):725-35. doi: 10.1172/JCI17786. PubMed PMID: 12952921; PubMed Central PMCID: PMC182196.
203. Higashi Y, Sasaki S, Nakagawa K, Fukuda Y, Matsuura H, Oshima T, et al. Tetrahydrobiopterin enhances forearm vascular response to acetylcholine in both normotensive and hypertensive individuals. American journal of hypertension. 2002;15(4 Pt 1):326-32. doi: 10.1016/s0895-7061(01)02317-2. PubMed PMID: 11991218.

204. Stroes E, Kastelein J, Cosentino F, Erkelens W, Wever R, Koomans H, et al. Tetrahydrobiopterin restores endothelial function in hypercholesterolemia. The Journal of clinical investigation. 1997;99(1):41-6. doi: 10.1172/JCI119131. PubMed PMID: 9011574; PubMed Central PMCID: PMC507765.
205. Cosentino F, Hurlimann D, Delli Gatti C, Chenevard R, Blau N, Alp NJ, et al. Chronic treatment with tetrahydrobiopterin reverses endothelial dysfunction and oxidative stress in hypercholesterolaemia. Heart. 2008;94(4):487-92. doi: 10.1136/hrt.2007.122184. PubMed PMID: 17916662.
206. Maier W, Cosentino F, Lutolf RB, Fleisch M, Seiler C, Hess OM, et al. Tetrahydrobiopterin improves endothelial function in patients with coronary artery disease. Journal of cardiovascular pharmacology. 2000;35(2):173-8. doi: 10.1097/00005344-200002000-00001. PubMed PMID: 10672847.
207. Setoguchi S, Mohri M, Shimokawa H, Takeshita A. Tetrahydrobiopterin improves endothelial dysfunction in coronary microcirculation in patients without epicardial coronary artery disease. Journal of the American College of Cardiology. 2001;38(2):493-8. doi: 10.1016/s0735-1097(01)01382-1. PubMed PMID: 11499743.
208. Heitzer T, Krohn K, Albers S, Meinertz T. Tetrahydrobiopterin improves endothelium-dependent vasodilation by increasing nitric oxide activity in patients with Type II diabetes mellitus. Diabetologia. 2000;43(11):1435-8. doi: 10.1007/s001250051551. PubMed PMID: 11126415.
209. Heitzer T, Brockhoff C, Mayer B, Warnholtz A, Mollnau H, Henne S, et al. Tetrahydrobiopterin improves endothelium-dependent vasodilation in chronic smokers : evidence for a dysfunctional nitric oxide synthase. Circ Res. 2000;86(2):E36-41. doi: 10.1161/01.res.86.2.e36. PubMed PMID: 10666424.
210. Worthley MI, Kanani RS, Sun YH, Sun Y, Goodhart DM, Curtis MJ, et al. Effects of tetrahydrobiopterin on coronary vascular reactivity in atherosclerotic human coronary arteries. Cardiovascular research. 2007;76(3):539-46. doi: 10.1016/j.cardiores.2007.07.009. PubMed PMID: 17689509.
211. Cunnington C, Van Assche T, Shirodaria C, Kylintireas I, Lindsay AC, Lee JM, et al. Systemic and vascular oxidation limits the efficacy of oral tetrahydrobiopterin treatment in patients with coronary artery disease. Circulation. 2012;125(11):1356-66. doi: 10.1161/CIRCULATIONAHA.111.038919. PubMed PMID: 22315282; PubMed Central PMCID: PMC5238935.
212. Takimoto E, Champion HC, Li M, Ren S, Rodriguez ER, Tavazzi B, et al. Oxidant stress from nitric oxide synthase-3 uncoupling stimulates cardiac pathologic remodeling from chronic pressure load. The Journal of clinical investigation. 2005;115(5):1221-31. doi: 10.1172/JCI21968. PubMed PMID: 15841206; PubMed Central PMCID: PMC1077169.
213. Hashimoto T, Sivakumaran V, Carnicer R, Zhu G, Hahn VS, Bedja D, et al. Tetrahydrobiopterin Protects Against Hypertrophic Heart Disease Independent of Myocardial Nitric Oxide Synthase Coupling. Journal of the American Heart Association. 2016;5(3):e003208. doi: 10.1161/JAHA.116.003208. PubMed PMID: 27001967; PubMed Central PMCID: PMC4943286.
214. Dumitrescu C, Biondi R, Xia Y, Cardounel AJ, Druhan LJ, Ambrosio G, et al. Myocardial ischemia results in tetrahydrobiopterin (BH4) oxidation with impaired endothelial function ameliorated by BH4. Proceedings of the National Academy of Sciences of the United States of America. 2007;104(38):15081-6. doi: 10.1073/pnas.0702986104. PubMed PMID: 17848522; PubMed Central PMCID: PMC1986616.

215. Ge ZD, Ionova IA, Vladic N, Pravdic D, Hirata N, Vasquez-Vivar J, et al. Cardiac-specific overexpression of GTP cyclohydrolase 1 restores ischaemic preconditioning during hyperglycaemia. Cardiovascular research. 2011;91(2):340-9. doi: 10.1093/cvr/cvr079. PubMed PMID: 21422102; PubMed Central PMCID: PMC3125073.
216. Gomez R, Caballero R, Barana A, Amoros I, Calvo E, Lopez JA, et al. Nitric oxide increases cardiac IK1 by nitrosylation of cysteine 76 of Kir2.1 channels. Circ Res. 2009;105(4):383-92. doi: 10.1161/CIRCRESAHA.109.197558. PubMed PMID: 19608980.
217. Brandacher G, Maglione M, Schneeberger S, Obrist P, Thoeni G, Wrulich OA, et al. Tetrahydrobiopterin compounds prolong allograft survival independently of their effect on nitric oxide synthase activity. Transplantation. 2006;81(4):583-9. doi: 10.1097/01.tp.0000188949.03683.fd. PubMed PMID: 16495807.
218. Pieper GM, Ionova IA, Cooley BC, Migrino RQ, Khanna AK, Whitsett J, et al. Sepiapterin decreases acute rejection and apoptosis in cardiac transplants independently of changes in nitric oxide and inducible nitric-oxide synthase dimerization. The Journal of pharmacology and experimental therapeutics. 2009;329(3):890-9. doi: 10.1124/jpet.108.148569. PubMed PMID: 19307452; PubMed Central PMCID: PMC2683770.
219. McNeill E, Crabtree MJ, Sahgal N, Patel J, Chuaiphichai S, Iqbal AJ, et al. Regulation of iNOS function and cellular redox state by macrophage Gch1 reveals specific requirements for tetrahydrobiopterin in NRF2 activation. Free radical biology & medicine. 2015;79:206-16. Epub 2014/12/03. doi: 10.1016/j.freeradbiomed.2014.10.575. PubMed PMID: 25451639; PubMed Central PMCID: PMCPMC4344222.
220. Jeong EM, Monasky MM, Gu L, Taglieri DM, Patel BG, Liu H, et al. Tetrahydrobiopterin improves diastolic dysfunction by reversing changes in myofilament properties. J Mol Cell Cardiol. 2013;56:44-54. Epub 2012/12/19. doi: 10.1016/j.yjmcc.2012.12.003. PubMed PMID: 23247392; PubMed Central PMCID: PMCPMC3666585.
221. Moens AL, Takimoto E, Tocchetti CG, Chakir K, Bedja D, Cormaci G, et al. Reversal of cardiac hypertrophy and fibrosis from pressure overload by tetrahydrobiopterin: efficacy of recoupling nitric oxide synthase as a therapeutic strategy. Circulation. 2008;117(20):2626-36. doi: 10.1161/CIRCULATIONAHA.107.737031. PubMed PMID: 18474817; PubMed Central PMCID: PMC2614930.
222. Envigo. Research Models and Services - Inbred Mice: C57BL/6. Envigo RMS Division; 2015.
223. Toye AA, Lippiat JD, Proks P, Shimomura K, Bentley L, Hugill A, et al. A genetic and physiological study of impaired glucose homeostasis control in C57BL/6J mice. Diabetologia. 2005;48(4):675-86. doi: 10.1007/s00125-005-1680-z. PubMed PMID: 15729571.
224. Laboratory TJ. C57BL/6J Mouse Strain Datasheet 2017 [cited 2017]. Available from: https://www.jax.org/strain/000664.
225. Truett GE, Heeger P, Mynatt RL, Truett AA, Walker JA, Warman ML. Preparation of PCR-quality mouse genomic DNA with hot sodium hydroxide and tris (HotSHOT). BioTechniques. 2000;29(1):52, 4. PubMed PMID: 10907076.
226. Nickel AG, von Hardenberg A, Hohl M, Loffler JR, Kohlhaas M, Becker J, et al. Reversal of Mitochondrial Transhydrogenase Causes Oxidative Stress in Heart Failure.

Cell metabolism. 2015;22(3):472-84. doi: 10.1016/j.cmet.2015.07.008. PubMed PMID: 26256392.
227. Schnedl WJ, Ferber S, Johnson JH, Newgard CB. STZ transport and cytotoxicity. Specific enhancement in GLUT2-expressing cells. Diabetes. 1994;43(11):1326-33. PubMed PMID: 7926307.
228. Lenzen S. The mechanisms of alloxan- and streptozotocin-induced diabetes. Diabetologia. 2008;51(2):216-26. doi: 10.1007/s00125-007-0886-7. PubMed PMID: 18087688.
229. Thorens B. GLUT2, glucose sensing and glucose homeostasis. Diabetologia. 2015;58(2):221-32. doi: 10.1007/s00125-014-3451-1. PubMed PMID: 25421524.
230. Chandramouli C, Reichelt ME, Curl CL, Varma U, Bienvenu LA, Koutsifeli P, et al. Diastolic dysfunction is more apparent in STZ-induced diabetic female mice, despite less pronounced hyperglycemia. Sci Rep. 2018;8(1):2346. Epub 2018/02/07. doi: 10.1038/s41598-018-20703-8. PubMed PMID: 29402990; PubMed Central PMCID: PMCPMC5799292.
231. Wolfensohn Sarah LM. Handbook of laboratory animal management and welfare. 3rd ed. Oxford: Blackwell Publishing Ltd; 2003.
232. Miura T, Miyazaki S, Guth BD, Indolfi C, Ross J, Jr. Heart rate and force-frequency effects on diastolic function of the left ventricle in exercising dogs. Circulation. 1994;89(5):2361-8. Epub 1994/05/01. doi: 10.1161/01.cir.89.5.2361. PubMed PMID: 8181162.
233. Chung CS, Kovacs SJ. Consequences of increasing heart rate on deceleration time, the velocity-time integral, and E/A. The American journal of cardiology. 2006;97(1):130-6. Epub 2005/12/27. doi: 10.1016/j.amjcard.2005.07.116. PubMed PMID: 16377298.
234. Nagueh SF, Appleton CP, Gillebert TC, Marino PN, Oh JK, Smiseth OA, et al. Recommendations for the evaluation of left ventricular diastolic function by echocardiography. Journal of the American Society of Echocardiography : official publication of the American Society of Echocardiography. 2009;22(2):107-33. Epub 2009/02/04. doi: 10.1016/j.echo.2008.11.023. PubMed PMID: 19187853.
235. Bland JM, Altman DG. Statistical methods for assessing agreement between two methods of clinical measurement. Lancet. 1986;1(8476):307-10. PubMed PMID: 2868172.
236. Schrickel JW, Bielik H, Yang A, Schimpf R, Shlevkov N, Burkhardt D, et al. Induction of atrial fibrillation in mice by rapid transesophageal atrial pacing. Basic research in cardiology. 2002;97(6):452-60. doi: 10.1007/s003950200052. PubMed PMID: 12395207.
237. Verheule S, Sato T, Everett Tt, Engle SK, Otten D, Rubart-von der Lohe M, et al. Increased vulnerability to atrial fibrillation in transgenic mice with selective atrial fibrosis caused by overexpression of TGF-beta1. Circ Res. 2004;94(11):1458-65. doi: 10.1161/01.RES.0000129579.59664.9d. PubMed PMID: 15117823; PubMed Central PMCID: PMC2129102.
238. MT HO. Simultane transösophageale elektrokardiographische Ableitung des linken Vorhofes und der linken Herzkammer. Wikimedia Commons2012.
239. Cygankiewicz I, Zareba W. Heart rate variability. Handb Clin Neurol. 2013;117:379-93. Epub 2013/10/08. doi: 10.1016/B978-0-444-53491-0.00031-6. PubMed PMID: 24095141.
240. Tomek J, Burton RA, Bub G. Ccoffinn: Automated Wave Tracking in Cultured Cardiac Monolayers. Biophysical journal. 2016;111(8):1595-9. doi:

10.1016/j.bpj.2016.08.049. PubMed PMID: 27760347; PubMed Central PMCID: PMC5072981.
241. O'Shea C, Holmes AP, Yu TY, Winter J, Wells SP, Correia J, et al. ElectroMap: High-throughput open-source software for analysis and mapping of cardiac electrophysiology. Sci Rep. 2019;9(1):1389. Epub 2019/02/06. doi: 10.1038/s41598-018-38263-2. PubMed PMID: 30718782; PubMed Central PMCID: PMCPMC6362081.
242. Ashrafian H, Czibik G, Bellahcene M, Aksentijevic D, Smith AC, Mitchell SJ, et al. Fumarate is cardioprotective via activation of the Nrf2 antioxidant pathway. Cell metabolism. 2012;15(3):361-71. doi: 10.1016/j.cmet.2012.01.017. PubMed PMID: 22405071; PubMed Central PMCID: PMC3314920.
243. Dodd MS, Ball DR, Schroeder MA, Le Page LM, Atherton HJ, Heather LC, et al. In vivo alterations in cardiac metabolism and function in the spontaneously hypertensive rat heart. Cardiovascular research. 2012;95(1):69-76. doi: 10.1093/cvr/cvs164. PubMed PMID: 22593200; PubMed Central PMCID: PMC4617603.
244. Schroeder MA, Swietach P, Atherton HJ, Gallagher FA, Lee P, Radda GK, et al. Measuring intracellular pH in the heart using hyperpolarized carbon dioxide and bicarbonate: a 13C and 31P magnetic resonance spectroscopy study. Cardiovascular research. 2010;86(1):82-91. doi: 10.1093/cvr/cvp396. PubMed PMID: 20008827; PubMed Central PMCID: PMC2836261.
245. Vanhamme L, van den Boogaart A, Van Huffel S. Improved method for accurate and efficient quantification of MRS data with use of prior knowledge. Journal of magnetic resonance. 1997;129(1):35-43. PubMed PMID: 9405214.
246. Naressi A, Couturier C, Castang I, de Beer R, Graveron-Demilly D. Java-based graphical user interface for MRUI, a software package for quantitation of in vivo/medical magnetic resonance spectroscopy signals. Computers in biology and medicine. 2001;31(4):269-86. PubMed PMID: 11334636.
247. Smith PK, Krohn RI, Hermanson GT, Mallia AK, Gartner FH, Provenzano MD, et al. Measurement of protein using bicinchoninic acid. Analytical biochemistry. 1985;150(1):76-85. PubMed PMID: 3843705.
248. Crabtree MJ, Tatham AL, Al-Wakeel Y, Warrick N, Hale AB, Cai S, et al. Quantitative regulation of intracellular endothelial nitric-oxide synthase (eNOS) coupling by both tetrahydrobiopterin-eNOS stoichiometry and biopterin redox status: insights from cells with tet-regulated GTP cyclohydrolase I expression. The Journal of biological chemistry. 2009;284(2):1136-44. doi: 10.1074/jbc.M805403200. PubMed PMID: 19011239.
249. de Bono JP, Warrick N, Bendall JK, Channon KM, Alp NJ. Radiochemical HPLC detection of arginine metabolism: measurement of nitric oxide synthesis and arginase activity in vascular tissue. Nitric oxide : biology and chemistry. 2007;16(1):1-9. doi: 10.1016/j.niox.2006.03.008. PubMed PMID: 16647284.
250. Schlattner U, Tokarska-Schlattner M, Wallimann T. Mitochondrial creatine kinase in human health and disease. Biochimica et biophysica acta. 2006;1762(2):164-80. Epub 2005/10/21. doi: 10.1016/j.bbadis.2005.09.004. PubMed PMID: 16236486.
251. Lygate CA, Bohl S, ten Hove M, Faller KM, Ostrowski PJ, Zervou S, et al. Moderate elevation of intracellular creatine by targeting the creatine transporter protects mice from acute myocardial infarction. Cardiovascular research. 2012;96(3):466-75. Epub 2012/08/24. doi: 10.1093/cvr/cvs272. PubMed PMID: 22915766; PubMed Central PMCID: PMCPMC3500046.
252. Neubauer S, Horn M, Naumann A, Tian R, Hu K, Laser M, et al. Impairment of energy metabolism in intact residual myocardium of rat hearts with chronic myocardial

infarction. The Journal of clinical investigation. 1995;95(3):1092-100. Epub 1995/03/01. doi: 10.1172/JCI117756. PubMed PMID: 7883957; PubMed Central PMCID: PMCPMC441445.
253. Zervou S, Whittington HJ, Ostrowski PJ, Cao F, Tyler J, Lake HA, et al. Increasing creatine kinase activity protects against hypoxia / reoxygenation injury but not against anthracycline toxicity in vitro. PLoS One. 2017;12(8):e0182994. Epub 2017/08/15. doi: 10.1371/journal.pone.0182994. PubMed PMID: 28806770; PubMed Central PMCID: PMCPMC5555628.
254. Spronk HM, De Jong AM, Verheule S, De Boer HC, Maass AH, Lau DH, et al. Hypercoagulability causes atrial fibrosis and promotes atrial fibrillation. European heart journal. 2017;38(1):38-50. Epub 2016/04/14. doi: 10.1093/eurheartj/ehw119. PubMed PMID: 27071821.
255. Prockop DJ, Udenfriend S. A specific method for the analysis of hydroxyproline in tissues and urine. Analytical biochemistry. 1960;1:228-39. PubMed PMID: 13738134.
256. Rubler S, Dlugash J, Yuceoglu YZ, Kumral T, Branwood AW, Grishman A. New type of cardiomyopathy associated with diabetic glomerulosclerosis. The American journal of cardiology. 1972;30(6):595-602. Epub 1972/11/08. doi: 10.1016/0002-9149(72)90595-4. PubMed PMID: 4263660.
257. Bugger H, Abel ED. Molecular mechanisms of diabetic cardiomyopathy. Diabetologia. 2014;57(4):660-71. Epub 2014/01/31. doi: 10.1007/s00125-014-3171-6. PubMed PMID: 24477973; PubMed Central PMCID: PMCPMC3969857.
258. Cassuto J, Dou H, Czikora I, Szabo A, Patel VS, Kamath V, et al. Peroxynitrite disrupts endothelial caveolae leading to eNOS uncoupling and diminished flow-mediated dilation in coronary arterioles of diabetic patients. Diabetes. 2014;63(4):1381-93. Epub 2013/12/20. doi: 10.2337/db13-0577. PubMed PMID: 24353182; PubMed Central PMCID: PMCPMC3964507.
259. Wu HE, Baumgardt SL, Fang J, Paterson M, Liu Y, Du J, et al. Cardiomyocyte GTP Cyclohydrolase 1 Protects the Heart Against Diabetic Cardiomyopathy. Sci Rep. 2016;6:27925. Epub 2016/06/15. doi: 10.1038/srep27925. PubMed PMID: 27295516; PubMed Central PMCID: PMCPMC4904741.
260. Harrison DG. Cellular and molecular mechanisms of endothelial cell dysfunction. The Journal of clinical investigation. 1997;100(9):2153-7. Epub 1997/12/31. doi: 10.1172/JCI119751. PubMed PMID: 9410891; PubMed Central PMCID: PMCPMC508409.
261. Herlein JA, Fink BD, O'Malley Y, Sivitz WI. Superoxide and respiratory coupling in mitochondria of insulin-deficient diabetic rats. Endocrinology. 2009;150(1):46-55. Epub 2008/09/06. doi: 10.1210/en.2008-0404. PubMed PMID: 18772240; PubMed Central PMCID: PMCPMC2630897.
262. Ye G, Metreveli NS, Donthi RV, Xia S, Xu M, Carlson EC, et al. Catalase protects cardiomyocyte function in models of type 1 and type 2 diabetes. Diabetes. 2004;53(5):1336-43. Epub 2004/04/28. doi: 10.2337/diabetes.53.5.1336. PubMed PMID: 15111504.
263. Van den Bergh A, Vanderper A, Vangheluwe P, Desjardins F, Nevelsteen I, Verreth W, et al. Dyslipidaemia in type II diabetic mice does not aggravate contractile impairment but increases ventricular stiffness. Cardiovascular research. 2008;77(2):371-9. Epub 2007/11/17. doi: 10.1093/cvr/cvm001. PubMed PMID: 18006491.
264. Ye G, Metreveli NS, Ren J, Epstein PN. Metallothionein prevents diabetes-induced deficits in cardiomyocytes by inhibiting reactive oxygen species production.

Diabetes. 2003;52(3):777-83. Epub 2003/02/28. doi: 10.2337/diabetes.52.3.777. PubMed PMID: 12606520.
265. Wold LE, Ceylan-Isik AF, Fang CX, Yang X, Li SY, Sreejayan N, et al. Metallothionein alleviates cardiac dysfunction in streptozotocin-induced diabetes: role of Ca2+ cycling proteins, NADPH oxidase, poly(ADP-Ribose) polymerase and myosin heavy chain isozyme. Free radical biology & medicine. 2006;40(8):1419-29. Epub 2006/04/25. doi: 10.1016/j.freeradbiomed.2005.12.009. PubMed PMID: 16631532.
266. An D, Rodrigues B. Role of changes in cardiac metabolism in development of diabetic cardiomyopathy. American journal of physiology Heart and circulatory physiology. 2006;291(4):H1489-506. Epub 2006/06/06. doi: 10.1152/ajpheart.00278.2006. PubMed PMID: 16751293.
267. Shivu GN, Phan TT, Abozguia K, Ahmed I, Wagenmakers A, Henning A, et al. Relationship between coronary microvascular dysfunction and cardiac energetics impairment in type 1 diabetes mellitus. Circulation. 2010;121(10):1209-15. Epub 2010/03/03. doi: 10.1161/CIRCULATIONAHA.109.873273. PubMed PMID: 20194884.
268. Scheuermann-Freestone M, Madsen PL, Manners D, Blamire AM, Buckingham RE, Styles P, et al. Abnormal cardiac and skeletal muscle energy metabolism in patients with type 2 diabetes. Circulation. 2003;107(24):3040-6. Epub 2003/06/18. doi: 10.1161/01.CIR.0000072789.89096.10. PubMed PMID: 12810608.
269. Garcia-Martinez C, Sibille B, Solanes G, Darimont C, Mace K, Villarroya F, et al. Overexpression of UCP3 in cultured human muscle lowers mitochondrial membrane potential, raises ATP/ADP ratio, and favors fatty acid vs. glucose oxidation. FASEB journal : official publication of the Federation of American Societies for Experimental Biology. 2001;15(11):2033-5. Epub 2001/08/21. doi: 10.1096/fj.00-0828fje. PubMed PMID: 11511517.
270. Matsumoto Y, Kaneko M, Kobayashi A, Fujise Y, Yamazaki N. Creatine kinase kinetics in diabetic cardiomyopathy. The American journal of physiology. 1995;268(6 Pt 1):E1070-6. Epub 1995/06/01. doi: 10.1152/ajpendo.1995.268.6.E1070. PubMed PMID: 7611380.
271. Carley AN, Severson DL. Fatty acid metabolism is enhanced in type 2 diabetic hearts. Biochimica et biophysica acta. 2005;1734(2):112-26. Epub 2005/05/21. doi: 10.1016/j.bbalip.2005.03.005. PubMed PMID: 15904868.
272. Zhou YT, Grayburn P, Karim A, Shimabukuro M, Higa M, Baetens D, et al. Lipotoxic heart disease in obese rats: implications for human obesity. Proceedings of the National Academy of Sciences of the United States of America. 2000;97(4):1784-9. Epub 2000/03/04. doi: 10.1073/pnas.97.4.1784. PubMed PMID: 10677535; PubMed Central PMCID: PMCPMC26513.
273. Kasuno K, Takabuchi S, Fukuda K, Kizaka-Kondoh S, Yodoi J, Adachi T, et al. Nitric oxide induces hypoxia-inducible factor 1 activation that is dependent on MAPK and phosphatidylinositol 3-kinase signaling. The Journal of biological chemistry. 2004;279(4):2550-8. Epub 2003/11/06. doi: 10.1074/jbc.M308197200. PubMed PMID: 14600153.
274. Myers RB, Fomovsky GM, Lee S, Tan M, Wang BF, Patwari P, et al. Deletion of thioredoxin-interacting protein improves cardiac inotropic reserve in the streptozotocin-induced diabetic heart. American journal of physiology Heart and circulatory physiology. 2016;310(11):H1748-59. Epub 2016/04/03. doi: 10.1152/ajpheart.00051.2016. PubMed PMID: 27037370; PubMed Central PMCID: PMCPMC4935523.

275. Weiss JN, Lamp ST. Glycolysis preferentially inhibits ATP-sensitive K+ channels in isolated guinea pig cardiac myocytes. Science. 1987;238(4823):67-9. Epub 1987/10/02. doi: 10.1126/science.2443972. PubMed PMID: 2443972.
276. Weiss J, Hiltbrand B. Functional compartmentation of glycolytic versus oxidative metabolism in isolated rabbit heart. The Journal of clinical investigation. 1985;75(2):436-47. Epub 1985/02/01. doi: 10.1172/JCI111718. PubMed PMID: 3973013; PubMed Central PMCID: PMCPMC423514.
277. Entam ML, Kanike K, Goldstein MA, Nelson TE, Bornet EP, Futch TW, et al. Association of gylcogenolysis with cardiac sarcoplasmic reticulum. The Journal of biological chemistry. 1976;251(10):3140-6. Epub 1976/05/25. PubMed PMID: 5455.
278. Schaffer SW, Ballard-Croft C, Boerth S, Allo SN. Mechanisms underlying depressed Na+/Ca2+ exchanger activity in the diabetic heart. Cardiovascular research. 1997;34(1):129-36. Epub 1997/04/01. doi: 10.1016/s0008-6363(97)00020-5. PubMed PMID: 9217882.
279. Zarain-Herzberg A, Yano K, Elimban V, Dhalla NS. Cardiac sarcoplasmic reticulum Ca(2+)-ATPase expression in streptozotocin-induced diabetic rat heart. Biochem Biophys Res Commun. 1994;203(1):113-20. Epub 1994/08/30. doi: 10.1006/bbrc.1994.2156. PubMed PMID: 8074644.
280. Krijthe BP, Kunst A, Benjamin EJ, Lip GY, Franco OH, Hofman A, et al. Projections on the number of individuals with atrial fibrillation in the European Union, from 2000 to 2060. European heart journal. 2013;34(35):2746-51. Epub 2013/08/01. doi: 10.1093/eurheartj/eht280. PubMed PMID: 23900699; PubMed Central PMCID: PMCPMC3858024.
281. Heijman J, Voigt N, Nattel S, Dobrev D. Cellular and Molecular Electrophysiology of Atrial Fibrillation Initiation, Maintenance, and Progression. Circulation Research. 2014;114(9):1483-99. doi: 10.1161/circresaha.114.302226.
282. Watanabe M, Yokoshiki H, Mitsuyama H, Mizukami K, Ono T, Tsutsui H. Conduction and refractory disorders in the diabetic atrium. American journal of physiology Heart and circulatory physiology. 2012;303(1):H86-95. doi: 10.1152/ajpheart.00010.2012. PubMed PMID: 22561303.
283. Calvo D, Atienza F, Jalife J, Martinez-Alzamora N, Bravo L, Almendral J, et al. High-rate pacing-induced atrial fibrillation effectively reveals properties of spontaneously occurring paroxysmal atrial fibrillation in humans. Europace : European pacing, arrhythmias, and cardiac electrophysiology : journal of the working groups on cardiac pacing, arrhythmias, and cardiac cellular electrophysiology of the European Society of Cardiology. 2012;14(11):1560-6. doi: 10.1093/europace/eus180. PubMed PMID: 22696516; PubMed Central PMCID: PMC3697800.
284. Dilaveris PE, Gialafos EJ, Andrikopoulos GK, Richter DJ, Papanikolaou V, Poralis K, et al. Clinical and electrocardiographic predictors of recurrent atrial fibrillation. Pacing and clinical electrophysiology : PACE. 2000;23(3):352-8. PubMed PMID: 10750136.
285. Agarwal YK, Aronow WS, Levy JA, Spodick DH. Association of interatrial block with development of atrial fibrillation. The American journal of cardiology. 2003;91(7):882. PubMed PMID: 12667579.
286. McDonagh EW, Rudolph CJ, Cheraskin E. The relationship of subtle differences in fasting blood glucose with subtle differences in the electrocardiogram: a study of the PR interval. Medical hypotheses. 1982;8(3):261-8. PubMed PMID: 7087823.
287. Demir K, Avci A, Kaya Z, Marakoglu K, Ceylan E, Yilmaz A, et al. Assessment of atrial electromechanical delay and P-wave dispersion in patients with type 2 diabetes

mellitus. Journal of cardiology. 2016;67(4):378-83. doi: 10.1016/j.jjcc.2015.06.003. PubMed PMID: 26164686.
288. Severson DL. Diabetic cardiomyopathy: recent evidence from mouse models of type 1 and type 2 diabetes. Canadian journal of physiology and pharmacology. 2004;82(10):813-23. doi: 10.1139/y04-065. PubMed PMID: 15573141.
289. Falcao-Pires I, Leite-Moreira AF. Diabetic cardiomyopathy: understanding the molecular and cellular basis to progress in diagnosis and treatment. Heart failure reviews. 2012;17(3):325-44. doi: 10.1007/s10741-011-9257-z. PubMed PMID: 21626163.
290. Boudina S, Abel ED. Diabetic cardiomyopathy, causes and effects. Reviews in endocrine & metabolic disorders. 2010;11(1):31-9. doi: 10.1007/s11154-010-9131-7. PubMed PMID: 20180026; PubMed Central PMCID: PMC2914514.
291. Dent CL, Bowman AW, Scott MJ, Allen JS, Lisauskas JB, Janif M, et al. Echocardiographic characterization of fundamental mechanisms of abnormal diastolic filling in diabetic rats with a parameterized diastolic filling formalism. Journal of the American Society of Echocardiography : official publication of the American Society of Echocardiography. 2001;14(12):1166-72. PubMed PMID: 11734783.
292. Gilca GE, Stefanescu G, Badulescu O, Tanase DM, Bararu I, Ciocoiu M. Diabetic Cardiomyopathy: Current Approach and Potential Diagnostic and Therapeutic Targets. Journal of diabetes research. 2017;2017:1310265. doi: 10.1155/2017/1310265. PubMed PMID: 28421204; PubMed Central PMCID: PMC5379137.
293. Lorenzo-Almoros A, Tunon J, Orejas M, Cortes M, Egido J, Lorenzo O. Diagnostic approaches for diabetic cardiomyopathy. Cardiovasc Diabetol. 2017;16(1):28. doi: 10.1186/s12933-017-0506-x. PubMed PMID: 28231848; PubMed Central PMCID: PMC5324262.
294. Chao TF, Suenari K, Chang SL, Lin YJ, Lo LW, Hu YF, et al. Atrial substrate properties and outcome of catheter ablation in patients with paroxysmal atrial fibrillation associated with diabetes mellitus or impaired fasting glucose. The American journal of cardiology. 2010;106(11):1615-20. doi: 10.1016/j.amjcard.2010.07.038. PubMed PMID: 21094363.
295. Akyel A, Oksuz F, Karadeniz M, Yarlioglues M, Ergun G, Cankurt T, et al. Atrial electromechanical delay in type 2 diabetes mellitus. Wiener klinische Wochenschrift. 2014;126(3-4):101-5. doi: 10.1007/s00508-013-0477-1. PubMed PMID: 24424433.
296. Teuwen CP, Kik C, van der Does L, Lanters EAH, Knops P, Mouws E, et al. Quantification of the Arrhythmogenic Effects of Spontaneous Atrial Extrasystole Using High-Resolution Epicardial Mapping. Circulation Arrhythmia and electrophysiology. 2018;11(1). doi: 10.1161/CIRCEP.117.005745. PubMed PMID: 29269560.
297. Chen J, Li Q, Dong R, Gao H, Peng H, Wu Y. The effect of the Ras homolog gene family (Rho), member A/Rho associated coiled-coil forming protein kinase pathway in atrial fibrosis of type 2 diabetes in rats. Experimental and therapeutic medicine. 2014;8(3):836-40. doi: 10.3892/etm.2014.1843. PubMed PMID: 25120610; PubMed Central PMCID: PMC4113648.
298. Fu H, Liu C, Li J, Zhou C, Cheng L, Liu T, et al. Impaired atrial electromechanical function and atrial fibrillation promotion in alloxan-induced diabetic rabbits. Cardiology journal. 2013;20(1):59-67. doi: 10.5603/CJ.2013.0010. PubMed PMID: 23558812.
299. Lamberts RR, Lingam SJ, Wang HY, Bollen IA, Hughes G, Galvin IF, et al. Impaired relaxation despite upregulated calcium-handling protein atrial myocardium from type 2 diabetic patients with preserved ejection fraction. Cardiovasc Diabetol.

2014;13:72. doi: 10.1186/1475-2840-13-72. PubMed PMID: 24708792; PubMed Central PMCID: PMC3997226.
300. Simon JN, Duglan D, Casadei B, Carnicer R. Nitric oxide synthase regulation of cardiac excitation-contraction coupling in health and disease. J Mol Cell Cardiol. 2014;73:80-91. Epub 2014/03/19. doi: 10.1016/j.yjmcc.2014.03.004. PubMed PMID: 24631761.
301. Gonzalez DR, Beigi F, Treuer AV, Hare JM. Deficient ryanodine receptor S-nitrosylation increases sarcoplasmic reticulum calcium leak and arrhythmogenesis in cardiomyocytes. Proceedings of the National Academy of Sciences of the United States of America. 2007;104(51):20612-7. doi: 10.1073/pnas.0706796104. PubMed PMID: 18077344; PubMed Central PMCID: PMC2154479.
302. Evers RAF, van Vliet D, van Spronsen FJ. Tetrahydrobiopterin treatment in phenylketonuria: A repurposing approach. J Inherit Metab Dis. 2019. Epub 2019/08/03. doi: 10.1002/jimd.12151. PubMed PMID: 31373030.
303. Bazett HC. An analysis of time relations of electrocardiograms. Heart. 1920;7:353-67.
304. Toivonen L. More light on QT interval measurement. Heart. 2002;87(3):193-4. Epub 2002/02/16. doi: 10.1136/heart.87.3.193. PubMed PMID: 11847147; PubMed Central PMCID: PMCPMC1767027.
305. Malik M, Farbom P, Batchvarov V, Hnatkova K, Camm AJ. Relation between QT and RR intervals is highly individual among healthy subjects: implications for heart rate correction of the QT interval. Heart. 2002;87(3):220-8. Epub 2002/02/16. doi: 10.1136/heart.87.3.220. PubMed PMID: 11847158; PubMed Central PMCID: PMCPMC1767037.
306. Roussel J, Champeroux P, Roy J, Richard S, Fauconnier J, Le Guennec JY, et al. The Complex QT/RR Relationship in Mice. Sci Rep. 2016;6:25388. Epub 2016/05/04. doi: 10.1038/srep25388. PubMed PMID: 27138175; PubMed Central PMCID: PMCPMC4853711.
307. Speerschneider T, Thomsen MB. Physiology and analysis of the electrocardiographic T wave in mice. Acta Physiol (Oxf). 2013;209(4):262-71. Epub 2013/10/15. doi: 10.1111/apha.12172. PubMed PMID: 24119104.
308. Monfredi O, Dobrzynski H, Mondal T, Boyett MR, Morris GM. The anatomy and physiology of the sinoatrial node--a contemporary review. Pacing and clinical electrophysiology : PACE. 2010;33(11):1392-406. Epub 2010/10/16. doi: 10.1111/j.1540-8159.2010.02838.x. PubMed PMID: 20946278.
309. Murphy C, Lazzara R. Current concepts of anatomy and electrophysiology of the sinus node. Journal of interventional cardiac electrophysiology : an international journal of arrhythmias and pacing. 2016;46(1):9-18. Epub 2016/05/05. doi: 10.1007/s10840-016-0137-2. PubMed PMID: 27142063.
310. Adlam D, Herring N, Douglas G, De Bono JP, Li D, Danson EJ, et al. Regulation of beta-adrenergic control of heart rate by GTP-cyclohydrolase 1 (GCH1) and tetrahydrobiopterin. Cardiovascular research. 2012;93(4):694-701. Epub 2012/01/14. doi: 10.1093/cvr/cvs005. PubMed PMID: 22241166; PubMed Central PMCID: PMCPMC3291091.
311. Pagliaro P, Dalla Valle R, Gattullo D, Merletti A, Marsh NA. The heart rate after inhibition of nitric oxide release in the anaesthetized dog. Gen Pharmacol. 1996;27(4):695-9. Epub 1996/06/01. doi: 10.1016/0306-3623(95)02042-x. PubMed PMID: 8853307.
312. Aisaka K, Gross SS, Griffith OW, Levi R. NG-methylarginine, an inhibitor of endothelium-derived nitric oxide synthesis, is a potent pressor agent in the guinea pig:

does nitric oxide regulate blood pressure in vivo? Biochem Biophys Res Commun. 1989;160(2):881-6. Epub 1989/04/28. doi: 10.1016/0006-291x(89)92517-5. PubMed PMID: 2719705.
313. Reid IA, Bui H, Chou L. Role of nitric oxide in the renin and heart rate responses to beta-adrenergic stimulation. Hypertension. 1994;23(1 Suppl):I49-53. Epub 1994/01/01. doi: 10.1161/01.hyp.23.1_suppl.i49. PubMed PMID: 8282375.
314. Exner DV, Goodhart DM, Anderson TJ, Duff HJ. Prolonged sinus node recovery time in humans after the intracoronary administration of a nitric oxide synthase inhibitor. Journal of cardiovascular pharmacology. 1999;34(1):1-6. Epub 1999/07/21. doi: 10.1097/00005344-199907000-00001. PubMed PMID: 10413059.
315. Breithardt G, Seipel L, Loogen F. Sinus node recovery time and calculated sinoatrial conduction time in normal subjects and patients with sinus node dysfunction. Circulation. 1977;56(1):43-50. Epub 1977/07/01. doi: 10.1161/01.cir.56.1.43. PubMed PMID: 862170.
316. Narula OS, Samet P, Javier RP. Significance of the sinus-node recovery time. Circulation. 1972;45(1):140-58. Epub 1972/01/01. doi: 10.1161/01.cir.45.1.140. PubMed PMID: 4108657.
317. Imai Y, Yokoyama Y, Watanabe T. Sinus Node Recovery Time Can Predict Maintenance of Sinus Rhythm After Catheter Ablation for Long-Standing Atrial Fibrillation. International heart journal. 2018;59(3):460-1. Epub 2018/06/01. doi: 10.1536/ihj.18-245. PubMed PMID: 29848892.
318. Yamaguchi N, Okumura Y, Watanabe I, Nagashima K, Takahashi K, Iso K, et al. Impact of Sinus Node Recovery Time after Long-Standing Atrial Fibrillation Termination on the Long-Term Outcome of Catheter Ablation. International heart journal. 2018;59(3):497-502. Epub 2018/05/11. doi: 10.1536/ihj.17-097. PubMed PMID: 29743409.
319. Hwang HJ, Ng FS, Efimov IR. Mechanisms of Atrioventricular Nodal Excitability and Propagation. In: Zipes DP, Jalife J, editors. Cardiac Electrophysiology: From Cell to Bedside. 6th ed: Elsevier Ltd; 2014.
320. Elvan A, Rubart M, Zipes DP. NO modulates autonomic effects on sinus discharge rate and AV nodal conduction in open-chest dogs. The American journal of physiology. 1997;272(1 Pt 2):H263-71. Epub 1997/01/01. doi: 10.1152/ajpheart.1997.272.1.H263. PubMed PMID: 9038946.
321. Fridericia LS. Die Systolendauer im Elektrokardiogramm bei normalen Menschen und bei Herzkranken. Acta Med Scand. 1920;53:469-86.
322. Shah SR, Park K, Alweis R. Long QT Syndrome: A Comprehensive Review of the Literature and Current Evidence. Curr Probl Cardiol. 2019;44(3):92-106. Epub 2018/05/23. doi: 10.1016/j.cpcardiol.2018.04.002. PubMed PMID: 29784533.
323. Khan IA. Long QT syndrome: diagnosis and management. Am Heart J. 2002;143(1):7-14. Epub 2002/01/05. doi: 10.1067/mhj.2002.120295. PubMed PMID: 11773906.
324. Iwasaki YK, Nishida K, Kato T, Nattel S. Atrial fibrillation pathophysiology: implications for management. Circulation. 2011;124(20):2264-74. doi: 10.1161/CIRCULATIONAHA.111.019893. PubMed PMID: 22083148.
325. Karam BS, Chavez-Moreno A, Koh W, Akar JG, Akar FG. Oxidative stress and inflammation as central mediators of atrial fibrillation in obesity and diabetes. Cardiovasc Diabetol. 2017;16(1):120. doi: 10.1186/s12933-017-0604-9. PubMed PMID: 28962617; PubMed Central PMCID: PMC5622555.
326. Kalla M, Chotalia M, Coughlan C, Hao G, Crabtree MJ, Tomek J, et al. Protection against ventricular fibrillation via cholinergic receptor stimulation and the

generation of nitric oxide. The Journal of physiology. 2016;594(14):3981-92. Epub 2016/01/12. doi: 10.1113/JP271588. PubMed PMID: 26752781; PubMed Central PMCID: PMCPMC4794549.
327. Wang L, Li D, Dawson TA, Paterson DJ. Long-term effect of neuronal nitric oxide synthase over-expression on cardiac neurotransmission mediated by a lentiviral vector. The Journal of physiology. 2009;587(Pt 14):3629-37. Epub 2009/06/06. doi: 10.1113/jphysiol.2009.172866. PubMed PMID: 19491240; PubMed Central PMCID: PMCPMC2742286.
328. Poulos TL, Li H. Nitric oxide synthase and structure-based inhibitor design. Nitric oxide : biology and chemistry. 2017;63:68-77. Epub 2016/11/29. doi: 10.1016/j.niox.2016.11.004. PubMed PMID: 27890696; PubMed Central PMCID: PMCPMC5569579.
329. Pigott B, Bartus K, Garthwaite J. On the selectivity of neuronal NOS inhibitors. British journal of pharmacology. 2013;168(5):1255-65. Epub 2012/10/18. doi: 10.1111/bph.12016. PubMed PMID: 23072468; PubMed Central PMCID: PMCPMC3594681.
330. Pugach EK, Richmond PA, Azofeifa JG, Dowell RD, Leinwand LA. Prolonged Cre expression driven by the alpha-myosin heavy chain promoter can be cardiotoxic. J Mol Cell Cardiol. 2015;86:54-61. Epub 2015/07/05. doi: 10.1016/j.yjmcc.2015.06.019. PubMed PMID: 26141530; PubMed Central PMCID: PMCPMC4558343.
331. Wang TJ, Larson MG, Levy D, Vasan RS, Leip EP, Wolf PA, et al. Temporal relations of atrial fibrillation and congestive heart failure and their joint influence on mortality: the Framingham Heart Study. Circulation. 2003;107(23):2920-5. Epub 2003/05/29. doi: 10.1161/01.CIR.0000072767.89944.6E. PubMed PMID: 12771006.
332. Intensive blood-glucose control with sulphonylureas or insulin compared with conventional treatment and risk of complications in patients with type 2 diabetes (UKPDS 33). UK Prospective Diabetes Study (UKPDS) Group. Lancet. 1998;352(9131):837-53. Epub 1998/09/22. PubMed PMID: 9742976.
333. Malmberg K, Ryden L, Wedel H, Birkeland K, Bootsma A, Dickstein K, et al. Intense metabolic control by means of insulin in patients with diabetes mellitus and acute myocardial infarction (DIGAMI 2): effects on mortality and morbidity. European heart journal. 2005;26(7):650-61. Epub 2005/02/25. doi: 10.1093/eurheartj/ehi199. PubMed PMID: 15728645.
334. Group AC, Patel A, MacMahon S, Chalmers J, Neal B, Billot L, et al. Intensive blood glucose control and vascular outcomes in patients with type 2 diabetes. The New England journal of medicine. 2008;358(24):2560-72. Epub 2008/06/10. doi: 10.1056/NEJMoa0802987. PubMed PMID: 18539916.
335. Group AS, Cushman WC, Evans GW, Byington RP, Goff DC, Jr., Grimm RH, Jr., et al. Effects of intensive blood-pressure control in type 2 diabetes mellitus. The New England journal of medicine. 2010;362(17):1575-85. Epub 2010/03/17. doi: 10.1056/NEJMoa1001286. PubMed PMID: 20228401; PubMed Central PMCID: PMCPMC4123215.
336. Group AS, Gerstein HC, Miller ME, Genuth S, Ismail-Beigi F, Buse JB, et al. Long-term effects of intensive glucose lowering on cardiovascular outcomes. The New England journal of medicine. 2011;364(9):818-28. Epub 2011/03/04. doi: 10.1056/NEJMoa1006524. PubMed PMID: 21366473; PubMed Central PMCID: PMCPMC4083508.
337. Kirchhof P, Benussi S, Kotecha D, Ahlsson A, Atar D, Casadei B, et al. 2016 ESC Guidelines for the management of atrial fibrillation developed in collaboration

with EACTS. European heart journal. 2016;37(38):2893-962. Epub 2016/08/28. doi: 10.1093/eurheartj/ehw210. PubMed PMID: 27567408.
338. Siebermair J, Kholmovski EG, Marrouche N. Assessment of Left Atrial Fibrosis by Late Gadolinium Enhancement Magnetic Resonance Imaging: Methodology and Clinical Implications. JACC Clin Electrophysiol. 2017;3(8):791-802. Epub 2018/05/16. doi: 10.1016/j.jacep.2017.07.004. PubMed PMID: 29759774.
339. Gal P, Marrouche NF. Magnetic resonance imaging of atrial fibrosis: redefining atrial fibrillation to a syndrome. European heart journal. 2017;38(1):14-9. Epub 2015/09/27. doi: 10.1093/eurheartj/ehv514. PubMed PMID: 26409008.
340. Hatem SN, Redheuil A, Gandjbakhch E. Cardiac adipose tissue and atrial fibrillation: the perils of adiposity. Cardiovascular research. 2016;109(4):502-9. doi: 10.1093/cvr/cvw001. PubMed PMID: 26790475.
341. Lau WB, Ohashi K, Wang Y, Ogawa H, Murohara T, Ma XL, et al. Role of Adipokines in Cardiovascular Disease. Circulation journal : official journal of the Japanese Circulation Society. 2017;81(7):920-8. doi: 10.1253/circj.CJ-17-0458. PubMed PMID: 28603178.
342. Jaganathan R, Ravindran R, Dhanasekaran S. Emerging Role of Adipocytokines in Type 2 Diabetes as Mediators of Insulin Resistance and Cardiovascular Disease. Canadian journal of diabetes. 2018;42(4):446-56 e1. doi: 10.1016/j.jcjd.2017.10.040. PubMed PMID: 29229313.
343. Gungor B. Obesity and atrial fibrillation: can adipokines help to solve this puzzle. Heart. 2016;102(17):1339-40. doi: 10.1136/heartjnl-2016-309751. PubMed PMID: 27250214.
344. Frati G, Schirone L, Chimenti I, Yee D, Biondi-Zoccai G, Volpe M, et al. An overview of the inflammatory signalling mechanisms in the myocardium underlying the development of diabetic cardiomyopathy. Cardiovascular research. 2017;113(4):378-88. doi: 10.1093/cvr/cvx011. PubMed PMID: 28395009.
345. Rosenthal N. A Guardian of the Heartbeat. The New England journal of medicine. 2017;377(1):84-6. doi: 10.1056/NEJMcibr1705327. PubMed PMID: 28679094.
346. Hulsmans M, Clauss S, Xiao L, Aguirre AD, King KR, Hanley A, et al. Macrophages Facilitate Electrical Conduction in the Heart. Cell. 2017;169(3):510-22 e20. doi: 10.1016/j.cell.2017.03.050. PubMed PMID: 28431249; PubMed Central PMCID: PMC5474950.
347. Monnerat G, Alarcon ML, Vasconcellos LR, Hochman-Mendez C, Brasil G, Bassani RA, et al. Macrophage-dependent IL-1beta production induces cardiac arrhythmias in diabetic mice. Nature communications. 2016;7:13344. doi: 10.1038/ncomms13344. PubMed PMID: 27882934; PubMed Central PMCID: PMC5123037.
348. Lin H, Ogawa K, Imanaga I, Tribulova N. Alterations of connexin 43 in the diabetic rat heart. Advances in cardiology. 2006;42:243-54. doi: 10.1159/000092573. PubMed PMID: 16646595.
349. Hiatt WR, Kaul S, Smith RJ. The cardiovascular safety of diabetes drugs--insights from the rosiglitazone experience. The New England journal of medicine. 2013;369(14):1285-7. Epub 2013/09/03. doi: 10.1056/NEJMp1309610. PubMed PMID: 23992603.
350. U.S. Department of Health and Human Services Food and Drug Administration. Guidance for Industry: Diabetes Mellitus - Evaluating Cardiovascular Risk in New Antidiabetic Therapies to Treat Type 2 Diabetes 2008. Available from: https://www.fda.gov/media/71297/download.

351. Zelniker TA, Bonaca MP, Furtado RHM, Mosenzon O, Kuder JF, Murphy SA, et al. Effect of Dapagliflozin on Atrial Fibrillation in Patients With Type 2 Diabetes Mellitus: Insights From the DECLARE-TIMI 58 Trial. Circulation. 2020;141(15):1227-34. Epub 2020/01/28. doi: 10.1161/CIRCULATIONAHA.119.044183. PubMed PMID: 31983236.
352. Bolzan AD, Bianchi MS. Genotoxicity of streptozotocin. Mutat Res. 2002;512(2-3):121-34. Epub 2002/12/05. doi: 10.1016/s1383-5742(02)00044-3. PubMed PMID: 12464347.
353. Iwase M, Nunoi K, Sadoshima S, Kikuchi M, Fujishima M. Liver, kidney and islet cell tumors in spontaneously hypertensive and normotensive rats treated neonatally with streptozotocin. The Tohoku journal of experimental medicine. 1989;159(2):83-90. Epub 1989/10/01. doi: 10.1620/tjem.159.83. PubMed PMID: 2532796.
354. Kume E, Aruga C, Ishizuka Y, Takahashi K, Miwa S, Itoh M, et al. Gene expression profiling in streptozotocin treated mouse liver using DNA microarray. Exp Toxicol Pathol. 2005;56(4-5):235-44. Epub 2005/04/09. doi: 10.1016/j.etp.2004.09.002. PubMed PMID: 15816352.
355. Wold LE, Ren J. Streptozotocin directly impairs cardiac contractile function in isolated ventricular myocytes via a p38 map kinase-dependent oxidative stress mechanism. Biochem Biophys Res Commun. 2004;318(4):1066-71. Epub 2004/05/19. doi: 10.1016/j.bbrc.2004.04.138. PubMed PMID: 15147982.
356. Brosius FC, 3rd, Alpers CE, Bottinger EP, Breyer MD, Coffman TM, Gurley SB, et al. Mouse models of diabetic nephropathy. J Am Soc Nephrol. 2009;20(12):2503-12. Epub 2009/09/05. doi: 10.1681/ASN.2009070721. PubMed PMID: 19729434; PubMed Central PMCID: PMCPMC4075053.
357. Kaese S, Verheule S. Cardiac electrophysiology in mice: a matter of size. Frontiers in physiology. 2012;3:345. doi: 10.3389/fphys.2012.00345. PubMed PMID: 22973235; PubMed Central PMCID: PMC3433738.
358. Manuel RPMKKEHRJRBCWDF-RSREYTDP-B. Dominant Frequency Increase Rate Predicts Transition from Paroxysmal to Long-Term Persistent Atrial Fibrillation. Circulation.

APPENDIX

Action potential duration calculation

MATLAB code for automatically calculating action potential duration (APD) from the fluorescence signal from several regions of interest (ROI).

```
function APD_analysis_function(file_folder, file_name, output_folder, save_figure,
AP_figure)
%APD_analysis_function Analyses action potentials for several ROIs
%   Every file contains several ROIs
%   Outputs APD30, APD50, APD80, AP intervals, AP amplitudes in csv files
%   Optional: saves figures as jpg files

%%%%%%%%%%%%%%%%%%%%%%%%%%%%%%%%%%%%%%%%%%%%%%%%%%%%%%%%
% Check if save_figure argument exists
if (~exist('save_figure', 'var'))
        save_figure = '0';
end

if (~exist('AP_figure', 'var'))
        AP_figure = '0';
end


%%%%%%%%%%%%%%%%%%%%%%%%%%%%%%%%%%%%%%%%%%%%%%%%%%%%%%%%
% Optical mapping APD analysis script
%
% by Klemen Ziberna
%%%%%%%%%%%%%%%%%%%%%%%%%%%%%%%%%%%%%%%%%%%%%%%%%%%%%%%%

%%%%%%%%%%%%%%%%%%%%%%%%%%%%%%%%%%%%%%%%%%%%%%%%%%%%%%%%
%
% v2 - updates:
% - better logic to handle APs close to the border
% - added feature to save results in csv file
%
%%%%%%%%%%%%%%%%%%%%%%%%%%%%%%%%%%%%%%%%%%%%%%%%%%%%%%%%

%clear;
%close all;

%%%%%%%%%%%%%%%%%%%%%%%%%%
% Load data

file_name2 = file_name(1:end-4);
raw_data = importdata([file_folder,file_name]);

n_rois = size(raw_data, 2)-1;
t = transpose(raw_data(:,1)); %time

for i=1:n_rois
   raw_signal{i} = transpose(raw_data(:,i+1));
end

%%%%%%%%%%%%%%%%%%%%%%%%%%
% SIGNAL PROCESSING
%%%%%%%%%%%%%%%%%%%%%%%%%%

t_max = max(t);

% Invert signals (i.e. multiply by -1)

for i=1:n_rois
    F_raw{i} = (-1)*raw_signal{i};
    F_raw_max{i} =  max(F_raw{i});
    F_raw_min{i} =  min(F_raw{i});
    F_raw_range{i} = abs(F_raw_max{i}-F_raw_min{i});
end

%%%%%%%%%%%%%%%%%%%%%%%%%%
% Signal smoothing

% Baseline drift correction (using the polynomial fit)
```

```matlab
opol = 3; %order of the fitted polynomial (customize!)

for i=1:n_rois
    [p,s,mu] = polyfit(t,F_raw{i},opol);
    f_y{i} = polyval(p,t,[],mu);
    F_BC{i} = F_raw{i} - f_y{i};
end

% Filter

% Option A: Moving average (simple, but bad option)

% Note: some of the functions bellow are dependent upon windowSize

% windowSize = 15; %customize!
% b = (1/windowSize)*ones(1,windowSize);
% a = 1;
%
% for i=1:n_rois
%     F_avg{i} = filter(b, a, F_BC{i});
%     %F_avg_max{i} =  max(F_avg{i});
%     %F_avg_min{i} =  min(F_avg{i});
%
%     %To avoid dips at the edges when using moving average
%     F_avg_max{i} =  max(F_avg{i}(2*windowSize:(end-2*windowSize)));
%     F_avg_min{i} =  min(F_avg{i}(2*windowSize:(end-2*windowSize)));
%     F_avg_range{i} = abs(F_avg_max{i}-F_avg_min{i});
% end


% Option B: IIR filter averaging (Butteworth)
% better approach
% Recommended values: 5th order, 0.6
% which corresponds to 100Hz filter using 1kHz sampling rate

% Formula to calculate the value 'a'
% a = (2*pi*Frequency_cutoff/sampling_frequency)


[b,a] = butter(6,0.4);
freqz(b,a);

for i=1:n_rois
    F_avg{i} = filtfilt(b, a, F_BC{i});
    F_avg_max{i} =  max(F_avg{i});
    F_avg_min{i} =  min(F_avg{i});
    F_avg_range{i} = abs(F_avg_max{i}-F_avg_min{i});
end



%%%%%%%%%%%%%%%%%%%%%%%%%%

% First derivative (dF/dt)

for i=1:n_rois
    dF_raw_dt{i} = diff(F_raw{i})./diff(t);
    dF_raw_dt_max{i} = max(dF_raw_dt{i});
    dF_raw_dt_min{i} = min(dF_raw_dt{i});
    dF_raw_dt_range{i} = abs(dF_raw_dt_max{i}-dF_raw_dt_min{i});
end

for i=1:n_rois
    dF_avg_dt{i} = diff(F_avg{i})./diff(t);
    dF_avg_dt_max{i} = max(dF_avg_dt{i});
    dF_avg_dt_min{i} = min(dF_avg_dt{i});

    % Use it with moving average
    %dF_avg_dt_max{i} =  max(dF_avg_dt{i}(2*windowSize:(end-2*windowSize)));
    %dF_avg_dt_min{i} =  min(dF_avg_dt{i}(2*windowSize:(end-2*windowSize)));
    dF_avg_dt_range{i} = abs(dF_avg_dt_max{i}-dF_avg_dt_min{i});
end

tt = t(1:end-1)+diff(t)./2; % Associated time values (central difference)
```

```
% Find peaks for analysis

F_peak_MinHeight_set = 0.7; % min peak fold increase above baseline
F_peak_MinDistance = 70; % min peak separation (customizable)

T_BEGIN_CUTOFF = 50; % time cutoff for the first AP to be analysed (default 50)
T_END_CUTOFF = 100; % time cutoff for the last AP to be analysed (default 100)

for i=1:n_rois
    [F_avg_peaks{i}, F_avg_peaks_ind{i}] = findpeaks(F_avg{i}, ...
        'MinPeakHeight', (F_avg_min{i}+F_avg_range{i}*F_peak_MinHeight_set), ...
        'MinPeakDistance', F_peak_MinDistance);

    % Cutoff at the beginning
    while t(F_avg_peaks_ind{i}(1)) < T_BEGIN_CUTOFF;
        F_avg_peaks{i} = F_avg_peaks{i}(2:end);
        F_avg_peaks_ind{i} = F_avg_peaks_ind{i}(2:end);
    end

    % Cutoff at the end
    while t_max - t(F_avg_peaks_ind{i}(end)) < T_END_CUTOFF;
        F_avg_peaks{i} = F_avg_peaks{i}(1:end-1);
        F_avg_peaks_ind{i} = F_avg_peaks_ind{i}(1:end-1);
    end

    mean_F_interval{i} = mean(diff(t(F_avg_peaks_ind{i})));
    N_F_avg_peaks{i} = length(F_avg_peaks{i});

end


% Intervals between the signals

for i=1:n_rois
    F_peak_interval{i} = diff(t(F_avg_peaks_ind{i}(:)));
    N_F_peak_interval{i} = length(F_peak_interval{i});
end



% Determine the baseline before the peak

baseline_det_rel_offset = 0.15; %relative (to mean PP) time before the peak
baseline_det_abs_offset = 25; %absolute offset before the peak

for i=1:n_rois
    for j=1:N_F_avg_peaks{i}

        baseline_start_ind{i}{j}= F_avg_peaks_ind{i}(j)-...
            round(baseline_det_rel_offset*mean_F_interval{i})-baseline_det_abs_offset;

        if baseline_start_ind{i}{j} <1
            baseline_start_ind{i}{j} = 1; %in case start border is out of range
        end

        baseline_end_ind{i}{j}= F_avg_peaks_ind{i}(j)-baseline_det_abs_offset;
        baseline_mean{i}{j} =
mean(F_avg{i}(baseline_start_ind{i}{j}:baseline_end_ind{i}{j}));

    end
end


% Max dF/dt and activation time

AP_border_left = 50; % n of points before every peak for max dF/dt detection!

for i=1:n_rois
    for j=1:N_F_avg_peaks{i}
        [dF_dt_max{i}(j), dF_dt_max_rel_ind{i}(j)] = ...
            max(dF_avg_dt{i}(F_avg_peaks_ind{i}(j)-
AP_border_left:F_avg_peaks_ind{i}(j)));
        t_act_ind{i}(j) = (F_avg_peaks_ind{i}(j) - AP_border_left...
            + dF_dt_max_rel_ind{i}(j)); %absolute time index
        t_act{i}(j) = t(t_act_ind{i}(j)); %absolute activation times
```

```
    end
end


% Rise time

for i=1:n_rois
    for j=1:N_F_avg_peaks{i}
        AP_rise_time{i}(j) = t(F_avg_peaks_ind{i}(j)) - t_act{i}(j);
    end
end

% APD calculations

for i=1:n_rois
    for j=1:N_F_avg_peaks{i}

        F_max{i}(j) = F_avg_peaks{i}(j);
        AP_amplitude{i}(j) = F_max{i}(j) - baseline_mean{i}{j};

        F_AP_30{i}(j) = F_max{i}(j) - 0.3*AP_amplitude{i}(j);
        APD30_rel_ind{i}(j) = ...
            find(F_avg{i}(F_avg_peaks_ind{i}(j):end)<F_AP_30{i}(j),1); %relative index
to peak
        APD30_ind{i}(j) = F_avg_peaks_ind{i}(j) + APD30_rel_ind{i}(j); %absolute index
        APD30{i}(j) = t(APD30_ind{i}(j)) - t_act{i}(j); %absolute APD time

        F_AP_50{i}(j) = F_max{i}(j) - 0.5*AP_amplitude{i}(j);
        APD50_rel_ind{i}(j) = ...
            find(F_avg{i}(F_avg_peaks_ind{i}(j):end)<F_AP_50{i}(j),1); %relative index
to peak
        APD50_ind{i}(j) = F_avg_peaks_ind{i}(j) + APD50_rel_ind{i}(j); %absolute index
        APD50{i}(j) = t(APD50_ind{i}(j)) - t_act{i}(j); %absolute APD time

        F_AP_80{i}(j) = F_max{i}(j) - 0.8*AP_amplitude{i}(j);
        APD80_rel_ind{i}(j) = ...
            find(F_avg{i}(F_avg_peaks_ind{i}(j):end)<F_AP_80{i}(j),1); %relative index
to peak
        APD80_ind{i}(j) = F_avg_peaks_ind{i}(j) + APD80_rel_ind{i}(j); %absolute index
        APD80{i}(j) = t(APD80_ind{i}(j)) - t_act{i}(j); %absolute APD time

    end
end



%%%%%%%%%%%%%%%%%%%%%%%%%%
% SAVE RESULTS - CSV FILE
%%%%%%%%%%%%%%%%%%%%%%%%%%

% Format:
% - one results file per loaded ROI file
% - one line for one variable (all results horizontaly)
% - naming: file name, ROI number, variable, N measurements, measurements
% - variables: APD30, APD50, APD80, peak_intervals, peak_amplitudes


% Format the output row

for i=1:n_rois

    % APD30
    outputAPD30Row{i} = [{file_name2, i, 'APD30', N_F_avg_peaks{i}},...
        num2cell(APD30{i})];
    outputAPD30RowString{i} = cellfun(@num2str, outputAPD30Row{i},...
        'UniformOutput', false);
    outputAPD30RowSingleString{i} = strjoin(outputAPD30RowString{i}, ',');

    % APD50
    outputAPD50Row{i} = [{file_name2, i, 'APD50', N_F_avg_peaks{i}},...
        num2cell(APD50{i})];
    outputAPD50RowString{i} = cellfun(@num2str, outputAPD50Row{i},...
        'UniformOutput', false);
    outputAPD50RowSingleString{i} = strjoin(outputAPD50RowString{i}, ',');

    % APD80
```

```
    outputAPD80Row{i} = [{file_name2, i, 'APD80', N_F_avg_peaks{i}},...
        num2cell(APD80{i})];
    outputAPD80RowString{i} = cellfun(@num2str, outputAPD80Row{i},...
        'UniformOutput', false);
    outputAPD80RowSingleString{i} = strjoin(outputAPD80RowString{i}, ',');

    % AP intervals
    outputF_peak_intervalRow{i} = [{file_name2, i, 'Peak_Intervals',...
        N_F_peak_interval{i}}, num2cell(F_peak_interval{i})];
    outputF_peak_intervalRowString{i} = cellfun(@num2str, ...
        outputF_peak_intervalRow{i}, 'UniformOutput', false);
    outputF_peak_intervalRowSingleString{i} = ...
        strjoin(outputF_peak_intervalRowString{i}, ',');

    % AP amplitude
    outputAP_amplitudeRow{i} = [{file_name2, i, 'AP_amplitude',...
        N_F_avg_peaks{i}}, num2cell(AP_amplitude{i})];
    outputAP_amplitudeRowString{i} = cellfun(@num2str, outputAP_amplitudeRow{i},...
        'UniformOutput', false);
    outputAP_amplitudeRowSingleString{i} = strjoin(outputAP_amplitudeRowString{i},
',');

end


% Merge rows

outputTableRows = [outputAPD30RowSingleString, outputAPD50RowSingleString,...
    outputAPD80RowSingleString, outputF_peak_intervalRowSingleString,...
    outputAP_amplitudeRowSingleString];


%Save file to the csv file

%outputTableFilename = [file_name2, '-table.csv'];
outputTableFilename = [output_folder, file_name2, '-table.csv'];
N_rows = length(outputTableRows);

fileID = fopen(outputTableFilename,'w');
fprintf(fileID,'%s,\n',...
    'file_name,ROI_N,Variable,N_measurements,Measurements>>>>>>'); % header line
for i=1:N_rows
    fprintf(fileID, '%s\n', outputTableRows{i});
end
fclose(fileID);

%%%%%%%%%%%%%%%%%%%%%%%%%%
% SUMMARY OF RESULTS
%%%%%%%%%%%%%%%%%%%%%%%%%%

if n_rois == 4;
    % OPTION A: Zoomed in left or right atria (ROI=4)
    disp('Zoomed atria summary results');

    % Convert the cell arrays to matrices for easier manipulation
    % Check if the number of APs is the same in all ROIs (-1 if not)

    APD30_size = cellfun(@length, APD30);
    if all(APD30_size == APD30_size(1));
        APD30_mat = vertcat(APD30{:});
    else
        disp('Number of APs in APD30 ROIs do not match - no summary analysis');
        APD30_mat = -1;
    end

    APD50_size = cellfun(@length, APD50);
    if all(APD50_size == APD50_size(1));
        APD50_mat = vertcat(APD50{:});
    else
        disp('Number of APs in APD50 ROIs do not match - no summary analysis');
        APD50_mat = -1;
    end

    APD80_size = cellfun(@length, APD80);
    if all(APD80_size == APD80_size(1));
        APD80_mat = vertcat(APD80{:});
```

```
    else
        disp('Number of APs in APD80 ROIs do not match - no summary analysis');
        APD80_mat = -1;
    end

    F_peak_interval_size = cellfun(@length, F_peak_interval);
    if all(F_peak_interval_size == F_peak_interval_size(1));
        F_peak_interval_mat = vertcat(F_peak_interval{:});
    else
        disp('Number of APs in F_peak_interval ROIs do not match - no summary
analysis');
        F_peak_interval_mat = -1;
    end

    AP_amplitude_size = cellfun(@length, AP_amplitude);
    if all(AP_amplitude_size == AP_amplitude_size(1));
        AP_amplitude_mat = vertcat(AP_amplitude{:});
    else
        disp('Number of APs in AP_amplitude ROIs do not match - no summary analysis');
        AP_amplitude_mat = -1;
    end

    % Calculations of summary variables

    APD30_avg = mean2(APD30_mat);
    APD30_STD = std2(APD30_mat);
    Loc_APD30_STD = std(mean(APD30_mat,2)); %STD of rows' means

    APD50_avg = mean2(APD50_mat);
    APD50_STD = std2(APD50_mat);
    Loc_APD50_STD = std(mean(APD50_mat,2)); %STD of rows' means

    APD80_avg = mean2(APD80_mat);
    APD80_STD = std2(APD80_mat);
    Loc_APD80_STD = std(mean(APD80_mat,2)); %STD of rows' means

    AP_interval_avg = mean(mean(F_peak_interval_mat));
    AP_interval_STD_avg = std2(mean(F_peak_interval_mat,1));

    AP_amp_CoefVar = mean(std(AP_amplitude_mat, 0, 2)./...
        mean(AP_amplitude_mat,2)); %mean AP amplitude CV of every row

    % Create summary variables csv string

    outputSummaryRow = [{file_name2, 'zoomed atria', ...
        AP_interval_avg, AP_interval_STD_avg, ...
        APD30_avg, APD50_avg, APD80_avg,...
        APD30_STD, APD50_STD, APD80_STD,...
        Loc_APD30_STD, Loc_APD50_STD, Loc_APD80_STD,...
        AP_amp_CoefVar}];
    outputSummaryRowString = cellfun(@num2str, outputSummaryRow,...
        'UniformOutput', false);
    outputSummaryRowSingleString = strjoin(outputSummaryRowString, ',');

    % Save summary variables in csv file

    outputSummaryFilename = [output_folder, file_name2, '-summary.csv'];

    fileID = fopen(outputSummaryFilename,'w');
    % Header line
    fprintf(fileID,'%s,\n',...

'file_name,Region,AP_interval_avg,AP_interval_STD_avg,APD30_avg,APD50_avg,APD80_avg,AP
D30_STD,APD50_STD,APD80_STD,Loc_APD30_STD,Loc_APD50_STD,Loc_APD80_STD,AP_amp_CoefVar')
;
    % Results line
    fprintf(fileID, '%s\n', outputSummaryRowSingleString);
    fclose(fileID);




elseif n_rois == 6;
    % OPTION B: Biatrial analysis (ROI=6)
    % LA - ROI1-2
    % RA - ROI3-4
```

```
% SAN1 - ROI5
% SAN2 - ROI6
disp('Biatrial summary results');

% Obtain cell arrays for a particalar ROI region(s)

% LA = ROI1 + ROI2
LA_APD30 = {APD30{1:2}};
LA_APD50 = {APD50{1:2}};
LA_APD80 = {APD80{1:2}};
LA_F_peak_interval = {F_peak_interval{1:2}};
LA_AP_amplitude = {AP_amplitude{1:2}};

% RA = ROI3 + ROI4
RA_APD30 = {APD30{3:4}};
RA_APD50 = {APD50{3:4}};
RA_APD80 = {APD80{3:4}};
RA_F_peak_interval = {F_peak_interval{3:4}};
RA_AP_amplitude = {AP_amplitude{3:4}};

% SAN1 = ROI5
SAN1_APD30 = {APD30{5}};
SAN1_APD50 = {APD50{5}};
SAN1_APD80 = {APD80{5}};
SAN1_F_peak_interval = {F_peak_interval{5}};
SAN1_AP_amplitude = {AP_amplitude{5}};

% SAN2 = ROI6
SAN2_APD30 = {APD30{6}};
SAN2_APD50 = {APD50{6}};
SAN2_APD80 = {APD80{6}};
SAN2_F_peak_interval = {F_peak_interval{6}};
SAN2_AP_amplitude = {AP_amplitude{6}};

% Convert the cell arrays to matrices for easier manipulation
% Need 'APD_ROI_mat_conv.m' function

LA_APD30_mat = APD_ROI_mat_conv(LA_APD30);
LA_APD50_mat = APD_ROI_mat_conv(LA_APD50);
LA_APD80_mat = APD_ROI_mat_conv(LA_APD80);
LA_F_peak_interval_mat = APD_ROI_mat_conv(LA_F_peak_interval);
LA_AP_amplitude_mat = APD_ROI_mat_conv(LA_AP_amplitude);

RA_APD30_mat = APD_ROI_mat_conv(RA_APD30);
RA_APD50_mat = APD_ROI_mat_conv(RA_APD50);
RA_APD80_mat = APD_ROI_mat_conv(RA_APD80);
RA_F_peak_interval_mat = APD_ROI_mat_conv(RA_F_peak_interval);
RA_AP_amplitude_mat = APD_ROI_mat_conv(RA_AP_amplitude);

SAN1_APD30_mat = APD_ROI_mat_conv(SAN1_APD30);
SAN1_APD50_mat = APD_ROI_mat_conv(SAN1_APD50);
SAN1_APD80_mat = APD_ROI_mat_conv(SAN1_APD80);
SAN1_F_peak_interval_mat = APD_ROI_mat_conv(SAN1_F_peak_interval);
SAN1_AP_amplitude_mat = APD_ROI_mat_conv(SAN1_AP_amplitude);

SAN2_APD30_mat = APD_ROI_mat_conv(SAN2_APD30);
SAN2_APD50_mat = APD_ROI_mat_conv(SAN2_APD50);
SAN2_APD80_mat = APD_ROI_mat_conv(SAN2_APD80);
SAN2_F_peak_interval_mat = APD_ROI_mat_conv(SAN2_F_peak_interval);
SAN2_AP_amplitude_mat = APD_ROI_mat_conv(SAN2_AP_amplitude);

% Calculations of summary variables

LA_APD30_avg = mean2(LA_APD30_mat);
LA_APD30_STD = std2(LA_APD30_mat);
Loc_LA_APD30_STD = std(mean(LA_APD30_mat,2)); %STD of rows' means
LA_APD50_avg = mean2(LA_APD50_mat);
LA_APD50_STD = std2(LA_APD50_mat);
Loc_LA_APD50_STD = std(mean(LA_APD50_mat,2)); %STD of rows' means
LA_APD80_avg = mean2(LA_APD80_mat);
LA_APD80_STD = std2(LA_APD80_mat);
Loc_LA_APD80_STD = std(mean(LA_APD80_mat,2)); %STD of rows' means
LA_AP_interval_avg = mean(mean(LA_F_peak_interval_mat));
LA_AP_interval_STD_avg = std2(mean(LA_F_peak_interval_mat,1));
LA_AP_amp_CoefVar = mean(std(LA_AP_amplitude_mat, 0, 2)./...
    mean(LA_AP_amplitude_mat,2)); %mean AP amplitude CV of every row
```

```
RA_APD30_avg = mean2(RA_APD30_mat);
RA_APD30_STD = std2(RA_APD30_mat);
Loc_RA_APD30_STD = std(mean(RA_APD30_mat,2)); %STD of rows' means
RA_APD50_avg = mean2(RA_APD50_mat);
RA_APD50_STD = std2(RA_APD50_mat);
Loc_RA_APD50_STD = std(mean(RA_APD50_mat,2)); %STD of rows' means
RA_APD80_avg = mean2(RA_APD80_mat);
RA_APD80_STD = std2(RA_APD80_mat);
Loc_RA_APD80_STD = std(mean(RA_APD80_mat,2)); %STD of rows' means
RA_AP_interval_avg = mean(mean(RA_F_peak_interval_mat));
RA_AP_interval_STD_avg = std2(mean(RA_F_peak_interval_mat,1));
RA_AP_amp_CoefVar = mean(std(RA_AP_amplitude_mat, 0, 2)./...
    mean(RA_AP_amplitude_mat,2)); %mean AP amplitude CV of every row

SAN1_APD30_avg = mean2(SAN1_APD30_mat);
SAN1_APD30_STD = std2(SAN1_APD30_mat);
Loc_SAN1_APD30_STD = std(mean(SAN1_APD30_mat,2)); %STD of rows' means
SAN1_APD50_avg = mean2(SAN1_APD50_mat);
SAN1_APD50_STD = std2(SAN1_APD50_mat);
Loc_SAN1_APD50_STD = std(mean(SAN1_APD50_mat,2)); %STD of rows' means
SAN1_APD80_avg = mean2(SAN1_APD80_mat);
SAN1_APD80_STD = std2(SAN1_APD80_mat);
Loc_SAN1_APD80_STD = std(mean(SAN1_APD80_mat,2)); %STD of rows' means
SAN1_AP_interval_avg = mean(mean(SAN1_F_peak_interval_mat));
SAN1_AP_interval_STD_avg = std2(mean(SAN1_F_peak_interval_mat,1));
SAN1_AP_amp_CoefVar = mean(std(SAN1_AP_amplitude_mat, 0, 2)./...
    mean(SAN1_AP_amplitude_mat,2)); %mean AP amplitude CV of every row

SAN2_APD30_avg = mean2(SAN2_APD30_mat);
SAN2_APD30_STD = std2(SAN2_APD30_mat);
Loc_SAN2_APD30_STD = std(mean(SAN2_APD30_mat,2)); %STD of rows' means
SAN2_APD50_avg = mean2(SAN2_APD50_mat);
SAN2_APD50_STD = std2(SAN2_APD50_mat);
Loc_SAN2_APD50_STD = std(mean(SAN2_APD50_mat,2)); %STD of rows' means
SAN2_APD80_avg = mean2(SAN2_APD80_mat);
SAN2_APD80_STD = std2(SAN2_APD80_mat);
Loc_SAN2_APD80_STD = std(mean(SAN2_APD80_mat,2)); %STD of rows' means
SAN2_AP_interval_avg = mean(mean(SAN2_F_peak_interval_mat));
SAN2_AP_interval_STD_avg = std2(mean(SAN2_F_peak_interval_mat,1));
SAN2_AP_amp_CoefVar = mean(std(SAN2_AP_amplitude_mat, 0, 2)./...
    mean(SAN2_AP_amplitude_mat,2)); %mean AP amplitude CV of every row

% Create summary variables csv string

LA_outputSummaryRow = [{file_name2, 'LA_biatrial', ...
    LA_AP_interval_avg, LA_AP_interval_STD_avg, ...
    LA_APD30_avg, LA_APD50_avg, LA_APD80_avg,...
    LA_APD30_STD, LA_APD50_STD, LA_APD80_STD,...
    Loc_LA_APD30_STD, Loc_LA_APD50_STD, Loc_LA_APD80_STD,...
    LA_AP_amp_CoefVar}];
LA_outputSummaryRowString = cellfun(@num2str, LA_outputSummaryRow,...
    'UniformOutput', false);
LA_outputSummaryRowSingleString = strjoin(LA_outputSummaryRowString, ',');

RA_outputSummaryRow = [{file_name2, 'RA_biatrial', ...
    RA_AP_interval_avg, RA_AP_interval_STD_avg, ...
    RA_APD30_avg, RA_APD50_avg, RA_APD80_avg,...
    RA_APD30_STD, RA_APD50_STD, RA_APD80_STD,...
    Loc_RA_APD30_STD, Loc_RA_APD50_STD, Loc_RA_APD80_STD,...
    RA_AP_amp_CoefVar}];
RA_outputSummaryRowString = cellfun(@num2str, RA_outputSummaryRow,...
    'UniformOutput', false);
RA_outputSummaryRowSingleString = strjoin(RA_outputSummaryRowString, ',');

SAN1_outputSummaryRow = [{file_name2, 'SAN1_biatrial', ...
    SAN1_AP_interval_avg, SAN1_AP_interval_STD_avg, ...
    SAN1_APD30_avg, SAN1_APD50_avg, SAN1_APD80_avg,...
    SAN1_APD30_STD, SAN1_APD50_STD, SAN1_APD80_STD,...
    Loc_SAN1_APD30_STD, Loc_SAN1_APD50_STD, Loc_SAN1_APD80_STD,...
    SAN1_AP_amp_CoefVar}];
SAN1_outputSummaryRowString = cellfun(@num2str, SAN1_outputSummaryRow,...
    'UniformOutput', false);
SAN1_outputSummaryRowSingleString = strjoin(SAN1_outputSummaryRowString, ',');

SAN2_outputSummaryRow = [{file_name2, 'SAN2_biatrial', ...
```

```
        SAN2_AP_interval_avg, SAN2_AP_interval_STD_avg, ...
        SAN2_APD30_avg, SAN2_APD50_avg, SAN2_APD80_avg,...
        SAN2_APD30_STD, SAN2_APD50_STD, SAN2_APD80_STD,...
        Loc_SAN2_APD30_STD, Loc_SAN2_APD50_STD, Loc_SAN2_APD80_STD,...
        SAN2_AP_amp_CoefVar}];
    SAN2_outputSummaryRowString = cellfun(@num2str, SAN2_outputSummaryRow,...
        'UniformOutput', false);
    SAN2_outputSummaryRowSingleString = strjoin(SAN2_outputSummaryRowString, ',');

    % Save summary variables in csv file

    outputSummaryFilename = [output_folder, file_name2, '-summary.csv'];

    fileID = fopen(outputSummaryFilename,'w');
    % Header line
    fprintf(fileID,'%s,\n',...
'file_name,Region,AP_interval_avg,AP_interval_STD_avg,APD30_avg,APD50_avg,APD80_avg,AP
D30_STD,APD50_STD,APD80_STD,Loc_APD30_STD,Loc_APD50_STD,Loc_APD80_STD,AP_amp_CoefVar')
;
    % Results line
    fprintf(fileID, '%s\n', LA_outputSummaryRowSingleString);
    fprintf(fileID, '%s\n', RA_outputSummaryRowSingleString);
    fprintf(fileID, '%s\n', SAN1_outputSummaryRowSingleString);
    fprintf(fileID, '%s\n', SAN2_outputSummaryRowSingleString);
    fclose(fileID);




else
    disp('N_ROI not recognized - no summary results generated');
end






%%%%%%%%%%%%%%%%%%%%%%%%%%
% GRAPHS
%%%%%%%%%%%%%%%%%%%%%%%%%%

% Switch for figure plots

if strcmp('jpg', save_figure);

    % Fontsize for plots
    fontSize = 4;


    %%%%%%%%%%%%%%%%%%%%%%%%%%
    % Signal smoothing plots

    % Loop for generating figures

    for i=1:n_rois

    signal_fig(i) = figure(i);

    subplot(5,4,1:3);
    set(gcf,'Visible','off'); %prevent figures to pop up on screen
    plot(t,F_raw{i}, 'b.-'), grid;
    set(gca,'FontSize',fontSize);
    title([file_name2, '_ROI', num2str(i), ' - Optical Mapping - Raw Signal'],...
        'Interpreter', 'none');
    xlim([0,t_max]);
    ylim([F_raw_min{i}-0.1*F_raw_range{i}, F_raw_max{i}+0.1*F_raw_range{i}]);
    xlabel 'Time (ms)', ylabel 'F (AU)';

    subplot(5,4,5:7);
    set(gcf,'Visible','off'); %prevent figures to pop up on screen
    plot(t,f_y{i}, 'g.-'), grid;
    set(gca,'FontSize',fontSize);
    title([file_name2, '_ROI', num2str(i), ' - Optical Mapping - Baseline
Correction'],...
        'Interpreter', 'none');
```

```
    xlim([0,t_max]);
    ylim([F_raw_min{i}-0.1*F_raw_range{i}, F_raw_max{i}+0.1*F_raw_range{i}]);
    xlabel 'Time (ms)', ylabel 'F (AU)';

    subplot(5,4,9:11);
    set(gcf,'Visible','off'); %prevent figures to pop up on screen
    %plot(t,F_avg{i}, 'b.-'), grid;
    plot(t,F_avg{i}, 'b.-', t(F_avg_peaks_ind{i}(1:N_F_avg_peaks{i})), ...
        F_avg_peaks{i}(1:N_F_avg_peaks{i}), 'oc'), grid;
    set(gca,'FontSize',fontSize);

    for f=1:N_F_avg_peaks{i}
    line([t(baseline_start_ind{i}{f}), t(baseline_end_ind{i}{f})],...
        [baseline_mean{i}{f}, baseline_mean{i}{f}],...
        'LineWidth', 2, 'Color', [0 0.6 0]) %baseline detection plot
    end

    title([file_name2, '_ROI', num2str(i), ' - Optical Mapping - Baseline Correction +
Smoothing'],...
        'Interpreter', 'none');
    xlim([0,t_max]);
    ylim([F_avg_min{i}-0.1*F_avg_range{i}, F_avg_max{i}+0.1*F_avg_range{i}]);
    xlabel 'Time (ms)', ylabel 'F (AU)';

    subplot(5,4,13:15);
    set(gcf,'Visible','off'); %prevent figures to pop up on screen
    plot(tt,dF_raw_dt{i}, 'r.-'), grid;
    set(gca,'FontSize',fontSize);
    title([file_name2, '_ROI', num2str(i), ' - Derivative - Raw
Signal'],'Interpreter', 'none');
    xlim([0,t_max]);
    ylim([dF_raw_dt_min{i}-0.1*dF_raw_dt_range{i},
dF_raw_dt_max{i}+0.1*dF_raw_dt_range{i}]);
    xlabel 'Time (ms)', ylabel 'dF/dt (AU/ms)';

    subplot(5,4,17:19);
    set(gcf,'Visible','off'); %prevent figures to pop up on screen
    %plot(tt,dF_avg_dt{i}, 'r.-'), grid;
    plot(tt,dF_avg_dt{i}, 'r.-', t(t_act_ind{i}(1:N_F_avg_peaks{i})), ...
        dF_dt_max{i}(1:N_F_avg_peaks{i}), 'oc'), grid;
    set(gca,'FontSize',fontSize);
    title([file_name2, '_ROI', num2str(i), ' - Derivative - Baseline Correction +
Smoothing'],...
        'Interpreter', 'none');
    xlim([0,t_max]);
    ylim([dF_avg_dt_min{i}-0.1*dF_avg_dt_range{i},
dF_avg_dt_max{i}+0.1*dF_avg_dt_range{i}]);
    xlabel 'Time (ms)', ylabel 'dF/dt (AU/ms)';

    % Zoomed in plots

    subplot(5,4,4);
    set(gcf,'Visible','off'); %prevent figures to pop up on screen
    plot(t,F_raw{i}, 'b.-'), grid;
    set(gca,'FontSize',fontSize);
    title(['Peak: ', num2str(round(N_F_avg_peaks{i}/2))],'Interpreter', 'none');
    xlim([t(F_avg_peaks_ind{i}(round(N_F_avg_peaks{i}/2)))-100,...
        t(F_avg_peaks_ind{i}(round(N_F_avg_peaks{i}/2)))+150]);
    ylim([F_raw_min{i}-0.1*F_raw_range{i}, F_raw_max{i}+0.1*F_raw_range{i}]);
    xlabel 'Time (ms)', ylabel 'F (AU)';

    subplot(5,4,8);
    set(gcf,'Visible','off'); %prevent figures to pop up on screen
    plot(t,f_y{i}, 'g.-'), grid;
    set(gca,'FontSize',fontSize);
    title(['Peak: ', num2str(round(N_F_avg_peaks{i}/2))],'Interpreter', 'none');
    xlim([t(F_avg_peaks_ind{i}(round(N_F_avg_peaks{i}/2)))-100,...
        t(F_avg_peaks_ind{i}(round(N_F_avg_peaks{i}/2)))+150]);
    ylim([F_raw_min{i}-0.1*F_raw_range{i}, F_raw_max{i}+0.1*F_raw_range{i}]);
    xlabel 'Time (ms)', ylabel 'F (AU)';

    subplot(5,4,12);
    set(gcf,'Visible','off'); %prevent figures to pop up on screen
    %plot(t,F_avg{i}, 'b.-'), grid;
    plot(t,F_avg{i}, 'b.-', t(F_avg_peaks_ind{i}), F_avg_peaks{i}, 'oc'), grid;
    set(gca,'FontSize',fontSize);
```

```
    title(['Peak: ', num2str(round(N_F_avg_peaks{i}/2))],'Interpreter', 'none');
    xlim([t(F_avg_peaks_ind{i}(round(N_F_avg_peaks{i}/2)))-100,...
        t(F_avg_peaks_ind{i}(round(N_F_avg_peaks{i}/2)))+150]);
    ylim([F_avg_min{i}-0.1*F_avg_range{i}, F_avg_max{i}+0.1*F_avg_range{i}]);
    xlabel 'Time (ms)', ylabel 'F (AU)';

    subplot(5,4,16);
    set(gcf,'Visible','off'); %prevent figures to pop up on screen
    plot(tt,dF_raw_dt{i}, 'r.-'), grid;
    set(gca,'FontSize',fontSize);
    title(['Peak: ', num2str(round(N_F_avg_peaks{i}/2))],'Interpreter', 'none');
    xlim([t(F_avg_peaks_ind{i}(round(N_F_avg_peaks{i}/2)))-100,...
        t(F_avg_peaks_ind{i}(round(N_F_avg_peaks{i}/2)))+150]);
    ylim([dF_raw_dt_min{i}-0.1*dF_raw_dt_range{i},
dF_raw_dt_max{i}+0.1*dF_raw_dt_range{i}]);
    xlabel 'Time (ms)', ylabel 'dF/dt (AU/ms)';

    subplot(5,4,20);
    set(gcf,'Visible','off'); %prevent figures to pop up on screen
    plot(tt,dF_avg_dt{i}, 'r.-'), grid;
    set(gca,'FontSize',fontSize);
    title(['Peak: ', num2str(round(N_F_avg_peaks{i}/2))],'Interpreter', 'none');
    xlim([t(F_avg_peaks_ind{i}(round(N_F_avg_peaks{i}/2)))-100,...
        t(F_avg_peaks_ind{i}(round(N_F_avg_peaks{i}/2)))+150]);
    ylim([dF_avg_dt_min{i}-0.1*dF_avg_dt_range{i},
dF_avg_dt_max{i}+0.1*dF_avg_dt_range{i}]);
    xlabel 'Time (ms)', ylabel 'dF/dt (AU/ms)';

    % Save figure

    %saveas(signal_fig(i), [file_name2, '_ROI', num2str(i), '_signal'], 'fig');

    %print('-djpeg', '-r300', [file_name2,'_signal.jpg']); %simple jpg export
    r = 300; % pixels per inch
    %set(gcf, 'PaperUnits', 'inches', 'PaperPosition', [0 0 3000 6000]/r); % -
>resolution: 1500x3000
    set(gcf, 'PaperUnits', 'inches', 'PaperPosition', [0 0 1000 2000]/r); % -
>resolution: 500x1000
    print(gcf, '-djpeg', [output_folder, file_name2, '_ROI', num2str(i),
'_signal.jpg']); %jpg export

    end



    %%%%%%%%%%%%%%%%%%%%%%%%%%
    % Electrophysiological variables

    if strcmp('true', AP_figure);

        % Signal action potential plots

        %Vertical plots
        % for i=1:n_rois
        %    AP_fig(i) = figure(n_rois+i);
        %
        %    for f=1:N_F_avg_peaks(358)
        %
        %     subplot(N_F_avg_peaks{i},1,f);
        %     %set(gcf,'Visible','off'); %prevent figures to pop up on screen
        %     plot(t,F_avg{i}, 'b.-'), grid;
        %     %plot(t,F_avg{i}, 'b.-', t(F_avg_peaks_ind{i}), F_avg_peaks{i}, 'oc'),
        %     %grid; plot the circle on top of the peak
        %
        %         for f_bc=1:N_F_avg_peaks{i}
        %             line([t(baseline_start_ind{i}{f_bc}),
t(baseline_end_ind{i}{f_bc})],...
        %             [baseline_mean{i}{f_bc}, baseline_mean{i}{f_bc}],...
        %             'LineWidth', 2, 'Color', [0 0.6 0]) %baseline detection plot
        %         end
        %
        %     title([file_name2, '_ROI', num2str(i), ' - AP number: ', ...
        %         num2str(f)],'Interpreter', 'none');
        %     xlim([t(F_avg_peaks_ind{i}(f))-50,...
        %         t(F_avg_peaks_ind{i}(f))+100]);
```

```
        %     ylim([F_avg_min{i}-0.1*F_avg_range{i},
F_avg_max{i}+0.1*F_avg_range{i}]);
        %     xlabel 'Time (ms)', ylabel 'F (AU)';
        %
        %     end
        %
        % end


        %Horizontal plots

        for i=1:n_rois
           AP_fig(i) = figure(n_rois+i);

           for f=1:N_F_avg_peaks{i}

            % Main AP plots

            subplot(2,N_F_avg_peaks{i},f);
            set(gcf,'Visible','off'); %prevent figures to pop up on screen
            plot(t,F_avg{i}, 'b.-'), grid;
            set(gca,'FontSize',fontSize);
            %plot(t,F_avg{i}, 'b.-', t(F_avg_peaks_ind{i}), F_avg_peaks{i}, 'oc'),
            %grid; plot the circle on top of the peak

            %Plot different lines to the plot

                for f_lines=1:N_F_avg_peaks{i}

                    line([t(baseline_start_ind{i}{f_lines}),
t(baseline_end_ind{i}{f_lines})],...
                    [baseline_mean{i}{f_lines}, baseline_mean{i}{f_lines}],...
                    'LineWidth', 2, 'Color', [0 0.6 0]); %baseline detection plot

                    line([t_act{i}(f_lines), t_act{i}(f_lines)],...
                    [baseline_mean{i}{f_lines}, F_max{i}(f_lines)],...
                    'LineWidth', 0.75, 'Color', [0 0 0],...
                    'LineStyle', '--'); %Activation time vertical line

                    line([t_act{i}(f_lines), t(F_avg_peaks_ind{i}(f_lines))],...
                    [F_max{i}(f_lines), F_max{i}(f_lines)],...
                    'LineWidth', 2, 'Color', [1 0 0]); %Rise time line

                    line([t_act{i}(f_lines), t(APD30_ind{i}(f_lines))],...
                    [F_AP_30{i}(f_lines), F_AP_30{i}(f_lines)],...
                    'LineWidth', 2, 'Color', [1 0 0]); %APD30 line

                    line([t_act{i}(f_lines), t(APD50_ind{i}(f_lines))],...
                    [F_AP_50{i}(f_lines), F_AP_50{i}(f_lines)],...
                    'LineWidth', 2, 'Color', [1 0 0]); %APD50 line

                    line([t_act{i}(f_lines), t(APD80_ind{i}(f_lines))],...
                    [F_AP_80{i}(f_lines), F_AP_80{i}(f_lines)],...
                    'LineWidth', 2, 'Color', [1 0 0]); %APD80 line

                end

            title([file_name2, '_ROI', num2str(i), ' - AP', ...
                num2str(f)],'Interpreter', 'none');
            xlim([t(F_avg_peaks_ind{i}(f))-100,...
                t(F_avg_peaks_ind{i}(f))+150]);
            ylim([F_avg_min{i}-0.1*F_avg_range{i}, F_avg_max{i}+0.1*F_avg_range{i}]);
            xlabel 'Time (ms)', ylabel 'F (AU)';



            % First derivative plot

            subplot(2,N_F_avg_peaks{i},N_F_avg_peaks{i}+f);
            set(gcf,'Visible','off'); %prevent figures to pop up on screen
            plot(tt,dF_avg_dt{i}, 'r.-', t(t_act_ind{i}(1:N_F_avg_peaks{i})), ...
            dF_dt_max{i}(1:N_F_avg_peaks{i}), 'oc'), grid;
            set(gca,'FontSize',fontSize);

            for f_lines=1:N_F_avg_peaks{i}
                line([t_act{i}(f_lines), t_act{i}(f_lines)],...
```

```
                    [dF_avg_dt_min{i}-0.1*dF_avg_dt_range{i}, ...
                    dF_avg_dt_max{i}+0.1*dF_avg_dt_range{i}],...
                    'LineWidth', 0.75, 'Color', [0 0 0],...
                    'LineStyle', '--'); %Activation time vertical line
            end

            title([file_name2, '_ROI', num2str(i), ' - AP', ...
                num2str(f)],'Interpreter', 'none');
            xlim([t(F_avg_peaks_ind{i}(f))-100,...
                t(F_avg_peaks_ind{i}(f))+150]);
            ylim([dF_avg_dt_min{i}-0.1*dF_avg_dt_range{i},
dF_avg_dt_max{i}+0.1*dF_avg_dt_range{i}]);
            xlabel 'Time (ms)', ylabel 'dF/dt (AU/ms)';


           end

           % Save figure

            %saveas(signal_fig(i), [file_name2, '_ROI', num2str(i), '_AP'], 'fig');

            %print('-djpeg', '-r300', [file_name2,'_signal.jpg']); %simple jpg export
            r = 300; % pixels per inch
            %set(gcf, 'PaperUnits', 'inches', 'PaperPosition', [0 0
900*N_F_avg_peaks{i} 2160]/r); % ->resolution: N_AP*450 x 1080
            set(gcf, 'PaperUnits', 'inches', 'PaperPosition', [0 0
300*N_F_avg_peaks{i} 720]/r); % ->resolution: N_AP*150 x 360
            print(gcf, '-djpeg', [output_folder, file_name2, '_ROI', num2str(i),
'_AP.jpg']); %jpg export


        end
    else
        disp('Plotting single AP figures: OFF');
    end

else
    disp('Plotting figures: OFF');

end

end
```

Atrial masking for optical mapping

MATLAB code for automatically masking the atria from the bright field image.

```
function [ image_measurements_output ] = ...
    Img_biatrial_separate_BF_Mask(...
    inputFolder, inputImageFile, outputFolder)
%Img_biatrial_BF_Mask Create a binary mask of the input biatrial image
%   Input variables:
%   - inputFolder - input path
%   - inputImageFile - input image file name
%   - outputFolder - path to save image files
%
%   Output variables:
%   - image_measurements



%%%%%%%%%%%%%%%%%%%%%%%%%%%%%%%%%%%%%%%%%%%%%%%%%%%%
% Image masking for optical mapping analysis
%
% by Klemen Ziberna
%%%%%%%%%%%%%%%%%%%%%%%%%%%%%%%%%%%%%%%%%%%%%%%%%%%%



%%%%%%%%%%%%%%%%%%%%%%%%%%
% Fileparts
IMAGE_FILE = [inputFolder, inputImageFile];

[image_path, image_name, image_ext] = fileparts(IMAGE_FILE);

% Load image

originalImage = imread(IMAGE_FILE);

% Image properties
[rows, columns, numberOfColorChannels] = size(originalImage);

% Double precision conversion and scaled to [0,1]
scaled_originalImage = double(originalImage);
scaled_originalImage = mat2gray(scaled_originalImage);

% Calculate size
[y_size, x_size] = size(scaled_originalImage);

%------------------------------------------------------------------------
%%%%%%%%%%%%%%%%%%%%%%%%%%
% Image pre-processing

image_processed = scaled_originalImage;

% Background - not needed
%image_processed = imtophat(scaled_originalImage, strel('disk', 128));

% Adjust (adjust image intensity)
image_processed = imadjust(image_processed);

% Filter - not needed
%image_processed2 = medfilt2(image_processed);
%filterType = fspecial('gaussian', 50, 10);
%image_processed3 = imfilter(image_processed, filterType);

%%%%%%%%%%%%%%%%%%%%%%%%%%
%%%%%%%%%%%%%%%%%%%%%%%%%%%%%%%%%%%%%%%%%%%%%%%%%%%%%%%%%%%%%%%%%%%%%%%%%%%%
%
% SEPARATE PROCESSING OF LEFT AND RIGHT HALF
%
%%%%%%%%%%%%%%%%%%%%%%%%%%%%%%%%%%%%%%%%%%%%%%%%%%%%%%%%%%%%%%%%%%%%%%%%%%%%
% Vertically split images into halves
```

```
% Middle image border
x_half = round(x_size/2) - 1;

% Split images
left_image = image_processed(1:end, 1:x_half);
right_image = image_processed(1:end, x_half+1:end);

% Calculate image dimensions
[left_y_size, left_x_size] = size(left_image);
[right_y_size, right_x_size] = size(right_image);

% Edge detection (canny algorithm)
canny_sigma_left = 6;  %high SD of Gaussian filter (defualt: 1.4)
canny_sigma_right = 4;

[image_edge_left, cannyTH_L] = ...
    edge(left_image, 'canny', [],canny_sigma_left);
[image_edge_right, cannyTH_R] = ...
    edge(right_image, 'canny', [],canny_sigma_right);

cannyTH = mean(cat(1, cannyTH_L, cannyTH_R),1);

% Merge halves together (for plotting)
image_edge_plot = cat(2, image_edge_left, image_edge_right);

% Remove artefacts (separately for left and right)

artefacts_image_left = ...
    EdgeArtefactRemoval_half(left_y_size, left_x_size, 60, 5); %default 120, 5
artefacts_image_right = ...
    EdgeArtefactRemoval_half(right_y_size, right_x_size, 120, 5); %default 120, 5

image_edge_left = logical(immultiply(image_edge_left, artefacts_image_left));
image_edge_right = logical(immultiply(image_edge_right, artefacts_image_right));

% Remove outer borders (separately for left and right)
outerBorderPixels = 0;

outerBorder_left = ...
    ZerosBorderImage(left_y_size, left_x_size, outerBorderPixels);
outerBorder_right = ...
    ZerosBorderImage(right_y_size, right_x_size, outerBorderPixels);

image_edge_left = immultiply(image_edge_left, outerBorder_left);
image_edge_right = immultiply(image_edge_right, outerBorder_right);

% Remove top and bottom part of image (separately for left and right)
zero_top = 65;
zero_bottom = 20;

TopBottomBorder_left = ...
    ZerosTopBottomImage(left_y_size, left_x_size, zero_top, zero_bottom);
TopBottomBorder_right = ...
    ZerosTopBottomImage(right_y_size, right_x_size, zero_top, zero_bottom);

image_edge_left = immultiply(image_edge_left, TopBottomBorder_left);
image_edge_right = immultiply(image_edge_right, TopBottomBorder_right);

% Remove left and right edge of image (separately for left and right)
zero_left = 15;
zero_right = 10;

LeftBorder_left = ...
    ZerosLeftImage(left_y_size, left_x_size, zero_left);
RightBorder_right = ...
    ZerosRightImage(right_y_size, right_x_size, zero_right);

image_edge_left = immultiply(image_edge_left, LeftBorder_left);
image_edge_right = immultiply(image_edge_right, RightBorder_right);


% Dilate edges (separately for left and right)
edge_se_left = strel('disk', 8); %CUSTOMIZE!!! value: 15-20
edge_se_right = strel('disk', 6);

image_edge_dilate_left = imdilate(image_edge_left, edge_se_left);
```

```
image_edge_dilate_right = imdilate(image_edge_right, edge_se_right);

% Erosion to make left and right similar size (compensate for different
% dilations sizes)
image_edge_dilate_left2 = imerode(image_edge_dilate_left, strel('disk', 2));
image_edge_dilate_right2 = imerode(image_edge_dilate_right, strel('disk', 1));

% Merge left and right images
%image_edge_dilate = ...
%    cat(2, image_edge_dilate_left, image_edge_dilate_right);
image_edge_dilate2 = ...
    cat(2, image_edge_dilate_left2, image_edge_dilate_right2);

% Dilate merged image (to connect borders in the middle)
image_edge_dilate2 = imdilate(image_edge_dilate2, strel('disk', 4));

% Final image
image_edge_beforeHoleFill = image_edge_dilate2;

%%%%%%%%%%%%%%%%%%%%%%%%%%%%%%%%%%%%%
% Hole fill
image_edge_fill = imfill(image_edge_beforeHoleFill, 'holes');

% Smooth the filled object
edge_open_se = strel('disk', 20); %Customize (values: 10-30)
image_edge_fill_erosion = imopen(image_edge_fill, edge_open_se);

% Remove outer border
outerBorderPixels_final = 0;
outerBorder_final = ...
    ZerosBorderImage(y_size, x_size, outerBorderPixels_final);
image_edge_fill_erosion = ...
    immultiply(image_edge_fill_erosion, outerBorder_final);

% Image errode (adjust the size of the mask)
all_final_mask = imerode(image_edge_fill_erosion, strel('disk', 10)); %CUSTOMIZE!!!
value: 15-20

% Take the biggest object for final maks (in case there is more than one)
[labelled_objects, n_objects] = bwlabel(all_final_mask);
object_measurements = regionprops(labelled_objects, 'Area', 'PixelIdxList');

% Display warnings
if n_objects > 1
    disp([inputImageFile, ' Warning: number of objects in mask: ',...
        num2str(n_objects)]);
end

if n_objects < 1
    disp([inputImageFile, ' Warning: empty mask!']);
    return;
end

% Get all the areas
allAreas = [object_measurements.Area];
[sortedAreas, sortIndexes] = sort(allAreas, 'descend');

% Extract the biggest object (could do multiple ones with sortIndexes(1:n)
biggestObject = ismember(labelled_objects, sortIndexes(1));
% Convert from integer labeled image into binary (logical) image.
final_mask = biggestObject > 0; %if more than one object


%---------------------------------------------------------------------------
%%%%%%%%%%%%%%%%%%%%%%%%%%%%%%%%%%%%
% IMAGE MEASUREMENTS TABLE
%%%%%%%%%%%%%%%%%%%%%%%%%%%%%%%%%%%%

image_measurements = struct();

% Obtain image measurements
[labelled_mask, n_obj_mask] = bwlabel(final_mask);
image_measurements = regionprops(labelled_mask, 'Area', 'Perimeter', ...
    'Centroid', 'MajorAxisLength', 'MinorAxisLength', 'Orientation');

% File name
```

```
image_measurements(1).FileName = inputImageFile;

% Number of objects
image_measurements(1).n_obj_mask = n_obj_mask;

% Image size
image_measurements(1).ImageSize = [y_size, x_size];

% Output
image_measurements_output = image_measurements(1);

% Display warnings
if n_obj_mask > 1
    disp([inputImageFile, ' Warning: number of objects in mask: ',...
        num2str(n_obj_mask)]);
end

if n_obj_mask < 1
    disp([inputImageFile, ' Warning: empty mask!']);
    return;
end


% Display information
disp([inputImageFile, ' - Masked area: ', ...
    num2str(image_measurements(1).Area)]);



%-------------------------------------------------------------------------
%%%%%%%%%%%%%%%%%%%%%%%%%%%%%%%%%%%%
% FINAL MASK IMAGE OUTPUT
%%%%%%%%%%%%%%%%%%%%%%%%%%%%%%%%%%%%
imwrite(final_mask, [outputFolder, image_name, '_mask.tif'],'tif');


%%%%%%%%%%%%%%%%%%%%%%%%%%%%%%%%%%%%
% PROCESSING SUMMARY IMAGE
%%%%%%%%%%%%%%%%%%%%%%%%%%%%%%%%%%%%

summary_image = figure;

% Row 1: image intensity scaling
SubplotHistogramMask(3, 1, scaled_originalImage, image_processed, cannyTH(2));
set(gcf,'Visible','off'); %prevent figures to pop up on screen

% Subtitles
subplot(3,3,1);
title('Original image');
subplot(3,3,2);
title('Histogram');
subplot(3,3,3);
title('Processed image');


% Row 2: Edge detection and hole fill
subplot(3, 3, 4);
set(gcf,'Visible','off'); %prevent figures to pop up on screen
imshow(image_edge_plot);
title('Edge detection');

subplot(3, 3, 5);
set(gcf,'Visible','off'); %prevent figures to pop up on screen
imshow(image_edge_beforeHoleFill);
title('Dilation and corners');

subplot(3, 3, 6);
set(gcf,'Visible','off'); %prevent figures to pop up on screen
imshow(final_mask);
title('Hole fill');

% Row 3.1: Final mask overlayed on original image

imageObject_boundaries = bwboundaries(final_mask);
subplot(3, 3, 7);
set(gcf,'Visible','off'); %prevent figures to pop up on screen
```

```
imshow(image_processed);
hold on;
plot(imageObject_boundaries(358)(:,2),...
    imageObject_boundaries(358)(:,1),...
    'r','LineWidth',3);
title('Mask overlay');

% Row 3.2: Major and minor axis overlayed on original image
subplot(3, 3, 8);
set(gcf,'Visible','off'); %prevent figures to pop up on screen
imshow(final_mask);

% Calculate major and minor axis
m_image = image_measurements(1);

xMajor = m_image.Centroid(1) + ...
    [-1 1]*(m_image.MajorAxisLength/2)*cosd(m_image.Orientation);
yMajor = m_image.Centroid(2) + ...
    [-1 1]*(m_image.MajorAxisLength/2)*sind(m_image.Orientation);

xMinor = m_image.Centroid(1) + ...
    [-1 1]*(m_image.MinorAxisLength/2)*sind(m_image.Orientation);
yMinor = m_image.Centroid(2) - ...
    [-1 1]*(m_image.MinorAxisLength/2)*cosd(m_image.Orientation);

% Plot major and minor axis
line(xMajor,yMajor, 'Color', 'g', 'LineWidth', 3);
line(xMinor,yMinor, 'Color', 'b', 'LineWidth', 3);

% Title
title('Major and minor axis');

% Row 3.3 Text data
text_plot = subplot(3, 3, 9);
set(gcf,'Visible','off'); %prevent figures to pop up on screen
title('Analysis');
t_text_plot = text(0, 0.6, sprintf('%s\n%s\n%s\n%s\n%s\n',...
    ['File name: ', inputImageFile], ...
    ['Area: ', num2str(m_image.Area)], ...
    ['Perimeter: ', num2str(m_image.Perimeter)], ...
    ['Major axis length: ', num2str(m_image.MajorAxisLength)], ...
    ['Minor axis length: ', num2str(m_image.MinorAxisLength)]),...
    'Parent', text_plot);
set(t_text_plot, 'interpreter', 'none', 'Color', 'black', 'FontSize', 10);
axis off

% Top title
annotation('textbox', [0 0.9 1 0.1], ...
    'String', ['Processing summary: ', inputImageFile], ...
    'EdgeColor', 'none', ...
    'HorizontalAlignment', 'center',...
    'interpreter', 'none',...
    'FontSize', 18)


%%%%%%%%%%%%%%%%%%%%%%%%%%
% Save figure

r = 150; % pixels per inch
set(gcf, 'PaperUnits', 'inches', 'PaperPosition', [0 0 2048 1536]/r);
print(gcf, '-djpeg', [outputFolder, image_name,'_summary.jpg']); %jpg export
print(gcf, '-depsc', '-tiff', [outputFolder, image_name,'_summary.eps']); %eps export

end
```

Analysis of the radioactively labelled products of arginine metabolism

MATLAB code for automatically detecting and analysing the HPLC scintillation detector trace of ^{14}C labelled arginine metabolism products.

```
function [...
    Arg_peak_time, Arg_peak_Signal, Arg_peak_Area, ...
    Arg_peak_start, Arg_peak_end, ...
    Arg_peak_startInd, Arg_peak_endInd,...
    Cit_peak_time, Cit_peak_Signal, Cit_peak_Area, ...
    Cit_peak_start, Cit_peak_end,...
    Cit_peak_startInd, Cit_peak_endInd,...
    Orn_peak_time, Orn_peak_Signal, Orn_peak_Area, ...
    Orn_peak_start, Orn_peak_end,...
    Orn_peak_startInd, Orn_peak_endInd]...
    = ...
    Analysis_NOS( trace_signal, trace_time )

%Analysis_NOS Analyse the trace for NOS metabolites: arginine, citrulline,
%ornithine
%   Input arguments:
%   - trace_signal
%   - trace_time
%
%   Output arguments:
%

%%%%%%%%%%%%%%%%%%%%%%%%%%
% Temporary variable
%trace_signal = signal;
%trace_time = t;


%%%%%%%%%%%%%%%%%%%%%%%%%%
% Calculate the sampling rate
SR = (length(trace_time)-1)/(trace_time(end)-trace_time(1));


%%%%%%%%%%%%%%%%%%%%%%%%%%
% PEAK ANALYSIS
%%%%%%%%%%%%%%%%%%%%%%%%%%

%%%%%%%%%%%%%%%%%%%%%%%%%%
% Peak specifications

% Arginine
[~, Arg_peak_timeInd] = max(trace_signal);
Arg_peak_time = trace_time(Arg_peak_timeInd);
Arg_minLeft_Peak = 1;
Arg_maxLeft_Peak = 0;
Arg_minRight_Peak = 0;
Arg_maxRight_Peak = 6;

% Citrulline
Cit_peak_time = Arg_peak_time - 2.96;
Cit_minLeft_Peak = 2;
Cit_maxLeft_Peak = 0;
Cit_minRight_Peak = 0.7;
Cit_maxRight_Peak = 2.5;

% Ornithine
Orn_peak_time = Arg_peak_time - 1.35;
Orn_minLeft_Peak = 0.75;
Orn_maxLeft_Peak = 0;
Orn_minRight_Peak = 0;
Orn_maxRight_Peak = 0.9;


%%%%%%%%%%%%%%%%%%%%%%%%%%
```

```
% Analyse peaks

% ARGININE PEAK

% Define the trace section (increase range by 1 to prevent exceeding matrix
dimensions)
Arg_minLeft_Peak_relInd = round(Arg_minLeft_Peak*SR)+1;
Arg_maxRight_Peak_relInd = round(Arg_maxRight_Peak*SR)+1;

% Select the trace section
Arg_time = trace_time(...
    Arg_peak_timeInd-Arg_minLeft_Peak_relInd:...
    Arg_peak_timeInd+Arg_maxRight_Peak_relInd);
Arg_signal = trace_signal(...
    Arg_peak_timeInd-Arg_minLeft_Peak_relInd:...
    Arg_peak_timeInd+Arg_maxRight_Peak_relInd);

% Analyse the trace section
[Arg_peak_time, Arg_peak_Signal, Arg_peak_Area, ...
    Arg_peak_start, Arg_peak_end,...
    Arg_peak_startInd, Arg_peak_endInd] = ...
    PeakAnalysis( Arg_signal, Arg_time,...
    Arg_minLeft_Peak, Arg_maxLeft_Peak, ...
    Arg_minRight_Peak, Arg_maxRight_Peak);

% Change the time indices to absolute indices
Arg_peak_startInd = Arg_peak_startInd + ...
    Arg_peak_timeInd-Arg_minLeft_Peak_relInd;
Arg_peak_endInd = Arg_peak_endInd + ...
    Arg_peak_timeInd-Arg_minLeft_Peak_relInd;

% CITRULLINE PEAK

% Define the trace section (increase range by 1 to prevent exceeding matrix
dimensions)
Cit_peak_timeInd = round(Cit_peak_time*SR);
Cit_minLeft_Peak_relInd = round(Cit_minLeft_Peak*SR)+1;
Cit_maxRight_Peak_relInd = round(Cit_maxRight_Peak*SR)+1;

% Select the trace section
Cit_time = trace_time(...
    Cit_peak_timeInd-Cit_minLeft_Peak_relInd:...
    Cit_peak_timeInd+Cit_maxRight_Peak_relInd);
Cit_signal = trace_signal(...
    Cit_peak_timeInd-Cit_minLeft_Peak_relInd:...
    Cit_peak_timeInd+Cit_maxRight_Peak_relInd);

% Analyse the trace section
[Cit_peak_time, Cit_peak_Signal, Cit_peak_Area, ...
    Cit_peak_start, Cit_peak_end,...
    Cit_peak_startInd, Cit_peak_endInd] = ...
    PeakAnalysis( Cit_signal, Cit_time,...
    Cit_minLeft_Peak, Cit_maxLeft_Peak, ...
    Cit_minRight_Peak, Cit_maxRight_Peak);

% Change the time indices to absolute indices
Cit_peak_startInd = Cit_peak_startInd + ...
    Cit_peak_timeInd-Cit_minLeft_Peak_relInd;
Cit_peak_endInd = Cit_peak_endInd + ...
    Cit_peak_timeInd-Cit_minLeft_Peak_relInd;


% ORNITHINE PEAK

% Define the trace section (increase range by 1 to prevent exceeding matrix
dimensions)
Orn_peak_timeInd = round(Orn_peak_time*SR);
Orn_minLeft_Peak_relInd = round(Orn_minLeft_Peak*SR)+1;
Orn_maxRight_Peak_relInd = round(Orn_maxRight_Peak*SR)+1;

% Select the trace section
Orn_time = trace_time(...
    Orn_peak_timeInd-Orn_minLeft_Peak_relInd:...
    Orn_peak_timeInd+Orn_maxRight_Peak_relInd);
Orn_signal = trace_signal(...
    Orn_peak_timeInd-Orn_minLeft_Peak_relInd:...
```

```
    Orn_peak_timeInd+Orn_maxRight_Peak_relInd);

% Analyse the trace section
[Orn_peak_time, Orn_peak_Signal, Orn_peak_Area, ...
    Orn_peak_start, Orn_peak_end,...
    Orn_peak_startInd, Orn_peak_endInd] = ...
    PeakAnalysis( Orn_signal, Orn_time,...
    Orn_minLeft_Peak, Orn_maxLeft_Peak, ...
    Orn_minRight_Peak, Orn_maxRight_Peak);

% Change the time indices to absolute indices
Orn_peak_startInd = Orn_peak_startInd + ...
    Orn_peak_timeInd-Orn_minLeft_Peak_relInd;
Orn_peak_endInd = Orn_peak_endInd + ...
    Orn_peak_timeInd-Orn_minLeft_Peak_relInd;


end
```

```
function [peak_time, peak_Signal, peak_Area, peak_start, peak_end,...
    peak_startInd, peak_endInd] = ...
    PeakAnalysis( input_signal, input_time,...
    minLeft_Peak, maxLeft_Peak, minRight_Peak, maxRight_Peak)

%PeakAnalysis Analysis of chromatographic peak
%   The function performs the following analysis:
%   - finds the peak, left and right border in the supplied signal
%   - calculates area under the curve
%   - returns the values
%
%   Input variables:
%   - input_signal
%   - input_time
%
%   Find peak edges region (in minutes):
%   - minLeft_Peak - min time left from peak to find start of peak
%   - maxLeft_Peak - max time left from peak to find start of peak
%   - minRight_Peak - min time right from peak to find end of peak
%   - maxRight_Peak - max time right from peak to find end of peak
%
%   Output variables:
%   - peak_time
%   - peak_timeInd
%   - peak_Signal
%   - peak_Area
%   - peak_start
%   - peak_end
%   - peak_startInd
%   - peak_endInd
%

%%%%%%%%%%%%%%%%%%%%%%%%%%%%%%
Switch_PlotAllFigures = 'no'; % turn on if 'yes'

%%%%%%%%%%%%%%%%%%%%%%%%%%%%%%


%%%%%%%%%%%%%%%%%%%%%%%%%%%%%%
% Temporary assignments
% input_time = t(30000:45000); %Arginine
% input_signal = signal(30000:45000);

% input_time = Arg_time;
% input_signal = Arg_signal;
%
% minLeft_Peak = Arg_minLeft_Peak;
% maxLeft_Peak = Arg_maxLeft_Peak;
% minRight_Peak = Arg_minRight_Peak;
% maxRight_Peak = Arg_maxRight_Peak;
%

% Arginine
% minLeft_Peak = 0;
% maxLeft_Peak = 1;
% minRight_Peak = 0;
```

```
% maxRight_Peak = 4;



%%%%%%%%%%%%%%%%%%%%%%%%%%%%%%

% Calculate the sampling rate
SR = (length(input_time)-1)/(input_time(end)-input_time(1));

% Convert the times in relative indices
minLeft_PeakInd = round(minLeft_Peak*SR);
maxLeft_PeakInd = round(maxLeft_Peak*SR);
minRight_PeakInd = round(minRight_Peak*SR);
maxRight_PeakInd = round(maxRight_Peak*SR);


% Step 1 - Find the peak
[peak_Signal, peak_SignalInd] = max(input_signal); %max
peak_timeInd = peak_SignalInd;
peak_time = input_time(peak_timeInd);

% Step 2 - Find the start of the peak
signal_leftStartInd = peak_SignalInd - minLeft_PeakInd;
if signal_leftStartInd < 1 %border condition
    signal_leftStartInd = 1;
end
signal_leftEndInd = peak_SignalInd-maxLeft_PeakInd;

findStart_peak = input_signal(signal_leftStartInd:signal_leftEndInd);
%[peak_SignalStart, peak_startRelInd] = min(findStart_peak);

% Find the first minimum left of the peak (=last minimum in the search
% region)
peak_SignalStart = min(findStart_peak);
peak_startRelInd = find(findStart_peak == peak_SignalStart,1,'last');

peak_startInd = peak_startRelInd + signal_leftStartInd;
peak_start = input_time(peak_startInd);


% Step 3 - Find the end of the peak
signal_rightStartInd = peak_SignalInd+minRight_PeakInd;
signal_rightEndInd = peak_SignalInd+maxRight_PeakInd;
if signal_rightEndInd > length(input_signal) %border condition
    signal_rightEndInd = length(input_signal)-1;
end

[peak_SignalEnd, peak_endRelInd] = ...
    min(input_signal(signal_rightStartInd:signal_rightEndInd));
peak_endInd = peak_endRelInd + signal_rightStartInd;
peak_end = input_time(peak_endInd);

% Step 4 - Calculate the area under the curve

% Create baseline of the input signal
%Minimum values -> baseline

min_input_signal = min(input_signal);
baseline_input_signal = transpose(ones(length(input_signal),1));
baseline_input_signal = baseline_input_signal * min_input_signal;

% Integration
peak_Area = trapz(input_signal(peak_startInd:peak_endInd) ...
    - baseline_input_signal(peak_startInd:peak_endInd)); %total integral
cum_peak_AreaSignal = ...
    cumtrapz(input_signal - baseline_input_signal); %cumulative integral
cumRel_peakAreaSignal = ...
    100*cum_peak_AreaSignal./peak_Area; %relative (%) cumulative integral



%%%%%%%%%%%%%%%%%%%%
% Plot a figure
if strcmpi(Switch_PlotAllFigures, 'yes')
    PeakAnalysisFig = figure;
```

```
    hold on
    yyaxis left
    plot(input_time, baseline_input_signal, 'g:');
    plot(input_time, input_signal);
    y1 = get(gca,'ylim');
    plot([peak_start, peak_start],y1, 'r--');
    plot([peak_end, peak_end],y1, 'r--');

    yyaxis right
    plot(input_time,cumRel_peakAreaSignal, 'color', [1 0.5 0]);
end


end
```

```
function [ output_fig_NOS ] = Figure_NOS( file_name2, signal, t,...
    Arg_peak_time,...
    Arg_peak_Area,...
    Arg_peak_Signal,...
    Arg_peak_start,...
    Arg_peak_end,...
    Arg_peak_startInd,...
    Arg_peak_endInd,...
    Cit_peak_time,...
    Cit_peak_Area,...
    Cit_peak_Signal,...
    Cit_peak_start,...
    Cit_peak_end,...
    Cit_peak_startInd,...
    Cit_peak_endInd,...
    Orn_peak_time,...
    Orn_peak_Area,...
    Orn_peak_Signal,...
    Orn_peak_start,...
    Orn_peak_end,...
    Orn_peak_startInd,...
    Orn_peak_endInd )

%Figure_NOS Function creates a figure of a trace with three individual
%peaks in separate plots
%   Input arguments:
%   - file_name2
%   - signal
%   - t - time
%   - Arg_peak_time
%   - Arg_area
%   - Arg_start_time
%   - Arg_end_time
%   - Cit_peak_time
%   - Cit_area
%   - Cit_start_time
%   - Cit_end_time
%   - Orn_peak_time
%   - Orn_area
%   - Orn_start_time
%   - Orn_end_time
%
%   Output arguments:
%   - output_fig_NOS


%%%%%%%%%%%%%%%%%%%%%%%%%%
% Temporary variables

% file_name2 = samples(3).file_name2;
% signal = samples(3).signal_BC;
% t = samples(3).t_BC;
%
% Arg_peak_time = samples(3).Arg_peak_time;
% Arg_peak_Area = samples(3).Arg_peak_Area;
% Arg_peak_Signal = samples(3).Arg_peak_Signal;
% Arg_peak_start = samples(3).Arg_peak_start;
% Arg_peak_end = samples(3).Arg_peak_end;
```

```
% Arg_peak_startInd = samples(3).Arg_peak_startInd;
% Arg_peak_endInd = samples(3).Arg_peak_endInd;
% Cit_peak_time = samples(3).Cit_peak_time;
% Cit_peak_Area = samples(3).Cit_peak_Area;
% Cit_peak_Signal = samples(3).Cit_peak_Signal;
% Cit_peak_start = samples(3).Cit_peak_start;
% Cit_peak_end = samples(3).Cit_peak_end;
% Cit_peak_startInd = samples(3).Cit_peak_startInd;
% Cit_peak_endInd = samples(3).Cit_peak_endInd;
% Orn_peak_time = samples(3).Orn_peak_time;
% Orn_peak_Area = samples(3).Orn_peak_Area;
% Orn_peak_Signal = samples(3).Orn_peak_Signal;
% Orn_peak_start = samples(3).Orn_peak_start;
% Orn_peak_end = samples(3).Orn_peak_end;
% Orn_peak_startInd = samples(3).Orn_peak_startInd;
% Orn_peak_endInd = samples(3).Orn_peak_endInd;


%%%%%%%%%%%%%%%%%%%%%%%%%%
% Signal processing

% Signal statistics
t_max = max(t);
signal_max =  max(signal);
signal_min =  min(signal);
signal_range = abs(signal_max - signal_min);


% Baseline = minimum value
minBaselineSignal = min(signal);
baselineSignal = transpose(ones(length(signal),1)); %preallocation
baselineSignal = baselineSignal*minBaselineSignal;

% Integration
totalArea = trapz(signal - baselineSignal); %total integral
cumAreaSignal = cumtrapz(signal - baselineSignal); %cumulative integral
cumRelAreaSignal = 100*cumAreaSignal./totalArea; %relative (%) cumulative integral

%%%%%%%%%%%%%%%%%%%%%%%%%%
% Plot trace

% Specifications
%set(0,'defaultlinelinewidth',1);
fontSize = 12;

output_fig_NOS = figure;

% Row 1 - whole trace
subplot(3,3,1:6);
set(gcf,'Visible','off'); %prevent figures to pop up on screen
hold on;
yyaxis left
plot(t,baselineSignal, 'g:');
plot(t,signal, 'b-'), grid;
ylim([signal_min-0.1*signal_range, signal_max+0.1*signal_range]);
ylabel 'Signal (AU)';
y1 = get(gca,'ylim'); %y-axis figure limits
plot([Cit_peak_start, Cit_peak_start],y1, '-.', 'color', [0 0.5 0]);
plot([Cit_peak_end, Cit_peak_end],y1, '-.', 'color', [0 0.5 0]);
plot([Orn_peak_start, Orn_peak_start],y1, '-.', 'color', [0 0 0.5]);
plot([Orn_peak_end, Orn_peak_end],y1, '-.', 'color', [0 0 0.5]);
plot([Arg_peak_start, Arg_peak_start],y1, '-.', 'color', [1 0 0]);
plot([Arg_peak_end, Arg_peak_end],y1, '-.', 'color', [1 0 0]);

yyaxis right
plot(t,cumRelAreaSignal, 'color', [1 0.5 0]);
ylabel 'Relative area (%)';
ylim([0, 100]);

set(gca,'FontSize',fontSize);
title([file_name2, ' - Radioactivity count'],...
    'Interpreter', 'none');
xlim([0, t_max]);
xlabel 'Time (min)';

% Row 2 - individual peaks
```

```
% Citrulline
subplot(3,3,7);
set(gcf,'Visible','off'); %prevent figures to pop up on screen
hold on;
yyaxis left
plot(t,baselineSignal, 'g:');
plot(t,signal, 'b-'), grid;
fill([t(Cit_peak_startInd:Cit_peak_endInd),...
    fliplr(t(Cit_peak_startInd:Cit_peak_endInd))], ...
    [baselineSignal(Cit_peak_startInd:Cit_peak_endInd),...
    fliplr(signal(Cit_peak_startInd:Cit_peak_endInd))],...
    'g');
ylim([signal_min-0.1*Cit_peak_Signal, 1.5*Cit_peak_Signal]);
y2 = get(gca,'ylim'); %y-axis figure limits
plot([Cit_peak_start, Cit_peak_start],y2, '-.', 'color', [0 0.5 0]);
plot([Cit_peak_end, Cit_peak_end],y2, '-.', 'color', [0 0.5 0]);
ylabel 'Signal (AU)';
text(Cit_peak_time, 1.3*Cit_peak_Signal, ...
    {['RT = ',num2str(Cit_peak_time,4)], ...
    ['Area = ',num2str(Cit_peak_Area,5)]}, ...
    'HorizontalAlignment', 'center',...
    'FontSize', 12,...
    'FontWeight', 'bold');

yyaxis right
plot(t,cumRelAreaSignal, 'color', [1 0.5 0]);
ylabel 'Relative area (%)';

set(gca,'FontSize',fontSize);
title(['Citrulline'], 'Interpreter', 'none');
xlim([Cit_peak_start-1,Cit_peak_end+1]);
xlabel 'Time (min)';

% Ornithine
subplot(3,3,8);
set(gcf,'Visible','off'); %prevent figures to pop up on screen
hold on;
yyaxis left
plot(t,baselineSignal, 'g:');
plot(t,signal, 'b-'), grid;
fill([t(Orn_peak_startInd:Orn_peak_endInd),...
    fliplr(t(Orn_peak_startInd:Orn_peak_endInd))], ...
    [baselineSignal(Orn_peak_startInd:Orn_peak_endInd),...
    fliplr(signal(Orn_peak_startInd:Orn_peak_endInd))],...
    'g');
ylim([signal_min-0.1*Orn_peak_Signal, 1.5*Orn_peak_Signal]);
y2 = get(gca,'ylim'); %y-axis figure limits
plot([Orn_peak_start, Orn_peak_start],y2, '-.', 'color', [0 0.5 0]);
plot([Orn_peak_end, Orn_peak_end],y2, '-.', 'color', [0 0.5 0]);
ylabel 'Signal (AU)';
text(Orn_peak_time, 1.3*Orn_peak_Signal, ...
    {['RT = ',num2str(Orn_peak_time,4)], ...
    ['Area = ',num2str(Orn_peak_Area,5)]}, ...
    'HorizontalAlignment', 'center',...
    'FontSize', 12,...
    'FontWeight', 'bold');

yyaxis right
plot(t,cumRelAreaSignal, 'color', [1 0.5 0]);
ylabel 'Relative area (%)';

set(gca,'FontSize',fontSize);
title(['Ornithine'], 'Interpreter', 'none');
xlim([Orn_peak_start-1,Orn_peak_end+1]);
xlabel 'Time (min)';

% Arginine
subplot(3,3,9);
set(gcf,'Visible','off'); %prevent figures to pop up on screen
hold on;
yyaxis left
plot(t,baselineSignal, 'g:');
plot(t,signal, 'b-'), grid;
fill([t(Arg_peak_startInd:Arg_peak_endInd),...
    fliplr(t(Arg_peak_startInd:Arg_peak_endInd))], ...
```

```
    [baselineSignal(Arg_peak_startInd:Arg_peak_endInd),...
    fliplr(signal(Arg_peak_startInd:Arg_peak_endInd))],...
    'g');
ylim([signal_min-0.1*Arg_peak_Signal, 1.5*Arg_peak_Signal]);
y2 = get(gca,'ylim'); %y-axis figure limits
plot([Arg_peak_start, Arg_peak_start],y2, '-.', 'color', [0 0.5 0]);
plot([Arg_peak_end, Arg_peak_end],y2, '-.', 'color', [0 0.5 0]);
ylabel 'Signal (AU)';
text(Arg_peak_time, 1.3*Arg_peak_Signal, ...
    {['RT = ',num2str(Arg_peak_time,4)], ...
    ['Area = ',num2str(Arg_peak_Area,5)]}, ...
    'HorizontalAlignment', 'left',...
    'FontSize', 12,...
    'FontWeight', 'bold');

yyaxis right
plot(t,cumRelAreaSignal, 'color', [1 0.5 0]);
ylabel 'Relative area (%)';

set(gca,'FontSize',fontSize);
title(['Arginine'], 'Interpreter', 'none');
xlim([Arg_peak_start-1,Arg_peak_end+1]);
xlabel 'Time (min)';


%%%%%%%%%%%%%%%%%%%%%%%%%%
% Save figure

%saveas(signal_fig(i), [file_name2, '_ROI', num2str(i), '_signal'], 'fig');

%print('-djpeg', '-r300', [file_name2,'_signal.jpg']); %simple jpg export
r = 150; % pixels per inch
set(gcf, 'PaperUnits', 'inches', 'PaperPosition', [0 0 2048 1536]/r);
%print(gcf, '-djpeg', [output_folder, file_name2, '_ROI', num2str(i), '_signal.jpg']);
%jpg export
print(gcf, '-djpeg', [file_name2,'_signal.jpg']); %jpg export
print(gcf, '-depsc', '-tiff', [file_name2,'_signal.eps']); %eps export

end
```